Proceedings

Seminar on

DESIGN OF EXPOSED BRIDGE PIERS

2. SCOUR, WAVES AND SHIP IMPACT

Seminar in Copenhagen, March 12, 1991

Published December 1993

DANSK VANDBYGNINGSTEKNISK SELSKAB
DANISH SOCIETY OF HYDRAULIC ENGINEERING

Copenhagen November 1993

INTRODUCTION

The present publication contains the contributions of invited speakers to a seminar arranged by the Danish Society of Hydraulic Engineering, March 12, 1991.

Members of the Danish Geotechnical Society, Danish Society of Structural Engineering and Danish Soeciety of Risk Analysis were invited to join the seminar.

The seminar is the second one in a serie covering design of exposed bridge piers exemplified through investigations carried out in connection with Storebæltsforbindelsen.

In the present proceeding various publications covering the themes of the speakers have been used to avoid double work for the speakers. The geotechnical aspects will be described in further detail in a planned Column of a dgf-Bulletin (Danish Geotechnical Society).

Two additional papers on "Geotechnical design for dynamic loading" and on "Die 6,6 km lange West-Brücke über den Grossen Belt als Beispiel einer Spannbetonbrücke für den Strassen- und Eisenbahnverkehr für gezielt hohe Lebensdauer" have been added to the proceeding.

We are very grateful to Storebæltsforbindelsen a/s (Great Belt a/s) for the permission to arrange the seminar and to publish the proceedings.

We hope through the seminar and the proceedings to have demonstrated the rather advanced design methods being used, so that the experiences being gained may be used for the coming bridge projects in Danish areas and elsewhere in the world.

Helge Gravesen

c/o Dansk Geoteknik a/s (Carl Bro Group)
Granskoven 6
DK 2600 Glostrup

Danish Society of Hydraulic Engineering

List of contents

Scour Around Vertical Pile in Waves

B. Mutlu Sumer, Jørgen Fredsøe and
Niels Christiansen

Institute of Hydrodynamics and Hydraulic Engineering
Technical University of Denmark

SCOUR AROUND VERTICAL PILE IN WAVES

By B. Mutlu Sumer,[1] Jørgen Fredsøe,[2] and Niels Christiansen[3]

ABSTRACT: This paper presents the results of an experimental investigation on scour around piles exposed to waves. In addition to the actual scour tests, bed shear-stress measurements and a flow visualization study are carried out. The effects of lee wake and horseshoe vortex are demonstrated to be the two key elements in the scour process. The development of these flow structures mainly depends on the Keulegan-Carpenter (KC) number that hereby becomes the main parameter that governs the equilibrium scour depth on a live bed. Based on the present data, a design equation is established, relating the scour depth to the Keulegan-Carpenter number. For the values of the Keulegan-Carpenter number below six, the scour around the pile practically ceases to exist. The scour depth normalized by the pile diameter is found to increase with increasing Keulegan-Carpenter number and approaches its steady-current value for Keulegan-Carpenter numbers above approximately 100.

INTRODUCTION

Scour around piles in steady currents has been investigated extensively in the last decades. The fluid mechanics of the scour process are relatively well understood. The key element in the scour process is the horseshoe vortex, formed around the pile just above the bed. This vortex, which is formed due to the presence of rotation in the incoming velocity profile, is able to erode a significant amount of sediment away from the neighborhood of the pile. The research indicates that the equilibrium scour depth lies in the interval 1–1.5 D; D being the pile diameter. A comprehensive review of the subject has been given by Breusers et al. (1977) and Hjorth (1975), the latter also presenting a detailed experimental investigation of the increase in the bed shear stress around a pile exposed to current.

Scour around piles in waves and in combined waves plus current, on the other hand, has attracted much attention in recent years, considering its application to offshore structures.

Some field data have been reported by Palmer (1969) where rate and magnitude of scour developed around obstructions exposed to oscillatory wave-induced flows were measured. Das (1970) presented a few laboratory tests made on local scour around vertical cylinders in an oscillating flume. Kawata and Tsuchiya (1988) made similar tests with real waves and further in combined waves and current.

Herbich and his coworkers [see, for example, Wang and Herbich (1983), Herbich et al. (1984), and Eadie and Herbich (1986)], on the other hand, have made an extensive study of scour around piles in combined waves and current.

---

[1] Assoc. Prof., Inst. of Hydrodynamics and Hydr. Engrg., Tech. Univ. of Denmark, DK-2800 Lyngby, Denmark.

[2] Prof., Inst. of Hydrodynamics and Hydr. Engrg., Tech. Univ. of Denmark, DK-2800 Lyngby.

[3] Grad. Student, Inst. of Hydrodynamics and Hydr. Engrg., Tech. Univ. of Denmark, DK-2800 Lyngby.

Note. Discussion open until June 1, 1992. To extend the closing date one month, a written request must be filed with the ASCE Manager of Journals. The manuscript for this paper was submitted for review and possible publication on July 12, 1990. This paper is part of the *Journal of Waterway, Port, Coastal, and Ocean Engineering*, Vol. 118, No. 1, January/February, 1992. ©ASCE, ISSN 0733-950X/92/0001-0015/ $1.00 + $.15 per page. Paper No. 78.

When the case of waves alone is considered, despite the effort put in the study of scour, even the basic scour-depth data are not fully available, however; the existing data are scarce, consisting of only a few test results reported by the previously mentioned investigators such as Das and as Kawata and Tsuchiya. This might be one reason why the resulting scour depth until now has not been evaluated in a systematic manner even in the simple case of waves alone.

The purpose of the present investigation is to study the scour in waves alone in a systematic manner. An extensive series of laboratory scour tests was conducted with piles subject to real waves. Furthermore, in order to enlighten the underlying mechanisms responsible for the scour, a flow visualization study was made, and also the bed shear stress around the pile was measured.

EXPERIMENTAL FACILITY

Scour Experiments

Test Series No. 1

These experiments were carried out in a wave flume, 0.6 m in width, 0.8 m in depth, and 26.5 m in length. The mean water depth was held constant at 40 cm. Four model piles were used with diameters D = 10 mm, 20 mm, 30 mm, and 50 mm. In all the tests, the pipe surface acted as a hydraulically smooth surface. Two sizes of sand grain were used with d_{50} = 0.18 mm and 0.58 mm.

Test Series No. 2

These experiments were carried out in a large wave flume, 4 m in width, 1 m in depth, and 28 m in length. The main purpose of these tests was to provide data with relatively larger diameter pile models. Two cylinders were used as pile models with diameters D = 100 mm and 200 mm. The experiments were conducted for only d_{50} = 0.18-mm size sand.

Test Series No. 3

A few tests were carried out in a 2-m-wide current flume in order to supplement the wave-flume experiments with data representing tidal flow situations. In these experiments the flow direction could be reversed with a period that was long enough for the flow to be considered quasi-steady in each half-cycle. Two model piles were used in these experiments with D = 50 mm and 110 mm. Sand grain size was d_{50} = 0.36 mm. One-directional, steady-current experiments were also conducted for reference purpose.

In test series 2, intense suspension of sand in the flume did not allow the continuous video monitoring of the scour process. Instead, the waves were stopped every 5 min, and the scour depth was measured; the scour-depth measurements were made at four points, namely at the upstream edge of the pipe, at the downstream edge of the pipe, and at the two side edges of it.

Velocity measurements were made by a Dantec laser doppler anemometer (LDA) in test series 1 and 3, and by an ultrasonic velocity meter in test series 2.

Test Conditions

The test conditions together with the experimental results regarding the scour depth are listed in Table 1. In the table: the Shields parameter θ is defined by

$$\theta = \frac{U_{fm}^2}{(s - 1)\,gd} \tag{1}$$

in which d = the sand grain size; g = the acceleration due to gravity; s = the relative density of sediment; and U_{fm} = the maximum value of the undisturbed bed shear velocity, which is calculated by

$$U_{fm} = \sqrt{\frac{f}{2}}\,U_m \tag{2}$$

where f = the friction coefficient; and U_m = the maximum value of the outer oscillatory flow velocity defined by

$$U = U_m \sin(\omega t) \tag{3}$$

where ω = the angular frequency of the motion. For steady current situations, U_{fm} and U_m are replaced by U_f and U, respectively, in which U_f = the undisturbed bed shear velocity and U = the mean flow velocity. Also, in the table, the Keulegan-Carpenter (KC) number is defined by

$$\mathrm{KC} = \frac{U_m T}{D} \tag{4}$$

and the pile Reynolds number by

$$\mathrm{Re} = \frac{U_m D}{\nu} \tag{5}$$

where T = the wave period; and ν = the kinematic viscosity.

Flow-Visualization Experiments

The purpose of the flow visualization experiments was to get an understanding of the near-bed flow processes around a pile exposed to waves, such as the horseshoe vortex and the downstream vortex shedding.

These experiments were conducted in the same wave flume as test series 1 scour experiments. The so-called hydrogen-bubble technique was employed in the experiments. A 25-cm-long and 0.050-mm-diameter copper wire was used as the hydrogen bubble wire. It was stretched in the transverse direction between two points in the transverse direction at a streamwise distance of about 1 cm from the edge of the model pile and at a vertical location of y = 2 mm away from the bed. The model pile was a smooth-surface cylinder with a diameter D = 4 cm. The lowermost 1.2-cm portion of the cylinder was made from a transparent material through which the light was spread out.

The KC number range of the experiments was from practically 0 to about 25 where KC was incremented by about 2. The range of pile Re number was from 2×10^3 to 9×10^3, the upper limit corresponding to the test where KC was 25.

Velocity profile measurements were made in the absence of the pile by the same LDA equipment as that used in the scour tests.

TABLE 1 Experimental Data on Scour Around Vertical Pile. All Data Presented in This Table Are for Live-Bed Conditions

Test series (1)	Run number (2)	Sand size d(mm) (3)	Pile diameter D(mm) (4)	Wave frequency f_w(s^{-1}) (5)	Maximum flow velocity (measured) U_m(cm/s) (6)	Maximum shear velocity U_{fm}(cm/s) (7)	Shields parameters θ (8)	Keulegan-Carpenter number KC (9)	Pile Reynolds number Re (10)	Nondimensional equilibrium scour depth S/D (11)
1[a]	1	0.18	50	0.84	20.8	3.3	0.37	4.9	$1.0 \cdot 10^4$	~0
	2	0.18	50	0.82	22.4	2.3	0.18	5.4	$1.1 \cdot 10^4$	~0
	3	0.18	50	0.40	11.4	1.3	0.06	5.7	$5.7 \cdot 10^3$	~0
	4	0.18	50	0.73	23.3	2.2	0.17	6.4	$1.2 \cdot 10^4$	0.12
	5	0.18	30	0.84	20.8	2.2	0.16	8.2	$6.2 \cdot 10^3$	0.06
	6	0.18	50	0.68	30.7	2.5	0.22	9.1	$1.5 \cdot 10^4$	0.22
	7	0.18	50	0.43	19.3	1.8	0.11	9.0	$9.7 \cdot 10^3$	0.15
	8	0.18	30	0.82	22.4	2.3	0.18	9.1	$6.7 \cdot 10^3$	0.17
	9	0.18	30	0.40	11.2	1.3	0.06	9.2	$3.4 \cdot 10^3$	0.08
	10	0.18	30	0.73	23.3	2.2	0.17	10.6	$7.0 \cdot 10^3$	0.20
	11	0.18	50	0.37	23.7	1.9	0.12	12.9	$1.2 \cdot 10^4$	0.30
	12	0.18	50	0.50	33.9	2.4	0.20	13.6	$1.7 \cdot 10^4$	0.30
	13	0.18	30	0.43	19.3	1.8	0.11	15.0	$5.8 \cdot 10^3$	0.37
	14	0.18	30	0.68	30.7	2.5	0.22	15.1	$9.2 \cdot 10^3$	0.55
	15	0.18	30	0.32	18.3	1.6	0.09	19.1	$5.5 \cdot 10^3$	0.25
	16	0.18	30	0.50	30.4	2.3	0.19	20.2	$9.1 \cdot 10^3$	0.75
	17	0.18	50	0.37	37.8	2.4	0.20	20.4	$1.9 \cdot 10^4$	0.43
	18	0.18	30	0.37	23.7	1.9	0.12	21.4	$7.1 \cdot 10^3$	0.42
	19	0.18	20	0.43	19.3	1.8	0.11	22.4	$3.9 \cdot 10^3$	0.43
	20	0.18	20	0.34	22.2	1.8	0.11	32.3	$4.4 \cdot 10^3$	0.58
	21	0.18	30	0.28	26.8	1.9	0.12	32.3	$8.0 \cdot 10^3$	0.42
	22	0.18	30	0.37	37.8	2.4	0.20	34.0	$1.1 \cdot 10^4$	0.67
	23	0.18	20	0.37	37.8	2.4	0.20	51.0	$7.6 \cdot 10^3$	0.80
	24	0.18	10	0.37	37.8	2.4	0.20	102	$3.8 \cdot 10^3$	1.10
	25	0.58	50	0.82	22.4	2.3	0.05	5.4	$1.1 \cdot 10^4$	~0
	26	0.58	50	0.73	23.3	2.2	0.05	6.4	$1.2 \cdot 10^4$	~0
	27	0.58	50	0.55	19.9	1.9	0.04	7.2	$1.0 \cdot 10^4$	~0
	28	0.58	30	0.82	22.4	2.3	0.05	9.1	$7.0 \cdot 10^4$	0.05
	29	0.58	30	0.73	23.3	2.2	0.05	10.6	$7.0 \cdot 10^4$	0.04
	30	0.58	30	0.55	19.9	1.9	0.04	12.1	$6.0 \cdot 10^4$	0.12
	31	0.58	50	0.37	23.7	1.9	0.04	12.9	$1.2 \cdot 10^4$	0.18
	32	0.58	50	0.50	33.9	2.4	0.06	13.6	$1.7 \cdot 10^4$	0.20

	33	0.58	20	0.55	19.9	1.9	0.04	18.1	$4.0 \cdot 10^3$	0.50
	34	0.58	30	0.37	23.7	1.9	0.04	21.4	$7.1 \cdot 10^3$	0.57
	35	0.58	20	0.43	19.3	1.8	0.04	22.4	$3.9 \cdot 10^3$	0.72
	36	0.58	30	0.50	33.9	2.4	0.06	22.6	$1.0 \cdot 10^4$	0.52
	37	0.58	20	0.37	23.7	1.9	0.04	32.1	$4.7 \cdot 10^3$	0.54
2[b]	38	0.18	100	0.53	23.1	2.0	0.14	4.4	$2.3 \cdot 10^4$	~0
	39	0.18	200	0.22	30.1	1.8	0.11	6.7	$6.0 \cdot 10^4$	0.032
	40	0.18	200	0.22	32.6	1.9	0.13	7.3	$6.5 \cdot 10^4$	0.055
	41	0.18	100	0.33	25.2	1.8	0.11	7.6	$2.5 \cdot 10^4$	0.12
	42	0.18	200	0.22	39.1	2.0	0.14	8.8	$7.8 \cdot 10^4$	0.057
	43	0.18	200	0.22	46.9	2.3	0.19	10.5	$9.4 \cdot 10^4$	0.085
	44	0.18	200	0.22	53.3	2.5	0.22	12.0	$1.1 \cdot 10^5$	0.11
	45	0.18	100	0.22	30.1	1.8	0.11	13.4	$3.0 \cdot 10^4$	0.15
	46	0.18	100	0.22	32.6	1.9	0.13	14.6	$3.3 \cdot 10^4$	0.22
	47	0.18	100	0.22	39.1	2.0	0.14	17.6	$3.9 \cdot 10^4$	0.25
	48	0.18	100	0.22	46.9	2.3	0.19	21.0	$4.7 \cdot 10^4$	0.24
	49	0.18	100	0.22	53.3	2.5	0.22	24.0	$5.3 \cdot 10^4$	0.31
3[c]	50	0.36	110	$3.3 \cdot 10^{-3}$	47.1	2.4	0.10	1.285	$5.2 \cdot 10^4$	0.92
	51	0.36	50	$3.3 \cdot 10^{-3}$	47.1	2.4	0.10	2.826	$2.4 \cdot 10^4$	1.56
	52	0.36	50	$1.7 \cdot 10^{-3}$	47.1	2.4	0.10	5.626	$2.4 \cdot 10^4$	1.20
	53	0.36	50		47.1	2.5	0.10	∞	$2.4 \cdot 10^4$	1.30

[a] Test series 1: Small wave-flume experiments.
[b] Test series 2: Large wave-flume experiments.
[c] Test series 3: Current flume experiments.

Bed Shear-Stress Measurements

These measurements were carried out in a *U*-shaped oscillatory flow tunnel, 30 cm in width and 29 cm in height. This tunnel is essentially the same as that described by Jensen et al. (1989). The bed shear stress was measured with a flush-mounted Dantec 55R46 hot-film probe. A cylinder, 5 cm in diameter and 29 cm in length, with a smooth surface was placed vertically in the tunnel, extending the whole tunnel height. The bed shear stress was measured at various streamwise and transverse distances of the cylinder from the shear-stress probe. The free-stream velocity at the centerline of the tunnel was measured simultaneously with the bed shear stress, using the LDA equipment.

The ratio of the tunnel width to the pipe diameter was 7.8. According to the potential flow theory, the blockage effect for this value of the width-to-diameter ratio is less than 1%. The range of the KC number in the bed shear-stress measurements was from 4 to 120 and that of the pile Re number from 10^3 to 3×10^4.

THE PROCESS OF SCOUR

The scour process around structures occurs because the sediment transport capacity is larger in the vicinity of the structure than away from it. This increase in local transport capacity can be caused by several factors.

If we consider current alone, the increase in the transport capacity is a combination of the local increase in the bed shear stress and the transporting current term.

The local increase in the bed shear stress occurs partly due to contraction in the streamlines and partly due to the occurrence of a complicated three-dimensional vortex system in front of and behind the cylinder. This system partly stems from the downstream vortex shedding and partly from the formation of the horseshoe vortex, which is a secondary vortex formed due to the unbalance between centrifugal forces and pressure forces because of rotation in the incoming flow velocity profile, like the helical flow in a river bend. In current alone, this horseshoe vortex has been described extensively in the literature (Breusers et al. 1977; Hjorth 1975).

It must be mentioned that the presence of the local vortex structures may change the flow pattern tremendously in the neighborhood of the cylinder. For instance, the local increase in the flow velocity due to the contraction of streamlines can no longer be described by the potential flow solution, as indicated by some of the experiments in the present work.

In the case of the combined waves and current, the presence of waves modifies the vortex structure considerably. As an example, if we compare the current-alone situation with the waves-alone case, the extension of the vortex shedding pattern becomes quite different. Also, the horseshoe vortex must be expected to differ very much from that of waves-alone situation as the distribution of rotation in a wave-boundary layer is highly different from that found in a steady-current boundary-layer velocity profile.

In the case of dominating wave-action, the transporting term responsible for carrying the sediment away from the structure also becomes more complex. Even in the case of waves alone, some steady current pattern due to steady streaming (Schlichting 1979, p. 431) around the cylinder must be expected. However, this pattern must also be expected to be quite different from that described by Schlichting when the vortex structures are present around the structure.

However, in the waves-alone case, the most important transporting term is probably the wave-orbital velocities themselves, which, for a slender cylinder, is able to transport sediment several pile diameters away from the structure where the sediment eventually may settle before the flow reversal.

Finally, it must be mentioned that it is common to distinguish between the live bed scour where sediment transport takes place, also far away from the cylinder, and the clear-water scour, in which case sediment transport takes place only close to the structure, due to the increased transport capacity.

Near-Bed Flow Around a Pile

The near-bed flow around a pile partly consists of the horseshoe vortex formed at the seabed and partly of the vortex shedding pattern at the lee side of the pile (Fig. 1), as mentioned previously.

Horseshoe Vortex

The horseshoe vortex is formed at the seabed because of the rotation in the incoming flow velocity (Fig. 1). In waves, this rotation is formed in the wave boundary layer. However, the horseshoe vortex is insignificant when the wave boundary layer is thin.

Fig. 2 presents the flow pictures at the upstream side of the pile for various values of KC number. In the figure, the thickness of the wave boundary layer δ is also given. Here δ is the thickness of the wave boundary layer that develops over the bed in the absence of the pile. The δ values are determined from the measured velocity profiles.

The crescent shape figure in the pictures, designated by A in Fig. 2(*b*), represents the lowermost, transparent portion of the cylinder through which the light spreads out. The existence of the horseshoe vortex manifests itself in the pictures by the absence of the bubbles in the immediate surrounding of the cylinder [Fig. 2(*d*)], while the presence of the bubbles in the immediate

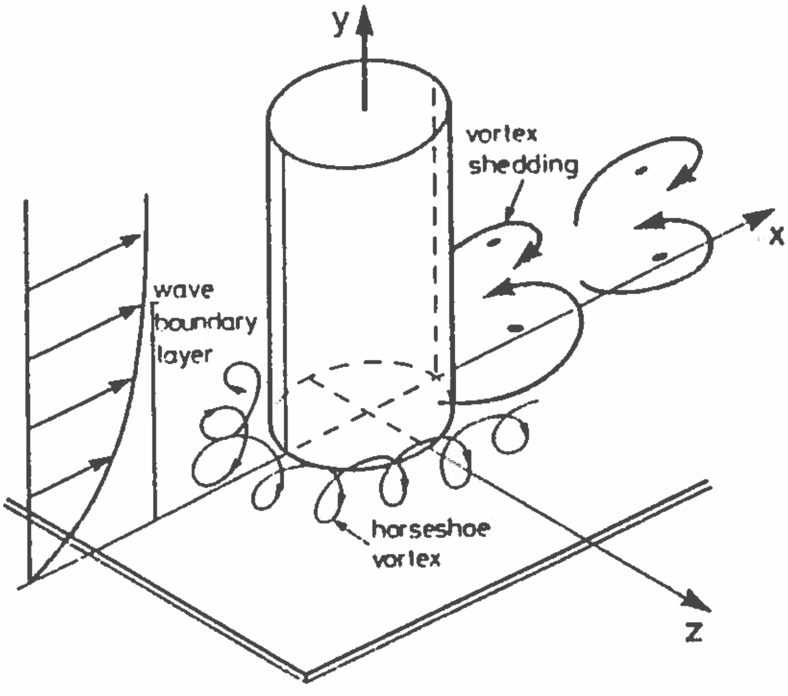

FIG. 1. Near-Bed Flow Around Pile

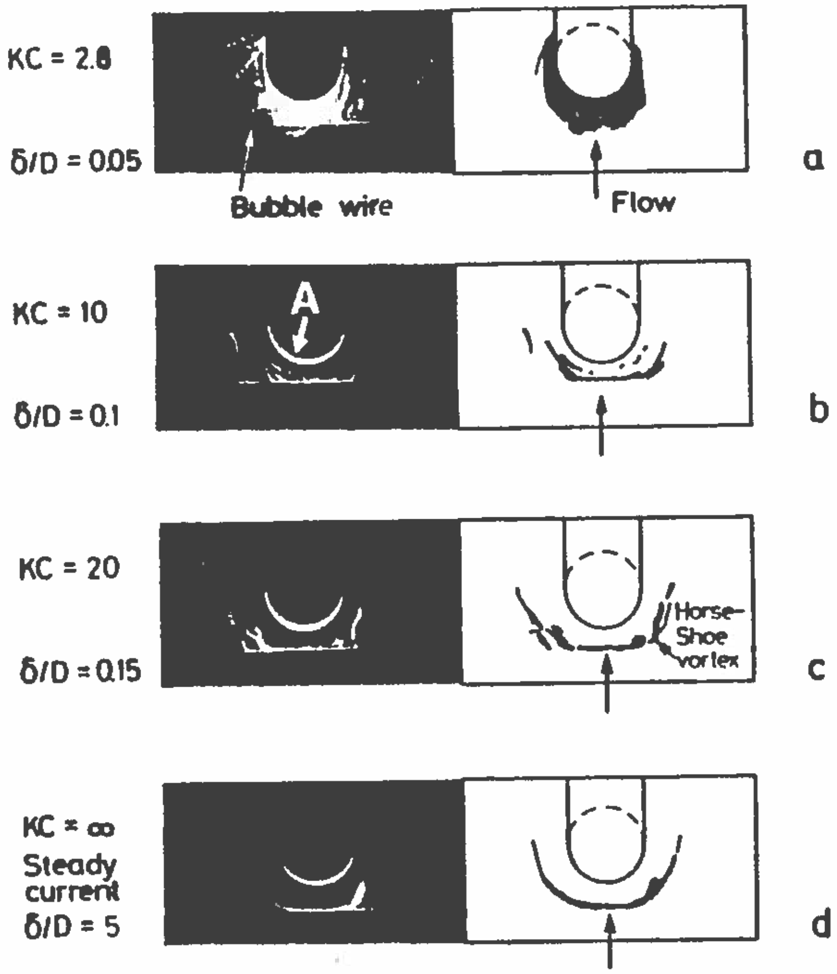

FIG. 2. Near-Bed Flow Picture at Upstream Side of Pile. A: Lowermost Portion of Cylinder (Made of Transparent Material) through which Light Spreads Out. The Horseshoe Vortex for (*b*), (*c*) and (*d*). ωt = 100° in (*a*), 130° in (*b*), and 120° in (*c*)

surrounding of the cylinder means that the horseshoe vortex is nonexistent [Fig. (2*a*)].

As is seen, the horseshoe vortex does not exist for the case where the wave boundary-layer thickness is the smallest [Fig. 2(*a*)]. As the wave boundary-layer thickness increases, however, the horseshoe vortex becomes more and more pronounced, [Figs. 2(*b*)–2(*d*)].

In Fig. 3, results are plotted of the present flow visualization analysis. The figure indicates that no horseshoe vortex exists for KC numbers below 6. The horseshoe vortex first comes into existence when KC becomes 6 and is maintained over a larger and larger span of ωt, thus it becomes more and more pronounced, as the KC number is increased. This is a direct consequence of the effect of the wave boundary layer thickness in relation to the pile diameter. As the KC number increases, the thickness of the wave boundary layer increases, and consequently the horseshoe vortex becomes more pronounced.

Vortex Shedding

The vortex shedding occurs at the lee side of the pile as a result of the interaction between the two shear layers issuing from the side edges of the pile. The vortex shedding pattern in oscillatory flows is governed primarily by the KC number (Williamson 1985).

Fig. 4 shows the vortex shedding pattern at the downstream side of the

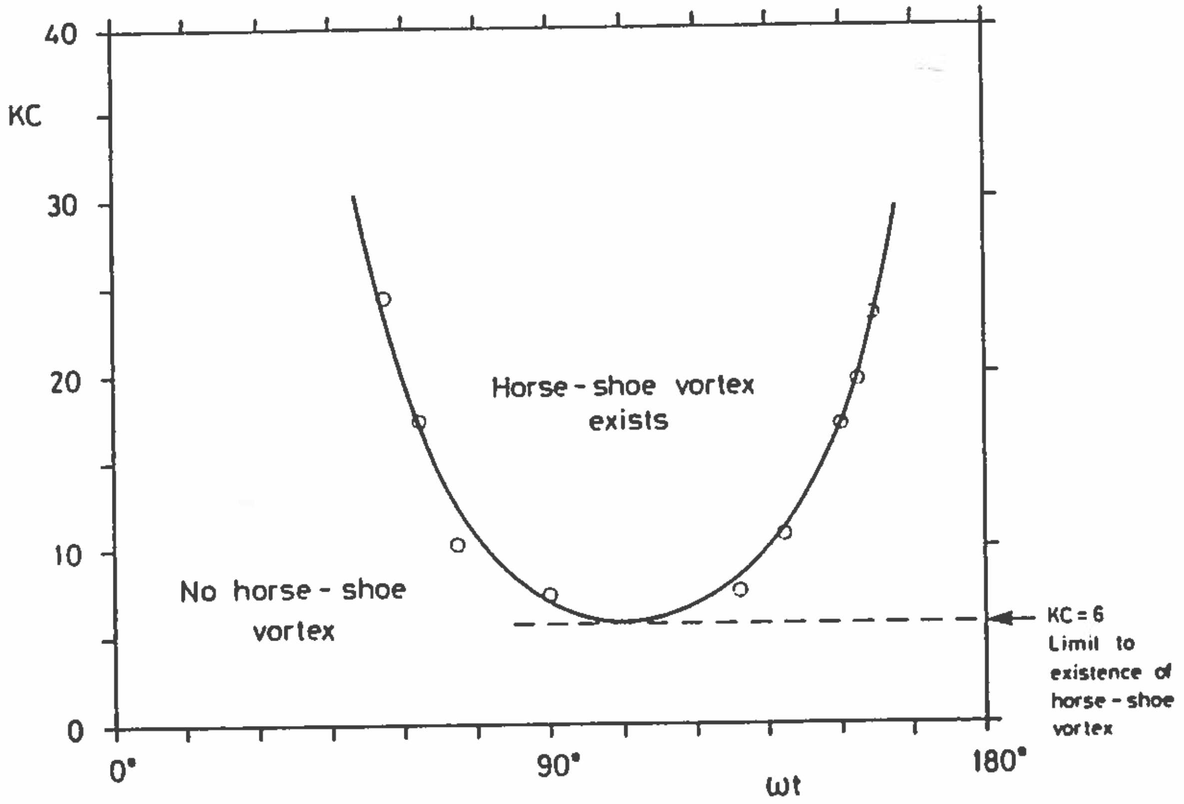

FIG. 3. Diagram Showing at which Value of ωt Horseshoe Vortex Exists

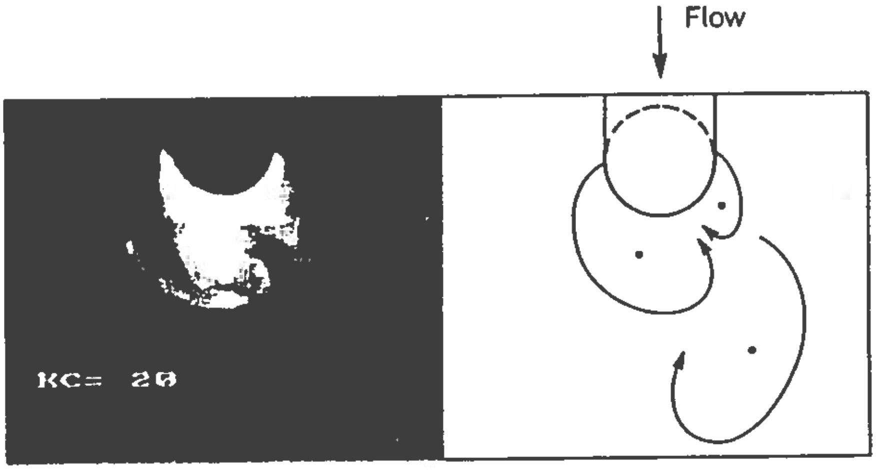

FIG. 4. Near-Bed Flow Picture at Downstream Side of Pile. Vortex Shedding. $\omega t = 115°$

cylinder obtained for the test where KC = 20. The results of the present flow visualization analysis indicate that no vortex shedding occurs for KC below 6. This result is in agreement with that corresponding to a free cylinder (Williamson 1985). For KC > 6, a vortex street is formed at the lee side of the pile by the vortices shed from the pile. The streamwise extent of this street, L, is increased linearly with KC, corresponding to

$$\frac{L}{D} = 0.3\text{KC} \quad \dots\dots\dots\dots\dots\dots\dots\dots\dots\dots\dots \quad (6)$$

The preceding equation is based on the present flow visualization data.

Bed Shear Stress

Figs. 5 and 6 present the bed shear stress data where the bed shear stress is plotted against the streamwise and transverse distances from the pile in the form of the amplification factor defined by

$$\alpha = \frac{\max|\bar{\tau}_0|}{\bar{\tau}_{0m}} \quad \text{(7)}$$

in which $\bar{\tau}_0$ = the mean bed shear stress in the presence of the pile; and $\bar{\tau}_{0m}$ = the maximum value of the undisturbed mean bed shear stress.

Fig. 7, on the other hand, illustrates how, at a given location, the amplification factor varies with the KC number.

RESULTS OF THE SCOUR EXPERIMENTS AND ANALYSIS

Fig. 8 gives a view of the scour hole corresponding to test 17 at stage t = 10 min in which t = the time measured from the instant where the onset of scour occurs. The scour hole has a shape of a truncated cone. As is seen from the figure, the streamwise extents and the transverse extents of the

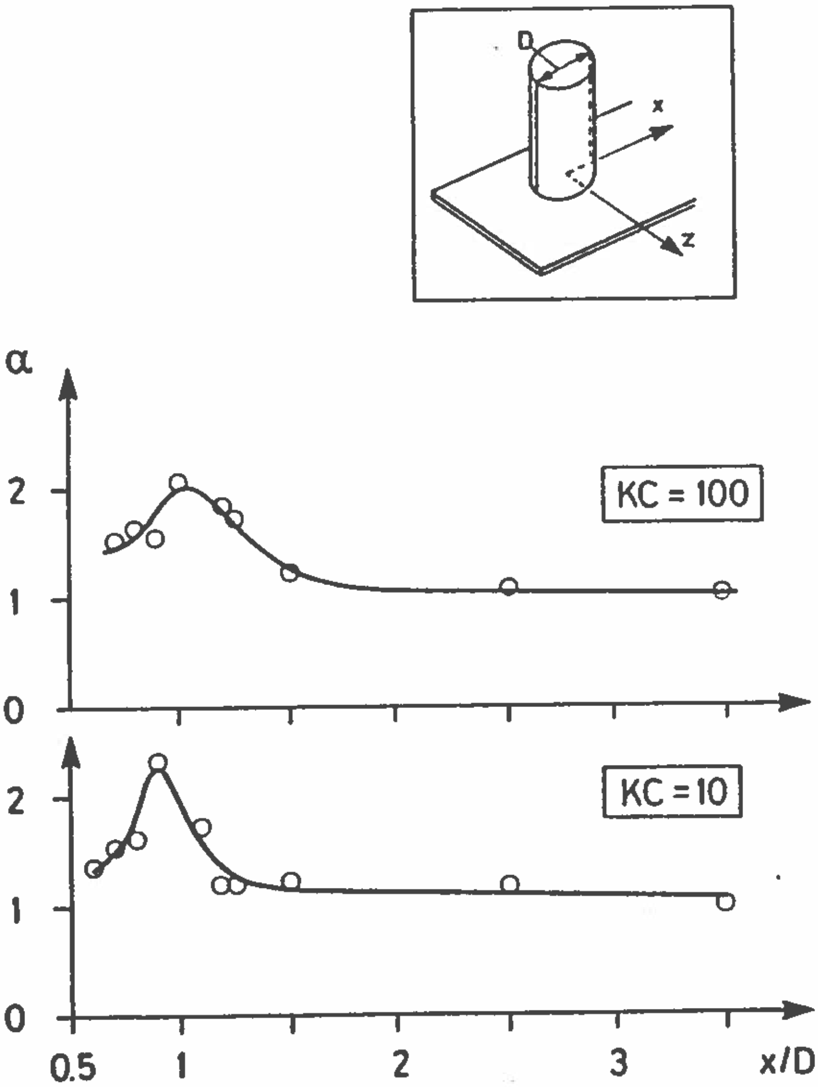

FIG. 5. Bed Shear-Stress Amplification with Respect to Streamwise Distance from Pile Along the x-Axis

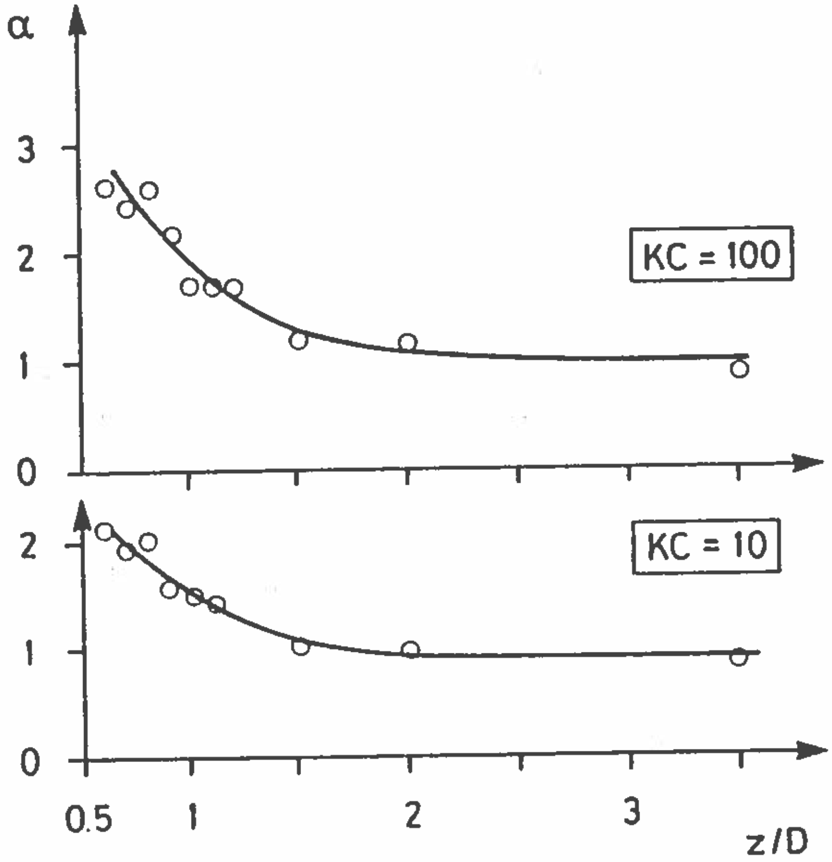

FIG. 6. Bed Shear-Stress Amplification With Respect to Transverse Distance from Pile along z-Axis

scour hole fit quite well with the bed shear-stress picture given in Figs. 5 and 6.

Fig. 9 gives an example, illustrating how the scour depth develops wit respect to time. Note that the scaling used to normalize the time, namely $D^2/\sqrt{g(s-1)d^3}$, has been obtained from dimensional considerations.

The equilibrium scour depth S is obtained when the sediment transport in the scour hole is equal to the sediment transport far from the pile. This depth normalized by the pile diameter may depend on the following nondimensional parameters:

$$\frac{S}{D} = \frac{S}{D}(\theta, \mathrm{Re}, k^*, \mathrm{KC}) \quad \ldots\ldots\ldots\ldots\ldots \quad (8)$$

in which $k^* = k/D$, k being the surface roughness of the pile.

Fig. 10 tests the dependence of the normalized equilibrium scour depth upon the Shields parameter θ and the Re number, using the data in Table 1.

As far as the influence of θ is concerned, this should be examined in two different categories: the clear-water case where the sediment far from the pile is not moving, and the live-bed case where it is in motion. It can be argued that, in the case of live bed, the variation of S/D with θ is weak, as has been discussed by the authors in the case of scour below a pipeline (Sumer and Fredsøe, 1990). The data plotted in Fig. 10 correspond to the live-bed category. Examination of Fig. 10 indicates that although there is a very weak tendency that S/D assumes slightly larger values with increasing θ in the upper two diagrams, this dependency does not even exist regarding the rest of the data plotted in the figure.

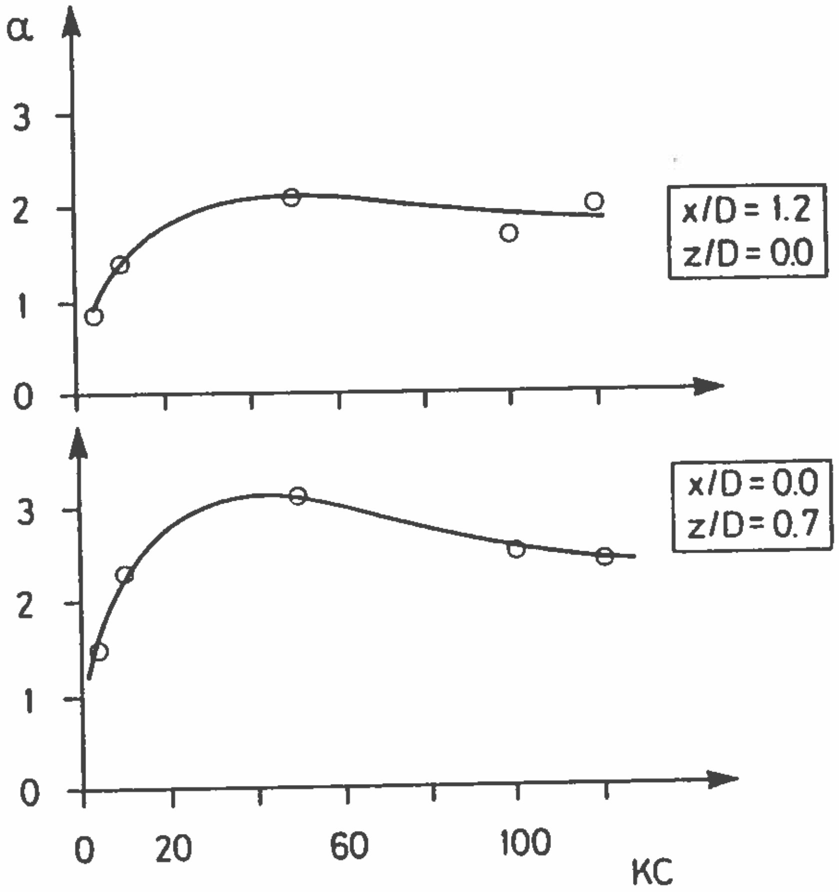

FIG. 7. Bed Shear-Stress Amplification as Function of KC Number

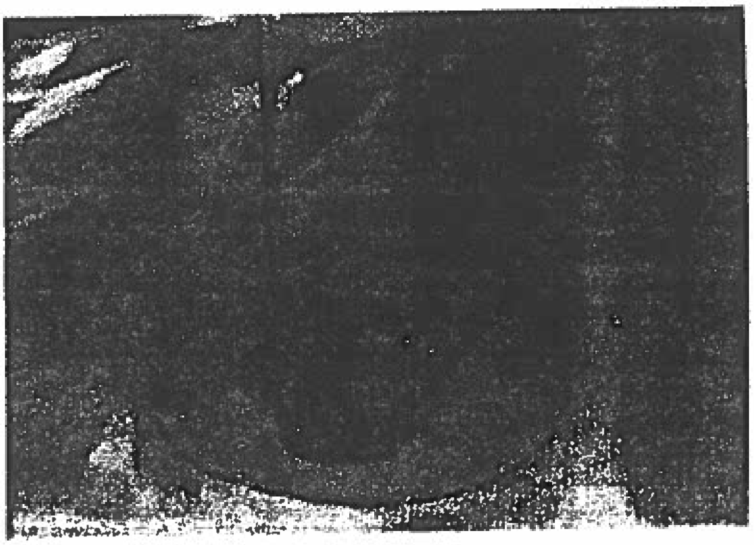

FIG. 8. Photograph of Scour Hole

As for the influence of Re number, this together with the influence of k^*, appear through their effects on the downstream flow of the pile. If the surface of the pile acts as a rough wall, the wake flow is almost unaffected by the Re number, while for a hydraulically smooth-surface pile, some influence of the Re number is expected on the downstream vortex shedding pattern, and thus on the scour depth. However, Fig. 10 indicates practically no Re number dependence, at least for the Re number range of the present data. Nevertheless, the following should be noted. For Re number around $10^5 - 3 \times 10^5$, the transition from subcritical to supercritical flow occurs

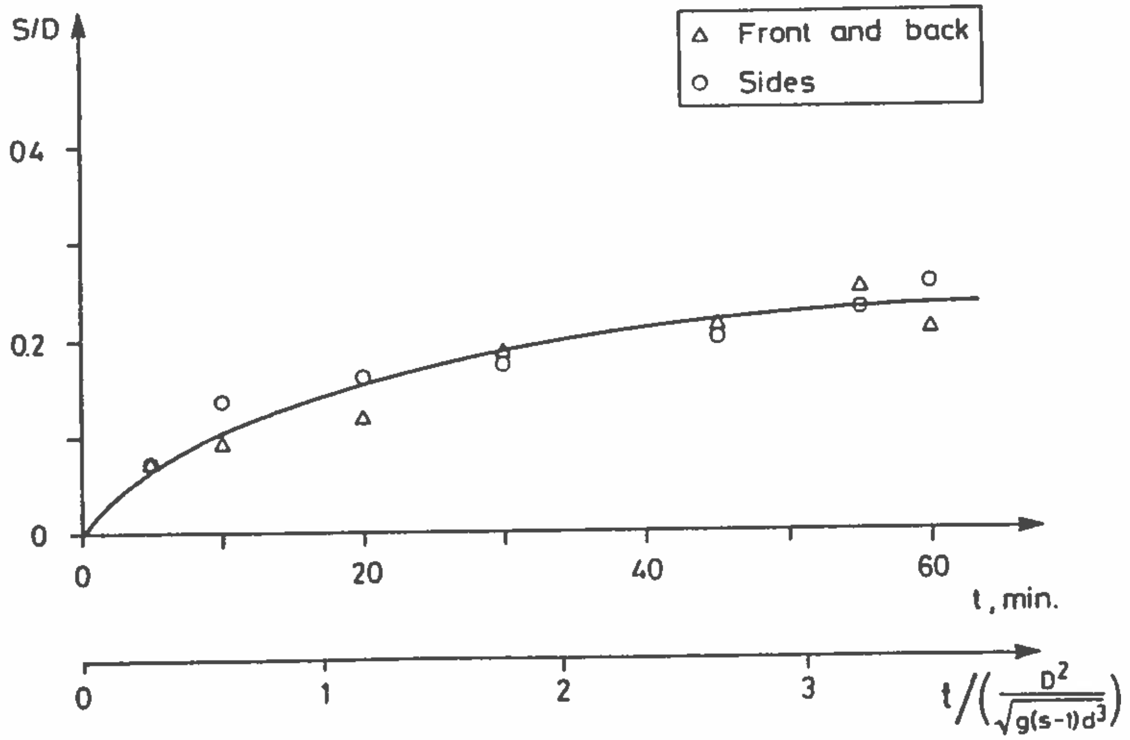

FIG. 9. Time Development of Scour Depth. Test 46

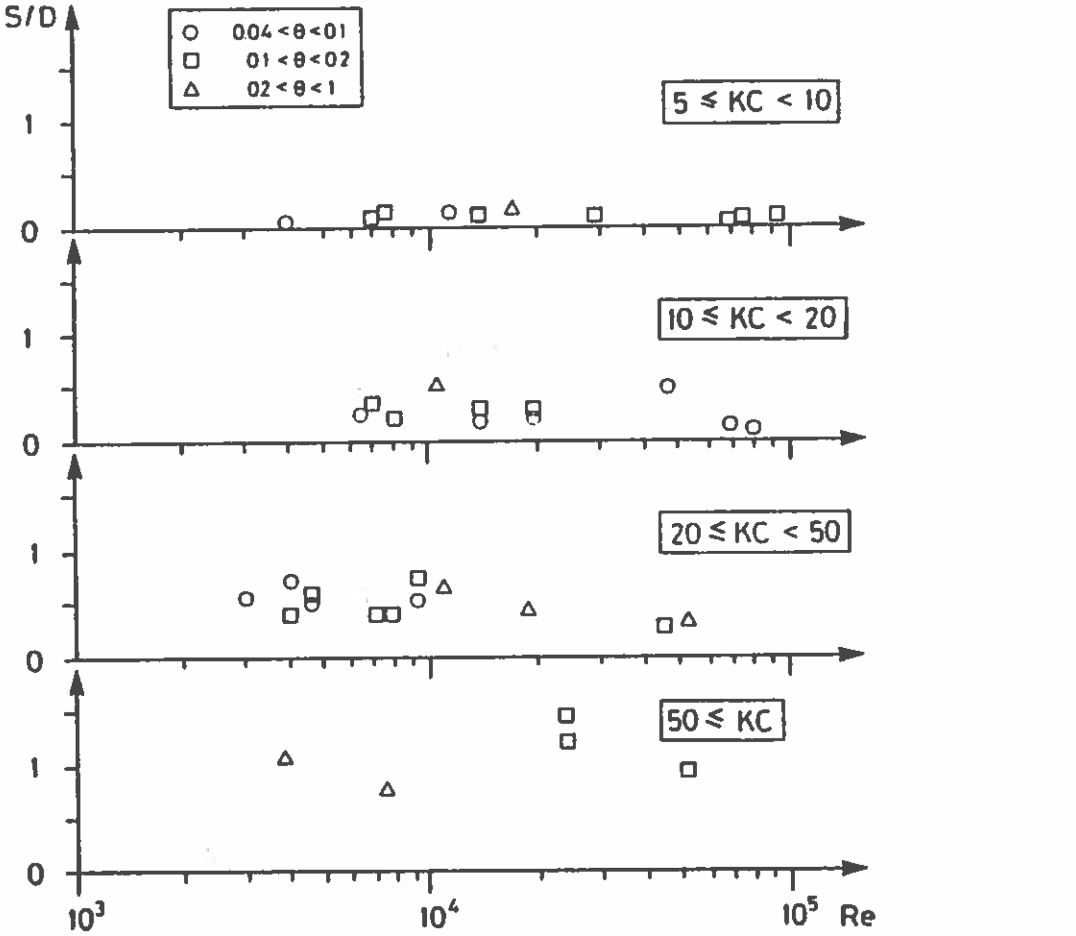

FIG. 10. Equilibrium Scour Depth Normalized with Pile Diameter as Function of θ, Re and KC. Live Bed ($\theta > \theta_{cr}$)

(Schewe 1983; Sumer and Fredsøe 1989). In a previous study (Sumer and Fredsøe 1990), it was demonstrated that this Re number range coincides with the range where a slight decrease in the scour depth occurs for the scour below a pipeline. As in the pipeline situation, a small decrease in the scour depth might be expected for this Re number range for the present case, too. However, it was not possible to verify this by the available experimental facility.

KC Dependence

The KC number in the formulation of the process makes its way through the two effects: (1) The vortex shedding at the lee side of the pile; and (2) the horseshoe vortex formed at the bed at the upstream side of the pile.

Observations show that the vortices shed from the pile erode the bed in such a way that each shed vortex acts like a cyclone, sweeping the sediment grains into its core region where the grains are lifted into the upper portion of the vortex by the updraft. Since the extension of the vortex shedding pattern plus the formation of shed vortices, including their circulation, are governed primarily by the KC number, it might therefore be expected that the resulting scour itself is governed mainly by this parameter, too. It should be noted that there are two other parameters, namely Re and k^*, which are involved in the process of formation and extension of the vortex shedding pattern. However, their role, regarding the formation and extension of the vortex shedding pattern, when compared with that of KC number, appears to be of secondary importance and therefore their influence in the resulting scour is insignificant, as has been demonstrated in the previous subsection.

The horseshoe vortex, on the other hand, is effective in eroding the bed at the upstream side of the pile. It is clear from the previous section that the formation and extension (both in space and in time) of the horseshoe vortex is also governed by the KC number. Thus it might be expected that the scour induced by the horseshoe vortex is governed by the same parameter, namely the KC number.

Fig. 11 shows the variation in the normalized equilibrium scour depth with the KC number. The figure clearly demonstrates that the normalized scour depth correlates remarkably well with the KC number. The figure further demonstrates the following.

1. The scour depth is practically nil for the values of KC number below 6. This is explained as follows. First of all, as mentioned previously, both the vortex shedding and the horseshoe vortex are nonexistent for this range of KC number, thus their contribution to the scour should be zero. The scour may still occur, however, simply because of the increase in the local velocities caused by the apparent contraction of the streamlines around the pile. Yet, for small KC numbers such as KC < 6, Fig. 7 indicates that this increase in the local velocities is insignificant; indeed, the bed shear stress in the immediate neighborhood of the pile appears to be quite close to its undisturbed value for such small KC numbers, so the scour at these low KC numbers should be expected to be insignificant, as observed in Fig. 11.

2. The scour depth increases with increasing KC number. This increase is partly due to the increased extension of the lee wake [(6)] and partly due to the increased presence and strength of the horseshoe vortex with increasing KC number.

3. The scour depth approaches a constant value for large values of KC num-

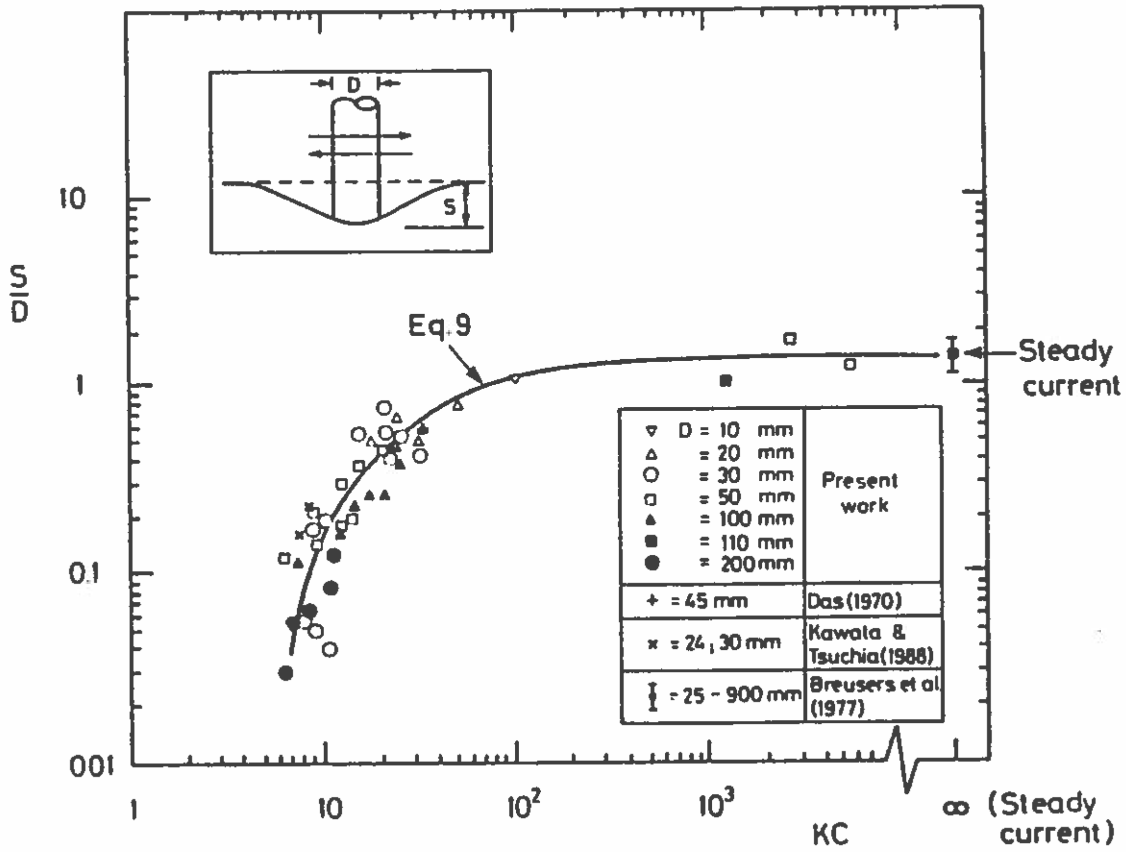

FIG. 11. Equilibrium Scour Depth versus KC Number. Live Bed ($\theta > \theta_{cr}$)

ber. This is expected, because, for large KC numbers: (1) The contribution of the lee-wake vortices to the equilibrium scour depth is expected to approach a constant value, considering the finite lifetime of the vortices; and (2) the contribution of the horseshoe vortex to the equilibrium scour depth is also expected to approach a constant value since the KC dependence of the horseshoe vortex disappears for large values of KC number.

Since the constant value attained by the normalized scour depth S/D is the same as that obtained for steady currents (namely $S/D \rightarrow 1.3$ as KC $\rightarrow \infty$), it can be concluded that the contribution to the equilibrium scour depth for large KC numbers is predominately coming from the horseshoe vortex.

The scour data in Fig. 11 can be represented by the following expression:

$$\frac{S}{D} = 1.3\,\{1 - \exp[-0.03(KC - 6)]\} \qquad KC \geq 6 \quad \ldots\ldots\ldots\ldots\ldots\ldots (9)$$

This equation is valid for the live-bed conditions ($\theta > \theta_c$).

Scale Effects

The effect of θ and Re number has been discussed in the preceding sections. This section will concentrate on the effect of ripple dimensions on the test results. The wave-generated ripples are present for θ values smaller than about 0.8–1. As is seen from Fig. 11, the pile diameter in the experiments was varied from 10 mm to 200 mm. This facilitated a wide range of ripple-length–to-pile-diameter ratio where the ripple length varied from about half a pile diameter to several pile diameters. Fig. 11 shows that the data points corresponding to this range of ripple-length–to-pile-diameter ratio collapse onto a common curve, confirming that the ripples are not an essential factor in the scour process. This aspect has been observed also for the scour below marine pipelines (Sumer and Fredsøe 1990). As was pointed out in that study, one reason for this may be the absence of ripples in the immediate neighborhood of the pile (where the flow field disturbed by the pile prevents ripple formation).

SUMMARY AND CONCLUSIONS

1. The scour around a pile in waves is governed by the action of both lee-wake vortices and the horseshoe vortex.
2. The main parameter that determines the equilibrium scour depth on a live bed is the Keulegan-Carpenter (KC) number.
3. The scour data of the present study, which are presented in Table 1 and Fig. 11, have been obtained for live-bed conditions only.
4. The data indicate that:
   a. The scour around the pile practically ceases to exist for KC below 6.
   b. The scour depth monotonously increases, as the KC number is increased. It approaches its steady-current value, namely $S/D = 1.3$, for KC numbers above approximately 100.
5. The data suggest that the relation between the equilibrium scour depth and the KC number is represented by the expression given by (9).

ACKNOWLEDGMENTS

This study is partially supported by the program "Marine Technique" for the Danish Technical Research Council (STVF). We thank Peter Roll, Di Yu, Lars Nicolaisen, and Martin Eskholm for their involvements in the conduct of the scour tests and Michael M. Arnskov for his participation in the flow-visualization study.

APPENDIX I. REFERENCES

Breusers, H. N. C., Nicollet, G., and Shen, H. W. (1977). "Local scour around cylindrical piers." *J. Hydr. Res.*, 15(3), 211–252.

Das, M. M. (1970). "A literature review on bed-load transport due to wave action and localized scour in non-cohesive sediments." *Final Report HEL 21-6: A Literature Review on Erosion and Deposition of Sediment near Structures in the Ocean*, H. A. Einstein and R. L. Wiegel, eds., Hydraulic Engrg. Lab., Coll. of Engrg., Univ. of California, Berkeley, Calif.

Eadie, IV, R. W., and Herbich, J. B. (1986). "Scour about a single, cylindrical pile due to combined random waves and a current." *Proc. 20th Coastal Engineering Conference*, ASCE Nov. 9–14, 1858–1870.

Herbich, J. B., Schiller, Jr., R. E., Dunlap, W. A., and Watanabe, R. K. (1984). *Seafloor Scour*. Marcel Dekker, Inc., New York, N.Y.

Hjorth, P. (1975). "Studies on the nature of local scour." *Bulletin Series A, No. 46*, Dept. of Water Resour. Engrg., Lund Inst. of Tech., Univ. of Lund, Sweden.

Jensen, B. L., Sumer, B. M., and Fredsøe, J. (1989). "Turbulent oscillatory boundary layers at high Reynolds numbers." *J. Fluid Mech.*, 206(Sept.), 265–297.

Kawata, Y., and Tsuchiya, Y. (1988). "Local scour around cylindrical piles due to waves and currents combined." *Proc. 21st Coastal Engrg. Conf.*, ASCE, 2(June 20–25), 1310–1322.

Palmer, H. D. (1969). "Wave-induced scour on the sea floor." *Proc. of the Civ. Engrg. in the Oceans II*, ASCE (Dec.), 703–716.

Schewe, G. (1983). "On the force fluctuations acting on a circular cylinder in crossflow from subcritical up to transcritical Reynolds numbers." *J. Fluid Mech.*, 133(Aug.), 265–285.

Schlichting, H. (1979). *Boundary-layer theory*. 7th Ed., McGraw-Hill Book Company.

Sumer, B. M., and Fredsøe, J. (1989). "Effect of Reynolds number on vibration of cylinders." *J. Offshore Mech. and Arctic Engrg.*, 111(May), 131–137.

Sumer, B. M., and Fredsøe, J. (1990). "Scour below pipelines in waves." *J. Waterways, Port, Coastal, and Ocean Engrg.*, ASCE, 116(3), 307–323.

Wang, R.-K., and Herbich, J. B. (1983). "Combined current and wave-produced scour around a single pile." *COE Report No. 269*, Texas Engrg. Experiment Station, Dept. Civ. Engrg., The Texas A&M Univ., College Station, Tex.

Williamson, C. H. K. (1985). "Sinusoidal flow relative to circular cylinders." *J. Fluid Mech.*, 155(June), 141.

APPENDIX II. NOTATION

The following symbols are used in this paper:

D = pile diameter;
d = sediment size;
f = friction factor;
f_w = wave frequency;
g = acceleration due to gravity;
k = roughness height of pile surface;
k^* = roughness height of pile surface normalized by pile diamater;
L = length of streamwise extension of lee-wake vortices;
Re = pile Reynolds number [(5)];
S = scour depth;
s = specific gravity of sediment;
T = wave period;
t = time from onset of scour;
U_m = maximum value of outer oscillatory flow velocity;
U_{fm} = maximum value of undistributed bed shear velocity;
x,y,z = coordinates axes (see Fig. 1);
α = bed shear-stress amplification factor [(7)];
δ = boundary layer thickness in absence of pile;
θ = Shields parameter [(1)];
$\bar{\tau}_0$ = mean bed shear stress in presence of pile;
$\bar{\tau}_{0m}$ = maximum value of undisturbed mean bed shear stress;
ν = kinematic viscosity; and
ω = angular frequency of the wave motion [(3)].

Influence of Cross Section on Wave Scour Around Piles

B. Mutlu Sumer, Jørgen Fredsøe and
Niels Christiansen

Institute of Hydrodynamics and Hydraulic Engineering
Technical University of Denmark

INFLUENCE OF CROSS SECTION ON WAVE SCOUR AROUND PILES

By B. M. Sumer,[1] N. Christiansen,[2] and J. Fredsøe[3]

ABSTRACT: The study extends the investigation of scour around circular vertical piles in waves, reported in 1992 in two works by Sumer et al. In the present paper, the influence of cross sectional shape of piles on scour is studied. An extensive series of tests was carried out with two kinds of cross sections: a circular cross section, and a square cross section tested at two orientations to the flow (namely, 90° orientation and 45° orientation), therefore giving three different test configurations. The equilibrium scour depth as well as the time scale of the scour process were investigated. Based on the present data, design equations are established relating the equilibrium scour depth, S_0, to the Keulegan-Carpenter number (KC). For a given KC where $KC \lesssim 100$, the scour depth is the largest for the square pile with 45° orientation and smallest for the square pile with 90° orientation, the circular-cylinder scour lying in between. In all three cases, the equilibrium scour depth normalized by the pile width (S_0/D) increases with increasing KC number. For $KC \gtrsim 100$, however, S_0/D approaches a constant value, which is about 2 for the square piles and about 1.3 for the circular pile. Regarding the time scale of the scour process, this quantity is governed by two parameters, namely the Keulegan-Carpenter number and the Shields parameter. Given the latter two parameters, the time scale was found to be somewhat smaller in the case of the square pile with a 90° orientation than those in the other two cases.

INTRODUCTION

When a pile is placed in an originally plane, erodible bed, scour will take place around it due to the action of waves and current. This process is of importance in connection with the stability of marine structures such as platforms, bridges, subsea templates, and so on. Extensive scour around the structure may reduce its stability, thus leading to its failure.

The process of scour is mainly due to two effects: (1) The structure blocks the flow, leading to increased flow velocity around the structure; and (2) the presence of the structure creates a local system of turbulent vortices (partly the horseshoe vortex, partly downstream vortex shedding), which increases the local transport capacity.

Items 1 and 2 depend strongly on the actual shape of the structure. This can for instance be quite open (like a grid cover of a small subsea structure) leading to only a slight blocking effect, but quite a high level local turbulence. Also, quite often these structures are three-dimensional, which leads to a relative small blocking.

Because the marine structures have a very wide variety of shapes, it is very difficult to give general rules for the expected process of scour in the marine environment.

---

[1] Assoc. Prof., Tech. Univ. of Denmark, Inst. of Hydrodynamics and Hydr. Engrg., DK-2800 Lyngby, Denmark.

[2] Grad. Student, Tech. Univ. of Denmark, Inst. of Hydrodynamics and Hydr. Engrg., DK-2800 Lyngby, Denmark.

[3] Prof., Tech. Univ. of Denmark, Inst. of Hydrodynamics and Hydr. Engrg., DK-2800 Lyngby, Denmark.

Note. Discussion open until February 1, 1994. To extend the closing date one month, a written request must be filed with the ASCE Manager of Journals. The manuscript for this paper was submitted for review and possible publication on April 6, 1992. This paper is part of the ***Journal of Waterway, Port, Coastal, and Ocean Engineering***, Vol. 119, No. 5, September/October, 1993. ©ASCE, ISSN 0733-950X/93/0005-0477/$1.00 + $.15 per page. Paper No. 3805.

This has been done previously for the special case of scour around cylindrical bridge piers exposed to pure currents, in which the effect of shape and angle of attack has been investigated experimentally; for a review see Breusers et al. (1977) and Hjorth (1975). Hjorth (1977) also measured the bed shear stress distribution around piles with different shapes, as shown in Fig. 1. It is clear that the bed shear-stress distribution (and hence the process of scour) is very different for the three cases considered.

No information, however, exists about the shape effect on scour for structures in the marine environment. Actually, only very few studies are available on wave scour. Oil companies have conducted numerous studies, but unfortunately, they are generally proprietary and not available in the literature. Some field data have been reported by Palmer (1969). Das (1970), Kawata and Tsuchiya (1988), and Chiew (1989) presented a few laboratory tests. In the case of coexisting waves and current, on the other hand, the extensive study made by Herbich and his coworkers [see for example Wang and Herbich (1983), Herbich et al. (1984), and Eadie and Herbich (1986)] can be mentioned.

For the pure wave case, Sumer et al. (1992a) made a detailed experimental investigation of the scour process around a circular pile. In a related work, Sumer et al. (1992b) considered the time scale for the scour around a circular pile. This time scale is of importance with respect to the behavior of the scour depth during a changing wave climate.

The results of these studies have indicated that: (1) The equilibrium scour

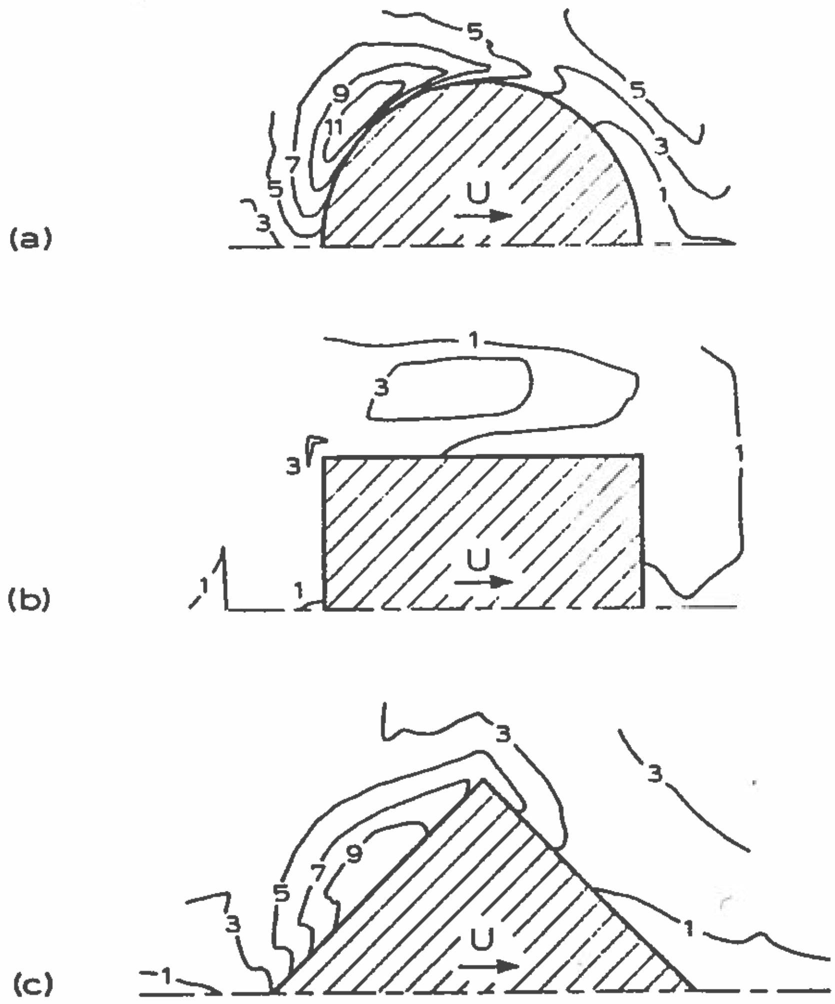

FIG. 1. Amplification in Time-Mean Bed Shear Stress [Flat Bed; Water Depth = 20 cm; Flow Velocity = 30 cm/s; Taken from Hjorth (1975)]

depth normalized by the pile diameter (S_0/D) is a function of the Keulegan-Carpenter number (KC); (2) S_0/D increases with increasing KC; (3) S_0/D approaches its steady-current value for KC-values above approximately 100; (4) the governing parameters with regard to the time scale of scour are KC and the Shields parameter (θ); and (5) the time scale increases with increasing KC and decreases with increasing θ.

The purpose of the present study is to investigate the simplest extension of the previously studied case of circular pile to that of a pile with a square section [as was done by Hjorth (1975) for the current alone case]. The investigation reveals the importance of this moderate change in the cross-sectional area on the process of scour due to the altered blocking effect and due to the changes in the vortex shedding regime and so on. The study comprises two angles of approach, namely 90° and 45°, the final scour depth, and the time scale for the process are studied.

EXPERIMENTAL FACILITY

Scour Experiments

The experiments of test series No. 1 were carried out in a wave flume (0.6 m in width, 0.8 m in depth, and 26.5 m in length). The mean water depth was maintained constant at 40 cm. Several square-section piles were used, with the size ranging from 9 mm × 9 mm to 40 mm × 40 mm. Also, some additional experiments were carried out with circular piles with the diameter range from 20 mm to 40 mm. One size of sand was used in the tests; namely, with $d_{50} = 0.18$ mm.

The experiments of test series No. 2 were carried out in a large wave flume, 4 m in width, 1 m in depth, and 28 m in length. The main purpose of these tests was to provide data with a relatively larger size pile model; namely, a 100 mm × 100 mm size pile. The sand size in the tests was $d_{50} = 0.18$ mm.

A few tests (test series No. 3) were carried out in a 2-m-wide current flume in order to supplement the wave-flume experiments with data representing tidal-flow situations. In these experiments the flow direction could be reversed with a period that was long enough for the flow to be considered quasi-steady in each half-cycle. A 40 mm × 40 mm size pile was used in these experiments. Sand-grain size was $d_{50} = 0.26$ mm. One-directional, steady-current experiments were also conducted for reference purpose.

The development of the scour process was videotaped using two obliquely positioned video cameras in test series 1. This arrangement enabled us to monitor the time development of the scour depth over the whole periphery of the tested pile. In test series 2, intense suspension of sand in the flume and the long distance of the pile from the camera prevented the continuous video monitoring of the scour process. Instead, the waves were stopped every 5 min and the scour depth was measured, again over the whole periphery of the tested pile. In test series 3, the scour process was videotaped as in test series 1; however, only one camera was used, because of experimental constraints. The camera was obliquely positioned and the scour depth over half the periphery of the pile (covering the upstream edge and the side edge of the section) was monitored.

Velocity measurements were made by a DANTEC Laser doppler anemometer (LDA) in test series 1, by an ultrasonic velocity meter in test series 2, and by a propeller in test series 3.

Monochromatic waves were used in the experiments in both test series 1 and test series 2. Waves were produced by a piston-type wave generator.

TABLE 1. Experimental Data

Run Number (1)	Pile (2)	Pile arrangement (degrees) (3)	Sand size d (mm) (4)	Pile width D (mm) (5)	Wave period T_w (s) (6)	Maximum flow velocity (measured) U_m (cm/s) (7)	Maximum shear velocity U_{fm} (cm/s) (8)	Shields parameter θ (9)	Keulegan-Carpenter number KC (10)	Pile Reynolds number R (11)	Nondimensional equilibrium scour depth S_0/D (12)	Nondimensional time scale T^* (13)
(a) Test Series 1: Small Wave-Flume Experiments												
1	Square	90	0.18	40	1.6	22	1.9	0.12	9	0.86×10^4	0	—
2	Square	90	0.18	40	1.4	31	2.3	0.18	11	1.24×10^4	0.05	0.032
3	Square	90	0.18	30	1.6	22	1.9	0.12	12	0.65×10^4	0.07	0.022
4	Square	90	0.18	30	2.1	21	1.9	0.11	15	0.63×10^4	0.20	0.11
5	Square	90	0.18	20	1.5	20	2.0	0.13	15	0.40×10^4	0.23	0.31
6	Square	90	0.18	30	1.4	31	2.3	0.18	15	0.93×10^4	0.16	0.21
7	Square	90	0.18	20	1.4	30	2.4	0.19	21	0.59×10^4	0.13	—
8	Square	90	0.18	20	2.1	21	1.9	0.11	22	0.42×10^4	0.32	0.44
9	Square	90	0.18	20	1.4	31	2.3	0.18	22	0.62×10^4	0.35	0.51
10	Square	90	0.18	20	2.7	24	1.9	0.12	33	0.49×10^4	0.57	—
11	Square	90	0.18	9	1.4	30	2.4	0.19	46	0.27×10^4	0.98	3.2
12	Square	90	0.18	9	2.7	24	1.9	0.12	73	0.22×10^4	1.22	2.8
13	Square	45	0.18	57	1.2	22	1.9	0.12	4.5	1.25×10^4	0.22	—
14	Square	45	0.18	57	2.0	17	1.6	0.09	6	0.96×10^4	0.11	—
15	Square	45	0.18	57	1.6	22	1.9	0.12	6	1.23×10^4	0.14	0.036
16	Square	45	0.18	42	2.0	17	1.6	0.09	8	0.71×10^4	0.23	—
17	Square	45	0.18	42	1.3	28	2.2	0.17	8	1.16×10^4	0.45	0.10
18	Square	45	0.18	42	2.1	21	1.9	0.11	11	0.88×10^4	0.42	0.32
19	Square	45	0.18	42	1.4	31	2.3	0.18	11	1.3×10^4	0.49	0.18
20	Square	45	0.18	28	1.6	22	1.9	0.12	13	0.60×10^4	0.25	0.32
21	Square	45	0.18	28	2.1	21	1.9	0.11	16	0.59×10^4	0.45	0.46
22	Square	45	0.18	28	1.4	31	2.3	0.18	16	0.87×10^4	0.54	0.24
23	Square	45	0.18	13	2.0	17	1.6	0.09	26	0.22×10^4	0.62	—
24	Square	45	0.18	28	2.7	24	1.9	0.12	23	0.68×10^4	0.58	0.77
25	Square	45	0.18	13	1.4	30	2.4	0.19	32	0.39×10^4	1.0	0.86
26	Square	45	0.18	13	2.7	24	1.9	0.12	51	0.32×10^4	1.08	0.71

27	Circular	—	0.18	40	1.4	31	2.3	0.18	11	1.2 × 10⁴	—	0.13
28	Circular	—	0.18	30	2.1	21	1.9	0.11	15	0.63 × 10⁴	—	0.91
29	Circular	—	0.18	20	1.5	20	2.0	0.13	15	0.40 × 10⁴	—	1.34
30	Circular	—	0.18	30	1.4	31	2.3	0.18	15	0.93 × 10⁴	—	0.26
31	Circular	—	0.18	20	2.1	21	1.9	0.11	22	0.42 × 10⁴	—	1.13
32	Circular	—	0.18	30	2.2	30	2.0	0.14	22	0.90 × 10⁴	—	0.48
33	Circular	—	0.18	20	1.4	31	2.3	0.18	22	0.62 × 10⁴	—	0.38
(*b*) Test Series 2: Large Wave-Flume Experiments												
34	Square	90	0.18	100	1.9	23.1	2.0	0.14	4.4	2.3 × 10⁴	~0	—
35	Square	90	0.18	100	3.0	25.2	1.8	0.11	7.6	2.5 × 10⁴	~0	—
36	Square	90	0.18	100	4.5	30.1	1.8	0.11	13.5	3.0 × 10⁴	0.1	—
37	Square	90	0.18	100	4.5	32.6	1.9	0.13	14.7	3.3 × 10⁴	0.1	—
38	Square	90	0.18	100	4.5	39.1	2.0	0.14	17.6	3.9 × 10⁴	0.2	—
39	Square	90	0.18	100	4.5	46.9	2.3	0.19	21.1	4.7 × 10⁴	0.2	—
40	Square	90	0.18	100	4.5	53.3	2.5	0.22	24.0	5.3 × 10⁴	0.2	—
41	Square	90	0.18	100	5.9	50.0	2.4	0.19	29.5	5.0 × 10⁴	0.325	—
42	Square	45	0.18	141	1.9	23.1	2.0	0.14	3.1	3.3 × 10⁴	0.03	—
43	Square	45	0.18	141	3.0	25.2	1.8	0.11	5.3	3.6 × 10⁴	0.06	—
44	Square	45	0.18	141	4.5	30.1	1.8	0.11	9.6	4.2 × 10⁴	0.20	—
45	Square	45	0.18	141	4.5	32.6	1.9	0.13	10.4	4.6 × 10⁴	0.23	—
46	Square	45	0.18	141	4.5	39.1	2.0	0.14	12.4	5.5 × 10⁴	0.3	—
47	Square	45	0.18	141	4.5	46.9	2.3	0.19	21.1	6.6 × 10⁴	0.41	—
48	Square	45	0.18	141	4.5	53.3	2.5	0.22	16.9	7.5 × 10⁴	0.32	—
(*c*) Test Series 3: Current-Flume Experiments												
49	Square	90	0.26	40	480	40.0	2.6	0.16	4,800	1.6 × 10⁴	2.2	—
50	Square	45	0.26	57	480	40.0	2.6	0.16	6,720	2.3 × 10⁴	1.74	—
51	Square	90	0.26	40	∞	40.0	2.6	0.16	∞	1.6 × 10⁴	2.3	—
52	Square	90	0.26	40	∞	40.0	2.6	0.16	∞	1.6 × 10⁴	1.90	—
53	Square	45	0.26	57	∞	40.0	2.6	0.16	∞	2.3 × 10⁴	1.88	—
54	Square	45	0.26	57	∞	40.0	2.6	0.16	∞	2.3 × 10⁴	1.75	—

A "Dutch-beach" type of wave absorber at the downstream end of the wave flume was used, to handle the reflection.

Before the start of each test the bed was leveled off. The test continued until the scour process attained its equilibrium stage.

Test Conditions

The test conditions, experimental results regarding the scour depth, and the time scale of the scour process are listed in Table 1. In Table 1, the Shields parameter θ is defined by

$$\theta = \frac{U_{fm}^2}{(s - 1)gd} \qquad (1)$$

in which d = sand-grain size; g = acceleration due to gravity; s = relative density of sediment; and U_{fm} = maximum value of the undisturbed bed shear velocity, which is calculated by

$$U_{fm} = \sqrt{\frac{f_w}{2}}\, U_m \qquad (2)$$

where f_w = wave friction coefficient; and U_m = maximum value of the orbital velocities of water particles at the bed in the absence of the pile, defined by

$$U = U_m \sin(\omega t) \qquad (3)$$

where ω = angular frequency of waves. For steady-current situations, U_{fm} and U_m are replaced by U_f and U, respectively, in which U_f = undisturbed bed shear velocity; and U = mean flow velocity. Also, in Table 1, the Keulegan-Carpenter number, KC, is defined by

$$KC = \frac{U_m T_w}{D} \qquad (4)$$

in which T_w = wave period; and D = pile width, i.e. the width of the pile projected on a cross-sectional plane perpendicular to the flow direction. For circular piles, D is obviously the pile diameter.

In Table 1, R = Reynolds number, defined by

$$\mathrm{R} = \frac{U_m D}{\nu} \qquad (5)$$

in which ν = kinematic viscosity; and T^* = normalized time scale defined by

$$T^* = \frac{[g(s - 1)d^3]^{1/2}}{D^2}\, T \qquad (6)$$

where T = time scale of the scour process.

As seen from the table, there are no entries in the column of the equilibrium scour depth in the case of circular cross-section pile (i.e., tests 27–33). The purpose of these latter tests was not to get further scour-depth data [because over 50 test results had been reported in previous work (Sumer et al. 1992a) with regard to the scour depth], but, rather, to get some more data regarding the time scale of scour process, to supplement the time-scale data already reported in Sumer et al. (1992b).

Flow-Visualization Experiments

The objective was to get an understanding of the near-bed flow processes around the pile, such as the horseshoe vortex and the vortex shedding.

The hydrogen-bubble technique was used. The experimental technique was exactly the same as that used in Sumer et al. (1992a). The visualization study made in this latter study for circular piles has in the present study been extended so as to cover the square-section piles for both the 45° and 90° orientations. For these latter experiments a 40 mm × 40 mm size square pile was used. The *KC*-number range covered was from practically 0 to about 25 where *KC* was incremented by about 2. The range of pile R number was from 2×10^3 to 9×10^3.

RESULTS OF EXPERIMENTS AND ANALYSIS

Fig. 2 is a sequence of photographs illustrating the time development of the scour holes around the model piles. The sequence indicates that although the scour pattern around the pile is different for different cross sections at the initial stages of the scour process, it eventually attains a constant shape; namely, a truncated cone.

Equilibrium Scour Depth

Fig. 3 depicts the development of the scour depth with respect to time for the square piles. The scour depth in Fig. 3, (and hereafter) is the average scour depth where the average is taken over eight values, four of them corresponding to the scour depth measured at the corners of the pile and the other four corresponding to the scour depths measured at the midpoints of the sides of the pile except in test series 3. In test series 3 the average is taken over four values, covering only half the pile periphery. In the case of circular pile, on the other hand, the average is taken over four values; namely, the downstream and upstream scour depth values, and the two side-edge scour-depth values. As seen from Fig. 3, the scour depth through a transitional period attains an equilibrium value.

Fig. 4 presents the data regarding the equilibrium scour depth for both the 90° arrangement and the 45° arrangement cross sections. The scour depth normalized by the pile width has been plotted in the figure against the Keulegan-Carpenter number following the dimensional considerations in Sumer et al. (1992a). All the tests included in Fig. 4 were carried out under live-bed conditions, i.e. $\theta > \theta_{cr}$ in which θ_{cr} = critical value of θ, corresponding to the initiation of sediment motion on the bed. As seen from the figure, the data are grouped around two different curves; one for the 45° arrangement and the other for the 90° arrangement. Fig. 5, on the other hand, depicts the data in linear scale for small *KC* numbers, illustrating the behavior of S_0/D, as $KC \to 0$.

Fig. 6 compares the present square-section pile results with the results obtained in Sumer et al. (1992a) for circular piles. To keep the figure relatively simple, the actual data points are not included.

The following observations can be made from the figures.

First, the scour depth is practically nil for very small *KC* numbers; namely, for $KC < 3$–4 for the square pile with 45° orientation, for $KC < 10$–11 for the square pile with 90° orientation (Fig. 5), and for $KC < 6$–7 for the circular pile [see Sumer et al. (1992a)].

As pointed out in Sumer et al. (1992a), the disappearance of the scour for very small *KC* numbers is due to the fact that the vortex shedding, the

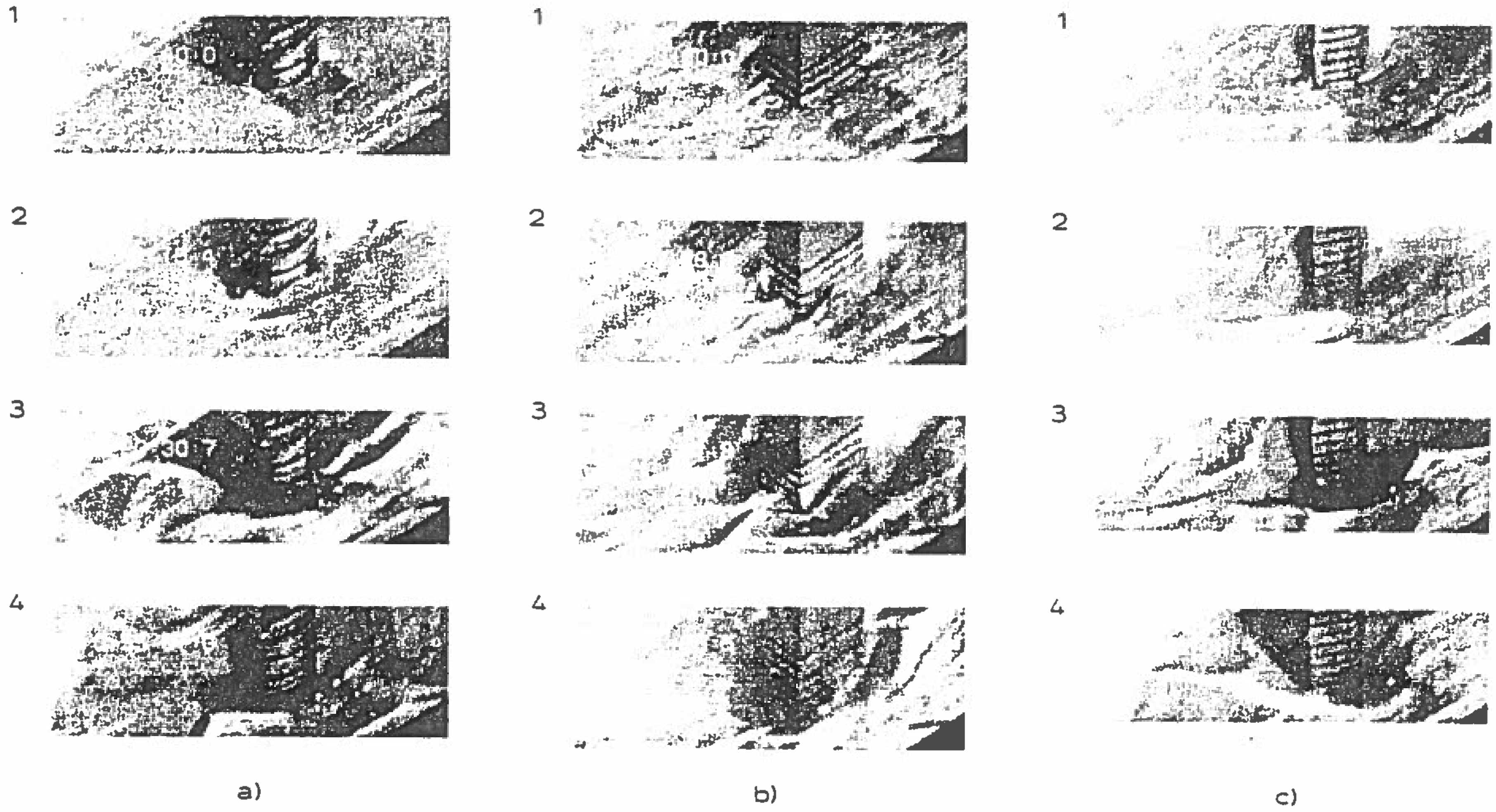

FIG. 2. Time Development of Scour Hole: (*a*) Circular Pile, D = 3 cm, KC = 15, Run No. 28; (*b*) Square Pile, 90° Orientation, D = 3 cm, KC = 15, Run No. 4; (*c*) Square Pile, 45° Orientation, D = 2.8 cm, KC = 15.7, Run No. 21

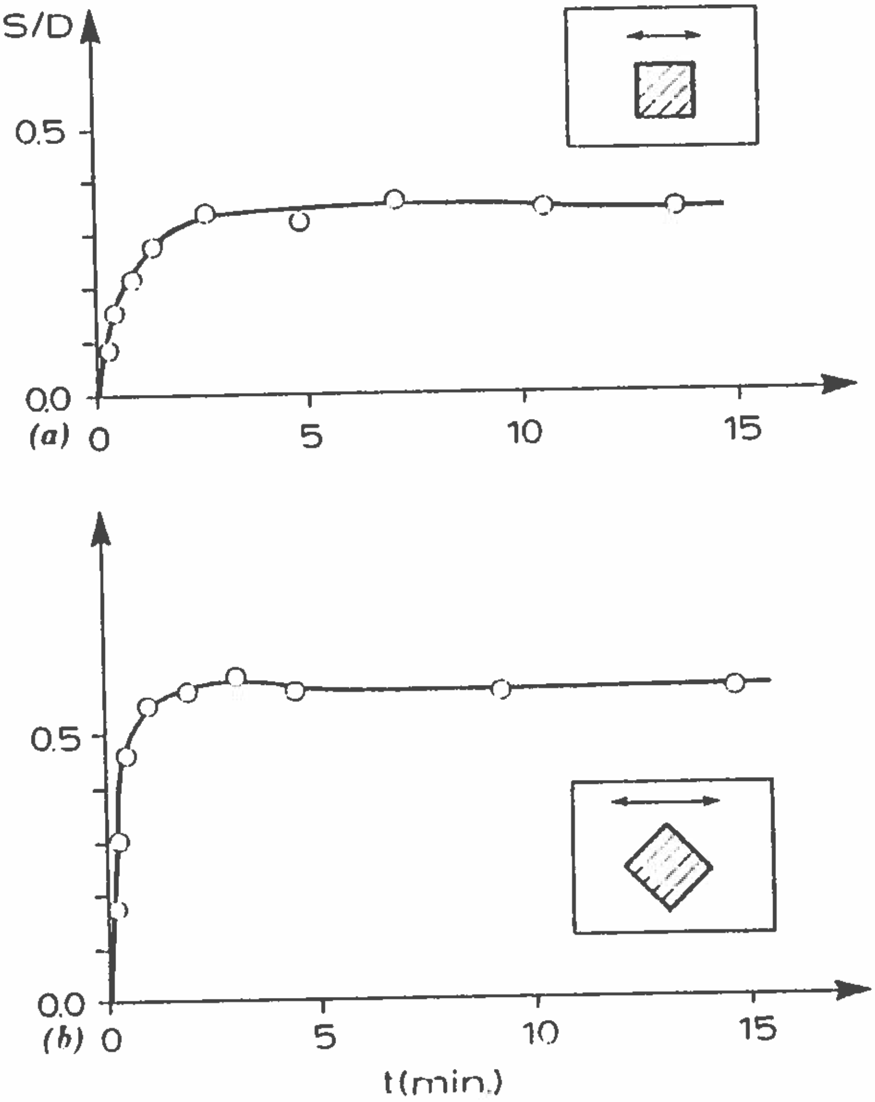

FIG. 3. Time Development of Scour Depth, Run No. 9 for 90° Arrangement Test and Run No. 22 for 45° Arrangement Test

major element in the scour process for small KC numbers, is actually nonexistent in this case. The scour may still occur due to the contraction of streamlines and also due to streaming; yet the bed shear-stress measurements of Sumer et al. (1992a) for circular piles indicated that the bed shear stress in the immediate neighborhood of the pile appears to be quite close to its undisturbed value for such small KC numbers.

The results of the present hydrogen-bubble flow-visualization study has indicated that no vortex shedding occurs for $KC < 4$ in the case of 45° arrangement square pile, for $KC < 6$ in the case of circular pile and for $KC < 11$ in the case of 90° arrangement square pile. The sequences of flow given in Fig. 7, which are taken from video frames, indicates that no vortex shedding occurs for $KC = 10$ and that shedding is existent for $KC = 13$.

The key role of the shedding phenomenon in the scour process is that each shed vortex sweeps the sediment grains into its core region and carries them away from the pile, while it is convected downstream (Fig. 8), thus causing a net scour around the pile. In the absence of shedding, however, the vortices that form behind the pile [Fig. 7(*a*)] sweep the sediment grains into their core region, but do not carry them away from the pile, because they themselves are not removed from the pile due to the absence of the shedding process. Therefore, the end result is that the mean scour around

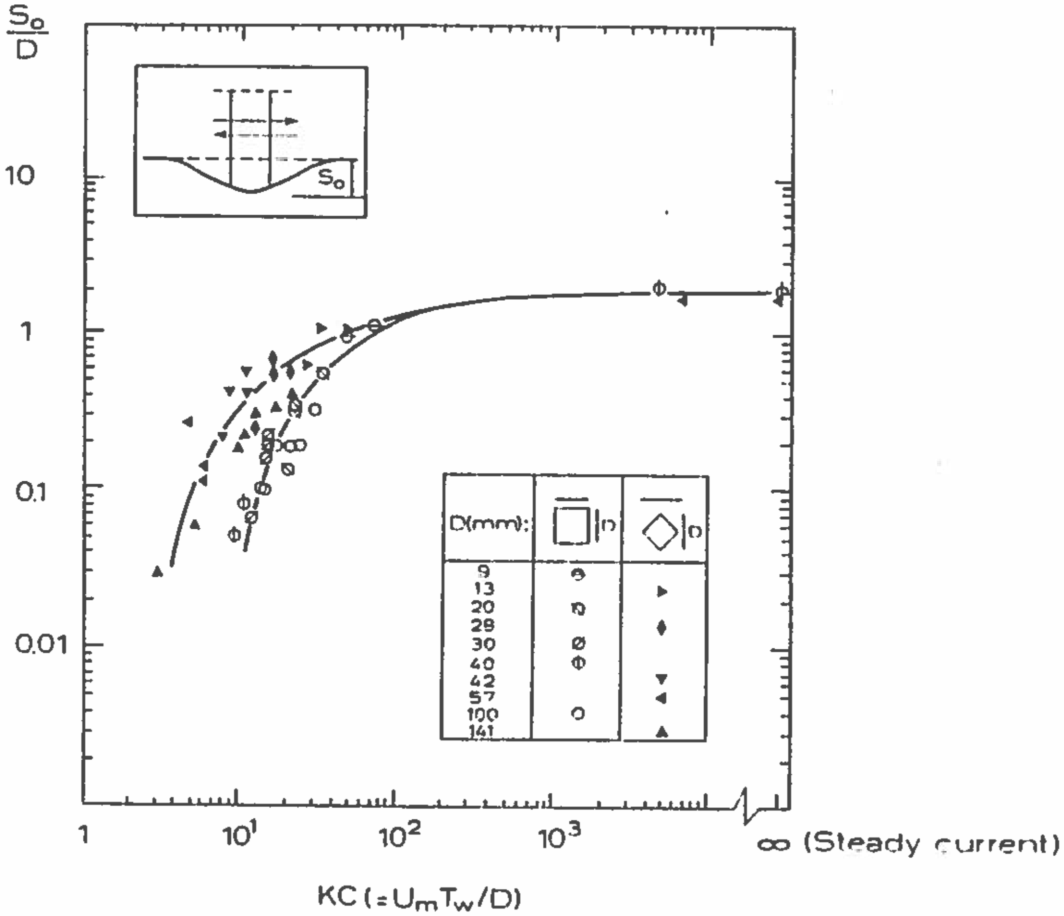

FIG. 4. Equilibrium Scour Depth versus KC Number, Live Bed ($\theta > \theta_{cr}$)

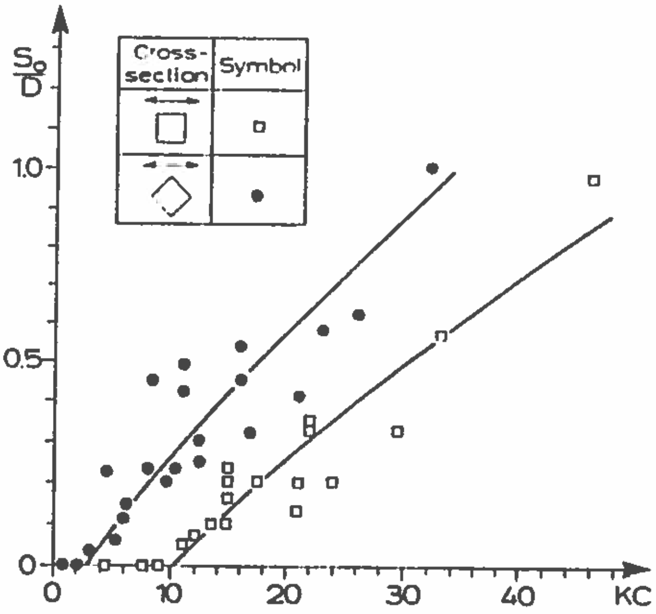

FIG. 5. Equilibrium Scour Depth versus KC Number, Small KC Numbers

the pile will be nil, as is clearly observed from Fig. 6. It is remarkable that the KC numbers at which the scour practically ceases to exist from Fig. 6 (namely, $KC \cong 3$–4 for the 45° arrangement square pile, $KC \cong 6$–7 for the circular pile, and $KC \cong 10$–11 for the 90° arrangement square pile) coincide with the KC numbers at which the vortex shedding disappears.

Second, the scour depth in all the three cases increases with increasing KC number. As demonstrated by Sumer et al. (1992a) for circular piles,

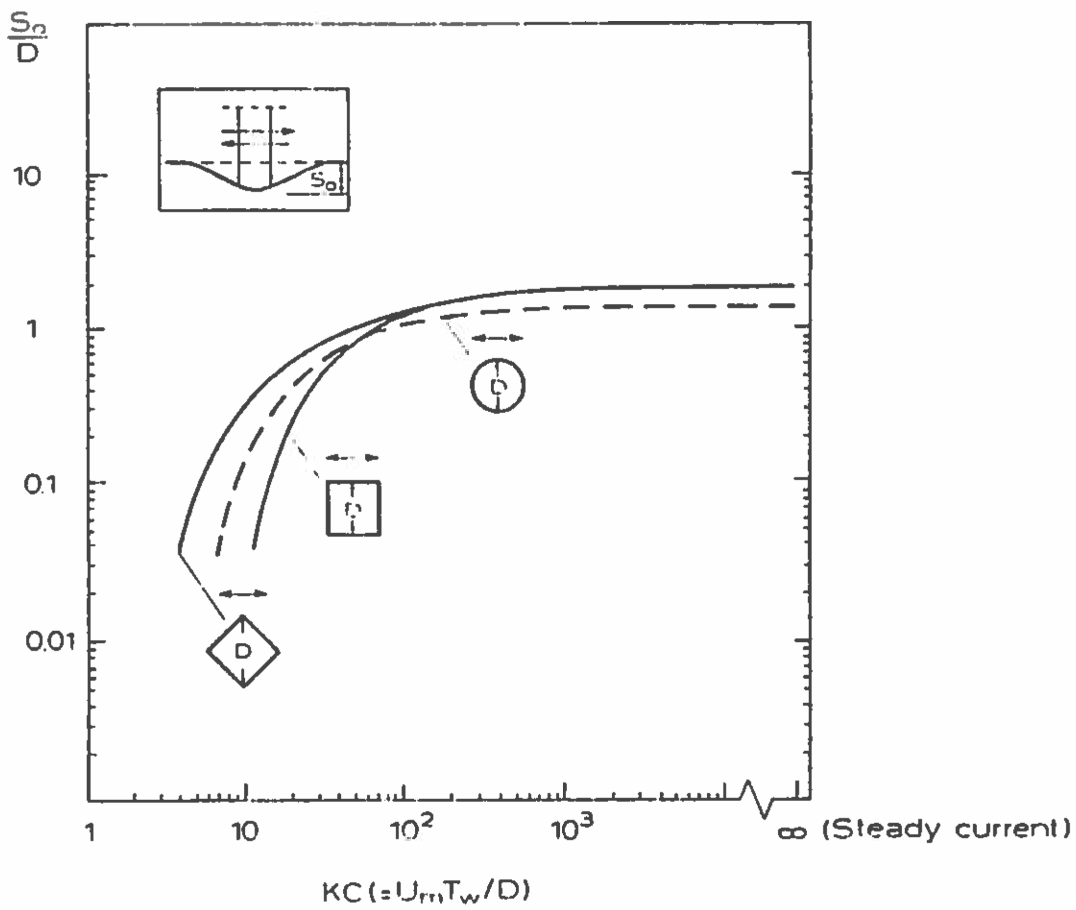

FIG. 6. Equilibrium Scour Depth versus *KC* Number, Live Bed ($\theta > \theta_{cr}$) [Curve Representing Circular Pile is Taken from Sumer et al. (1992a)]

this increase is partly due to the increased extension of the lee wake (which is an agglomeration of the shed vortices) and partly due to the increased presence and the increased strength of the horseshoe vortex with increasing *KC* number.

Third, the difference between the three cases becomes relatively smaller, as *KC* is increased (Fig. 6). This effect may be attributed to the decreasing importance of the vortex shedding with increasing *KC*, considering the finite lifetime of the vortices.

Fourth, furthermore, Fig. 6 indicates that the scour depth approaches a constant value (namely, $S_0/D \rightarrow 2$ for the square section piles and $S_0/D \rightarrow 1.3$ for the circular section piles) for large values of *KC* number.

Regarding these asymptotic values of the scour depth, there is a substantial decrease in the scour depth in the case of circular piles. This decrease may be linked to the horseshoe-vortex formation. Previous work in connection with circular piles (Sumer et al. 1992a) has indicated that the contribution to the equilibrium scour depth for large *KC* numbers predominately comes from the horseshoe vortex. The streamwise extent of the horseshoe vortex in the case of circular piles is smaller than in the case of square-section piles (Fig. 9). The smaller the streamwise extent of the horseshoe vortex, the smaller the scour depth. Therefore, the scour depth should be smaller in the case of circular piles.

Finally, the scour data in Fig. 6 can be represented by the following expressions.

Circular pile

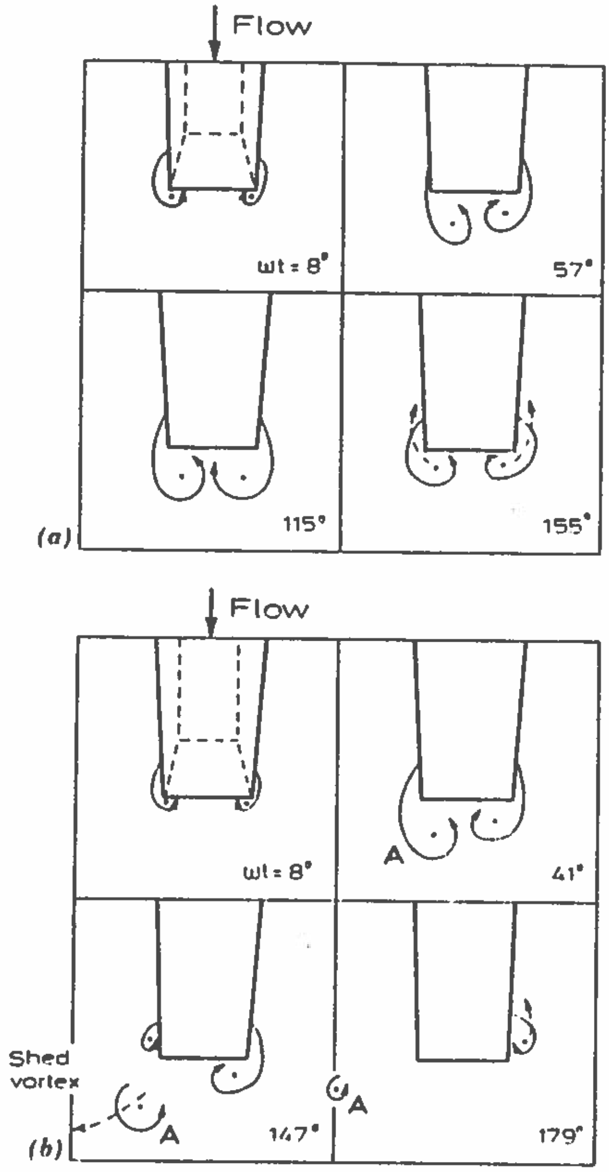

FIG. 7. Evolution of Vortex Motions Around 90° Arrangement Square Pile: (a) $KC = 10$; (b) $KC = 13$

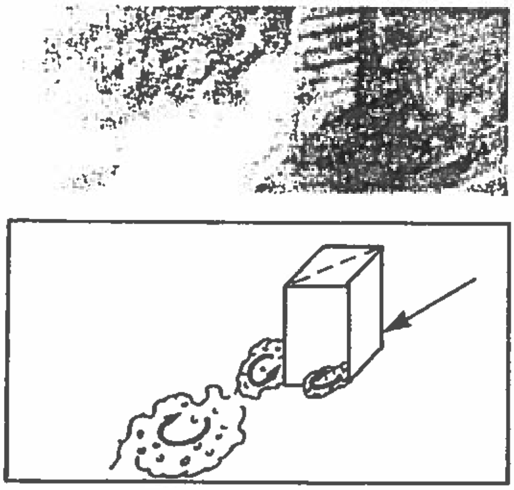

FIG. 8. Scour and Eventual Transport of Sediment Away from Pile by Shed Vortices

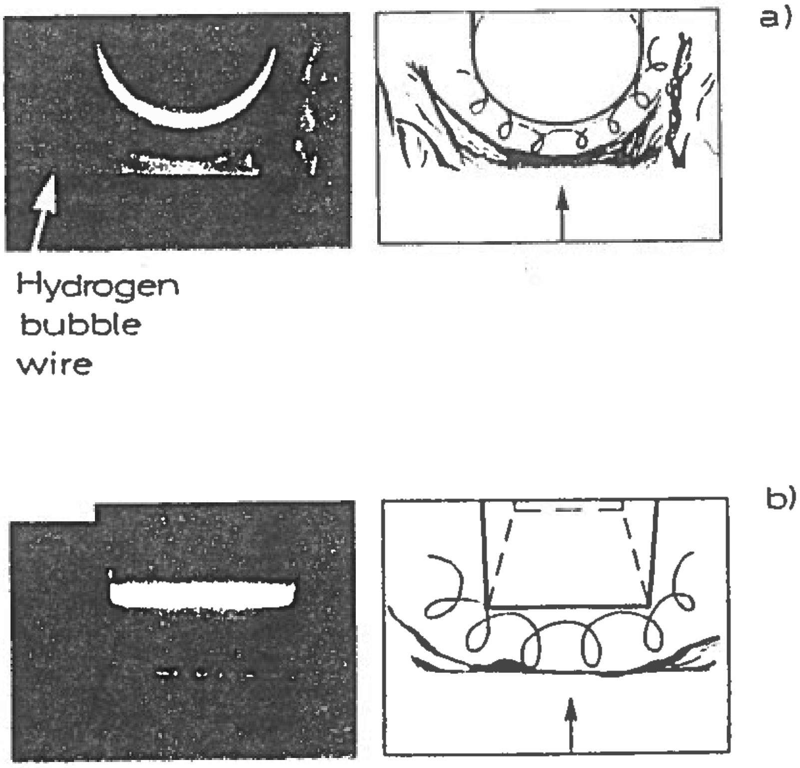

FIG. 9. Horseshoe Vortex in Front of Pile: (a) Circular Pile; and (b) Square Pile with 90° Arrangement

$$\frac{S_0}{D} = 1.3\{1 - \exp[-0.03(KC - 6)]\}; \qquad KC \geq 6 \quad \ldots\ldots\ldots\ldots\ldots\ldots \quad (7)$$

Square pile (90° orientation)

$$\frac{S_0}{D} = 2\{1 - \exp[-0.015(KC - 11)]\}; \qquad KC \geq 11 \quad \ldots\ldots\ldots\ldots\ldots \quad (8)$$

Square pile (45° orientation)

$$\frac{S_0}{D} = 2\{1 - \exp[-0.019\,(KC - 3)]\}; \qquad KC \geq 3 \quad \ldots\ldots\ldots\ldots\ldots\ldots \quad (9)$$

These equations are valid for scour on a live bed ($\theta > \theta_{cr}$).

Time Scale

As mentioned previously, scour depth develops toward the equilibrium stage through a transitional period (Fig. 3). From Fig. 3, it is seen that the time variation of the scour depth can approximately be represented by the following relation:

$$S = S_0\left(1 - \exp\frac{-t}{T}\right) \quad \ldots\ldots\ldots\ldots\ldots\ldots\ldots\ldots\ldots\ldots\ldots\ldots \quad (10)$$

in which S_0 = equilibrium scour depth. The quantity T is defined as the time scale of the scour process and represents the time period during which substantial scour develops. The time scale T can be predicted from the scour-depth-versus-time information by calculating the slope of the tangent line to the $S(t)$ curve at $t = 0$, as schematically illustrated in the small box at the top of Fig. 10.

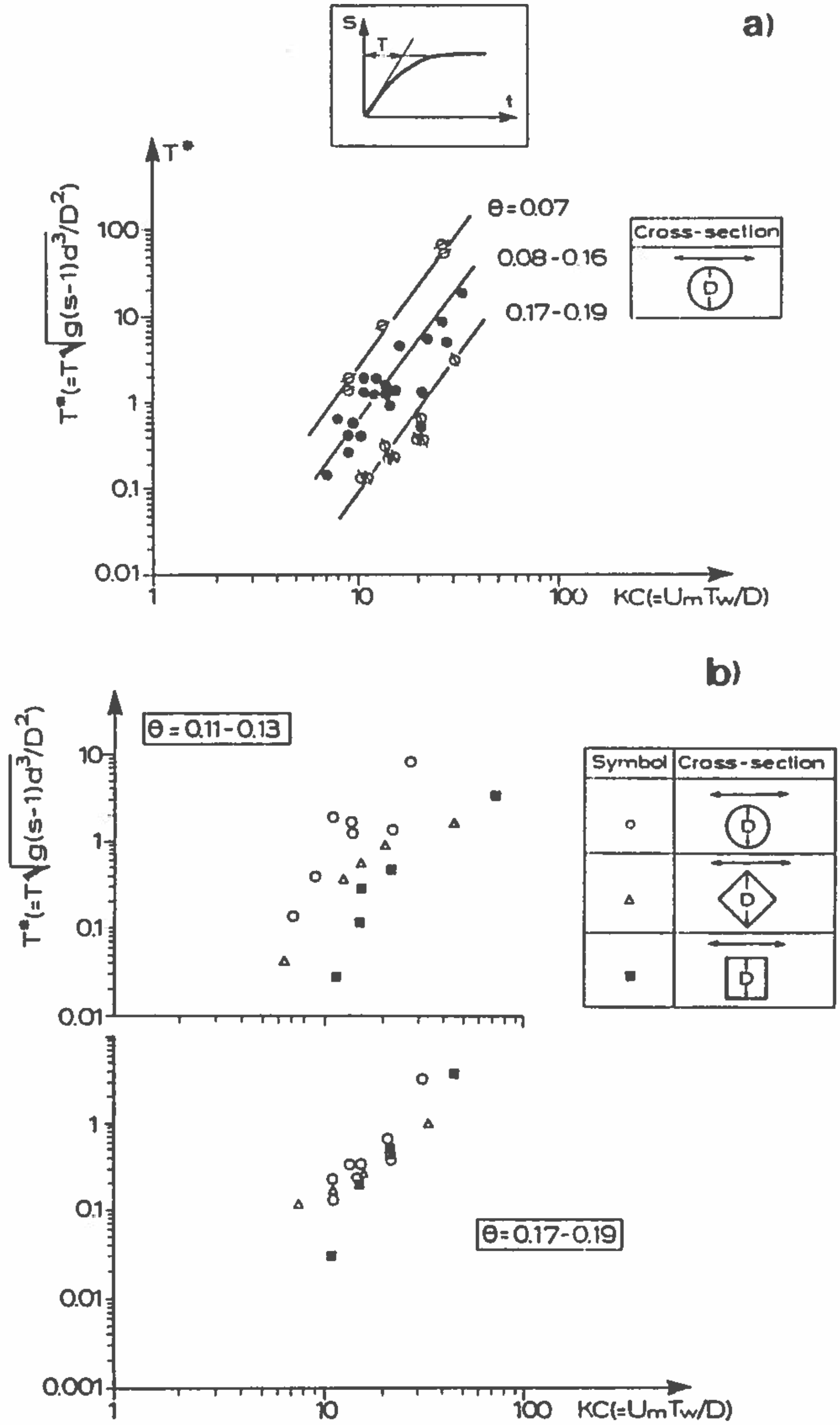

FIG. 10. Time Scale of Scour versus KC, Live Bed ($\theta > \theta_{cr}$): (a) Effect of θ, Circular Pile; (b) Effect of Cross-Sectional Shape

On dimensional grounds, the time scale can be written in the following functional form (Sumer et al. 1992b):

$$T^* = T^*(KC, \theta) \quad \text{.......................................} \quad (11)$$

in which T^* = normalized time scale defined in (6). This relation has been tested against the data obtained for circular piles in Sumer et al. (1992b).

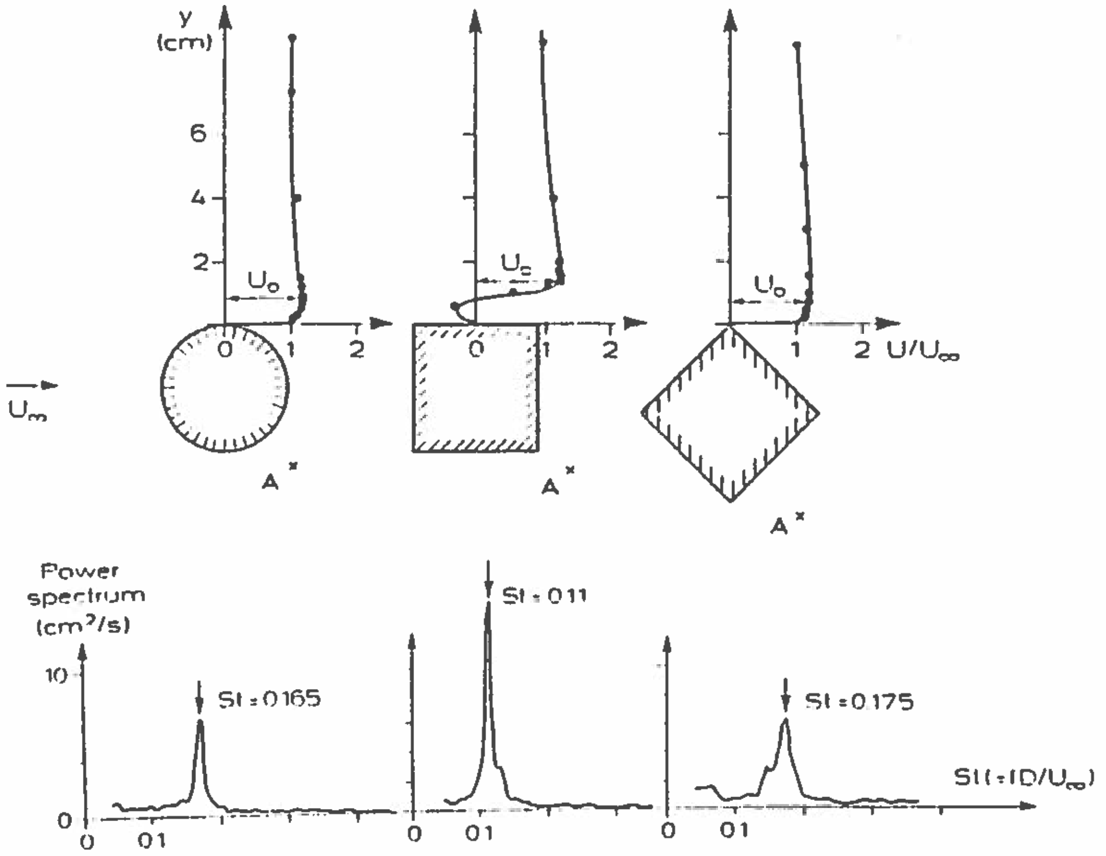

FIG. 11. Velocity Distributions and Power Spectra in Steady Current

The latter data are reproduced in Fig. 10(*a*), where the present supplementary data (tests 27–33) are also plotted. The following observations can be made from Fig. 10(*a*).

First, it is seen that the time scale increases with increasing *KC*. This is related to the fact that the volume of sediment to be eroded increases with increasing *KC*.

Second, the time scale decreases with increasing θ. This is consistent with the previously obtained knowledge regarding the time scale in scour processes, [e.g. Fredsøe et al. (1992) for time scale of scour process below pipelines]. This behavior is related to the higher capacity of erosion per unit time with increasing θ.

Fig. 10(*b*) illustrates the cross-section influence on the time scale. The data obtained in the case of square-section piles are plotted in the figure together with the previously mentioned circular-pile data. From the figure, the time scale for the 45° arrangement square pile is not extremely different from that for circular piles, although T^* for the former case appears to be slightly smaller than that for the latter situation. Regarding the 90° arrangement square piles, however, the figure shows that the time scale in this case is somewhat smaller than that for the circular piles. The figure also shows that this discrepancy becomes more pronounced with decreasing θ.

The variation in the time scale with respect to the cross-sectional shape may be related to the strength of the shed vortices. The latter can be approximated by the following relation:

$$\frac{\Gamma}{DU_\infty} = \frac{1}{4}\left(\frac{U_0}{U_\infty}\right)^2 \frac{1}{St} \quad \ldots\ldots\ldots\ldots\ldots\ldots\ldots\ldots (12)$$

in which Γ = strength of the vortices shed from a free cylinder, which is exposed to a steady current; U_∞ = undisturbed flow velocity, U_0 = potential flow velocity measured at the top of the cylinder boundary-layer at the point of separation in the case of circular and 45° arrangement square sections or, alternatively, at the top of the shear layer issuing from the separation point in the case of 90° arrangement square section (Fig. 11), and S = Strouhal frequency, defined by

$$S = \frac{fD}{U_\infty} \quad \text{(13)}$$

in which f = vortex-shedding frequency.

The preceding relation [(12)] stems from

$$\frac{d\Gamma}{dt} = \int_a^b \omega u dy = \int_a^b \left(\frac{1}{2} u \frac{\partial u}{\partial y}\right) dy \quad \text{(14)}$$

in which the right-hand side represents the flux of vorticity, which is fed into a developing vortex behind the pile per unit time and per unit pile length [see Bearman (1984), for instance]. Here the integral limits a and b = levels at which the velocity becomes nil and U_0, respectively.

To estimate the normalized vortex strength $\Gamma/(DU_\infty)$ from (12) for each cross section, velocity-profile measurements were conducted away from the bed in steady current with U_∞ = 10.5 cm/s, employing cylinders with D = 4 cm, using a DANTEC one-component laser Doppler anemometer (Fig. 11). Also, the vortex-shedding frequency was measured from the FFT (fast Fourier transform) analysis of the velocity signal received from the cylinder wake (Fig. 11).

The results indicate that U_0/U_∞ = 1.2–1.3, irrespective of the cross section, while S = 0.165 for circular section and 0.11 for 90° arrangement square section. This will give from (12) the strength of shed vortices as follows: $\Gamma/(DU_\infty)$ = 2.2 for circular section, while $\Gamma/(DU_\infty)$ = 3.6 for 90° arrangement square section. In other words, the shed vortices are stronger in the case of 90° arrangement square section than in the case of circular section. The stronger the vortices, the faster the scour process. Therefore, the time scale in the case of 90° square cylinder should be smaller than in the other two cases, as exhibited in Fig. 10.

Furthermore, the previously mentioned velocity measurements have indicated that, in the case of 45° arrangement square section pile, S = 0.175 and $\Gamma/(DU_\infty)$ = 2.15, meaning that the shed vortices in this case are in almost the same strength as in the case of circular section. This explains why the time scale in the case of 45° arrangement square pile is not extremely different from that of circular pile.

Other Factors Influencing Scour Process

First we consider the equilibrium scour depth. The equilibrium scour depth normalized by the pile width may, in addition to KC and α, depend on the following parameters: θ, R and k^*, where α is the shape factor regarding the cross-sectional shape of the pile, and $k^* = k/D$, k being the surface roughness of the pile. Although the equilibrium scour depth varies with θ strongly in the case of clear-water scour, it can be argued that in the case of a live bed the variation of S_0/D with θ is weak, as has been demonstrated by Breusers et al. (1977) for the current case and by Sumer et al. (1992a) for the wave case.

As for the influence of R and k^*, if the surface of the pile acts as a rough wall, the wake flow is almost unaffected by the R number, therefore no effect is expected on the scour depth; for a hydraulically smooth-surface pile, a small decrease in the scour depth might be expected for the R number range of 10^5 to 3×10^5 where the transition from subcritical to supercritical flow occurs, as pointed out in Sumer et al. (1992a) in conjunction with scour around circular piles. For square-section piles, however, the flow separation is fixed at the corners, consequently no significant change is expected in the shedding process, thus in the scour depth, with increasing R number.

Regarding the time scale of the scour process, in addition to the studied effects [namely, the effects of KC, α and θ (Fig. 10)] other nondimensional parameters such as R and k^* may influence the end results. As mentioned in the preceding, if the pile is rough, the wake flow will be almost unaffected by the R number, therefore no influence of the R number will be expected on the time scale. If the pile is smooth, however, the wake flow will be influenced by the R number; the Strouhal frequency S will be increased to a value of about 0.45 in the range of $10^5 \lesssim \mathrm{R} \lesssim 1.5 \times 10^6$ and then will drop to about 0.15 at $\mathrm{R} \cong 1.5 \times 10^6$, from where it will constantly increase with increasing R, reaching about 0.3 at $\mathrm{R} \cong 7 \times 10^6$ for circular piles (Schewe 1983). This change in S affects the strength of the shed vortices [(12)], therefore the time scale of the scour process might be affected by an increase in R. From (12), it might be anticipated that the time scale may become larger—by a factor of 2 or so for large R numbers ($\mathrm{R} \gtrsim 10^5$), particularly for the range $10^5 \lesssim \mathrm{R} \lesssim 1.5 \times 10^6$—than Fig. 10 predicts. However, no data are available to verify this. For the square piles, on the other hand, practically no Reynolds-number dependence should be expected because of the fixed separation points at the corners.

Finally, it may be mentioned that the effect of ripple dimensions on the test results has been discussed in Sumer et al. (1992a) in conjunction with the laboratory study of scour around circular piles for a wide range of ripple-length-to-pile-diameter ratio, for which the ripple length varied from about half a pile diameter to several pile diameters; and it was concluded that the ripples are not an essential factor in the scour process.

CONCLUSIONS

The equilibrium scour depth on a live bed normalized by the pile width, S_0/D, is a function of the Keulegan-Carpenter number (KC), based on the pile width. It increases with increasing KC and eventually attains a constant value for large values of KC ($KC \gtrsim 100$).

Given the Keulegan-Carpenter number, S_0/D varies with respect to the cross-sectional shape of the pile. For $KC \gtrsim 100$ the scour depth is the largest for the square-section pile with 45° arrangement; and it assumes its smallest value for the square-section pile with 90° arrangement. The scour depth for circular piles lies between the two (Fig. 6). For $KC \gtrsim 100$, the scour depth approaches a constant value, $S_0/D \cong 2$ for square piles and 1.3 for circular piles.

The empirical relations given in (7)–(9) relating S_0/D to the KC number for the three sections studied may be used as design equations. It is valid only for scour on live beds.

The time scale of the scour process is governed by two parameters, namely the Keulegan-Carpenter number (KC) and the Shields parameter (θ).

Given the Keulegan-Carpenter number and the Shields parameter, the time scale varies with the cross-sectional shape of the pile. It is somewhat smaller in the case of square-section pile with 90° arrangement than in the other two cases studied (the circular pile and the square pile with 45° arrangement).

The study shows the importance of even a moderate change in the cross-sectional shape (such as the one investigated in the present work) on the process of scour.

ACKNOWLEDGMENTS

This study is partially supported by the Marine Technique program of the Danish Technical Research Council (STVF). We thank Di Yu and Jan B. Jakobsen for their involvements in conducting some of the scour tests.

APPENDIX I. REFERENCES

Bearman, P. W. (1984). "Vortex shedding from oscillation bluff bodies." *Ann. Rev. Fluid Mech.*, Vol. 16, 195–222.

Breusers, H. N. C., Nicollet, G., and Shen, H. W. (1977). "Local scour around cylindrical piers." *J. of Hydr. Res.*, 15(3), 211–252.

Chiew, Y. M. (1989). "Local scour at vertical piles under wave action." *9th Australian Conf. on Coast. and Oc. Engrg.*, Adelaide, Australia, 393–396.

Das, M. M. (1970). "A literature review on bed-load transport due to wave action and localized scour in non-cohensive sediments." *A literature review on erosion and deposition of sediment near structures in the ocean; Final Rep. HEL 21-6*, H. A. Einstein and R. L. Wiegel, eds., University of California, Berkeley, Calif.

Eadie, R. W. IV, and Herbich, J. B. (1986). "Scour about a single, cylindrical pile due to combined random waves and a current." *Proc., 20th Coast. Engrg. Conf.*, ASCE, New York, N.Y., 1858–1870.

Fredsøe, J., Sumer, B. M., and Arnskov, M. M. (1992). "Time scale for wave/current scour below pipelines." *Int. J. of Offshore and Polar Engrg.*, 2(1).

Herbich, J. B., Schiller, R. E. Jr., Dunlap, W. A., and Watanabe, R. K. (1984). *Seafloor scour*. Marcel Dekker, Inc., New York, N.Y.

Hjorth, P. (1975). "Studies on the nature of local scour." *Bull. Series A, No. 46*, Univ. of Lund, Lund, Sweden.

Kawata, Y., and Tsuchiya, Y. (1988). "Local scour around cylindrical piles due to waves and currents combined." *Proc., 21st Coast. Engrg. Conf., Vol. 2*, ASCE, New York, N.Y., 1310–1322.

Palmer, H. D. (1969). "Wave-induced scour on the sea floor." *Proc., Civil Engineering in the Oceans II*, ASCE, New York, N.Y., 703–716.

Schewe, G. (1983). "On the force fluctuations acting on a circular cylinder in crossflow from subcritical to transcritical Reynolds numbers." *J. Fluid Mech.*, 133 (Aug.), 265–285.

Sumer, B. M., Fredsøe, J., and Christiansen, N. (1992a). "Scour around vertical pile in waves." *J. of Wtrwy., Port, Coast., and Oc. Engrg.*, ASCE, 117(1), 15–31.

Sumer, B. M., Christiansen, N., and Fredsøe, J. (1992b). "Time scale of scour around a vertical pile." *Proc., 2nd Int. Offshore and Polar Engrg. Conf.*, International Society of Offshore and Polar Engineers, San Francisco, Calif., Vol. III, 308–315.

Wang, R-K., and Herbich, J. B. (1983). "Combined current and wave-produced scour around a single pile." *COE Rep. No. 269*, Texas A&M University.

APPENDIX II. NOTATION

The following symbols are used in this paper:

D = pile width (see Fig. 6);
d = sediment size;
f = vortex-shedding frequency;

f_w = wave-friction factor;
g = acceleration due to gravity;
KC = Keulegan-Carpenter number (4);
R = Reynolds number for pile (5);
S = scour depth;
S_0 = equilibrium scour depth;
S = Strouhal frequency (13);
s = specific gravity of sediment;
T = time scale of scour process;
T^* = normalized time scale of scour process (6);
T_w = wave period;
t = time from onset of scour;
U_m = maximum value of orbital velocity of water particles at bed;
U_{fm} = maximum value of undisturbed bed shear velocity;
U_∞ = undisturbed flow velocity in steady current;
U_0 = potential flow velocity measured at top of pile boundary layer or, alternatively, at top of its related shear layer after separation (Fig. 11);
Γ = vortex strength;
θ = shields parameter (1);
ν = kinematic viscosity; and
ω = angular frequency of wave motion (3).

Turbulent oscillatory boundary layer over a bed with a change in roughness

B. Mutlu Sumer, Jørgen Fredsøe and Niels Christiansen (ISVA)

Prog. Rep. 72, pp. 3-16, October 1990
Inst. Hydrodyn. and Hydraulic Eng.
Tech. Univ. Denmark

1. TURBULENT OSCILLATORY BOUNDARY LAYER OVER A BED WITH A CHANGE IN ROUGHNESS

by

B. Mutlu Sumer, Thorkild S. Laursen and Jørgen Fredsøe

ABSTRACT

This study deals with turbulent oscillatory boundary-layer flows over a plane bed with a sudden spatial change in roughness, namely, from a roughness equal 4.8 mm to a smooth wall. The free-stream flow is a purely oscillating flow with sinusoidal velocity variation. Mean flow and turbulence properties were measured. The results indicate that the flow properties undergo marked changes in the streamwise direction. The results further indicate that the two half periods, namely the half period where the flow is from the smooth bed section to the rough and vice versa, are different, as far as the mean flow and the turbulence properties are concerned.

EXPERIMENTAL FACILITY

The experiments were carried out in a U-shaped oscillatory-flow water tunnel which has a working section 10 m in length. This tunnel is the same as that described by Jensen et al. (1989). The bottom wall of the tunnel in the present tests was rough over about half of the length of the working section, while the other half was smooth (Fig. 1). The rough wall was achieved by gluing pebbles of fairly uniform size one layer deep to plastic plates and then the plastic plates were fixed rigidly to the bottom of the tunnel. The mean roughness height of the wall was $k = 4.8$ mm. Its k_s value (Nikuradse's equivalent sand roughness) was measured to be $k_s = 15$ mm. For the smooth-bed section, PVC plates were fixed directly to the bottom of the tunnel. This was done in such a way that the level of the smooth bed section lay at a distance of 0.25 k below the top of the roughness elements of the rough-bed section of the bottom (Fig. 2). The latter is the distance of the theoretical wall of a rough boundary from the top of the roughness elements, known from the steady boundary layer flow research (Bayazit, 1976).

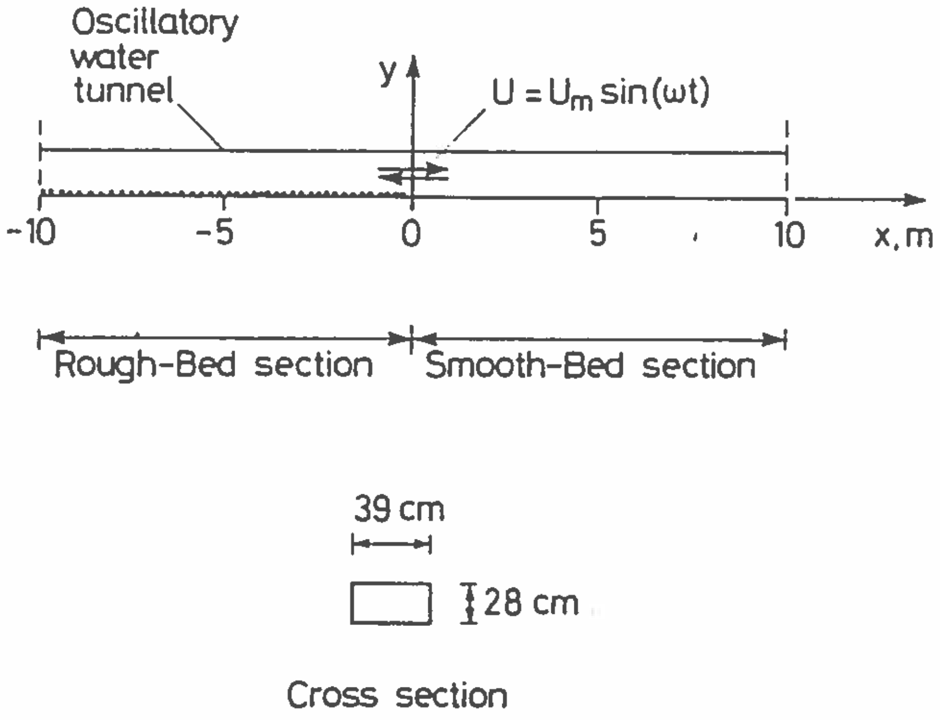

Fig. 1. Test tunnel

The velocity distribution over the depth was measured by a two-component Dantec laser Doppler anemometer.

The measurements were conducted at the following stations: x = 2.5 cm, 5 cm, 10 cm, 20 cm, 40 cm and 206 cm along the smooth-bed section and x = -2.3 cm, -5 cm, -20,4 cm, -79.2 cm and -302 cm along the rough-bed section. Here x = the distance from the joint section (Fig. 2). The test conditions are summarized as follows:

Test No.	U_m (m/s)	a (m)	Re $= \frac{aU_m}{\nu}$	a/k_s
1	0.57	0.88	5×10^5	60
2	1.97	3.04	6×10^6	200

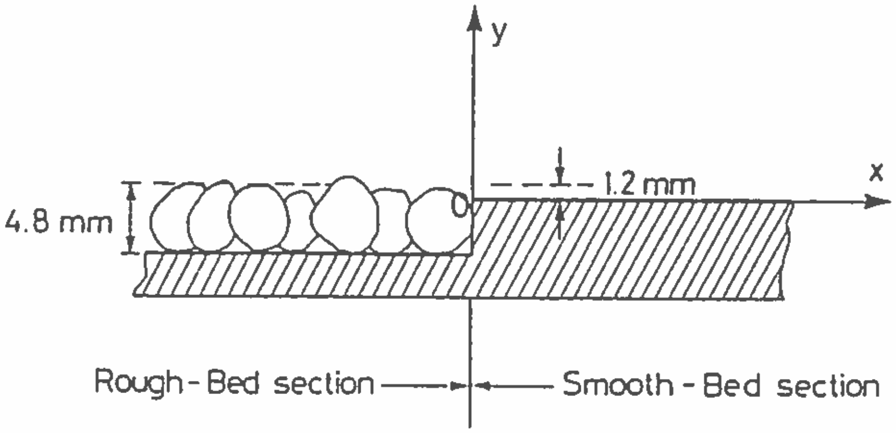

Fig. 2. Close-up picture of the section where the roughness changes.

The period of the oscillatory flow in all the tests was 9,75 s. In the table U_m = the maximum value of the free-stream velocity and a = the amplitude of the free-stream motion.

EXPERIMENTAL RESULTS AND DISCUSSION

Figs. 3 - 6 present the mean velocity profiles over one period of the motion for four measurement stations; two of the stations lie in the smooth-bed section and the other two in the rough-bed section.

Figs. 7 and 8 depict the bed shear-stress velocity data obtained for Test 2. The data for Test 1 show the same behaviour. The shear-stress velocity U_f is defined by

$$U_f = (\bar{\tau}_0/\rho)^{1/2} \qquad (1)$$

in which $\bar{\tau}_o$ = the mean bed shear stress. U_f was obtained by fitting straight lines to the logarithmic-layer portion of the mean velocity distribution (see Figs. 3 - 6). In Figs. 7 and 8 the asymptotic values regarding the maximum value of U_f are plotted for comparison. From the figures, the following conclusions can be drawn:

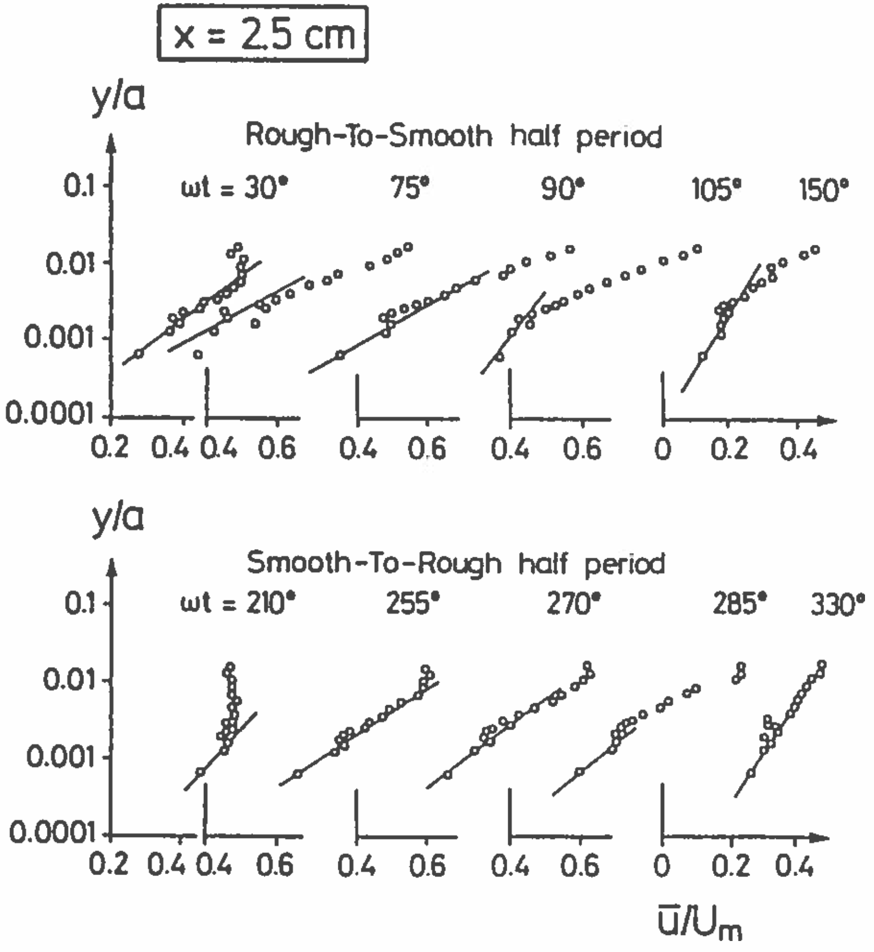

Fig. 3. Mean velocity distribution in semi-log plot. Straight lines: Log law. Test 2.

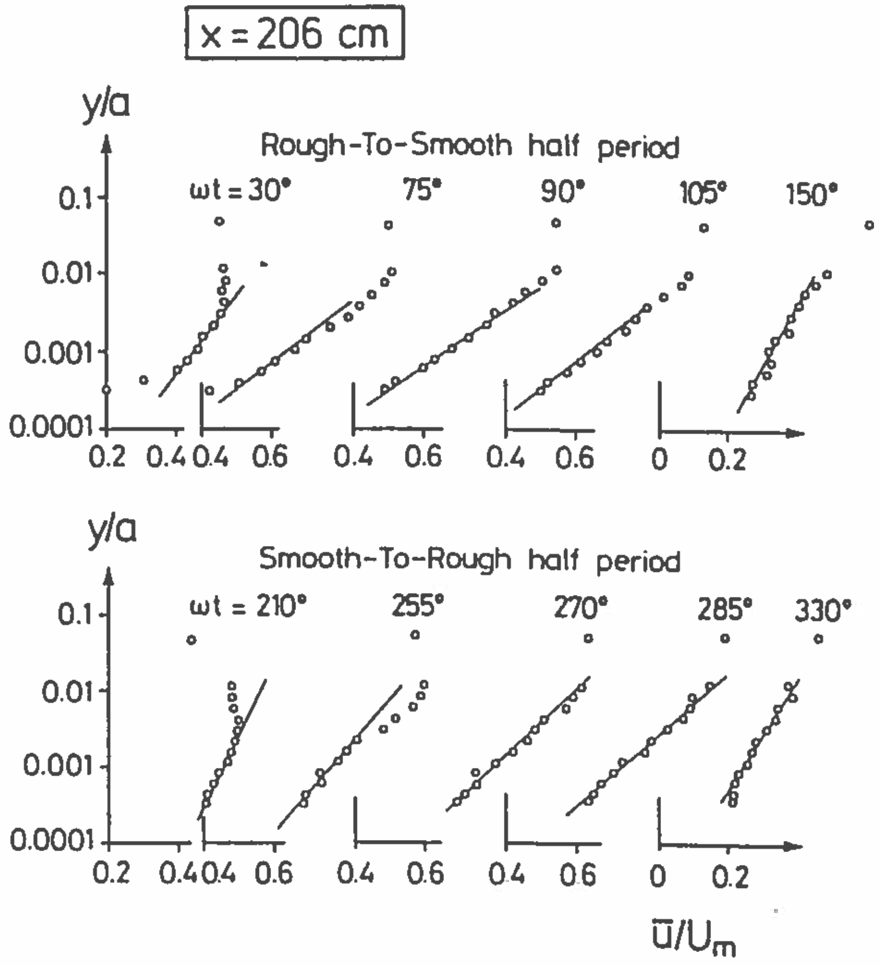

Fig. 4. Mean velocity distribution in semi-log plot. Straight lines: Log law. Test 2.

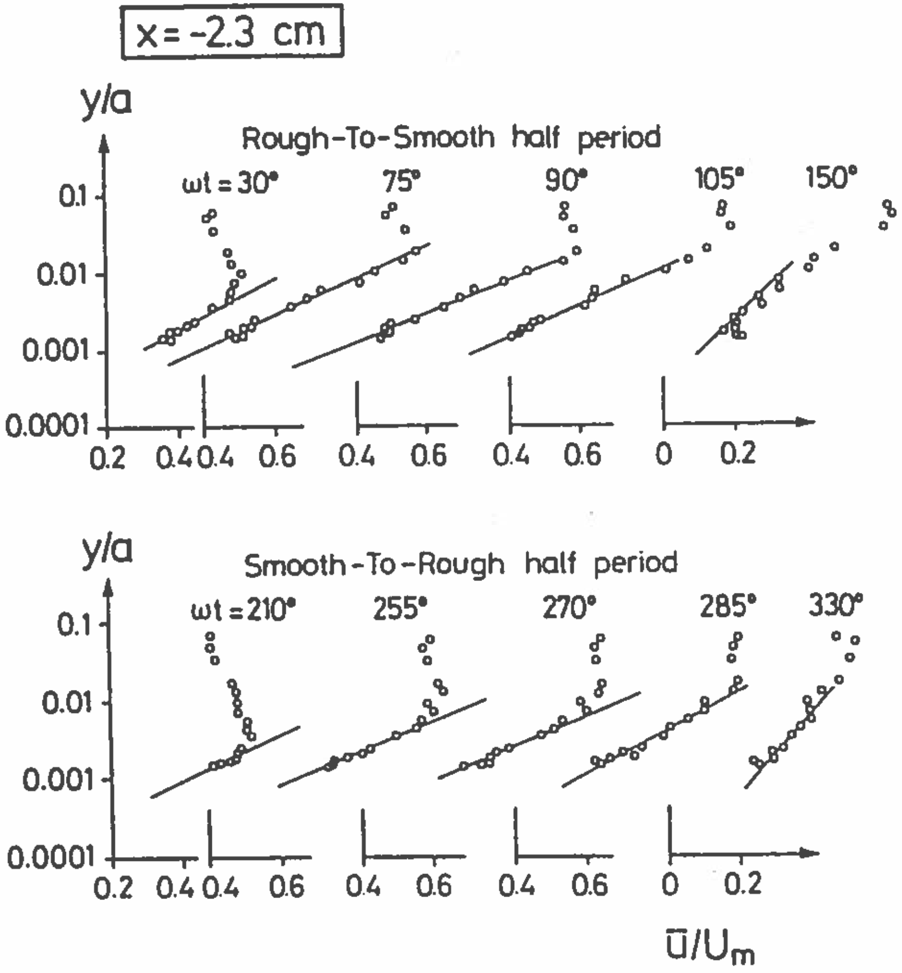

Fig. 5. Mean velocity distribution in semi-log plot. Straight lines: Log law. Test 2.

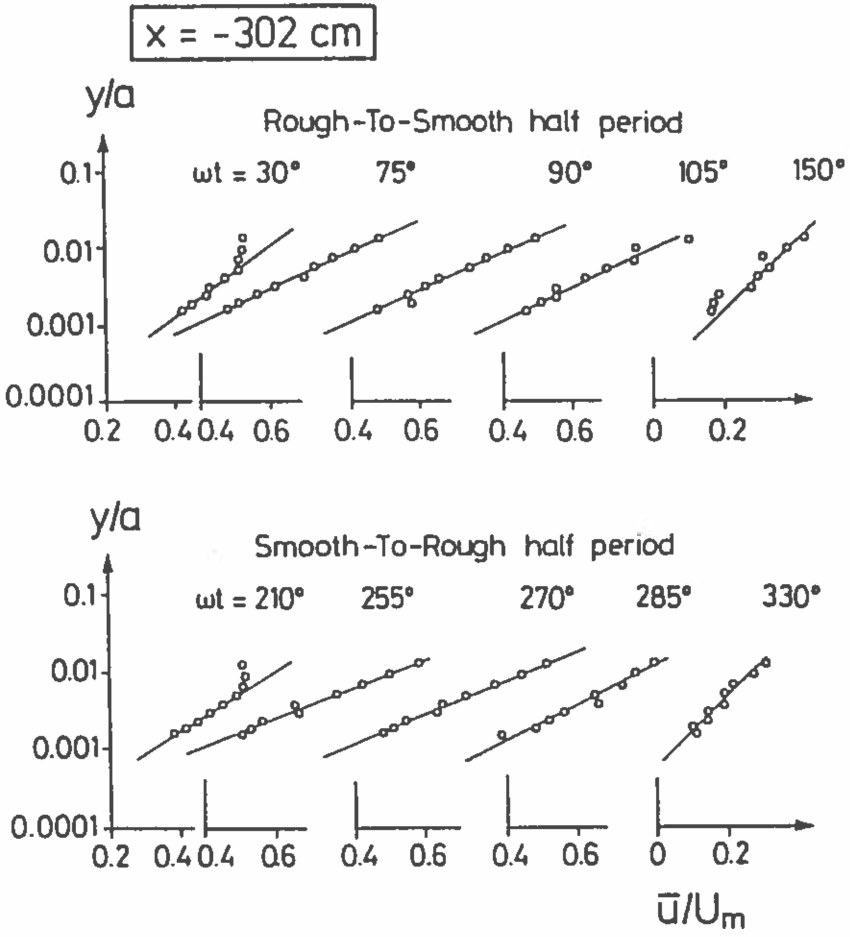

Fig. 6. Mean velocity distribution in semi-log plot. Straight lines: Log law. Test 2.

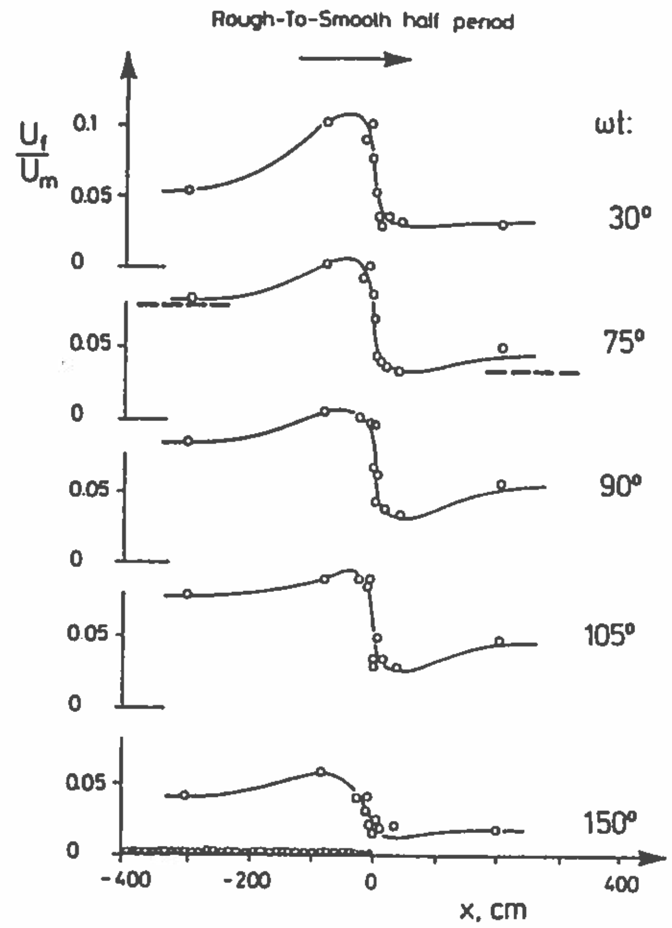

Fig. 7. Time evolution of bed shear stress velocity. Test 2. Dashed lines: Asymptotic values obtained from friction diagrams given by Jensen et al. (1989)

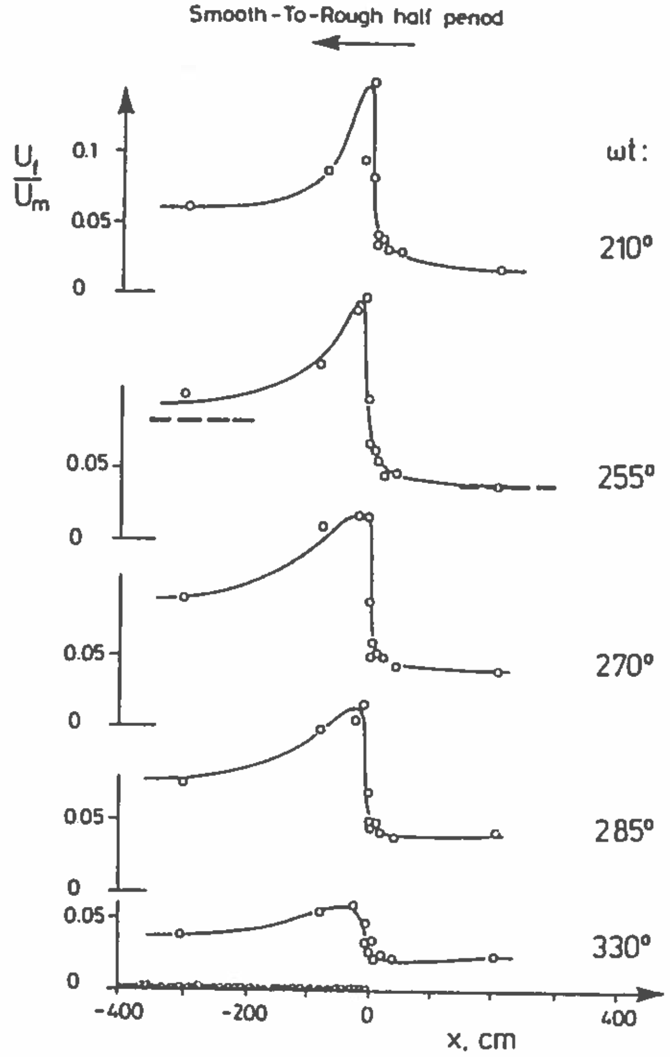

Fig. 8. Time evolution of bed shear stress velocity. Test 2. Dashed lines: Asymptotic values obtained from friction diagrams given by Jensen et al. (1989)

1. There is a peak in the bed shear stress in its variation with x, and this peak occurs over the rough-bed section in the neighbourhood of the location where the roughness changes.
2. The peak is much larger in the smooth-to-rough half period than in the rough-to-smooth half period.
3. As far as the magnitudes of these peaks are concerned, the increase in U_f with respect to its rough-bed value in the rough-to-smooth half period is a factor of 1.5 at its maximum, and, correspondingly, the increase in U_f with respect to its smooth-bed value in the smooth-to-rough half period is a factor of 4-5.

Fig. 9 presents the period-averaged velocity profiles. The figure indicates that there is a constant streaming of fluid near the bed in the direction of the rough-bed section. The figure further indicates that this flow near the bed is balanced by a flow in the opposite direction at higher elevations from the bed. The streaming is explained as follows.

Consider an observer standing a little distance away from the rough bed at an x-location in the neighbourhood of the section where the roughness changes. This observer will experience velocities which are relatively higher in the smooth-to-rough half period than in the rough-to-smooth half period. This obviously will result in a non-zero period-averaged velocity which is directed towards the rough-bed section. The counter flow at the higher elevations, on the other hand, is due to continuity.

The effect which creates streaming will of course decrease with the distance from the section where the roughness changes. This is in fact quite clear from Fig. 9.

Fig. 10 illustrates the phase lead data obtained from the present velocity measurements. Since the phase lead plotted in the figure corresponds to that of the velocity measured at the y-location nearest the bed, it can be expected to be quite close to the phase lead of the bed shear stress over the free-stream velocity. Indeed the asymptotic values agree fairly well with the values reported in Jensen (1989).

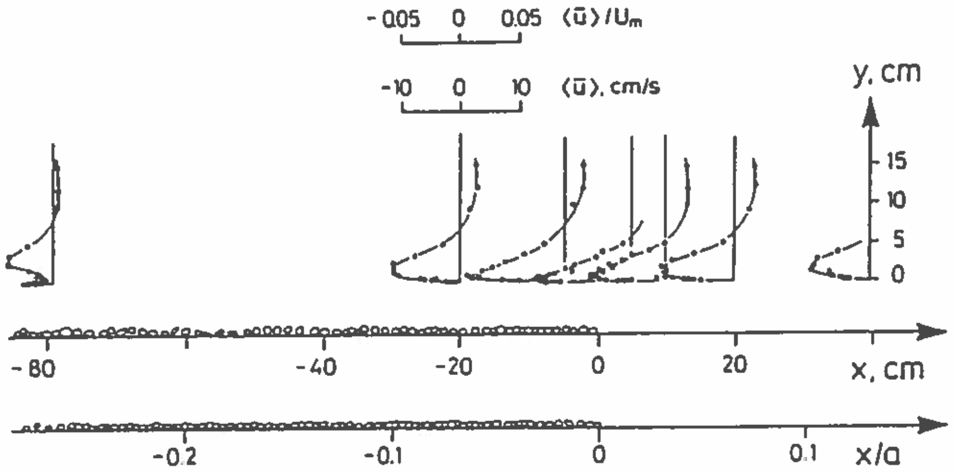

Fig. 9. Period-averaged velocity profiles and streaming. Test 2.

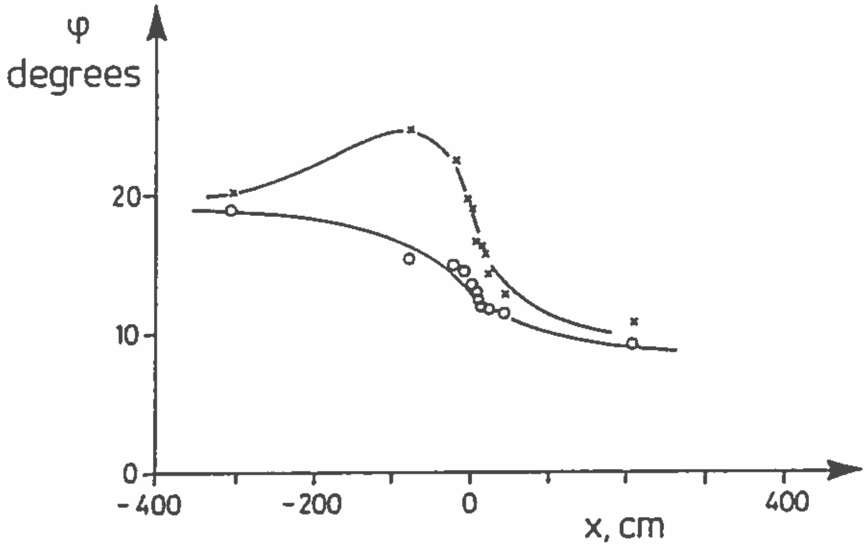

Fig. 10. Phase lead of the near-bed velocity over the velocity in the free-stream region. The y-location of the point where the velocity was measured near the bed is y = 0.5 mm over the smooth-bed section and 1 mm (from the theoretical bed) over the rough-bed section. Crosses: Test 1. Circles: Test 2.

Finally, Figs. 11 - 13 present the turbulence data at different phases. At $\omega t = 0^{\circ}$ there is a more or less evenly distributed turbulence in the tunnel, which is the reminiscence of the turbulence from the previous half period. As the flow progresses during the half period from $\omega t = 0^{\circ}$ to 180°, more and more turbulence is created near the bed and brought into the free stream

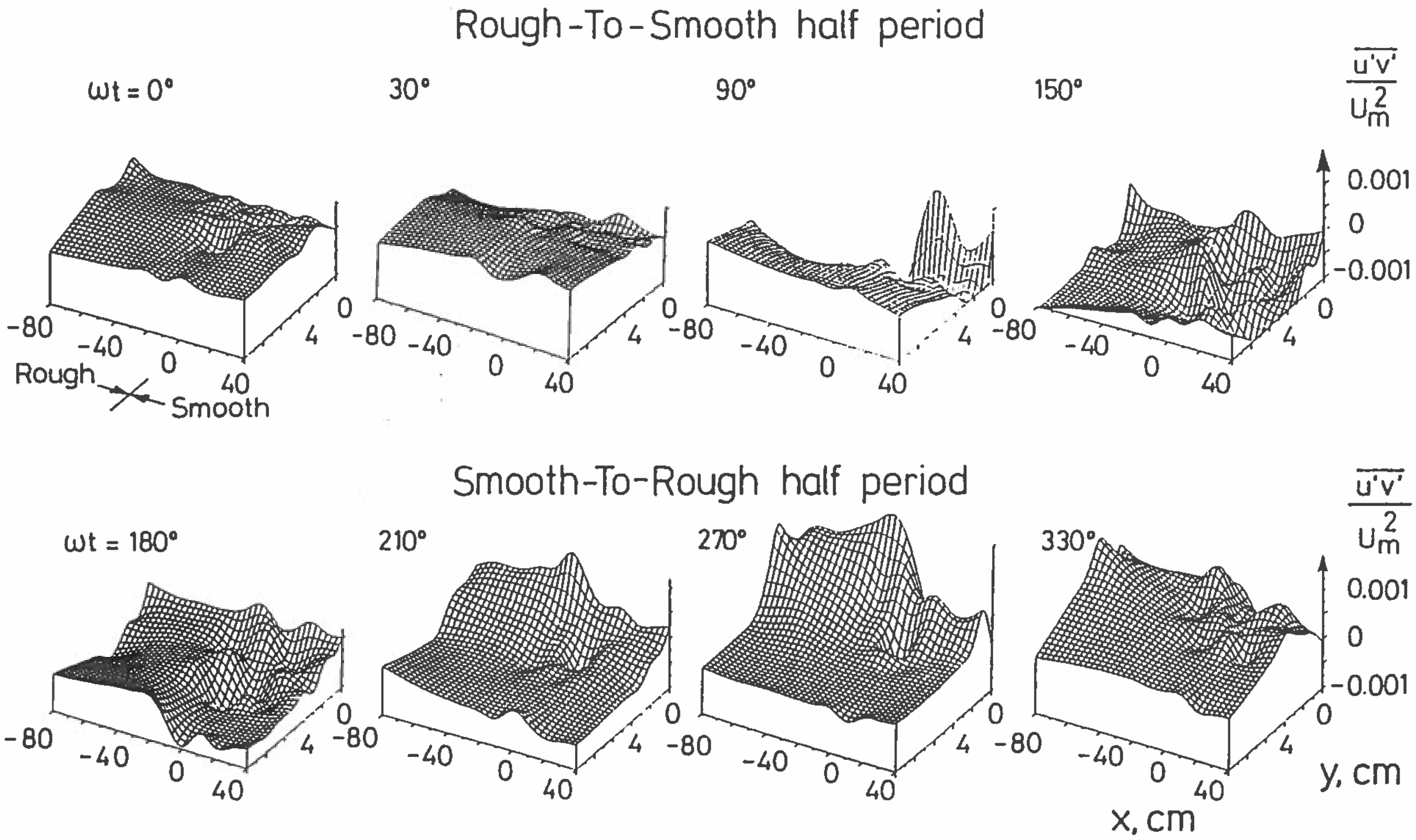

Fig. 11. R.m.s. value of x-component of the fluctuating velocity, u'. Test 2.

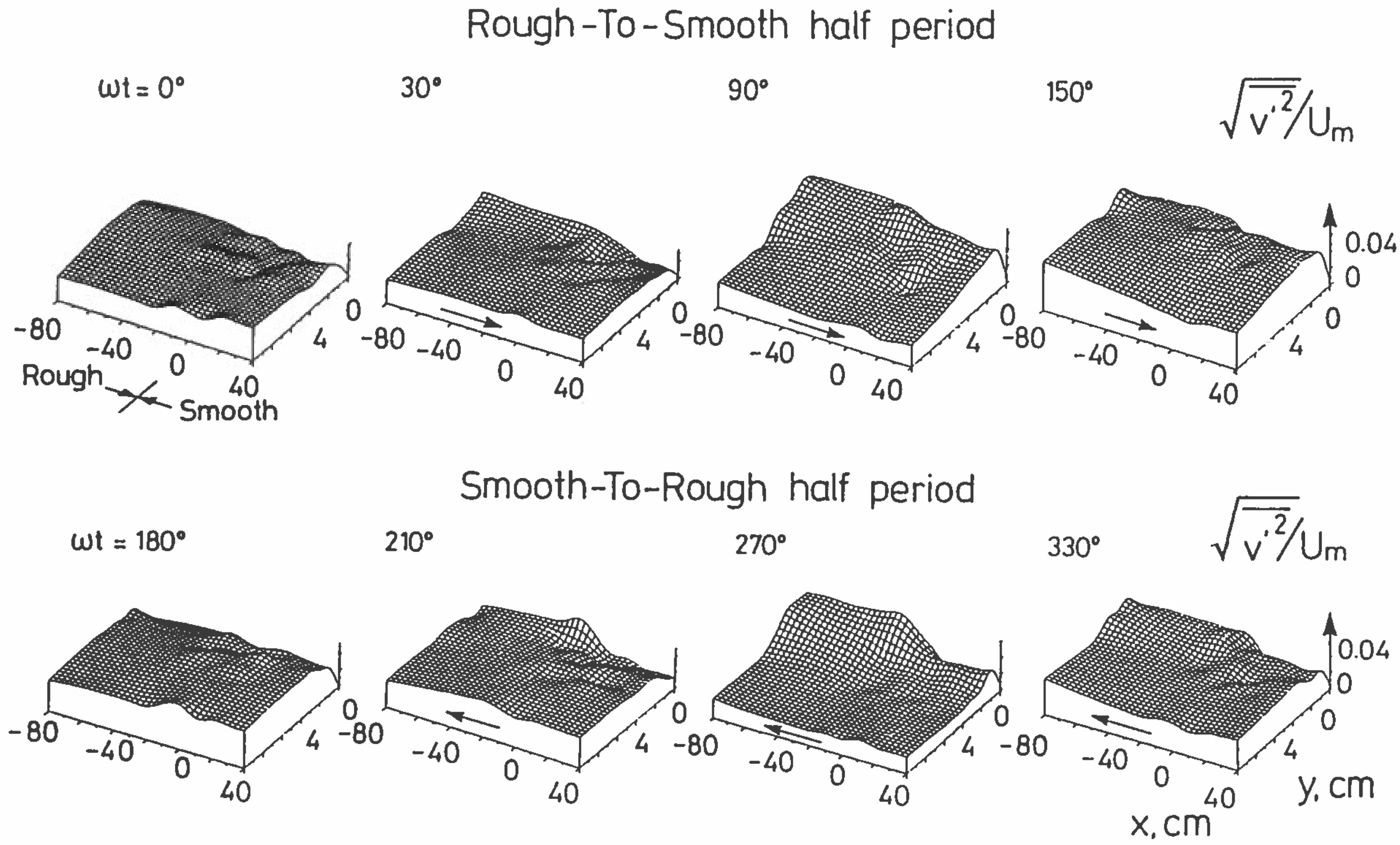

Fig. 12. R.m.s. value of y-component of the fluctuating velocity, v'. Test 2.

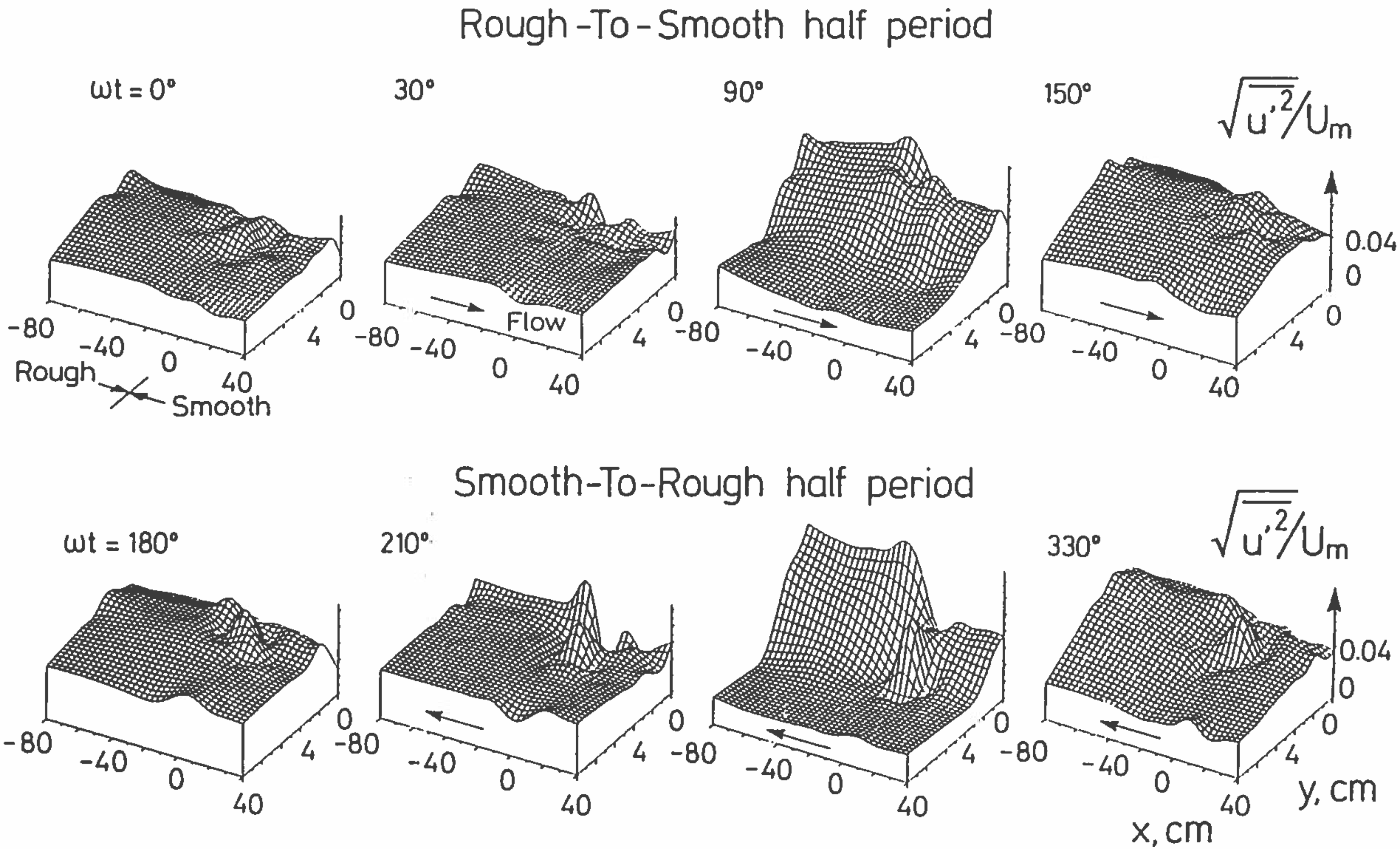

Fig. 13. Reynolds stress $\overline{u'v'}$. Test 2.

region. As the half period comes to an end (ωt = 180 °), again the turbulence is more or less evenly distributed over the (x,y) plane. Matters develop in a similar way in the other half period.

From Figs. 11 - 12 three points can be noted: 1) The turbulence left in the tunnel at the end of the rough-to-smooth half period (i.e. at $\omega t = 180^{\circ}$) is distinctly larger than that at the end of the smooth-to-rough half period (i.e. at $\omega t = 0^{\circ}$). 2) The turbulence over the rough-bed section is always larger than that over the smooth-bed section. 3) The turbulence experienced through the two half periods is not necessarily the same.

CONCLUSION

The main results of this study are summarized as follows:

1) The bed shear-stress velocity in its variation with the streamwise distance experiences a peak over the rough-bed section in the neighbourhood of the location where the roughness changes.

2) In the rough-to-smooth half period, the increase in the bed shear stress velocity (due to this peak) with respect to its rough-bed value is a factor of 1.5. Correspondingly, in the smooth-to-rough half period, the increase in the bed shear stress velocity with respect to its smooth bed value is a factor of 4-5.

3) There exists a streaming near the bed in the direction from the smooth- to the rough-bed section. This flow is balanced with a counter flow at a higher elevation from the wall.

4) The turbulence left in the flow at the end of the rough-to-smooth half period is distinctly larger than that at the end of the smooth-to-rough half period.

5) Also, the turbulence is generally different in the two half periods.

ACKNOWLEDGEMENT

The study is partially supported by the research programme "Marine Science" of the Danish Scientific Council (STVF).

REFERENCES

Bayazit, M. (1976). Free surface flow in a channel of large relative roughness. J. Hydraulic Research, Vol. 14, No. 2, pp. 115-126.

Jensen, B.L. (1989). Experimental investigation of turbulent oscillatory boundary Layers. Series Paper 45, ISVA.

Jensen, B.L., Sumer, B.M. and Fredsøe, J. (1989). Turbulent oscillatory boundary layers at high Reynolds numbers. J. Fluid Mech., Vol. 206, pp. 265-297.

Scour model tests with bridge piers

Mogens Hebsgaard (DHI), Finn Ennemark and Søren Spangenberg (SBF), Jørgen Fredsøe (ISVA) and Helge Gravesen (CCL)

SCOUR MODEL TESTS WITH BRIDGE PIERS

by

Mogens Hebsgaard, Danish Hydraulic Institute, DK-2970 Hørsholm
Finn Ennemark and Søren Spangenberg, A/S Storebæltsforbindelsen (Great Belt A/S), DK-1601 Copenhagen
Jørgen Fredsøe, Professor, Consultant to A/S Storebæltsforbindelsen, DK-2800 Lyngby
Helge Gravesen, CCL Joint Venture (COWI-Carl Bro-Leonhardt), DK-2830 Virum

ABSTRACT

In the design of the Western Bridge accross the western channel of the Great Belt in Denmark, the scour protection of the 64 bridge piers was designed on basis of numerical analysis and physical modelling. The numerical analysis contained determination of the wave and current induced bed shear stresses along the bridge alignment in order to determine the piers where the largest bed shear stresses occur. These piers were thus investigated in a hydraulic model. Phase 1 of the model tests contained tests to determine the shear stress amplification pattern around the piers, and Phase 2 contained stability tests with the proposed scour protection. This article describes the design philosophies, and their implications for the applied methods for determination of the necessary scour protection.

KEYWORDS

Design philosophy, scour protection, bed shear stress amplification.

SOMMAIRE

Pour le projet du Pont Ouest à travers le chenal ouest du Great Belt au Danemark, la protection contre l'érosion des 64 piliers du pont fut projetée à partir des analyses numériques et des études sur modèle réduit. Les analyses numériques contenaient la détermination des efforts de cisaillement au fond induits par les vagues et les courants le long de l'alignement du pont pour déterminer les piliers où les plus grands efforts de cisaillement au fond ont lieu. Ces piliers furent donc étudiés dans un modèle hydraulique. La Phase 1 des études sur modèle réduit comprenait les essais pour déterminer le plan d'amplification des efforts de cisaillement autour des piliers et la Phase 2 comprenait les essais de stabilité avec la protection proposée contre l'érosion. Cet article décrit les conceptions du projet et leurs implications dans la détermination de la protection nécessaire contre l'érosion.

MOTS-CLEFS

Conception du projet, protection contre l'érosion, amplification de l'effort de cisaillement au fond.

1 INTRODUCTION

The fixed link across the 18 km Great Belt in Denmark will consist of four main elements: 1) a combined railway and road bridge across the western channel between Funen and Sprogø, the small island in the middle of the Great Belt, 2) a land reclamation increasing Sprogø to three times its original size, 3) a railway tunnel under the eastern channel between Sprogø and Zealand, and 4) a suspension bridge for road traffic across the eastern channel which is the main shipping route to the Baltic Sea.

This article concerns the design of the scour protection of the bridge piers for the Western Bridge between Knudshoved (Funen) and Sprogø Island. Earlier articles concerning other aspects in the design of the Western Bridge are for instance Refs /4/, /5/, /6/ and /7/.

The proposed design of the scour protection for the bridge piers has been investigated through both numerical and physical model studies carried out by Danish Hydraulic Institute (DHI).

2 DESIGN PHILOSOPHY

The Western Bridge is a 6.6 km long low clearance (18 m) concrete structure. The bridge is designed as a combined road/railway bridge with 63 spans (12x71.75 m and 51x110.40 m). The bridge rests on 64 bridge piers. The piers which are located in water depths up to about 30 m must be designed to withstand environmental loads caused by wind, current, waves, ice pressure, settlements and temperature changes as well as loads from traffic, ship collisions, etc. The location of the western bridge is shown on Fig 1.

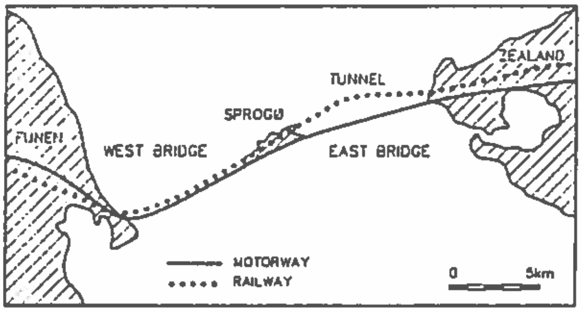

Fig 1 Location plan, alignment of the Western Bridge.
Fig 1 Carte synoptique, alignement du Pont Ouest.

The combined load from current and waves may cause scouring around the bridge piers. The criteria for the stability of the scour protection states that limited damages are acceptable in storm situations with a probability of occurrence of 10^{-2} per year. Additionally, the damage on the scour protection should in no way cause reduction of the bearing capacity of the foundation and should be repairable within one month in storm events with a probability of occurrence of 10^{-5} per year. A further discussion on the risk acceptance criteria for disruption is not presented here. A presentation of safety criteria, etc, is given by Vincentsen and Spangenberg (1990) (Ref /1/).

The bridge piers are caissons reaching from the foundation level to 3.5 m below mean sea level. The cross-section of the lower 7.5 to 9 m of the caisson is 17x30 m and 6.4x30 m for the upper part. On the plinth in level -3.5 m, the two columns supporting the railway and road part of the bridge are resting. The layout of the bridge piers is shown in Fig 2.

The soils at the bridge are generally erodible material, either easy erodible like sand, silt of gytje or more resistant as clay till. The presence of the piers means that the flow conditions due to waves and currents will cause an increase of the turbulence intensity (formation of eddies) and local increase in the current velocity in the immediate vicinity of the structure, see Sumer, Fredsøe and Christensen (Ref /3/). If erodible soils, the soil material may be eroded close to the piers. If the erosion is extensive, it may cause failure of the foundation for the piers. Due to this, the area around the bridge piers has to be secured by a scour protection. In the present project, a stone protection around the piers was proposed (see Fig 3). Originally, the piers were proposed with large quarry stones protecting the sand fill in the side cells. In the final layout, a concrete slab was introduced as cover instead.

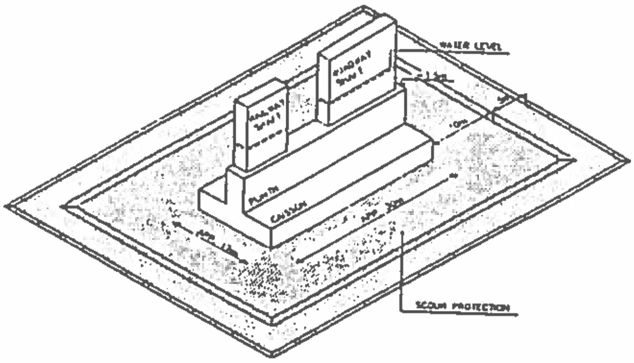

Fig 2 Layout of bridge pier.
Fig 2 Plan-masse d'un pilier du pont.

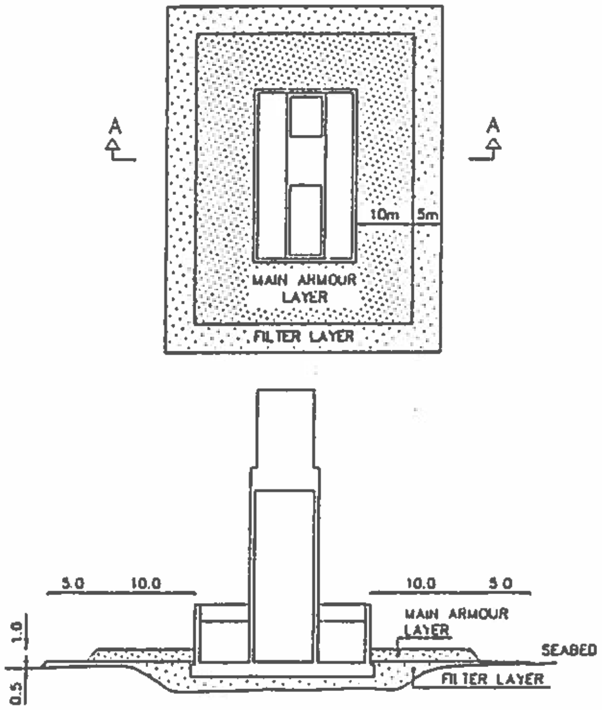

SECTION A – A

Fig 3 Layout of proposed scour protection.
Fig 3 Plan-masse de la protection proposée contre l'érosion.

In order to investigate the necessary extent and stone sizes of the protection as function of the water depth and wave/current conditions, extensive hydraulic investigations were carried out.

3 CONTENT OF HYDRAULIC INVESTIGATIONS

The hydraulic investigations comprised the following tasks:

- review of hydrographic conditions
- a numerical model analysis to determine the wave and current induced bed shear stresses along the bridge alignment
- physical modelling with measurements of bed shear stress amplifications around the bridge piers
- physical model tests with the scour protection to investigate the stability of the protection

In the following, each investigation task is described. The main emphasis has been put on the physical model tests carried out, whereas the hydrographic conditions and the numerical modelling are described more briefly.

4 HYDROGRAPHIC CONDITIONS

The hydrographic conditions for the scour investigations have been based on measurements carried out in the Great Belt and results from numerical modelling. Waves and current from respectively northerly and southerly directions have been considered.

4.1 Wave Conditions

The estimation of the design wave conditions has been based on measurements carried out at 10 m water depth (SW of Sprogø Island) combined with numerical refraction calculations. The estimated significant wave heights along the bridge alignment with a probability of occurrence of 10^{-2} per year are shown in Fig 4.

The wave heights with a probability of occurrence of 10^{-3} per year are estimated to be 30-35% higher.

4.2 Current Conditions

The design current conditions were determined based on results from current measurements at two locations close to the middle of the western channel combined with numerical simulations carried out with DHI's hydrodynamic model, MIKE 21.

The estimated current conditions with a probability of occurrence 10^{-2} per year are shown in Fig 5.

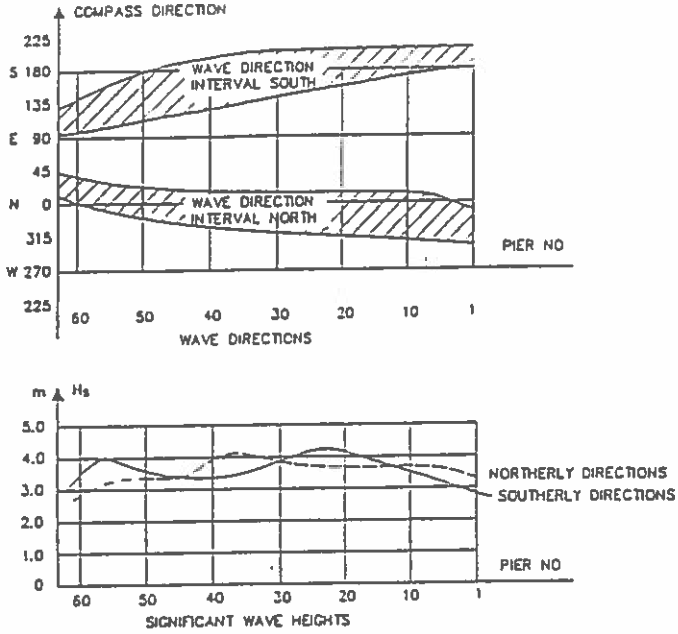

Fig 4 Design wave conditions: waves from northerly and southerly directions with a probability of occurrence of 10^{-2} per year.

Fig 4 Conditions des vagues: vagues provenant de directions nord et sud avec une probabilité d'occurrence de 10^{-2} par année.

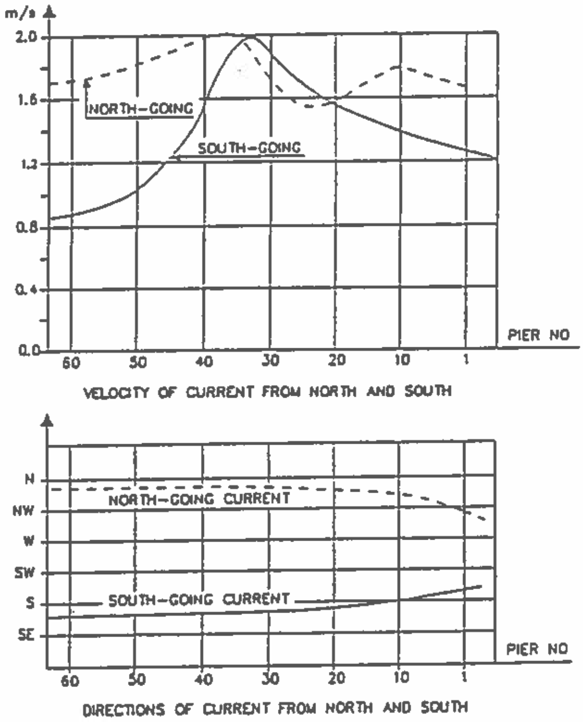

Fig 5 Design current conditions: current from northerly and southerly directions with a probability of occurrence of 10^{-2} per year.

Fig 5 Conditions des courants: Courants provenant de directions nord et sud avec une probabilité d'occurrence de 10^{-2} par année.

The current velocities with a probability of occurrence 10^{5} per year are 10-15% higher.

5 NUMERICAL MODELLING OF SHEAR STRESS

A numerical model was used to estimate the wave and current induced bed shear stress along the bridge alignment before placing of the piers. The purpose of these calculations was to identify the locations where the largest bed shear stresses occur. The bridge piers to be located at these positions were then selected for further investigations in the physical model.

The numerical model calculates the bed shear stress due to waves and currents on basis of the theory outlined by Fredsoe 1984 (Ref /2/).

The bed shear stress was calculated for the wave and current conditions from northerly respectively southerly directions for the probability of occurrence 10^{2} and 10^{-5} per year. The current direction was kept constant at the location of each bridge pier, whereas the wave direction was varied within the limits described in Fig 4. The main results of the calculations are shown in Fig 6.

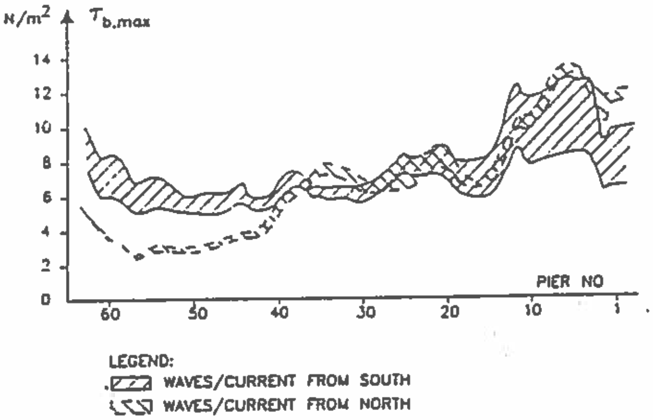

Fig 6 Wave and current induced bed shear stresses.

Fig 6 Efforts de cisaillement au fond induits par vagues et courants.

On basis of the results presented in Fig 6, piers Nos 13, 22 and 36 were selected for further investigations in the physical model representing a 'shallow', 'medium' and 'deep' water pier.

The wave and current conditions at those piers to be considered in the model tests were as shown in Table 1.

Table 1 Design wave and current conditions for piers Nos 13, 22 and 36.

Pier No	Water Depth (m)	Wave/ Current coming from	Flow dir. related to pier (°)	Prob. of occurrence 10^{2} per year			Prob. of occurrence 10^{5} per year		
				H_s (m)	T_p (s)	u_c (m/s)	H_s (m)	T_p (s)	u_c (m/s)
13	9.5	South	0-35	3.6	8.9	1.7	4.8	10.3	1.9
22	15	North	0-30	4.0	9.4	1.5	5.3	10.8	1.65
36	25	North	5-30	4.1	9.4	1.85	5.4	10.8	2.1

6 HYDRAULIC MODEL TESTS

6.1 General

The documentation of adequacy of the proposed scour protection was made through physical model tests. It was decided to adopt an untraditional approach for the tests. Instead of the traditional test procedure of testing the stability of the scour protection on an erodible bed for different combinations of wave/current direction relative to the bridge orientation, the tests were divided in two phases, with Phase 2 as the traditional scour tests. Phase 1 included a series of tests with bed shear stress measurements in order to determine the amplification of the bed shear stress around the bridge piers for different angles of wave/current attack. The traditional scour test then only included the most critical wave/current direction.

Phase 2 included primarily model tests to verify the stability of the proposed scour protection at the three pier positions, but also tests to determine the rate of scour development and to elucidate scale effects were made during this phase.

All the tests were carried out in a 5.5 m wide current and wave flume at DHI. Maximum water depth was 0.5 m, the maximum current velocity which could be reproduced was 0.40 m/s with this water level. The flume only allowed for unidirectional waves and currents. Such situations were estimated to create the most critical conditions for the scour protection.

The flume and test setup is shown in Fig 7.

The models of piers Nos 13, 22 and 36 were built to different scales as shown in Table 2.

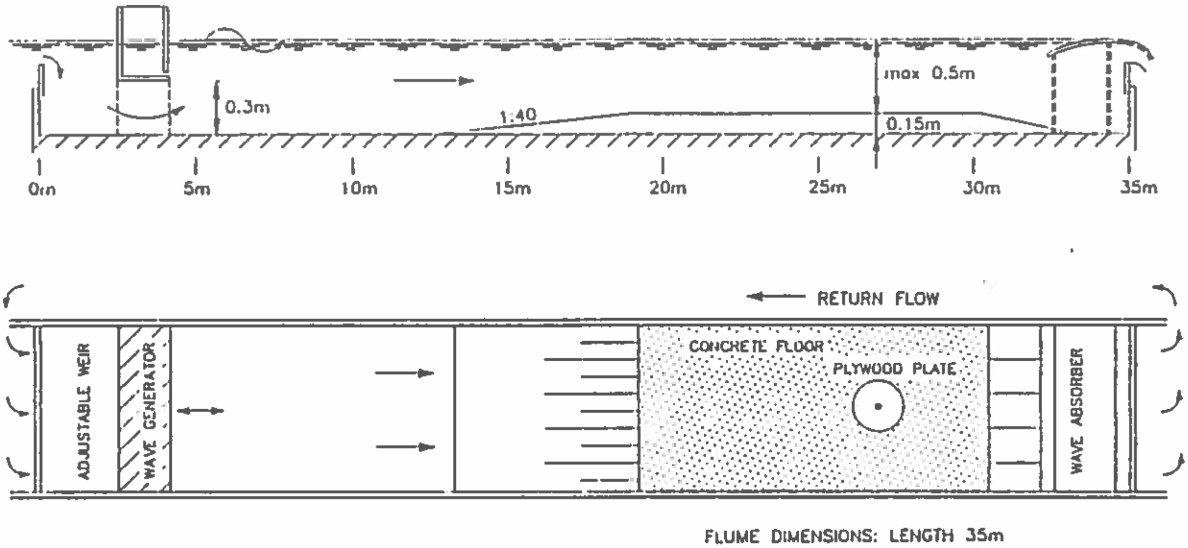

Fig 7 Test setup.

Fig 7 Plan du modèle.

Table 2 Scales of piers in model tests.

Deep water piers		Shallow water pier
Pier No 36 Depth 25 m	Pier No 22 Depth 15 m	Pier No 13 Depth 9.5 m
1:50 -	1:35 1:50	1:30 -

6.2 Model tests, measurements of bed shear stress amplifications

The bed shear stress around the pier structures was measured by means of a hot film anemometer probe. The probe was mounted in a fixed position in the flume floor (in the centre of a smooth plate, see Fig 7). The shear stress around the structure was measured by moving the pier in a grid system around the probe position. The measured bed shear stress was related to the undisturbed bed shear stress measured without the presence of the bridge piers.

The current velocity in the flume was measured by means of ultrasonic current meters and by float trackings, and the waves were measured by resistance type wave gauges.

Tests were made both with current alone, and combined current and waves. Examples of results from the tests are given in Fig 8.

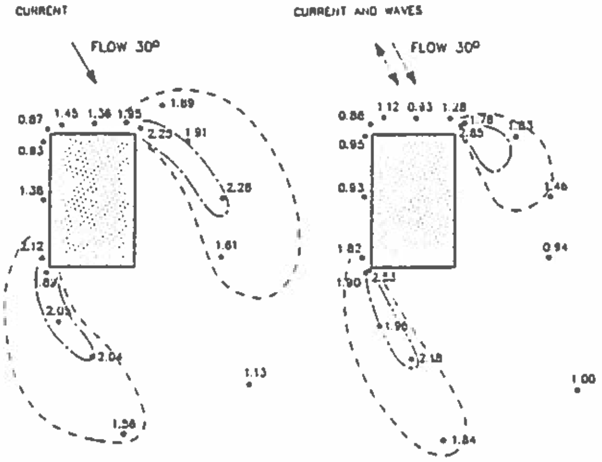

Fig 8 Examples on test results. Bed shear stress amplification pattern around the bridge pier. Comparison for magnitude of current/waves refers to current without and with waves. Probability of occurrence 10^{-2} per year.

Fig 8 Exemples de résultats d'essais. Plan d'amplification des efforts de cisaillement autour d'un pilier de pont. La comparaison entre le courant et les vagues se rapporte au courant sans et avec vagues. Probabilité d'occurrence 10^{-2} par année.

The model tests included:

- three different bridge piers with different model scales were applied for the individual piers
- four test conditions per pier:
  - current alone (probability of occurrence 10^{-2} and 10^{-5} per year)
  - current and waves (probability of occurrence 10^{-2} and 10^{-5} per year)
- two different current (waves) directions respectively 0-5° and 30-35° relative to the pier orientation

An example of the effect of wave/current direction on the bed shear stress amplification is given in Fig 9.

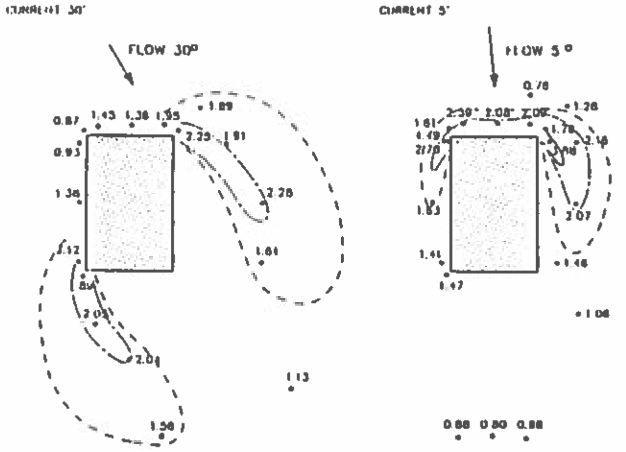

Fig 9 Example on effect of current direction on the bed shear stress amplification pattern. Magnitude of current refers to a probability of occurrence of 10^2 per year.

Fig 9 Exemple de l'effet de la direction du courant sur le plan d'amplification des efforts de cisaillement. Le courant se rapporte à une probabilité d'occurrence de 10^2 par année.

The results obtained in the Phase 1 model tests can be summarised in following points:

- the maximum amplification factor of the bed shear stress in a position about 1 m from the bridge pier was generally 4-6 both in pure current and in combined current and waves
- the amplification pattern in the influenced areas was almost independent of current velocity
- the influenced area was largest for oblique current/wave attack (compared to an incident current/wave direction of 0° relative to the pier orientation)
- the area influenced by the structure is smaller in current and waves compared to pure current
- the amplification pattern is almost independent of the water depth

The results were used to estimate the proposed extent and stone size of the scour protection.

The stability of this proposed protection was only tested for the worst wave/current direction found in the bed shear stress amplification tests.

6.3 Model tests, stability of scour protection

In continuation of the bed shear stress amplification tests, a test series was made to document the stability of the proposed scour protection. Tests series with the three selected piers in respectively 9.5, 15 and 25 m of water depth were carried out. The tests were generally carried out in test series each with up to 20 individual tests. The proposed layout of the scour protection is shown in Fig 3.

Following tests were performed:

Table 3 Characteristics of cover layer in the test series performed (full scale values).

Pier No	Water depth	Stone size cover layer	Mean Weight M_{50} (kg)	No of test series performed	Duration of test series (h)
13	9.5 m 9.5 m	35-150 kg 85-270 kg	100 170	1 2	2¼ ¼-1½
22	15 m 15 m 15 m	20-100 kg 80-240 kg 35-115 kg	55 150 72	2 1 2	6-7 2¾ 16¼
36	25 m 25 m	10-35 kg 30-100 kg	20 62	1 1	2¼ 3¼

The scour depths were registered during the tests in a predetermined grid around the bridge pier both on and outside the scour protection. After each test series, the flume was drained and a detailed levelling of the seabed performed.

Examples of the test results from the test series with pier No 22 are shown in Fig 10.

The areas where the scour protection is most exposed are at the two outer corners of the piers where also the largest shear stress amplifications were measured. From the results shown in Fig 10, it is seen that the scour holes here are maximum ~1.5 m. This means, as the thickness of the main scour protection is about 1 m, that the entire armour layer was removed due to wave and current action. This result was seen both for stone classes 20-100 kg and 35-115 kg.

Apart from the erosion close to the pier corners, also erosion at the edges of the scour protection at the down-stream sides of pier took place. The erosion here initiates at the seabed outside the scour protection. Maximum scour depths during the tests reached here about 3 m. The development of these scour holes will continue, but with reduced rate. Estimates on the scour development rate were made on basis of the measured development of scour depth and evaluated time scales for the scour development. The derived expression for the time scale λ_T is:

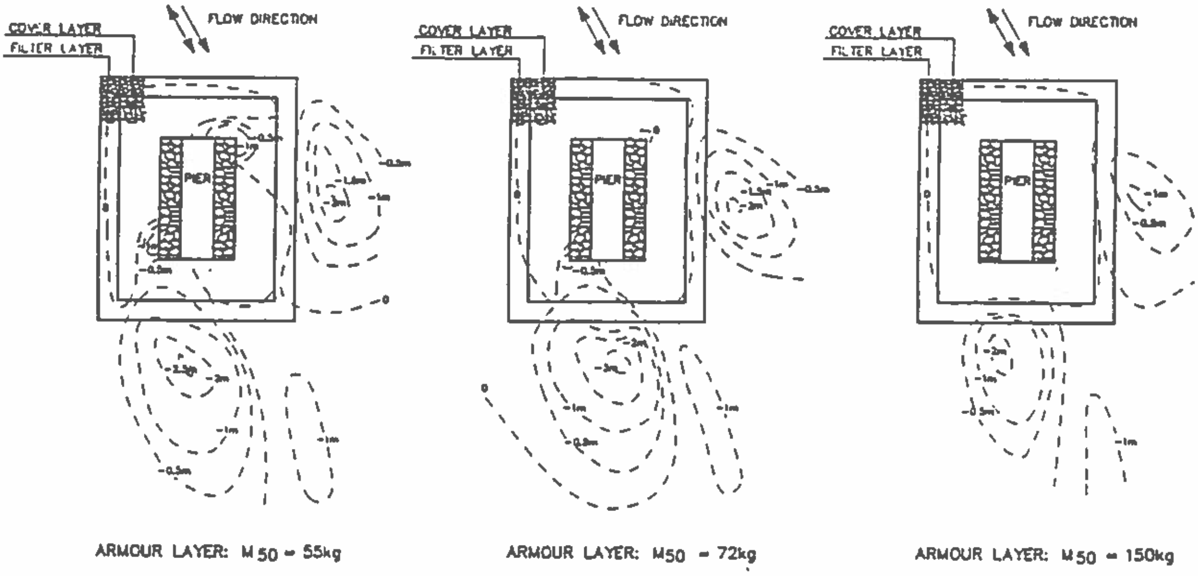

Fig 10 Scour pattern after test series with pier No 22.
Fig 10 Erosion après la série d'essais avec le pilier no 22.

$$\lambda_T = \lambda_L^2 \frac{\Delta \phi_{SM}}{\Delta \phi_{SP}} \left(\frac{d_M}{d_P}\right)^{3/2}$$

λ_L: model length scale
$\Delta\phi$ = $\Delta\phi(\Theta)$, dimensionless transport parameter
Θ: Shield's parameter
d: grain diameter
M: model
P: prototype
$d_{50,M}$: 0.2 mm

Utilising this expression for the time scale in combination with the wave and current statistics, the relation shown in Fig 11 between the time scale and the probability of occurrence was derived.

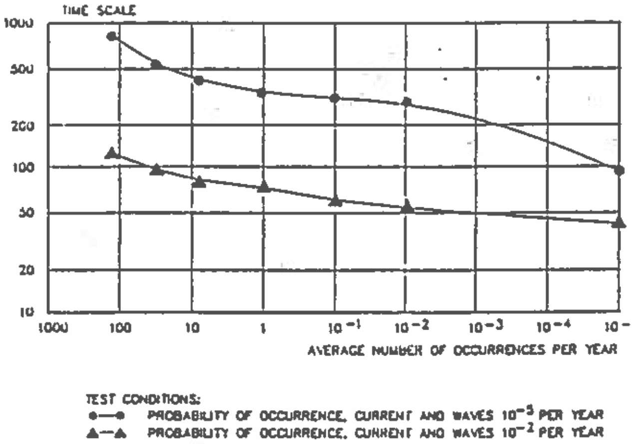

Fig 11 Time scale for scour development versus probability of occurrence (Pier No 22).
Fig 11 Echelle du temps du développement de l'érosion en fonction de la probabilité d'occurrence (pilier no 22).

Explanation:
A model test was carried out with a wave/current condition with a probability of occurrence 10^5 per year. The time scale for a wave/current situation with a probability of occurrence 1 per year is then 350 ($d_{50,P}$ = 0.2 mm).

Based on the model test results and the time scale, the development of the scour holes outside the scour protection was estimated. In Fig 12, the results in terms of scour development at pier No 22 are presented in relation to time at the two most exposed positions.

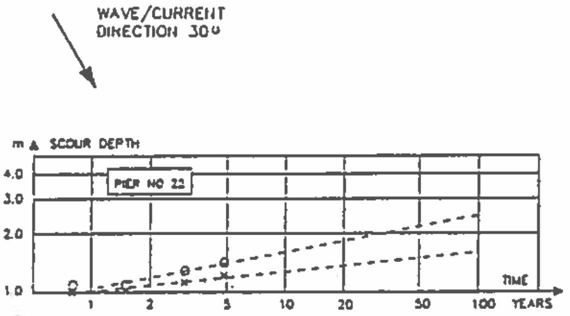

Fig 12 Development of scour depth outside the scour protection, 20-25 m from the pier at the two most exposed positions (Pier No 22), current/wave direction 30-35° relative to pier.
Fig 12 Développement de la profondeur d'érosion hors de la protection, à 20-25 m du pilier sur les deux positions les plus exposées (pilier no 22), direction du courant/de vague 30-35° par rapport au pilier.

The estimation of scour depths is based on the assumption that only one wave and current direction is acting on the structure. This is of course not the case in reality where wave and current directions vary. This means that the area where scour will occur outside the protection will vary with the wave and current direction and the depths of the scour holes will accordingly be smaller because different wave and current directions will result in different positions of scour holes and may even to a certain degree backfill the holes created for other wave directions.

As described earlier, stability tests with the protection of the three bridge piers were made with different sizes of the armour stones in order to determine the necessary armouring of the scour protection for these piers. Utilising then these test results in combination with the results of the mathematically computed bed shear stress, the necessary stone sizes of the scour protection for the different piers can be estimated.

The stone sizes recommended at the individual pier are shown in Fig 13 together with the stone sizes estimated from the theoretical assessment. The large stone sizes recommended for piers Nos 45 and 46 are due to a general sloping seabed (−1:5) at these positions.

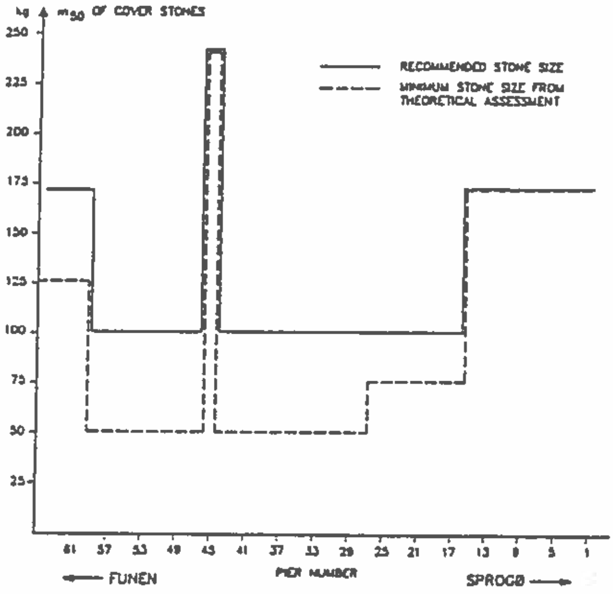

Fig 13 Recommended stone sizes of the main scour protection for piers Nos 1-64. The large stone sizes recommended for piers Nos 45 and 46 are caused by sloping seabed at these positions.

Fig 13 Enrochements recommandés pour la protection principale contre l'érosion pour les piliers nos 1-64. L'importance des enrochements recommandée pour les piliers nos 45 et 46 est due à la pente du fond à ces positions.

The general layout of the scour protection as recommended is shown in Fig 14.

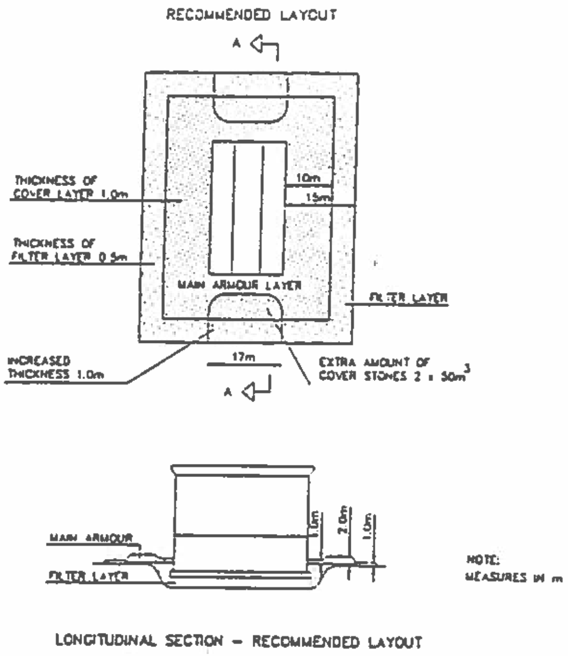

Fig 14 Recommended layout of scour protection.

Fig 14 Plan-masse recommandé pour la protection contre l'érosion.

It was thus recommended to place an extra amount of cover stones along the short sides of the piers, as the tests showed the deepest scour holes in the sand bed at these positions.

The displacement of armour stones is a result of 'secondary' damage, ie a result of the scour action in the seabed outside the protection. The erosion rate on the pier side of the scour holes will gradually be reduced, as the cover stones displaced from the armour layer will delay the erosion.

At locations where the upper layer of the seabed consists of soft material (eg gytje, silt), the filter layer was increased to an overall thickness of 1.0 m.

The maximum amount of stone protection to be displaced has been estimated on basis of the test results and the scour development outside the protection. Following estimates were made:

Table 4 Estimated amount of scour protection displaced at the three pier locations.

Pier No	Displaced amount of stone protection			
	After (years)	m^3	After (years)	m^3
13	12	125	100	190
22	5	65	100	120
36	2	65	100	100

7 CONCLUDING REMARKS

The recommendation for the scour protection for the Western Bridge piers has been based on a combination of results from traditional scour model tests and more untraditional tests with determination of the bed shear stress amplification around the bridge piers. This combination has obvious advantages as the bed shear stress measurements in a comparably simple way give a reliable picture of the most exposed areas, the most critical wave/current direction relative to the structure and the general amplification pattern for the most critical situations. In this way, it is only necessary to test very few combinations (often only one combination) in the traditional way, and accordingly it is estimated that this concept for physical scour investigation is optimal with respect to time consumption and design of scour protection. It is therefore believed that this investigation concept will be commonly used in the future.

REFERENCES

/1/ Vincentsen, L.J. and S. Spangenberg (1990): *Safety management system for the Great Belt Link.* Proc. 2nd symposium on Strait Crossing, Trondheim, Norway.

/2/ Fredsøe, J. (1984): *The turbulent layer in combined wave-current motion.* Journal of Hydraulic Engineering, ASCE, Vol 110, No Hy 8, pp 1103-1120.

/3/ Sumer, B.M., Fredsøe, J., Christiansen, N.: *Scour around vertical pile in waves.* Journal of Waterway, Port, Coastal and Ocean Engineering, ASCE, Vol 118, No 1, January/February 1992.

/4/ Christensen, F.T. et al (1991): *Accidental limit state ice loads on bridge piers.* PIANC Buletin 1991 - No 72.

/5/ Kristensen, P.S. et al (1992): *Great Belt - Foundation of the West Bridge.* NGM-92, 11. Nordiske Geoteknikermøde, Aalborg, Denmark, 1992.

/6/ Mose Poulsen, K., J. Dietrich (1991): *Environmental management for the Great Belt.* IABSE Colloquium, Nyborg, Denmark, 1991.

/7/ Steen Møller, J., H. Smith Nielsen (1991): *The Great Belt Link: Zero environmental impact on the Baltic Sea.* IABSE Colloquium, Nyborg, Denmark, 1991.

Improved methods for determination of design waves and a bit on the 1872 storm

Morten Rugbjerg (DHI)

Improved methods for determination of design waves and a bit on the 1872 storm

by

Morten RUGBJERG, Danish Hydraulic Institute

1 Introduction

The present paper is an extract of a note, which describes the results of an investigation of the wave height variation along the West Bridge alignment for waves from north-northeast to east-northeast occurring with a probability of 0.0001% (approximately corresponding to 1 h/100 years).

2 General Model Description

The wave heights have been computed using DHI's mathematical wind wave model, MIKE 20 OSW. This model calculates the energy spectra (and thus all spectrally derived wave parameters) on a computational grid for a given wind field, which may be constant or may vary in time and in space. Refraction, shoaling and wave breaking are included.

MIKE 20 OSW in its present form taking the water depth into consideration was developed in 1983 and has since then been applied without any modifications in wind-wave studies in many parts of the world. However, the present study varies in one respect from previous studies as the grid spacing used in the present model is much smaller than in previous models. Therefore a validation of the model has been carried out prior to the wave simulations in Storebælt.

3 Model Setup

The model areas are shown in Figures 1 and 2. A coarse grid with a grid spacing of 1500 m covers the northern part of Storebælt, while a 500 m grid covers the central part. This two-grid approach was chosen in order to save computational time, while the results are still available on a 500 m grid in the area of importance. The water depths are relative to DNN +1.70 m, which corresponds to a high water level with a recurrence interval of 100 years.

A directional discretisation of 11.25° was applied, while the wave frequencies covered were: 0,10, 0.12, 0.14, 0.16, ..., 0.40 hertz (ie wave periods from 2.5 s to 10.0 s).

4 Wind Description

Estimation of the wind speed with a return period of 100 years has been based on Ref /1/, which comprises extreme wind statistics for Sprogø based on a nine-year record (1977-86) of ten minutes average wind speeds. The wind speed and wind direction have been measured from a 70 m meteorological mast as ten minutes consecutive recordings by an anemometer placed at $z = 70$ m relative to DNN.

In Ref /1/, an extreme ten minutes mean wind analysis has been carried out applying an exponential distribution. For northeast a wind speed of 28.3 m/s (with a standard deviation of 2.13 m/s) occurring once each 100 years is found. As the wave heights to be computed are the fetch limited wave heights and not the wave heights limited by the period of time, the wind is blowing, the wind speed to be used should be sustained long enough for the fetch limited sea state to be reached. It takes approximately five hours for the 1 h/100 years wave height to develop, but anyhow a wind speed which occurs 1 h/100 years will be used in the wave calculations. Selecting a wind speed occurring 5 h/100 years would have been on the very low side, as it can be assumed that the sea state is already rough when the period of high wind speeds occurs.

According to Ref /2/ the ratio between the ten minutes average and the 60 minutes average wind speed is 1.048. Furthermore, the wind speeds measured at $z = 70$ m is transformed to a level of $z = 10$ m by applying a factor of 0.80 (Ref /1/).

All in all this yields a one hour average wind speed at $z = 10$ m for the 100 years event of

$$U = ([28.3 \text{ m/s} + 2.13 \text{ m/s}] / 1.048) \cdot 0.80 = 23.2 \text{ m/s}$$

It is noted that one standard deviation is added to the wind speed at $z = 70$ m.

As the various parameters and the numerical wave hindcast model calculations are associated with scatter, it is recommended to add 15% to all wave heights as a safety factor. This corresponds to multiplying the wind speed by approximately 1.15 (using Ref /2/ with a depth of 15 m and a fetch of 35 km). It is more convenient to include this safety factor in the wind speed as the results of the wave hindcast would be directly applicable. All numerical hindcast calculations of the $p = 0.0001\%$ waves from northeast have correspondingly been performed using a wind speed of 27 m/s.

It is important to notice that in the most severe storm known from northeast, the storm of 12-14 November 1872, a wind speed of 85 Danish feet per second is reported for Sprogø from direction east-northeast. This corresponds to 26.7 m/s (see Ref /4/).

5 Simulation of Wave Heights

The purpose of the study is to compute the wave heights for winds from northeast. However, in order to test the directional sensitivity of the results, winds from four additional directions were applied to the wave model, thus yielding the following wave simulations:

- wind from north-northeast
- wind from northeast - 11.25°
- wind from northeast
- wind from northeast + 11.25°
- wind from east-northeast

It is assumed that no waves penetrate into the area of interest from Kattegat for the given wind directions.

The resulting wave parameters (H_{mo}, T_{02} and mean wave direction) along the alignment of the West Bridge for a wind from north-northeast are shown in Figure 3. Furthermore, the total wave field in the western part of Storebælt for the same wind direction is shown in Figure 4. The relationship between H_{mo} and H_s is: $H_s = 0.95 \cdot H_{mo}$.

In Table 1, a comparison between the computed wave heights and wave heights obtained from extrapolation of measurements in various ways are made and a satisfactory agreement is found. The computed wave heights are, however, on the average slightly lower than the extrapolated wave heights, but no corrections are made to the computed wave heights, as the combination of a 100 years wind speed based on nine years of measurements combined with a well tested wave model is considered more accurate than the extrapolation of one year of wave measurements. Furthermore, a safety margin of 15% has already been added to all wave heights.

6 Wave Directions

Wave direction intervals for waves above a given level are listed in Table 2 for four different confidence intervals. The calculation of these intervals is based on the following assumptions:

- the governing process of the sea is Gaussian and linear
- the directional distribution is symmetrical around the mean direction
- the directional spread within $0.8 < f/T_p < 1.2$ is dominant with respect to the direction of the larger waves
- the wave energy spectrum in Storebælt is in its non-dimensional form compatible with North Sea and Baltic Sea spectra.

From Table 2, it is thus seen that there is a probability of 95% that the direction of waves with a height equal to or larger than $0.95 \cdot H_{max} = 1.73 \cdot H_{mo}$ lies within ±14° of the mean wave direction. It is recommended that the above spreading on the mean wave direction is applied directly in the calculation of the design wave forces on the bridge piers.

7 Recommendations

It is recommended that the results presented in Figure 3 together with the results for the other directions, giving the details of design waves with return period of 100 years as function of direction and position, are used directly as design basis for the bridge.

8 References

/1/ Risø National Laboratory, *Extreme Values of Wind Speeds in Denmark*, December 1989.

/2/ U.S. Army Coastal Engineering Research Center, *Shore Protection Manual*, Vol 1, 1984.

/3/ Danish Hydraulic Institute/LIC Engineering, *Hydrographic Conditions in Storebælt*, 0.4 Final Design Criteria, Issue 1, 09.05.1988.

/4/ Colding, A., *Stormen over Nord- og Mellem-Europa af 12te - 14de November 1872*, Vidensk. Selsk. Skr., 6. Række, Naturvidenskabelig og matematisk Afd. I. 4., Kjøbenhavn, 1881.

/5/ U.S. Army Coastal Engineering Research Center, *Shore Protection Manual*, Vol 1, 1973.

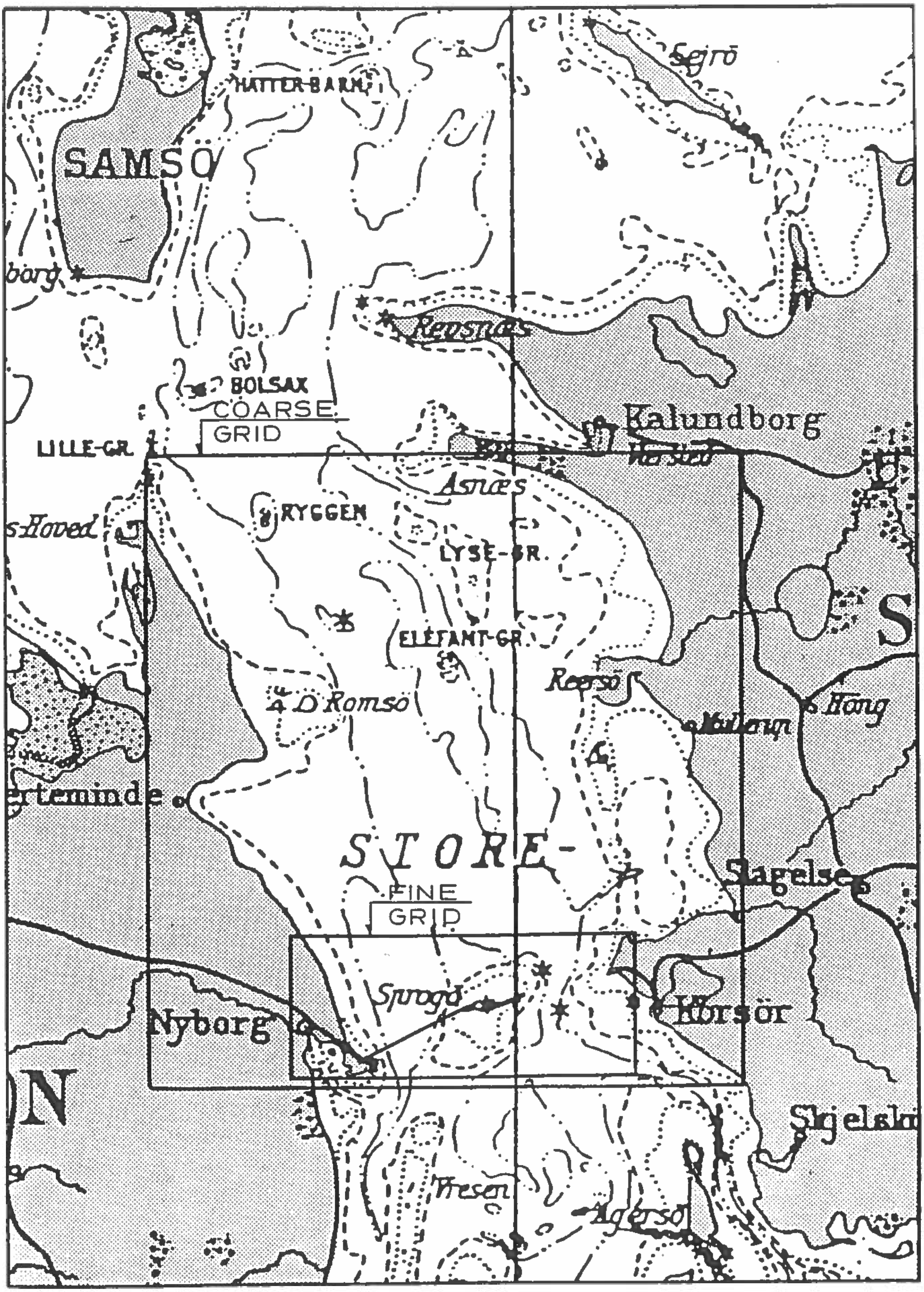

Figure 1 Coarse and fine grid model areas for wind-wave model

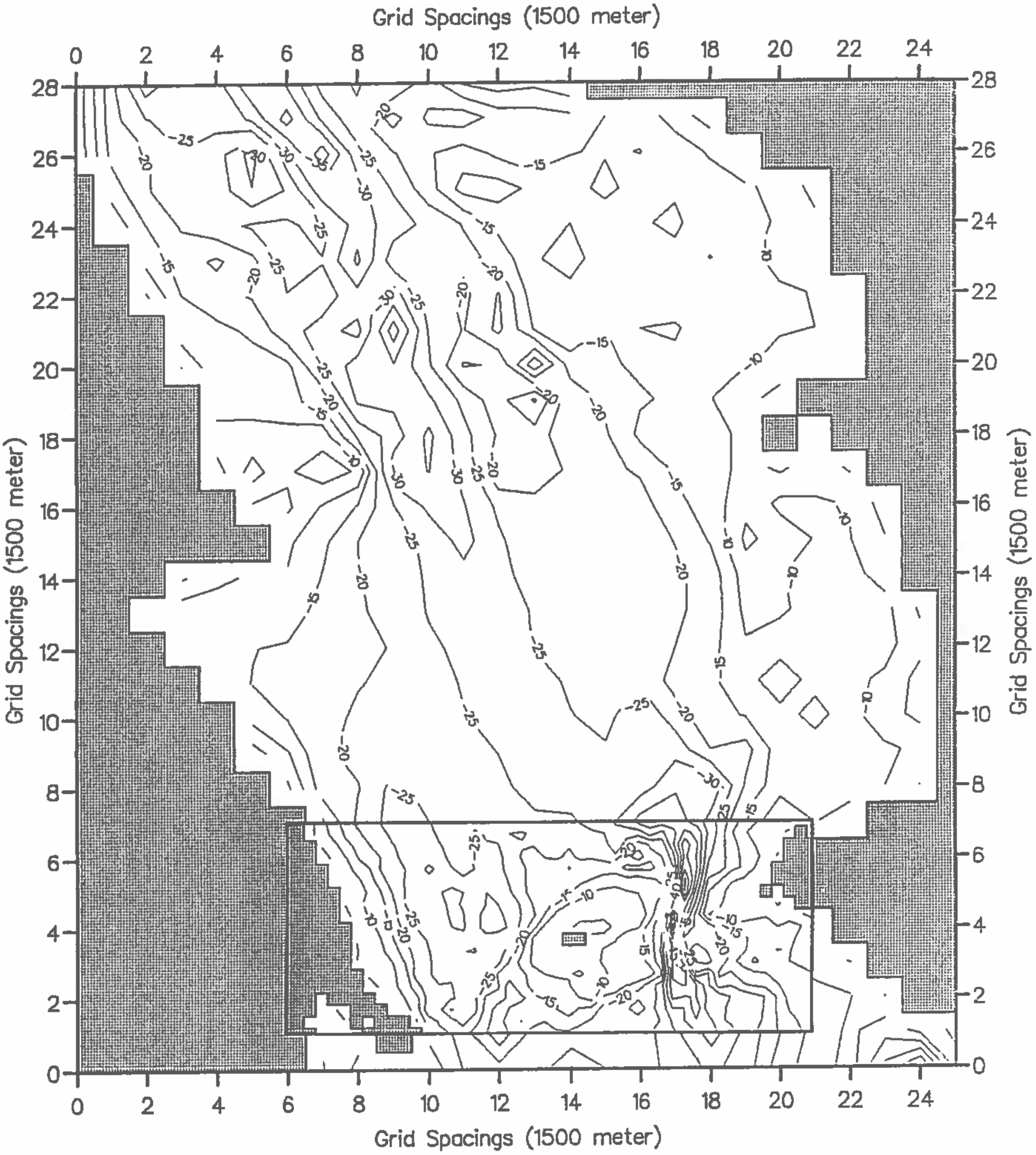

Figure 2 Model areas for wind-wave model showing actual resolution

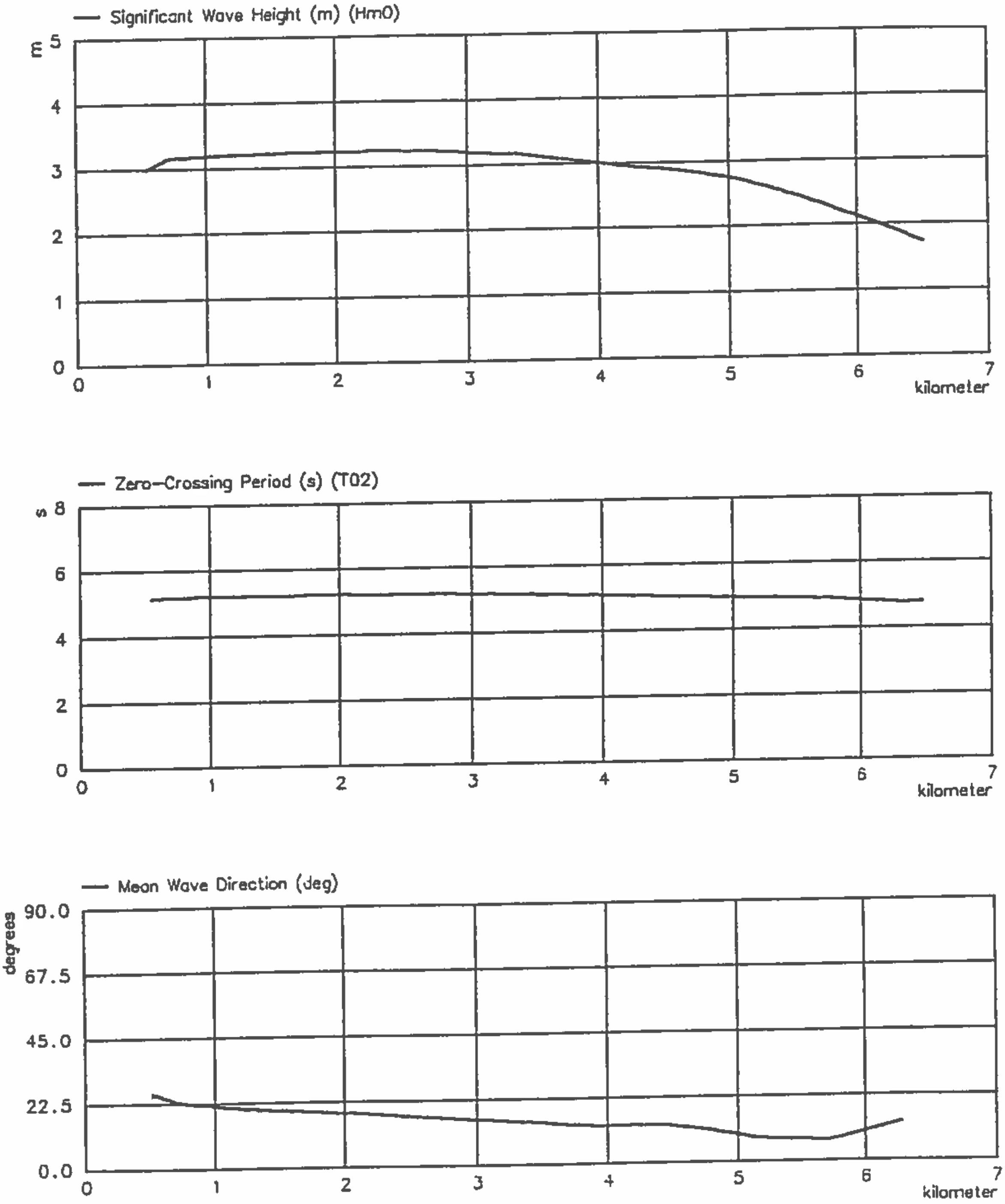

Figure 3 One hour sea state parameters along West Bridge for wind from north-northeast (direction 22.50°)
x-axis: 0 km corresponds to Knudshoved (Chainage 28 km) and 7 km corresponds to Sprogø (Chainage 21 km)

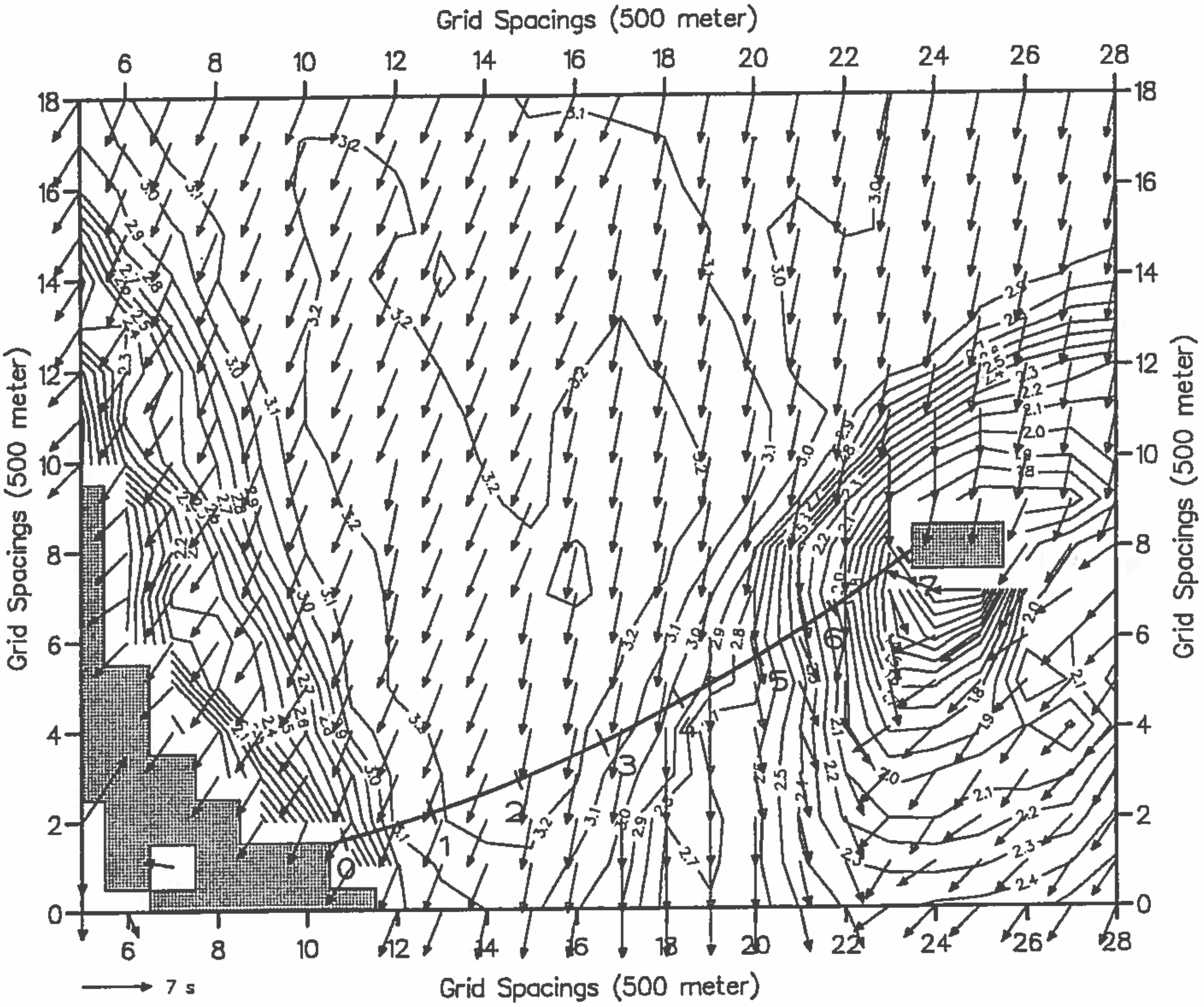

Figure 4 Wave field in western part of Storebælt for wind from north-northeast.

Contours: Significant wave height, H_{mo} (m).

Arrows: Zero-crossing period, T_{02} (s) and peak wave direction

Table 1 *Comparison of computed one hour sea state wave heights and design one hour sea state from Ref /3/*
Depth at all positions: 10 m
*) *Wave height computed using fetch diagrams in Ref /5/*

Position	Design H_s for NE (m)	Method of calculation	H_{mo} from wave model				
			NNE (m)	NE- 11.25° (m)	NE (m)	NE+ 11.25° (m)	ENE (m)
Off Funen	2.7	SMB*)	2.4	2.4	2.3	2.3	2.2
W of Sprogø	2.2	Corrected measurements	2.4	2.3	2.2	1.9	1.8
SW of Sprogø	2.1	Measurements (one year)	2.4	2.4	2.0	1.8	1.9
NE of Sprogø	2.8	Measurements (one year)	2.4	2.3	2.3	2.1	2.0

Table 2 *Wave direction intervals (in degrees) around the mean wave direction for four probability levels*

H/H_{mo}	Probability level			
	80%	90%	95%	99%
1.65	±9°	±12°	±14°	±19°
1.70	±9°	±12°	±14°	±18°
1.75	±9°	±11°	±14°	±18°
1.80	±8°	±11°	±13°	±17°
1.85	±8°	±11°	±13°	±16°

Dansk Geoteknik a|s

Carl Bro Group

Wave Forces on Bridge Piers

Examples of determination by desk calculations and computer models applied on the West Bridge, Storebælt

Helge Gravesen, Dansk Geoteknik as, Carl Bro Group

LIST OF CONTENTS

1. SUMMARY

The present paper describes various analyses of the wave forces to the piers of the West Bridge of Storebælt. Current forces amounting to only a small percentage of the wave forces were estimated by the methods traditionally used in the offshore industry and simply superimposed on the wave forces. Estimates of wave forces derived by desk calculations are described in addition to the main results of the final detailed analyses carried out by computer analyses. The latter have been calculated through utilization of diffraction theory supplemented by a post processing analysis including effects due to finite wave heights.

The elementary analysis being carried out to estimate forces from breaking waves is finally described.

The desk analyses are mainly based on utilization of professor Lundgren's direct method of estimating inertia forces through added mass determined by acceleration nets (H. Lundgren, 1972, and Jan Larsen, 1984).

They rely to a certain extent also on determination of forces obtained for different vertical structures by means of diffraction theory (Sarpkaya and Isaacson, 1981 and Chakrabarti, 1987).

H. Lundgren's quite impressive analysis giving an independent check of the diffraction analysis through utilization of the Sommerfield's theory is further included as an appendix.

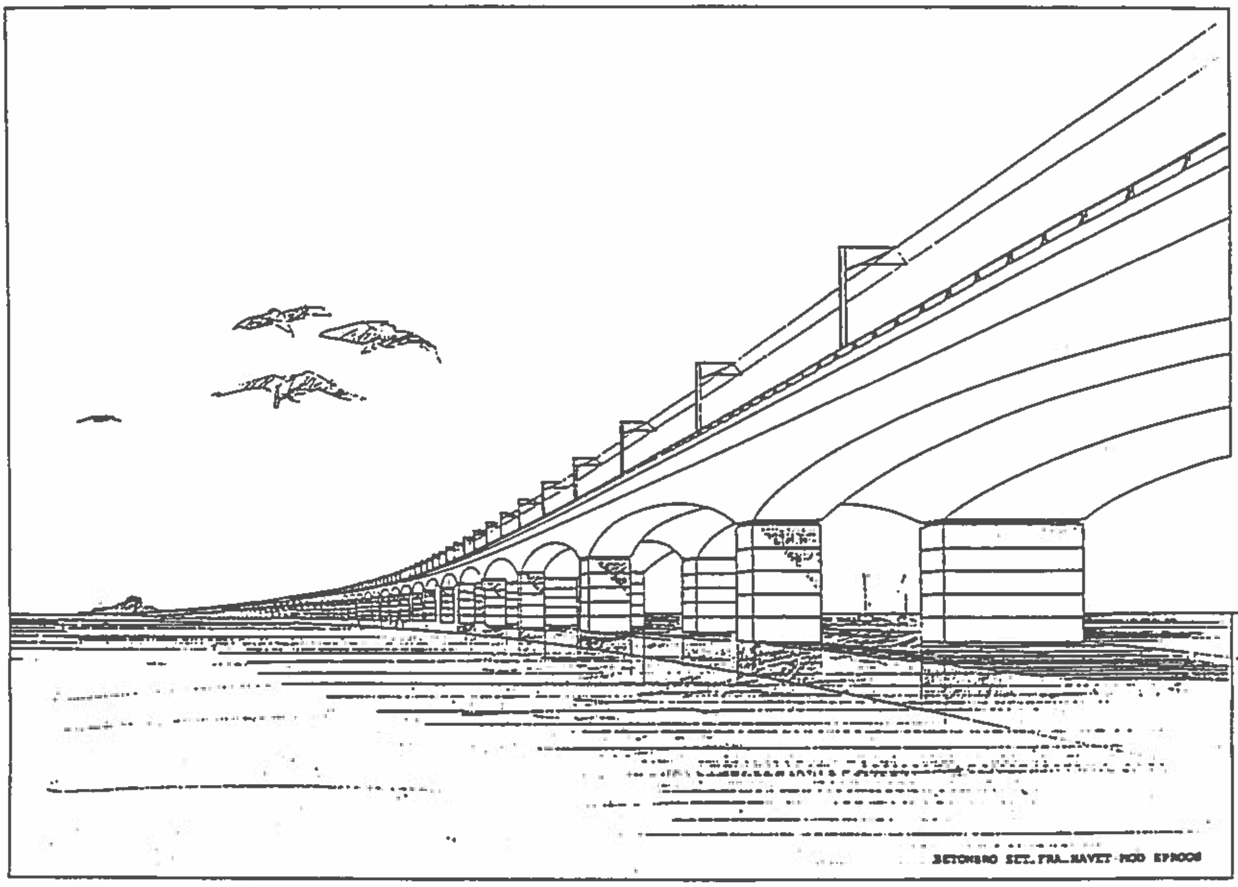

Fig. 1.1 The 6.6-km West Bridge between Funen and Sprogø will be a concrete bridge carrying both railway and road links.

2. BRIDGE PIERS AT WEST BRIDGE, STOREBÆLT

The bridge piers of the West Bridge in Storebælt are large rectangular caissons from foundation level to elevation -3.5 m from which two rectangular pier shafts separated by a gap penetrate the water surface.

The geometry of the bridge piers are illustrated on fig. 2.1 and 2.2.

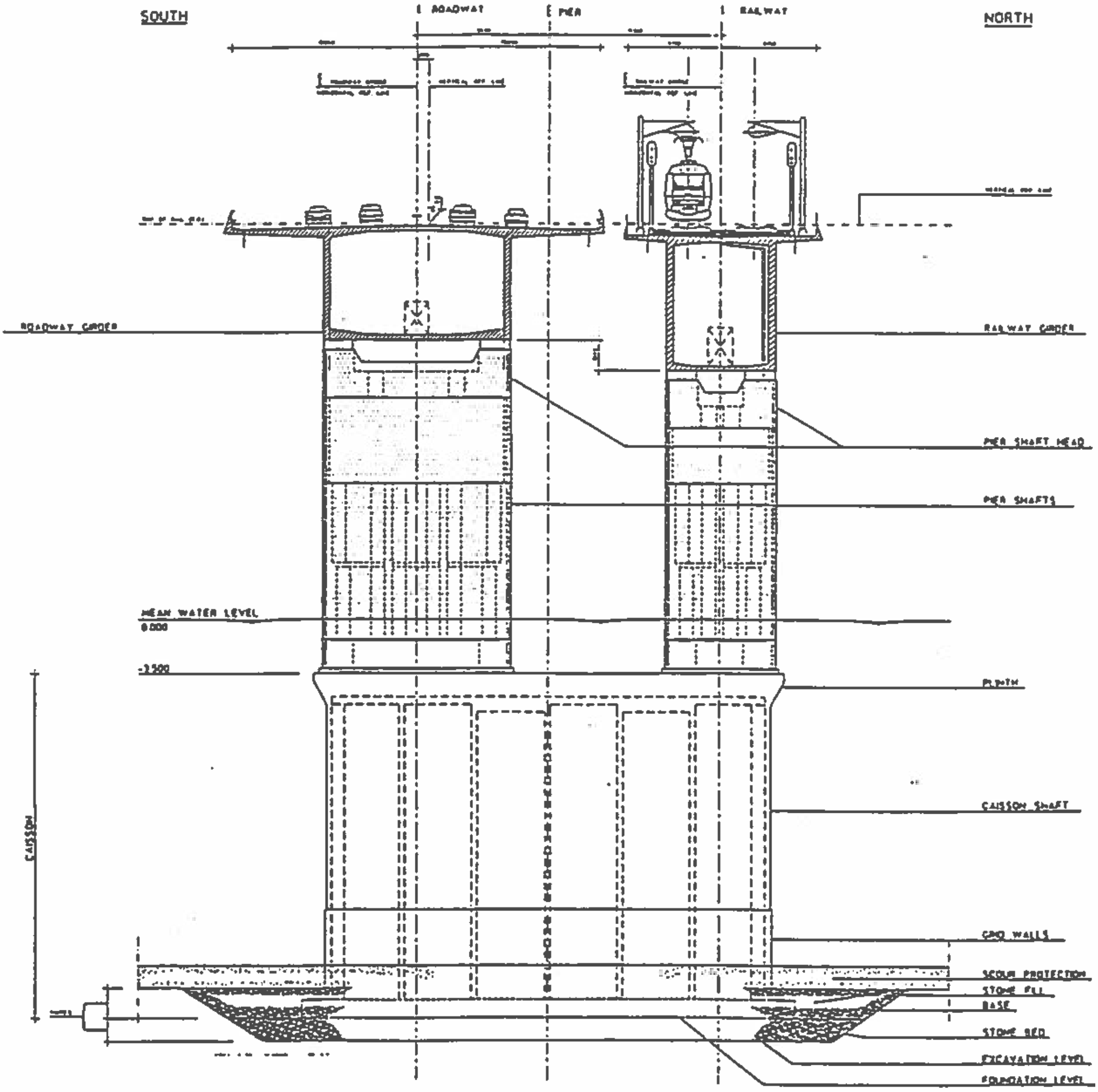

Fig. 2.1 Typical cross section of bridge.

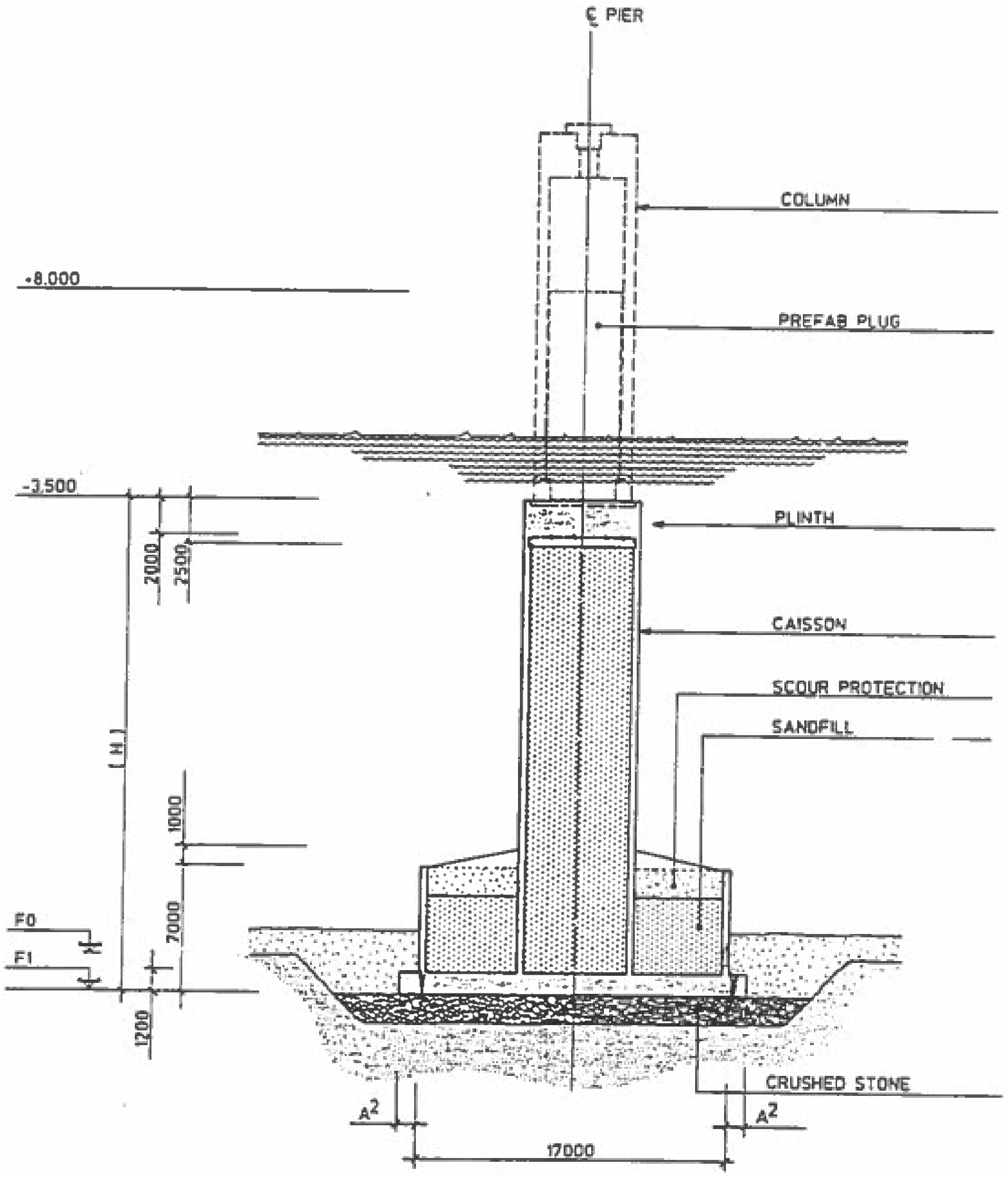

Fig. 2.2 Cross section of deep water caisson.

It is important to understand that the reasons why wave loads are one of the dominant load cases are

- Bridge alignments WSW to ENE
- Large wind fetches in the sector N-NE, (see Rugbjerg, 1991)
- Rare but strong storms may occur in N-NE-E sector (see Rugbjerg, 1991)

- Bridge piers inclusive "added mass" have dimensions close to one half design wave length so almost the maximum pressure gradient in the waves is transferred to forces (see section 3 below)

- Diffraction amplify the simple inertia force being calculated for a small structure not influencing the passing wave (see section 4 below)

- Effect of finite wave height increase the forces, especially the overturning moment with a quite large correction factor (see section 5 below).

3. FORCES ESTIMATED BY ADDED MASS ESTIMATES

The preliminary analysis performed by the contractor for the West Bridge, European Storebælt Group (ESG), utilized a simple added mass estimate. This is described in appendix A. The method used by ESG is a conventional method used in the offshore industry.

Lundgren (1972) proposed to consider inertia forces by means of the wave pressure gradient acting on a structure, increased by the effective added mass (fig. 3.1, 3.2 and 3.3). The added mass is by Lundgren used to increase the effective volume of the structure and thereby over which length the pressure gradient is felt by the structure.

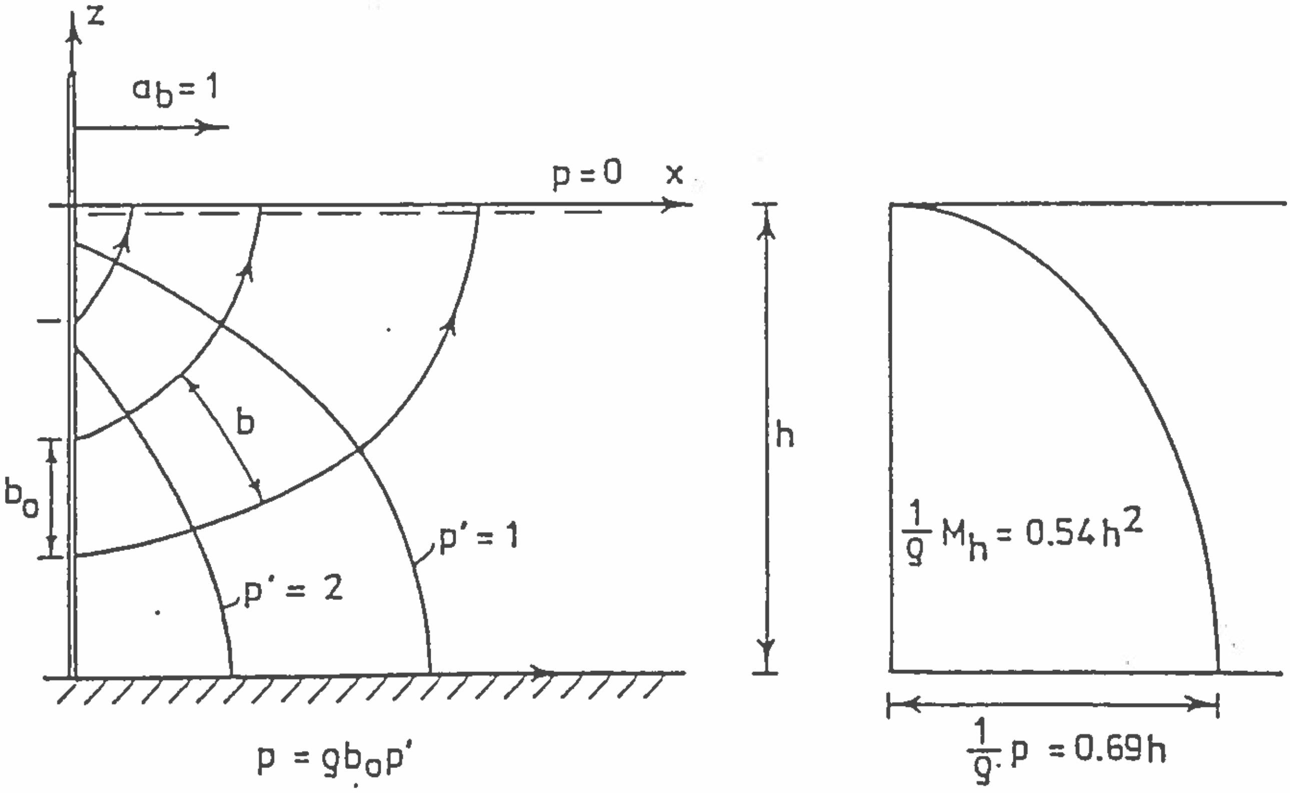

Fig. 3.1 Acceleration net and hydrodynamic mass for a vertical plate and a free water surface (for Lundgren 1972).

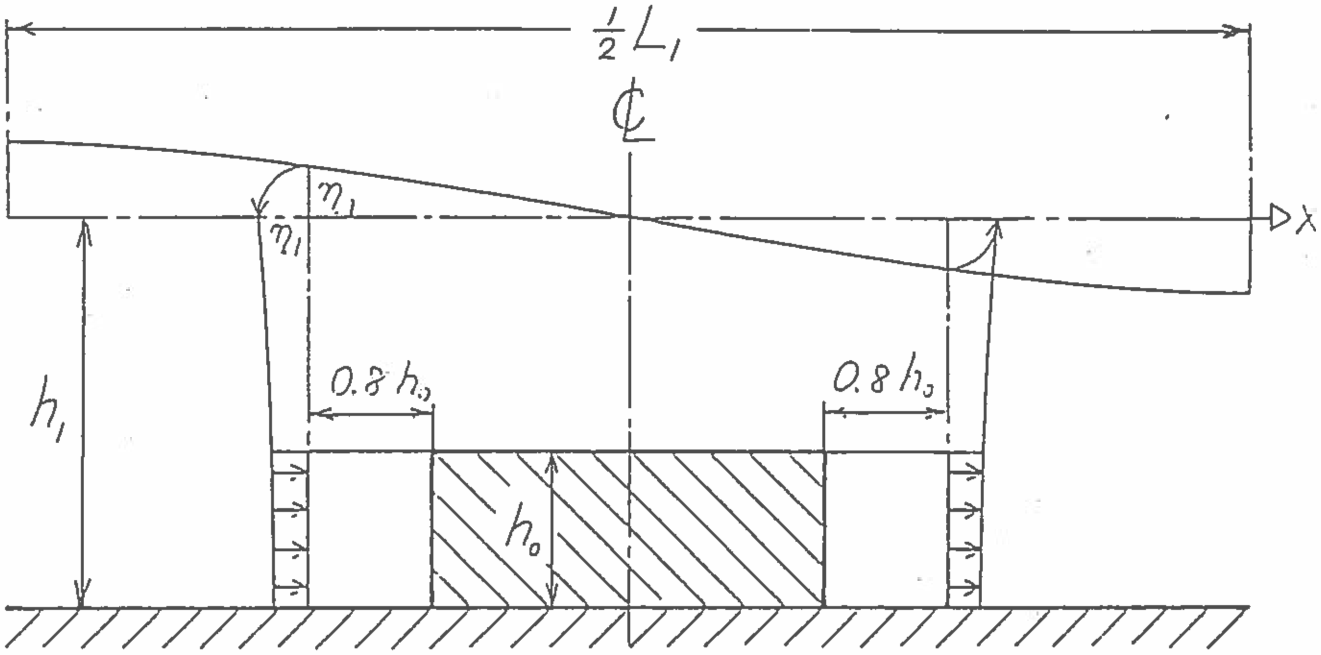

Fig. 3.2 Horizontal force from undisturbed wave motion (from Lundgren, 1972)

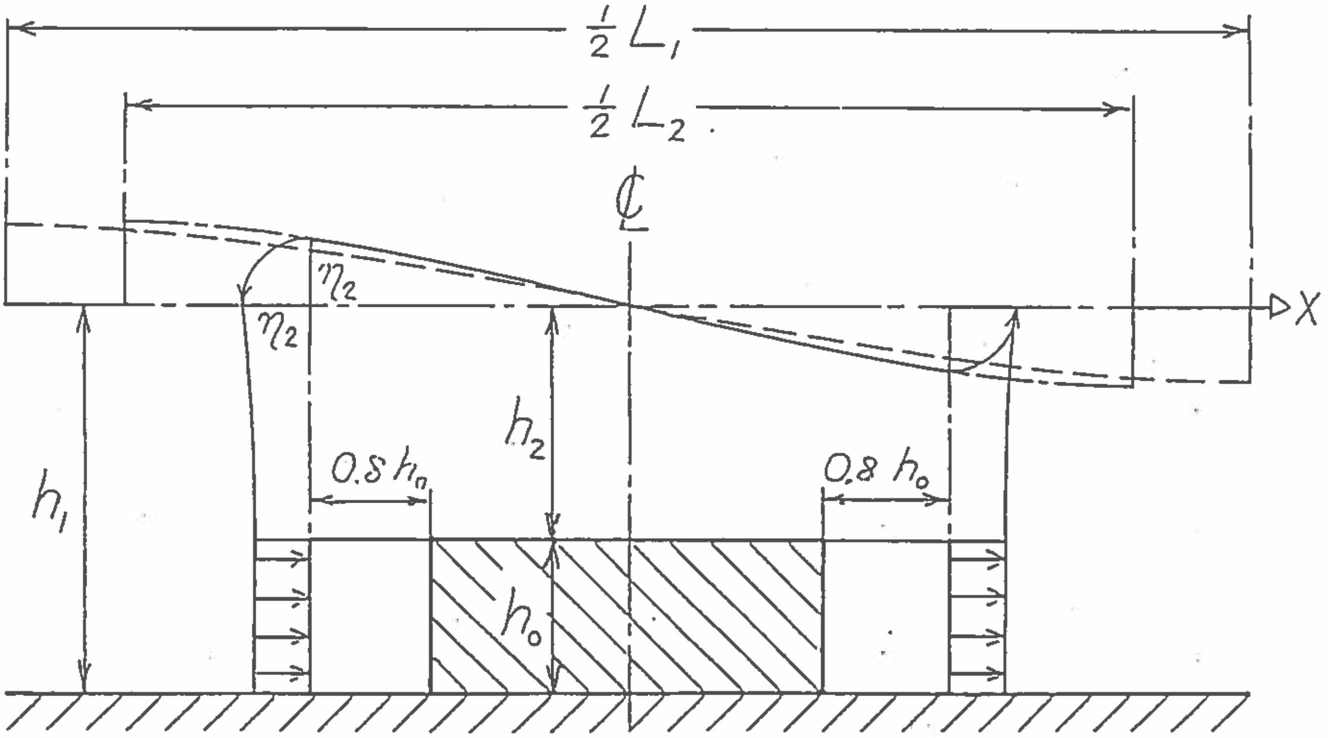

Fig. 3.3 Horizontal force when shoaling effect is considered (from Lundgren, 1972)

This principle was utilized in the consulting engineers (Cowi, Carl Bro and Leonhardt = CCL) check of the contractors preliminary analysis, see fig. 3.4 and 3.5.

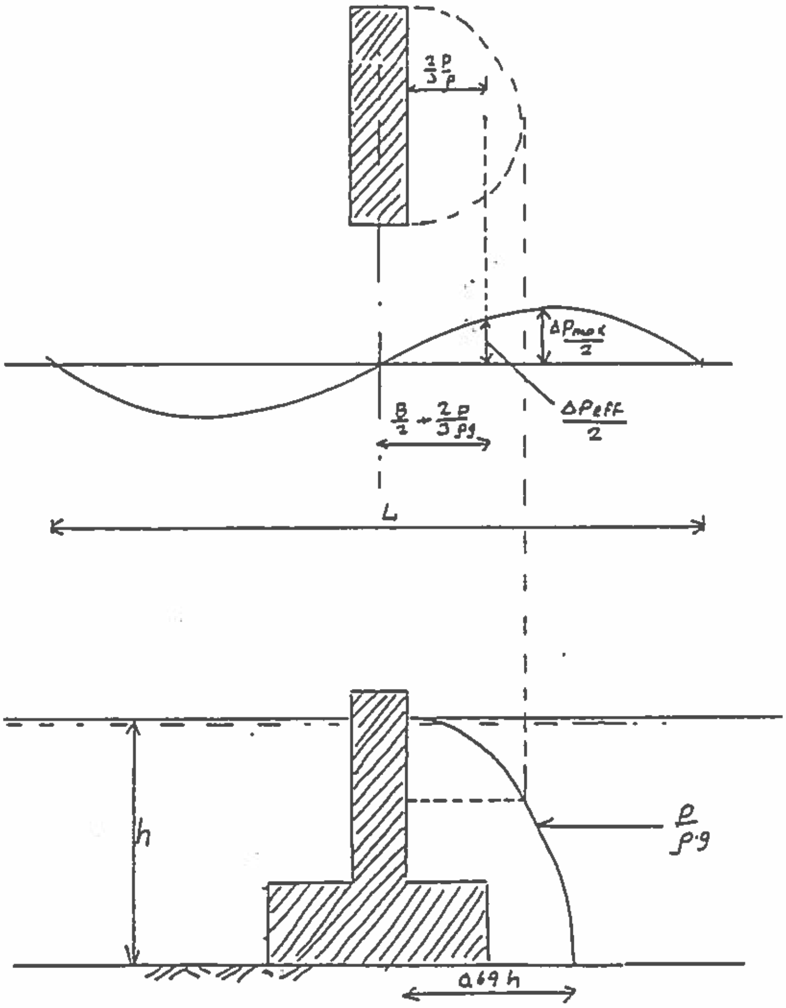

$$\Delta p_{eff} = \Delta p_{max} \sin \frac{\left(\frac{B}{2} + \frac{2p}{3\rho g}\right) 2\pi}{L}$$

$$\Delta p_{max} = \rho \cdot g \, H_{max} \frac{1}{\cosh kh}$$

Fig. 3.4 Desk analysis for estimating wave forces on bridge piers. Assumed no effect of lower cell and no shoaling (wave not disturbed by caisson)

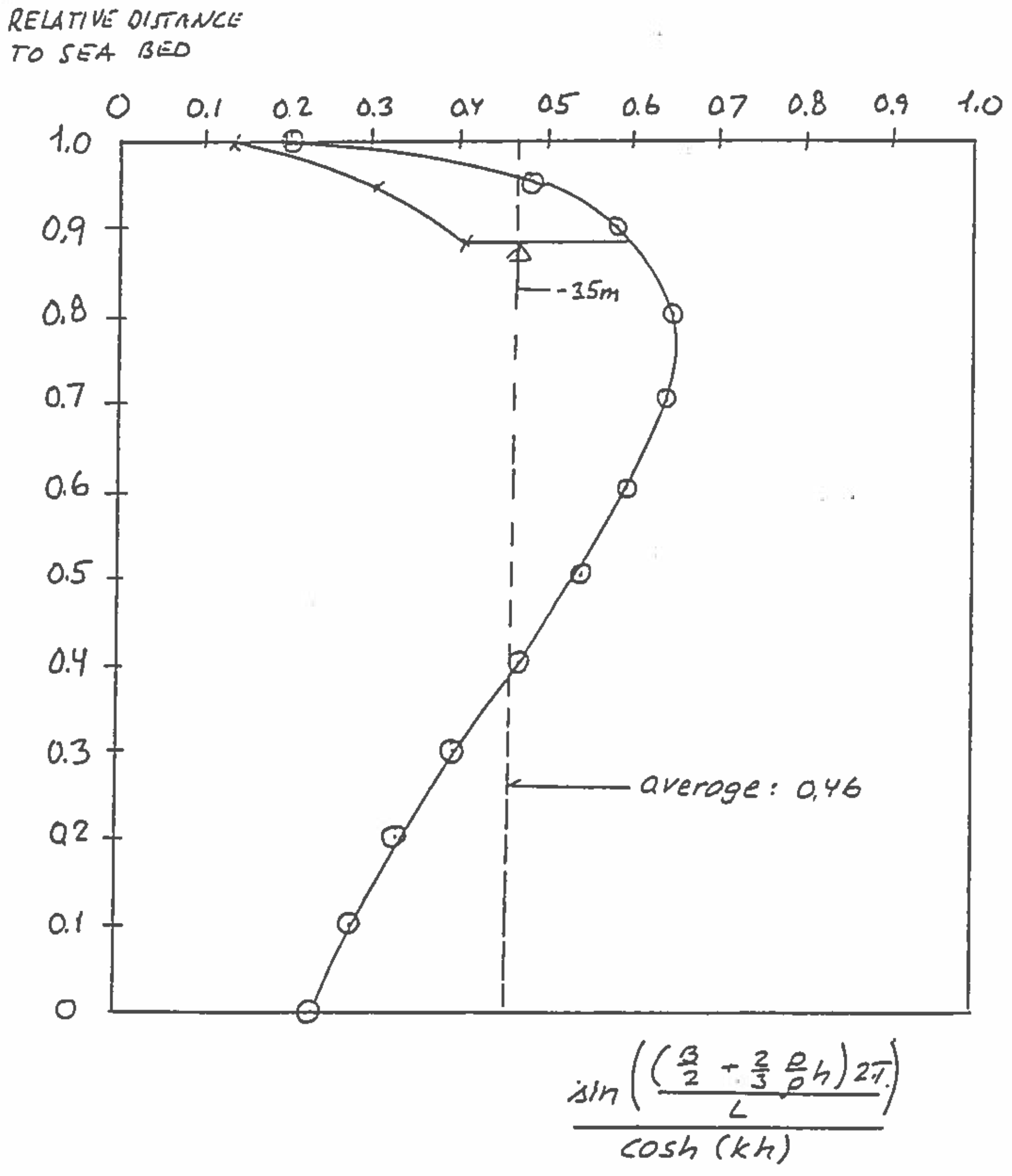

Fig. 3.5 Estimated effective factor on surface pressure gradient.

It was assumed that the pressure gradient reduced by cosh(kh) acts at an average distance of 2/3 p/ρ from the upper section of the caisson. It was estimated that a lower wider section of the pier caisson had no influence on the wave pressure because it was geometrically enclosed in the added mass volume (see fig. 3.1 and 3.4).

Both ESG's and CCL's simple analysis require addition of the effect due to finite wave height and shoaling (increased steepness of wave profile caused by the presence of the structure), see fig. 3.3.

Table 3.1 shows an example of the results of the CCL analysis.

α = 0°

H_{max} = 5.0 m T_p = 7.6 s

h = 28 m   l = 29.3 m   b = 6.4 m

$F = \Delta P_{eff} \cdot A$

$F = 0.46 \cdot 5.0 \cdot 9.81 \cdot 1{,}020 \cdot 28 \cdot 29.3$

F = 18.9 MN

Add estimate of effect due to large volume ≈ +15%

F = 21.7 MN

Table 3.1 Summary of Simple Force Estimate

4. FORCES DETERMINED BY DIFFRACTION THEORIES ON SIMILAR STRUCTURES

In the published literature there exist several published solutions for diffraction forces on cylindrical vertical structures. The solutions most relevant for comparison with the actual bridge piers are those referring to circular or rectangular cylinders.

The overturning moment on a vertical cylinder is shown in fig. 4.1. Fig. 4.2 shows effective inertia and diffraction coefficients for the same case.

Attention id drawn to the increase of the coefficients in the range ka = 0.7 á 0.9 relative to the standard coefficients for ka = 0. This is caused by increased wave steepness due to the presence of the structure.

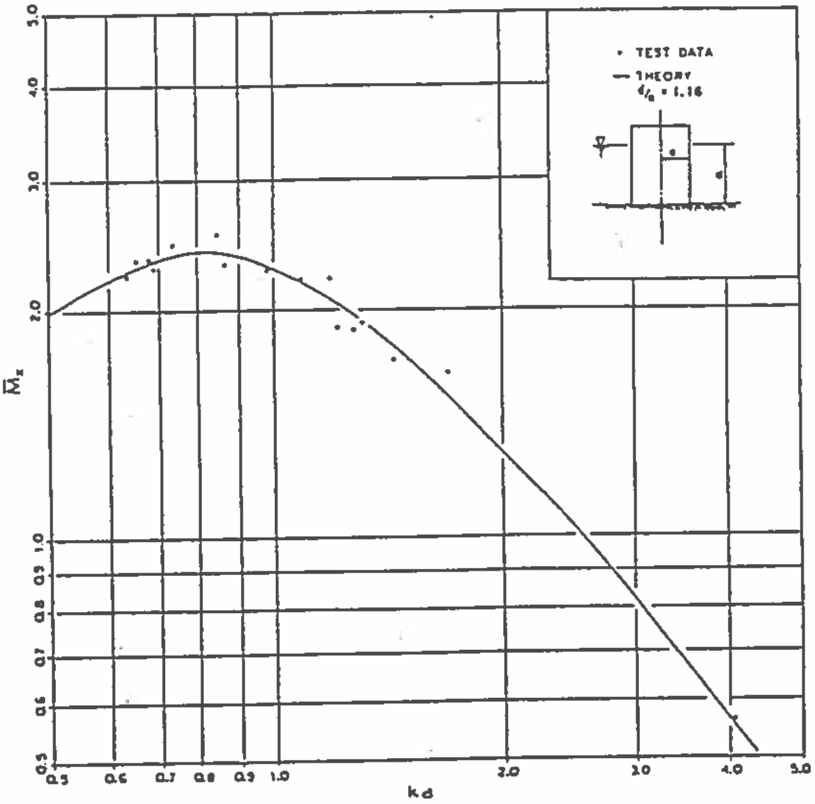

Fig. 4.1 Overturning moment on a vertical cylinder (from Chakrabarti, 1987)

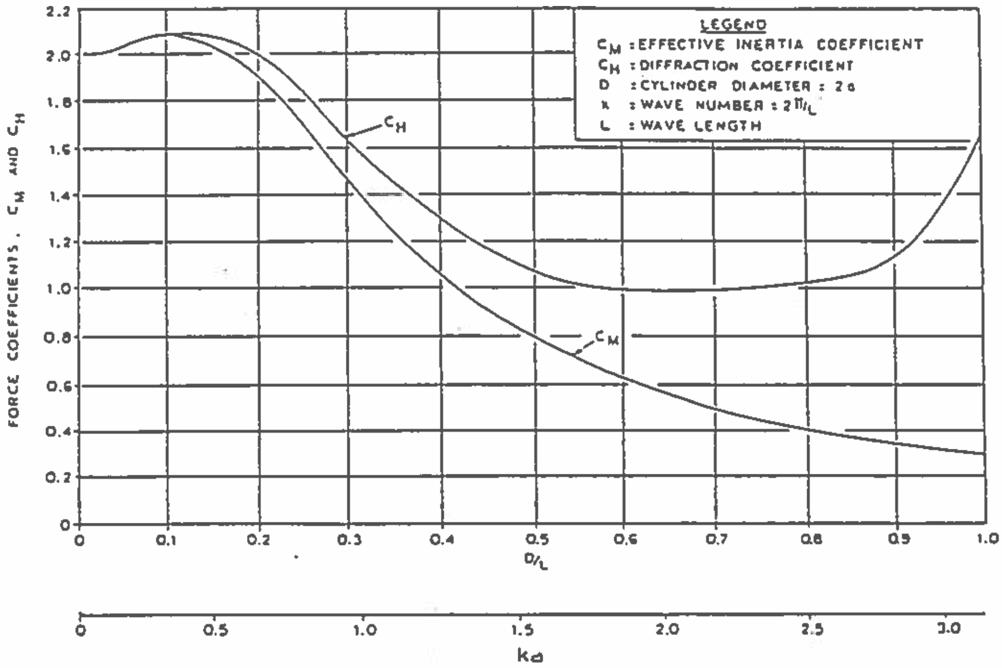

Fig. 4.2 Effective inertia and diffraction coefficients for a vertical cylinder (from Chakrabarti, 1987).

Fig. 4.3 shows similar results for a rectangular cylindrical structure. The maximum values for kb ≈ 0.5 are being plotted on fig. 4.4. Here the effective inertia coefficients C_m have been plotted. The total force is equal to the submerged volume of the structure multiplied by C_m, by the water density and by the acceleration in the undisturbed wave field.

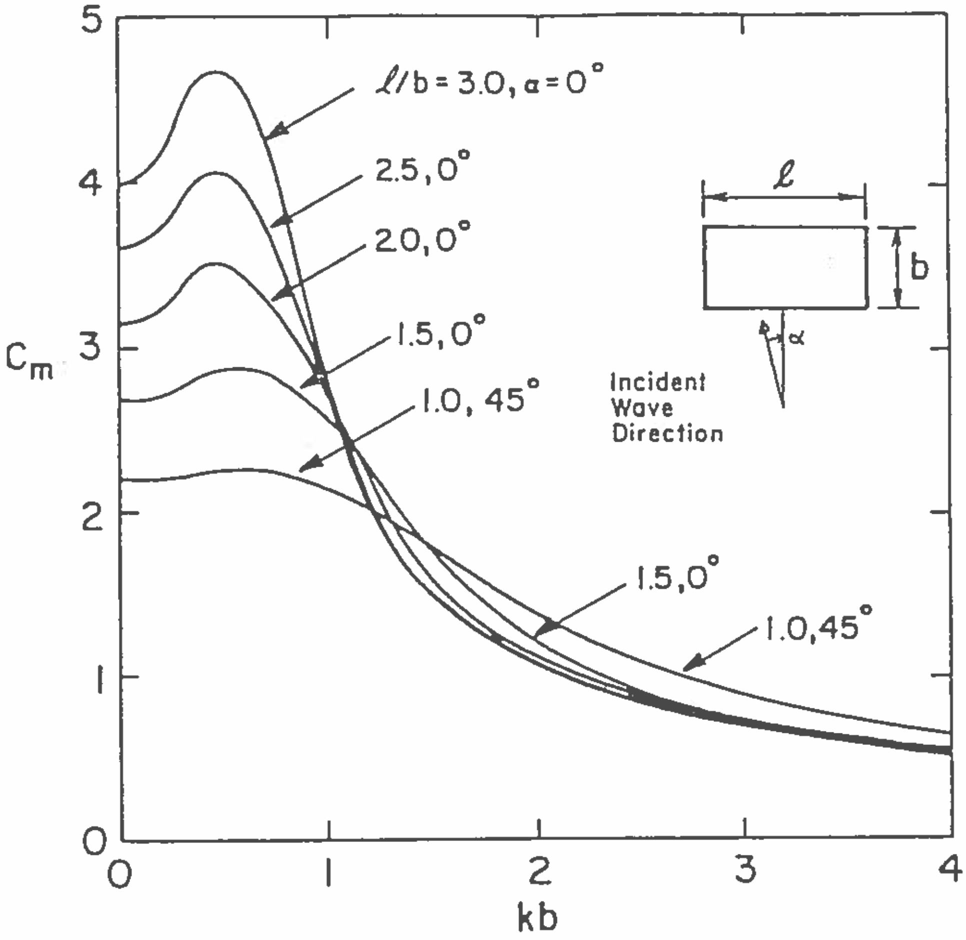

Fig. 4.3 Inertia coefficients for rectangular, vertical cylinder (from Sarpkaya and Isaacson, 1981)

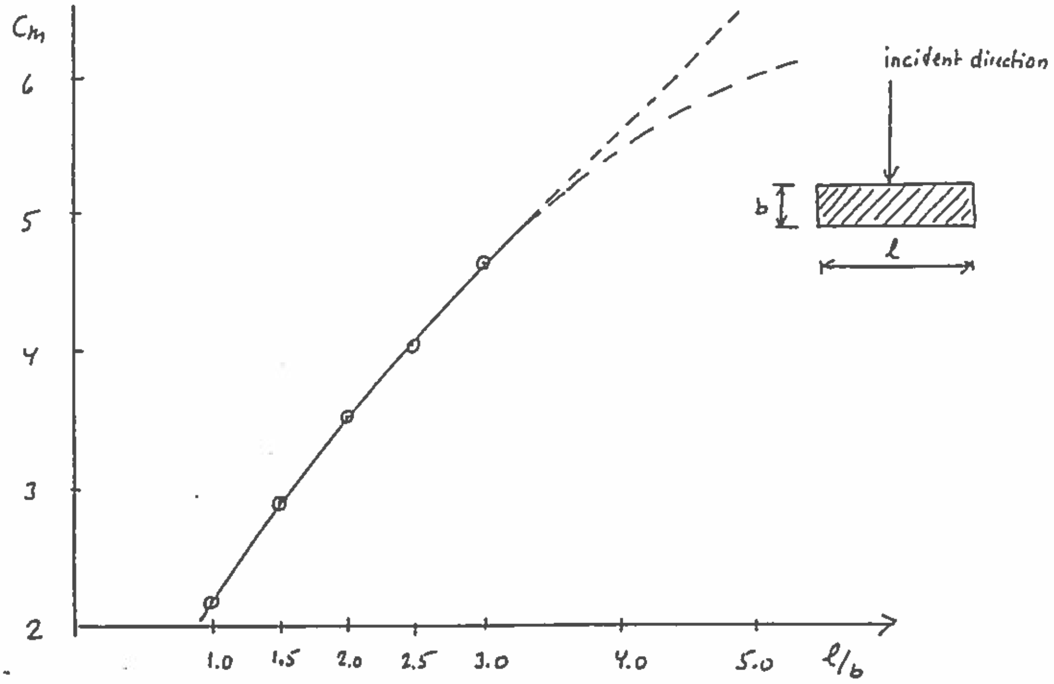

Fig. 4.4 Maximum inertia coefficient for rectangular, vertical cylinder (for kb ≈ 0.5, see fig. 4.3)

5. BMT DIFFRACTION ANALYSIS WITH ESG POST PROCESSING CORRECTING

British Maritime Technology (BMT) performed the diffraction force analysis of the piers for ESG. Shown below are some illustrative examples from their analysis.

The actual system of surface facets used in the diffraction analysis is illustrated on fig. 5.1 for a pier on 29 m water depth.

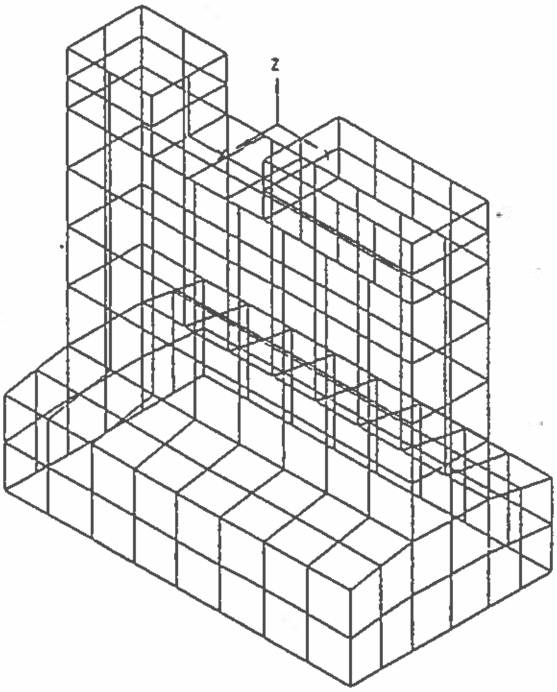

Fig. 5.1 Example of surface facets used for diffraction analysis, Great Belt bridge pier No. 44 datum +1.0 m

The local wave pressure amplitude and the phase angle in all facets are determined through diffraction analysis.

By superimposing the facet pressures with their individual phase angle, the total forces and moments amplitudes may be determined.

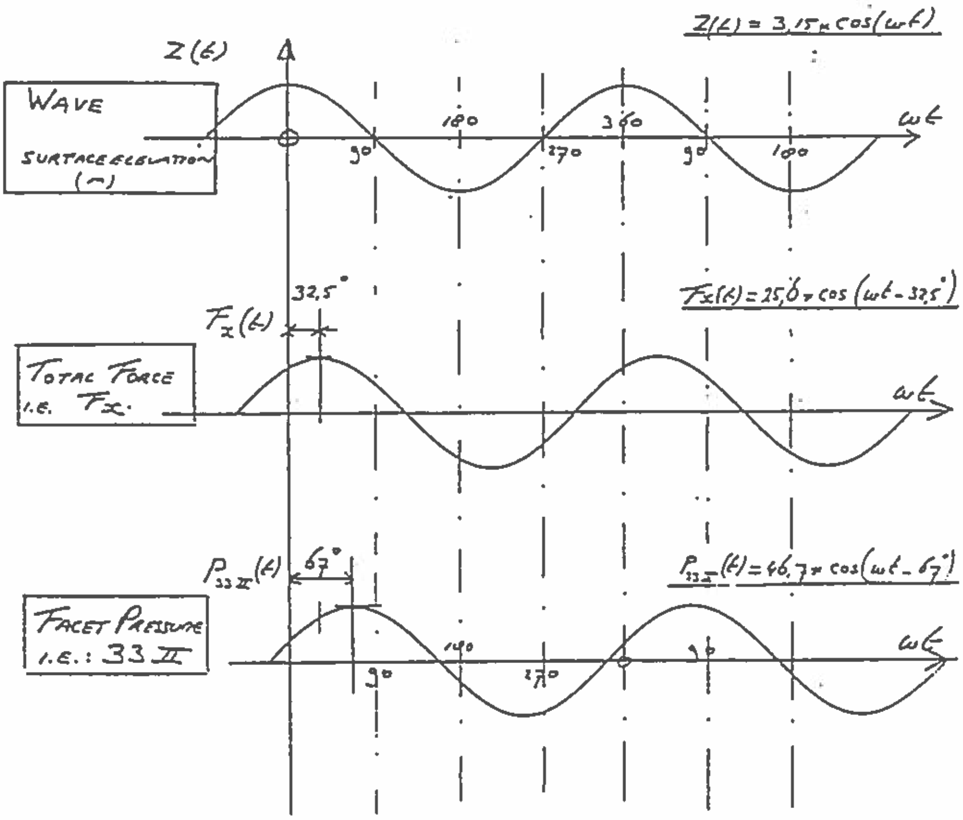

Fig. 5.2 Wave force and pressures as function of time (t)

In this linear analysis two major components are lacking

- effect of finite wave height on vertical sides (effects to forces and moments)

- effect of pressure on the bottom of the structure (effect to moments)

The effect of the finite wave height consists mainly of a triangular over pressure correction on the upstream side and a triangular suction pressure correction on the downstream side. The effect on the forces and moments from this correction is principally proportional to the wave height squared (see fig. 5.3).

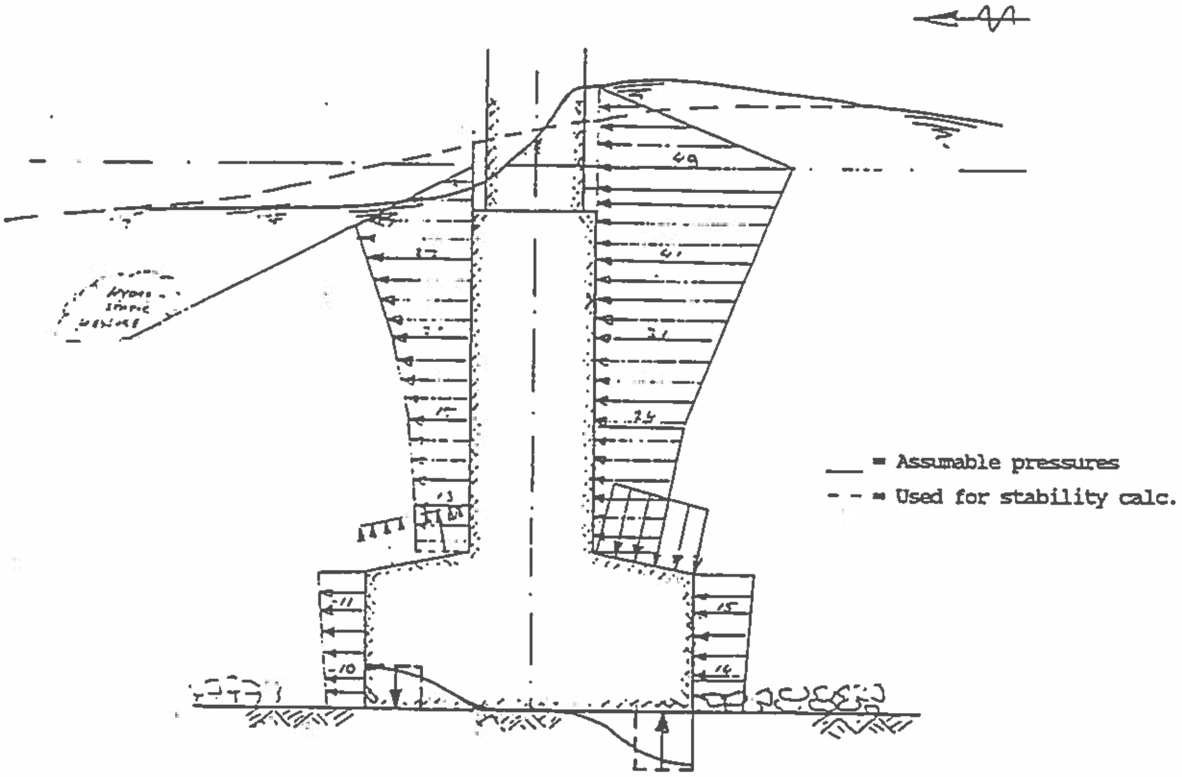

Fig. 5.3 Correction NMIWAVE results due to wave pressures underneath baseslab bridge piers

The effective pressure on the bottom of the pier caisson was estimated from experiences obtained in connection with the Eastern Schelde investigations.

An example is shown in fig. 5.4.

This correction is also indicated on fig. 5.3.

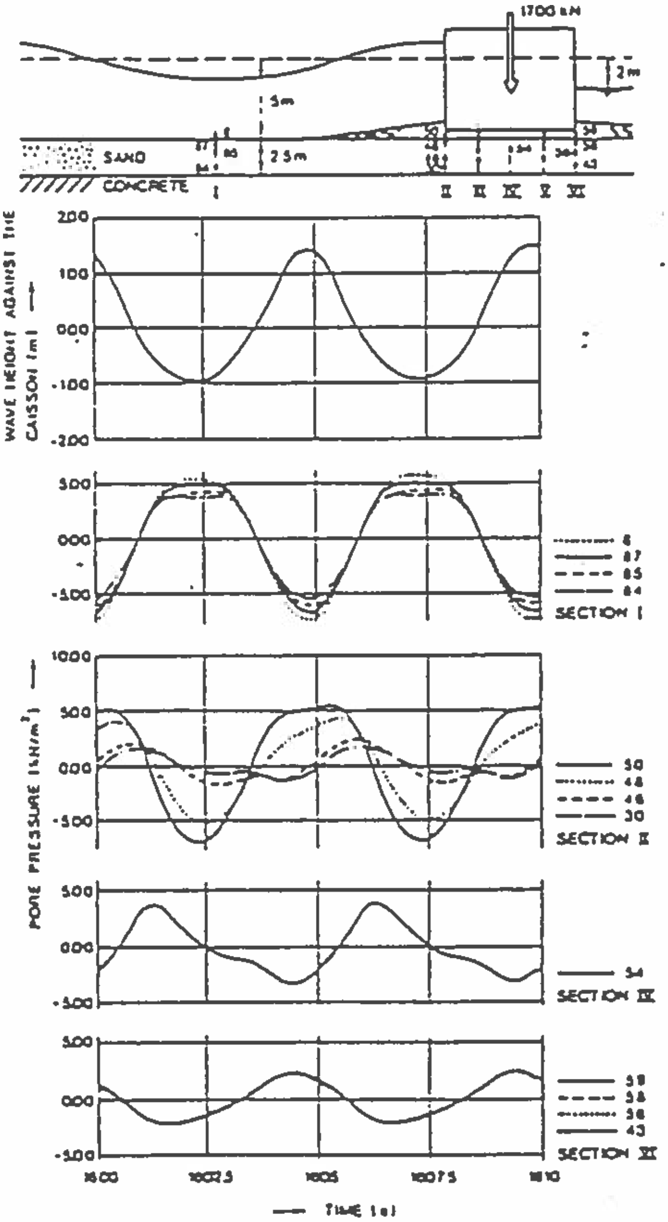

Fig. 5.4 Measured pore pressures in the sand in front of and below the caisson

Table 5.1 show examples of final results from this analysis. "BMT" represents the diffraction linear solution and "ESG" represents the BMT analysis corrected as illustrated on fig. 5.3.

CALCULATIONS No.	Pier no.	W.L. (m)	H. (m)	T. (s)	DIR. (°)	F x				M Y			
						BMT	ESG	%	Phase (°)	BMT	ESG	%	Phase (°)
A.1	44	-1,2	5	7	0°	20,4	21,4	1,05	37	319	355	1,11	37
A.2	44	-1,2	6,3	7,6	22,5°	25,6	27,0	1,05	33	380	434	1,14	33
A.3	44	-1,2	6,3	7,6	45°	18,6	19,01	1,03	33	275	300	1,09	33
A.4	44	-1,2	6,3	7,6	90°	—	—	—	—	—	—	—	—
A.5	44	-1,2	5,0	7,6	0°	22,5	—	—	32	333	—	—	32
A.6	44	-1,2	6,3	7,0	22,5°	23,0	N.A	—	38	360	N.A.	—	38
A.7	44	-1,2	6,3	7,0	90°	—	—	—	—	—	—	—	—

Table 5.1 Example on final results from BMT and final results from ESG including finite wave height and pressures on the bottom of the piers.

Professor H. Lundgren's independent use of Sommerfeld's theory to check and verify the diffraction solution is illustrated in Appendix B.

6. FORCES ON PIERS FROM BREAKING WAVES

For piers at shallow water depths, where wave breaking may occur, the wave forces may be larger than estimated from diffraction/pressure gradient considerations. Usually such piers are designed by means of design methods for caisson breakwaters.

ESG chose to base their evaluation mainly on Goda (1985). Goda's wave force analysis corresponds to composite breakwaters.

The actual piers have certain similarities with composite breakwaters in the sense, that the wider lower part of the caisson may influence the waves approaching the piers in a similar way as the substructure influence the waves for a composite structure.

Goda's method is a simple but physically sound and recognized design method.

Below is illustrated the main contents of Goda's method.

Fig. 6.1 shows the parameters used in Goda's method.

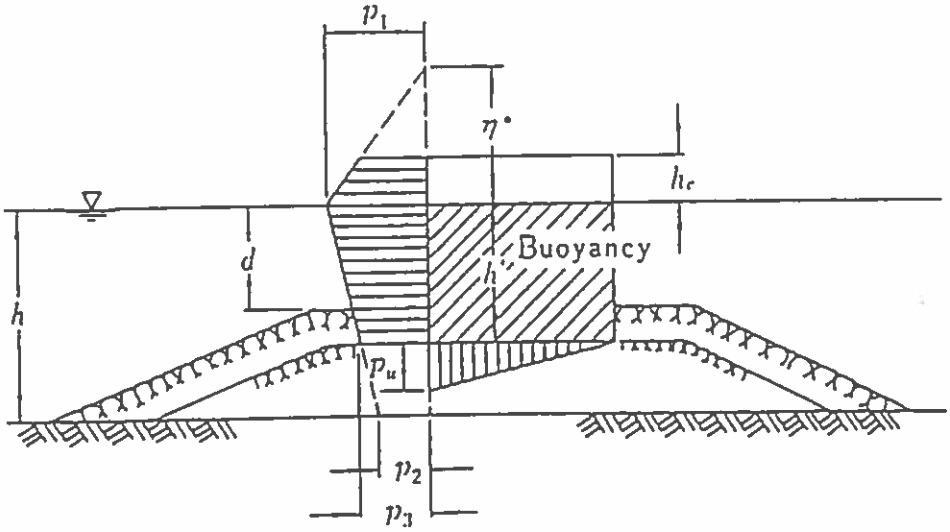

Fig. 6.1 Distribution of a wave pressure on an upright section of a vertical breakwater

The formulas in Goda's wave pressure method are as follows (with L = local wave length):

Wave pressure on the front of a vertical wall

$$p_1 = \frac{1}{2}(1 + \cos\beta)(\alpha_1 + \alpha_2 \cos^2\beta) w_0 H_{max},$$

$$p_2 = \frac{p_1}{\cosh(2\pi h/L)},$$

$$p_3 = \alpha_3 p_1,$$

in which

$$\alpha_1 = 0.6 + \frac{1}{2}\left[\frac{4\pi h/L}{\sinh(4\pi h/L)}\right]^2,$$

$$\alpha_2 = \min\left\{\frac{h_b - d}{3h_b}\left(\frac{H_{max}}{d}\right)^2, \frac{2d}{H_{max}}\right\},$$

$$\alpha_3 = 1 - \frac{h'}{h}\left[1 - \frac{1}{\cosh(2\pi h/L)}\right],$$

min $\{a, b\}$: Smaller of a and b,
h_b : water depth at the location at a distance 5 $H_{1/3}$ seaward of the breakwater.

The required parameters, α_1 and 1/cosh (2π h/L) are given in respectively fig. 6.2 and fig. 6.3.

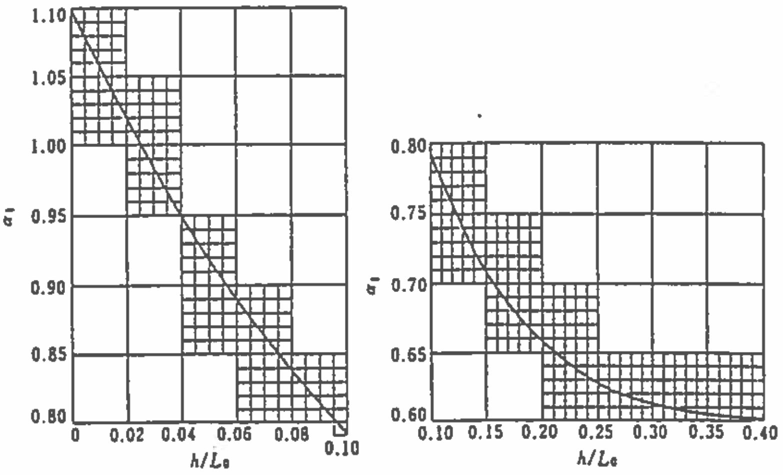

Fig. 6.2 Calculation diagrams for the parameter α_1

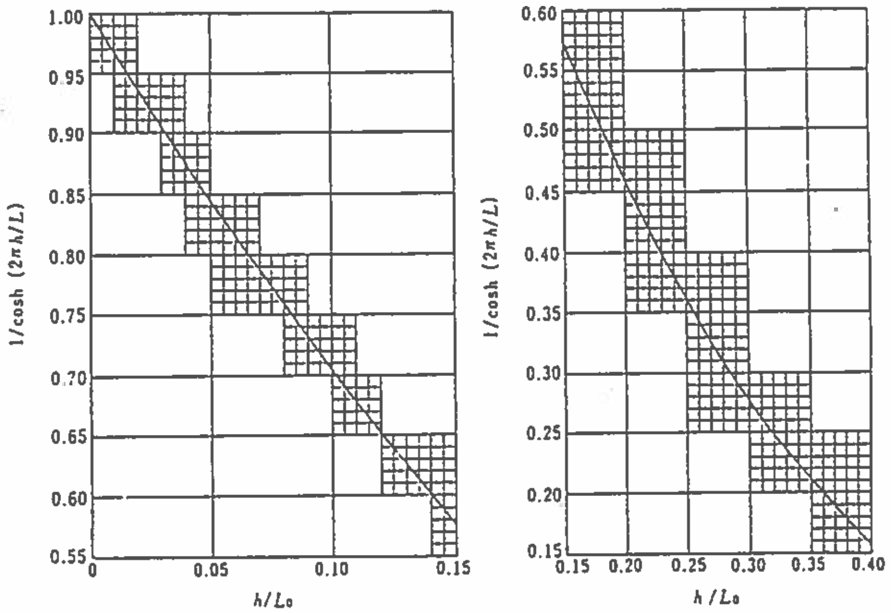

Fig. 6.3 Calculation diagrams for the factor of 1/cosh ($2\pi h/L$)

Previous experimental investigations by DHI carried out mainly by H. Lundgren and the author show quite similar results for $F_3 = F_{0.1\%}$ = maximum force during 1000 incident waves. (See fig. 6.4 from Gravesen, (1979)). The graph includes estimate of the logarithmic slope of the force around $F_{0.1\%} = LSF_3$. Through use of these two parameters a statistical integration (see Lundgren 1974) may lead to the design force. Utilisation of the results published by Lundgren and Gravesen in various papers for bridge piers require estimate of the height of the resultant force in order to calculate the overturning moment for which similar data unfortunately have never been published. But it may however be estimated for example as shown in CERC (1984).

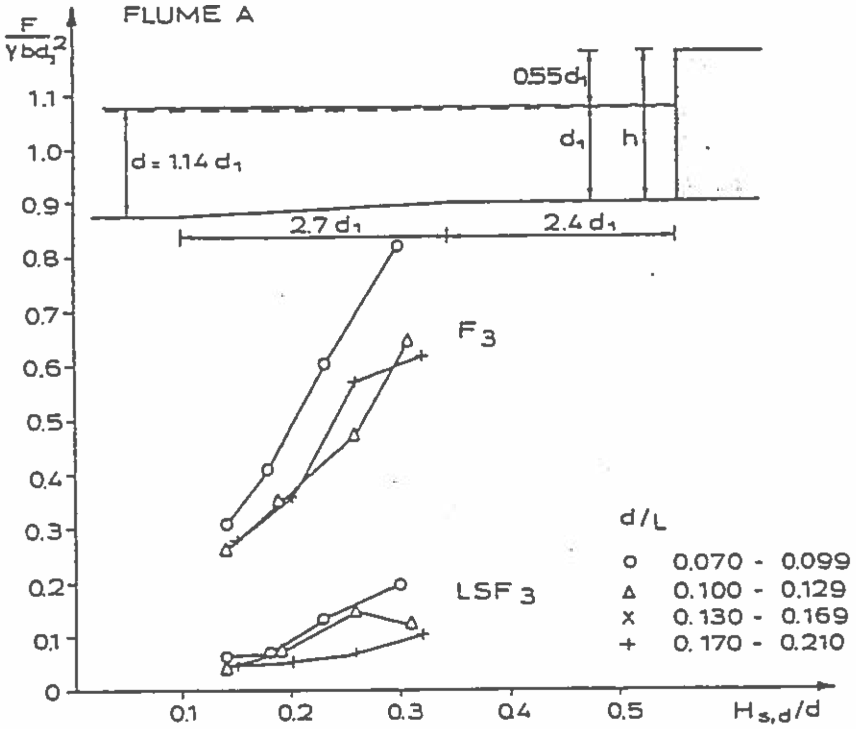

Fig. 6.4 Example of wave forces on vertical breakwater (Gravesen, 1979).

7. TOTAL DESIGN FORCES

7.1 Shielding

The length of the piers ≈ 30 m relative to the distance between the piers (90 to 110 m) give rise to, for wave directions close to the alignment of the bridge, the fact that shielding may occur.

An estimate of this is performed by utilizing diffraction graphs in C.E.R.C. (1984) see fig. 7.1. Superposition of the three components (①, ② and ③ in fig. 7.2) leads to a relative incident design wave height varying from 0.84 to 1.03 over the pier length with a relative average of approximately 0.92 for an incident direction of α = 22.5°. α = 0 corresponds to a wave orthogonal direction equal to the bridge alignment.

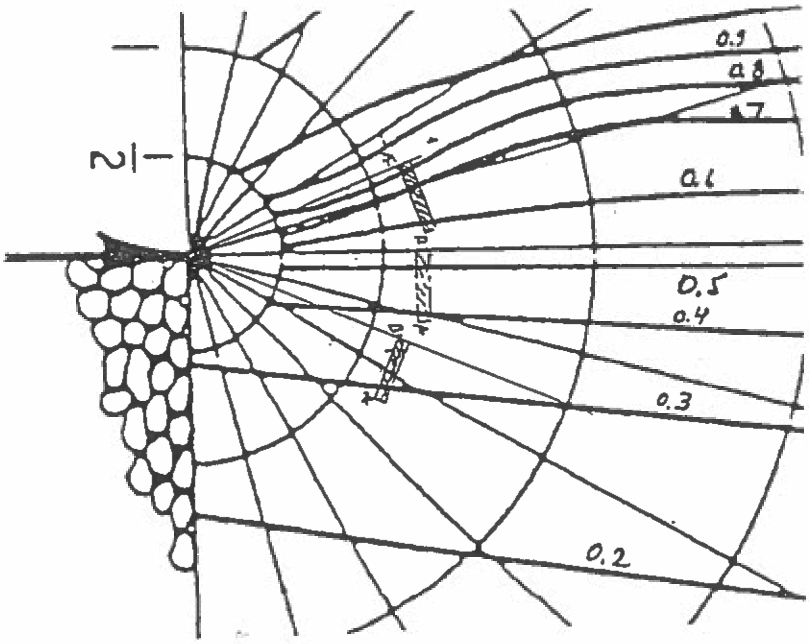

Fig. 7.1 Wave diffraction for α = 22.5°

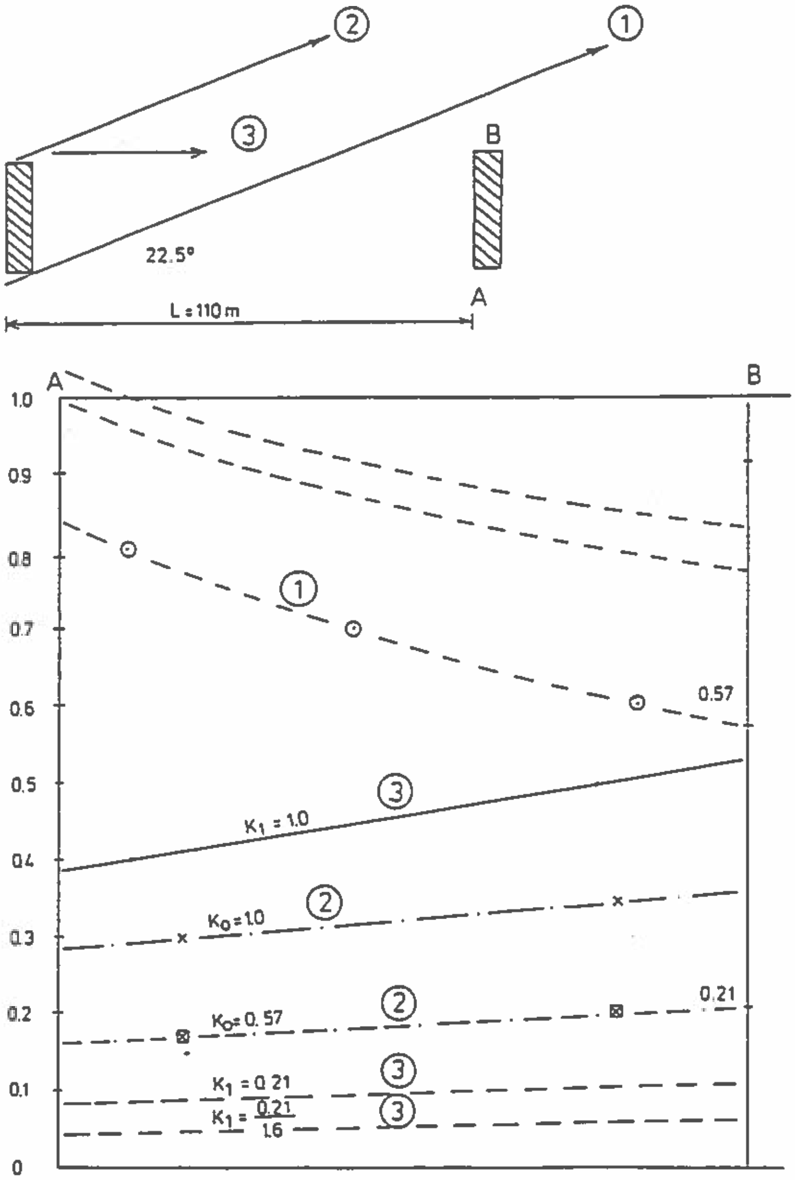

Fig. 7.2 Superposition of 3 diffraction components for α = 22.5°. (③ is diffraction from upstream pier)

7.2 Total Design Forces

The results of the detailed wave study (see Rugbjerg, 1991) lead to a general revised design basis (BBD) as shown in fig. 7.3.

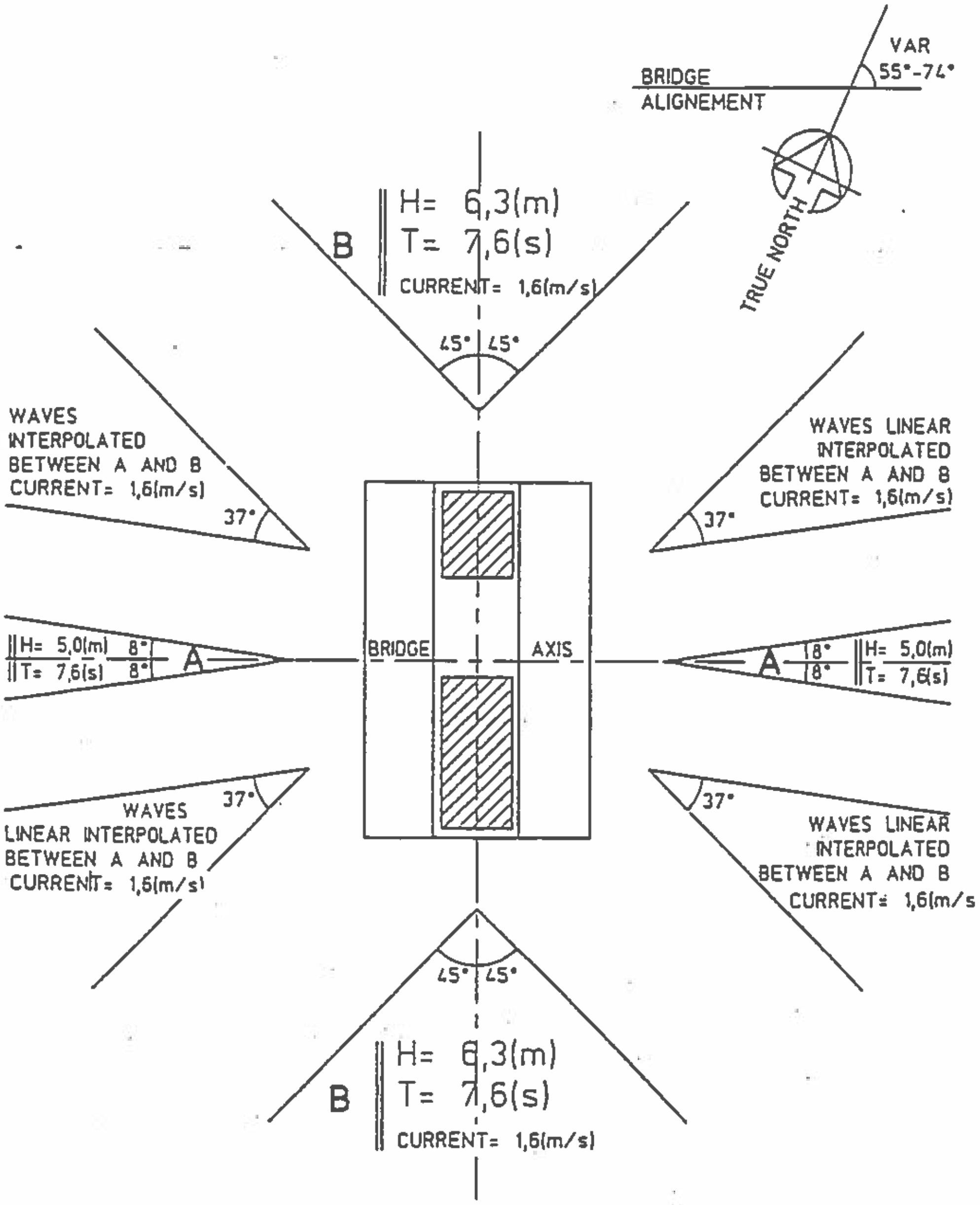

Fig. 7.3 Revised wave and current design basis for West Bridge.

The total design takes account of force variations with relative wave incident direction and wave height variations with relative wave direction. The relative effect of the combination of these two variations is shown in fig. 7.3. In fig. 7.3 the relative consequences, if shielding had been included in the analysis, is also estimated. The latter was not taken into account in the project but it correspond to a wave load estimate being approximately 8% too high by disregarding this effect.

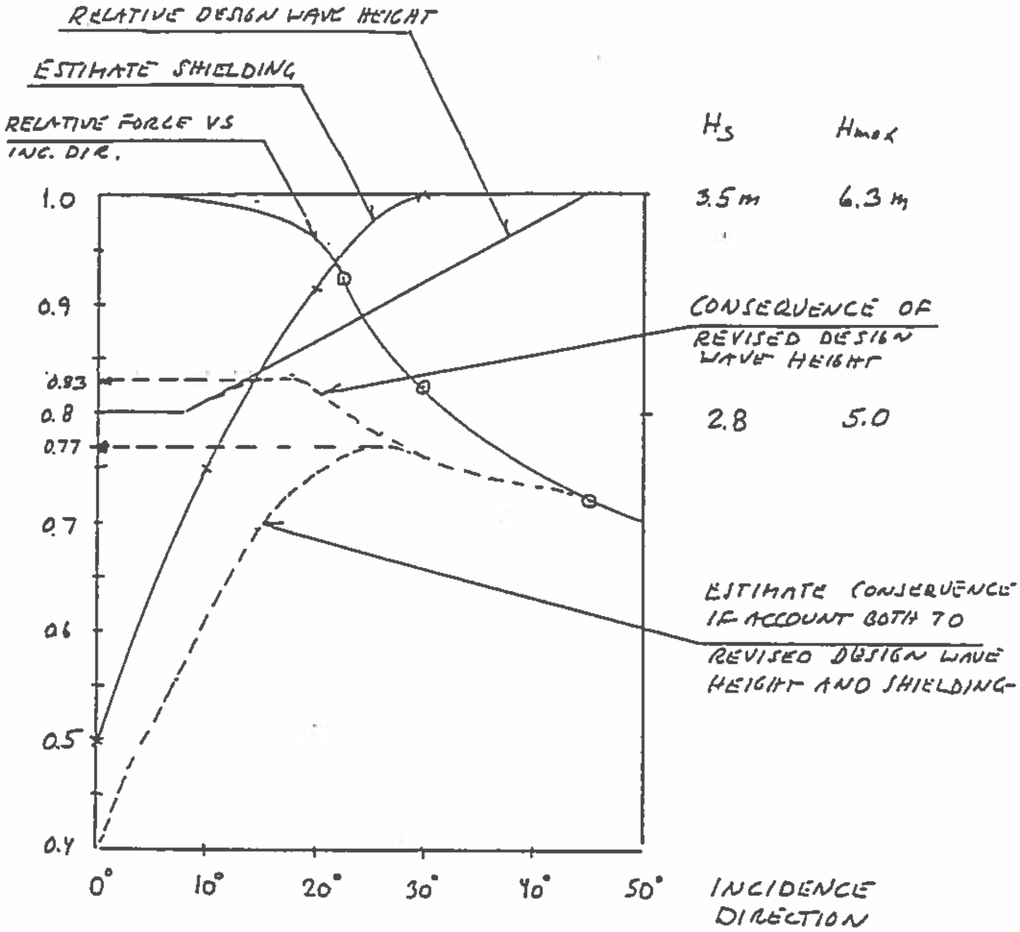

Fig. 7.4 Relative reduction coefficients to wave forces versus incident direction

7.3 Discussion

The wave load design for the bridge piers was mainly carried out by utilization of diffraction theories describing the relative pressures around the pier during passing of a maximum design wave.

Uncertainties in the design mainly relate to local effects of water passing the gap between the two pier shafts, separation reduced around the verticals and by shielding not accounted for in the design.

Physical model tests would most likely have given lower design forces due to shielding. But also effect from separation, wave breaking in the gap, and irregular waves including assymetries may have given deviations from the linear theoretical results of a diffraction analysis.
Important lessons have been that desk calculations may give quite a good preliminary estimate if account is taken that:

- diffraction/shoaling may amplify the pressure gradient because the structure "raise" the wave profile

- finite wave height effects and pressure on the caisson bottom should be included in the design.

A closer stability design for wave load could also have included experiences obtained in connection with dynamic ice load design through determination of soil strength parameters representative of the cyclic wave load.

It may also be mentioned that accidental wave loads are not much larger than the ultimate limit wave loads. This is due to the fact that even if the wave height increases, the associated wave length is also increased, so that the inertia forces are increased less than proportional to the wave height.

In the project the wave/current forces were only considered as an ultimate limit load but they were not included in the accidental risk analysis. This places a question mark on the overall design philosophy. There ought to be consistence between accidental stage load and ultimate limit stage load in that sense that the safety included by the partical coefficients in ultimate limit stage should correspond to reducing the risk of rupture to a level of 10^{-4} per year or less equal to the risk level used in accidental load. Use of traditional partial coefficients on nature load gives however in the present case a risk of rupture much less than 10^{-4} per year.

The partial coefficient for wave load ought to be selected on the basis of an analysis describing the ratio of an ultimate load wave force relative to a accidental wave force with a chosen probability of exceedance. The present nature load partical coefficient is basicly only describing that frequently maximum wave height is estimated to be increased by a 1.3 factor when the probability is reduced by a 100 factor.

APPENDIX A

Preliminary Force Analysis performed by ESG

(iii) Calculation of wave loads on piers

Section 5.3 of BBD stipulates that wave and current action on the finished structures shall be determined in accordance with DS 449, Code of Practice for the Design and Construction of Pile supported Offshore Steel Structures, I. edition, April 1983. Because the piers are massive structures which are also affected by inertia and diffraction effects, the following method was used to evaluate these forces.

Wave forces on an object are generally regarded to be split into a drag force, proportional to the square of the velocity of the water particles, and an inertia force, proportional to the acceleration of the water particles. For slender steel structures, drag forces usually predominate but for massive concrete structures, the drag components are of little consequence.

The shape of the plinths was idealised to a rectangular block of the same volume, height and length (across the bridge), and wave forces were calculated for the plinths surmounted by three cylindrical columns. The method of calculation of horizontal wave forces on the plinths was as follows:

1) The wave pressures were evaluated over the surface of the plinths in the absence of the plinth and resolved to give the forces in the horizontal and vertical directions.

2) To take account of the scattering of waves by the plinth, the forces were multiplied by a diffraction coefficient, made up of two parts:
    a) The mass coefficient in long waves. The added mass for horizontal wave forces was taken as the minimum of the two masses shown below. The mass coefficient was taken as 1 plus the added mass divided by the mass of water displaced by the plinth.

$$\text{i.e} \quad \text{min} \left\{ \begin{array}{l} 1 + \frac{\pi}{4} \cdot \frac{B}{L} \\ \\ 1 + \frac{\pi}{2} \cdot \frac{H}{L} \end{array} \right\}$$

This is illustrated by Figure 1.

b) The diffraction effect in short wave was taken as

$$1 - 0.5 \times \left(\frac{\pi W}{L} \right)^2$$

Where L is the wave length
W is the width of the plinth in the direction of wave approach.

Figure 2 shows a comparison of forces calculated by this method with those calculated by a general diffraction analysis and with model experiments of a gravity base for an offshore structure. The agreement is extremely good.

Horizontal wave forces on the cylindrical towers were calculated using the intertial terms of Morrisons equation i.e. by evaluating the water particle accelaration at a number of points on the centre-line of each tower and multiplying this acceleration by the mass of water displaced per unit length and a mass coefficient of each tower from the top of the plinth to the still water level using Simpons's Rule.

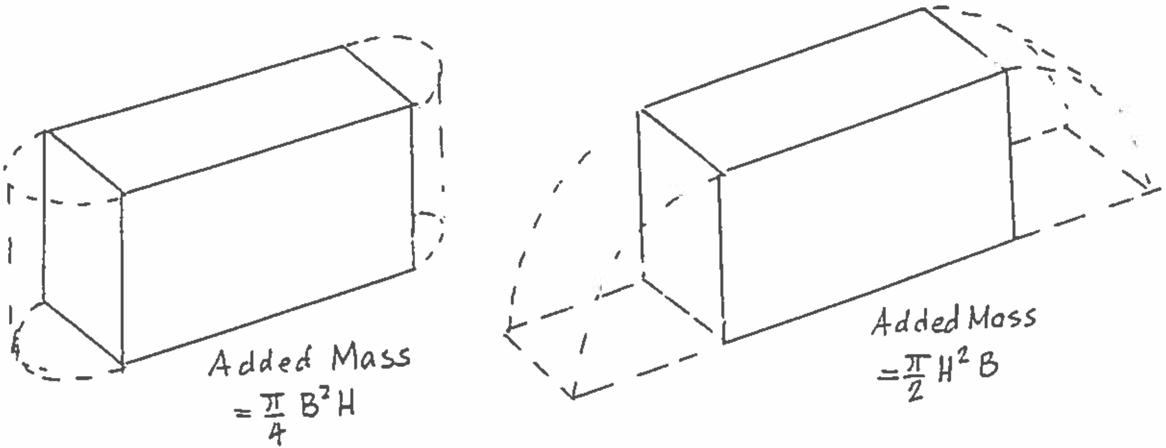

Figure 1

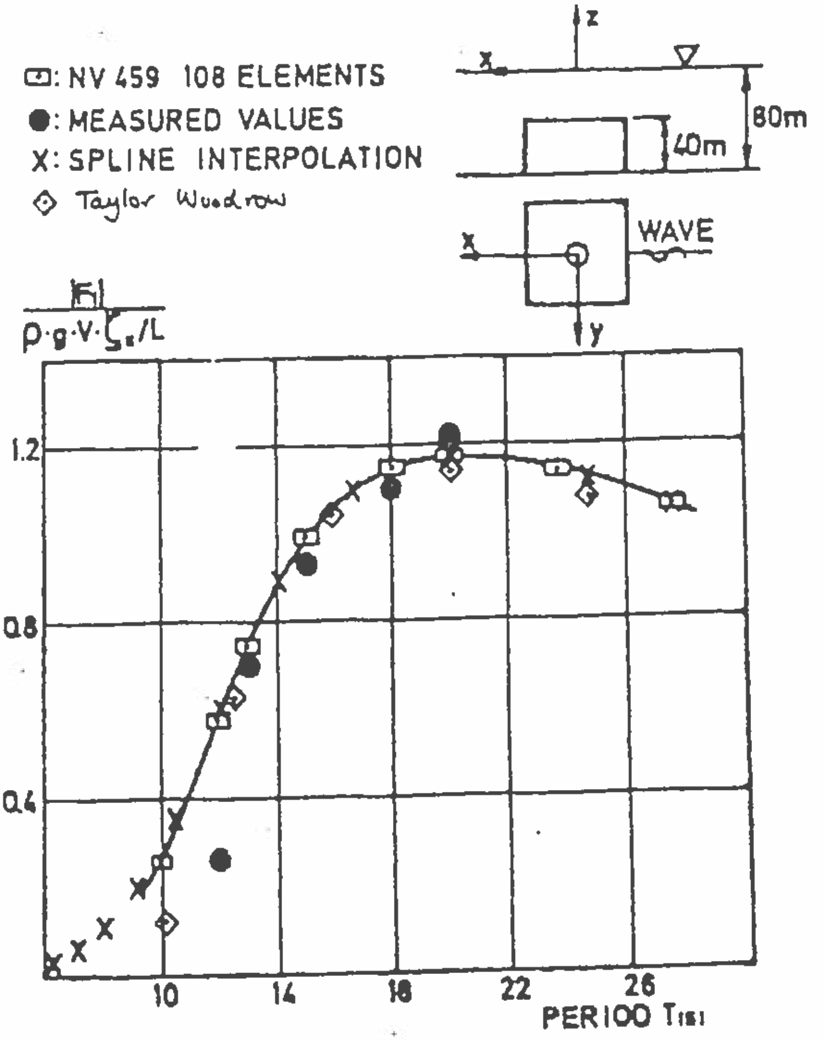

Fig. 2—Horizontal force on a caisson
(L × B × H = 90 × 90 × 90 m).

APRIL, 1978

Comparison of the design method of calculating wave forces on a rectangular box with a diffraction analysis and model tests.

Source: "Diffraction theory and statistical methods to predict wave-induced motions and loads for large structures".
A.E. Loken and O.A. Olsen

Journal of Petroleum
Technology, April 1978

APPENDIX B

H. Lundgren: Review of wave and Current Loads on Bridge Piers

1. Conclusions

BMT's numerical model NMIWAVE is an efficient, well-established method of calculating wave forces on offshore structures by determining the oscillating wave pressures (sources) at a number of facets covering the surface of the structure, so that the velocities normal to all facets vanish. (In Fig. 1 there are 194 facets requiring the solution of 194 equations for 194 complex unknowns.)

An alternative method of calculation described below has confirmed the results found by BMT. Indeed, with reference to Fig. 1, the two methods have given the results indicated in Table 1 for the horizontal rows 1 - 57. The table has two sections, I and II, I representing the rear side (W-E) of the pier and II the front side (N-E). Each facet number is used (symmetrically) on both sides. The columns marked "BMT" give the results found directly by the NMIWAVE analysis. The columns marked "Corr.BMT" give the results of an approximate analysis, by which DHI has attempted, on the basis of the BMT figures, to eliminate so far as possible the influence of the 9.42 m long opening between the railway shaft and the motorway shaft. Finally, the columns marked "Altern." give the results of DHI's alternative calculations, which also contain some approximations.

For each column (and facet) the first figure gives the pressure amplitude A in kN/m², followed directly by the phase Φ, defined so that the actual pressure on the facet is $p = A \cos(wt + \Phi)$, where $w = 2\pi/T$ and t is time. (BMT uses the phase $\alpha = -\Phi$.) The table shows that all phases Φ are negative. The incoming, undiffracted wave is $z = H/2 \cos(wt - 90°)$ at the point $x = y = 0$.

Table 1: Pressures on Facets 1 - 57.

Facet	I = Rear Face			II = Front Face		
	BMT	Corr.BMT	Altern.	BMT	Corr.BMT	Altern.
1	25.9-171°	28-172°	29-169°	33.9-79°	35-79°	35-76°
9	28.1-172°	31-173°	32-171°	40.1-71°	42-71°	42-67°
17	28.6-166°	33-170°	33-172°	44.0-68°	47-67°	45-61°
25	28.7-152°	32-165°	32-169°	46.5-68°	47-64°	46-56°
33	29.0-140°	30-160°	30-165°	46.7-67°	47-61°	46-53°
41	28.0-134°	27-152°	26-157°	44.5-64	45-58°	43-50°
49	24.5-131°	23-142°	21-143°	40.1-58°	41-55°	39-49°
57	20.3-118°	18-123°	17-116°	34.6-53°	36-52°	33-50°

ESG has not discussed the shielding effect of the neighbouring pier. It would seem that this effect might reduce the wave forces essentially.

The second order wave effects are dealt with by ESG in a satisfactory manner. The correction for wave pressures underneath the base slab is reasonable. Incidentally, it amounts to only 3% of the overturning moment.

The analysis of the (relatively less important) current loads is satisfactory.

2. Alternative Method of Calculation

Because of BMT"s many years of experience with NMIWAVE, DHI has had no reason to doubt the validity of the BMT results (for first order wave theory). We have understood, however, the request from CLL in the manner that it would be desirable with an independent check. In addition, there could be a question of the mesh applied by BMT, considering the abrupt variation of the pressure phases around the corners. For example, for the 4 neighbouring facets 1,I - 65,I - 65,II and 1,II the BMT-values are $\Phi = -171°, -141°, -110°$ and -79, respectively with four consecutive differences of 30°. Similarly, between 57,I and 75,I the phase jumps 43° from -118° to -75°.

Establishing an alternative method has not been a simple task. We have chosen to consider a pier of rectangular cross section, 6.4 x 29.28 m, extending from the seabed to above the sea surface. This implies two simplifications relative to the actual pier configuration:

a. The widening of the lowermost 8 m from 6.4 m to 17 m is neglected. This widening has, however, not a large influence, partly because the wave pressures, varying approximately as cosh k(z+h), reduce from 100% at the sea surface to 27% at the seabed, partly because the width, 5.3 m, of the "foundation berm" corresponds to a phase variation of only 22° for a wave length of 86.96 m.

b. The opening, 2.3 m deep and 9.42 m long, between the two pier shafts has been eliminated. This opening has an essential influence on the wave pressures in the vicinity. Therefore, it has been necessary to try and correct the BMT-values before the comparison with the alternative analysis, cf. the columns "Corr.BMT" in Table 1. This correction is explained in Sec. 4 3 below.

With these simplifications the problem is reduced to that of the wave scattering in two dimensions by a rectangle. This is far from being a simple problem. Because the width, 6.4 m, of the rectangle is small compared with the wavelength L = 86.96 m, it has been decided to determine approximate values of the wave pressures as a combination of two (independent) contributions:

1. Diffraction around a thin wall extending from N to E, i.e. placed along the front side, which is hit first by the waves. The pressures found on the rear side of the thin wall are assumed to occur at the corresponding points on the rear side of the pier.
2. The Froude-Krylov force, i.e. the force exerted on the volume of the pier by the incoming, undisturbed wave. As a consequence of contribution 1. this force is applied to the rear side in the following manner: For facet 57, for example, the difference between the Froude-Krylov pressure on 57,I and that on 57,II is applied to 57,I.

It is evident that, in reality, the two contributions are not completely independent. We are dealing with an "engineering" method, which becomes asymptotically correct when the thickness of the pier converges towards nil.

The diffraction problem for the thin wall N-E can be solved exactly by means of (the rather complicated) Mathieu functions. In order to obtain a workable solution, it has further been decided to apply (the simpler) Sommerfeld's theory for a semi-infinite reflecting screen, i.e. to combine the diffraction around a semi-infinite screen ending at the point N with that of a screen ending at the point E. (This superposition necessitates the subtraction of an incoming + a reflected wave from an infinite screen along the front N-E.)

The superposition would be accurate if the wavelength were short compared with the distance N-E. Unfortunately, it is three times as long as N-E. The error involved in the superposition can be estimated by considering the diffraction coefficients along the front. By diffraction around N the coefficient at E is 1.080+11.1°. By diffraction around E it is 1.146-3.3° at N. Since these coefficients differ from 1.000+0.0°, the superposition of the two diffractions cannot, at the same time, satisfy the boundary condition along the front and yield undisturbed, incoming waves to be diffracted around N and E for the determination of the pressures on the rear side of the front.

On the other hand, it will be seen that the two diffraction coefficients are not very different from one. It was decided to "split the difference" between the front and rear sides, i.e. at N the incoming wave was taken with a factor of 1.073-1.6° (for both sides), while at E it was taken with a factor of 1.040+5.5°. (As an example, Facet 9,II was chosen for calculating the various corrections. It was found that the 50% diffraction correction made the alternative method's pressure approach the "Corr.BMT"-value, while a 100% correction would have given complete agreement.)

3. Correction of BMT-values for Opening

Presumably, the rather shallow opening has little influence on the pressures on the deeper parts of the pier. Therefore, the corrections from the BMT-values to the "Corr.BMT"-values have been based on the rows 4-60, 17.61 m below the sea surface.

With regard to the phases Φ, the differences between the facets in rows 1-57 and those in rows 4-60 were plotted, including the facets 65, 68, 75, 78 at the pier ends, where the influence of the opening is a minimum. The plots showed excessive "bulges" around the opening, with a maximum at facet 33. A smoothed elimination of the "excesses" required a maximum correction of 20° at 33,I and 6° at 33,II.

With regard to the pressure amplitudes, it was not possible to trace any systematic influence of the opening upon the ratios between the values in rows 1-57 and those in rows 4-60, again including the facets on the pier ends. It was therefore decided to base the "Corr.BMT"-values on the BMT-values for the rows 4-60 by applying a factor corresponding to the cosh-variation of pressures. The cosh being 1.000 at the seabed, it is 1.283 at Facet 4 and 2.787 at Facet 1. Hence, the ratio of 2.787:1.283 = 2.172 has been applied as a factor on all BMT-values in rows 4-60.

Needless to say that the above (estimated) corrections from BMT-values to "Corr.BMT"-values were established before the alternative analysis was carried out.

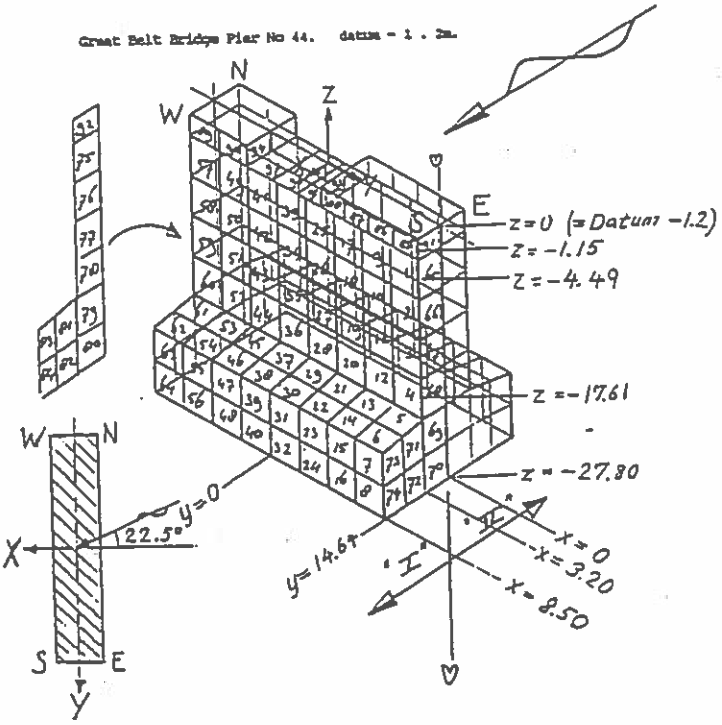

Fig. 1: Computer schematization of Pier 44

Foundation level 29 m.

Water level - 1.2 m, i.e. water depth h = 27.8 m.

The waves approach the front face II from a direction 22.5° north of the negative X-axis.

Wave period T = 7.6 s. Corresponding wave length L = 86.96 m.

Wave height H = 6.3 m.

MODELLING OF SHIP IMPACT ON BRIDGE PIERS AND ON BRIDGE GIRDERS

Main Result of the Investigations for West Bridge, Storebælt

by Helge Gravesen,
Dansk Geoteknik, Carl Bro Group

LIST OF CONTENTS

1. INTRODUCTION

The present paper describes main results of the dynamic ship collision analysis carried out for the West Bridge of Storebælt by CCL (Cowi, Carl Bro and Leonhardt) (see CCL, 1990).

The analysis and selection of load cases is described in Kampmann (1991) in the present proceedings.

Section 2 below describes the accidental load cases and damage design criteria associated therewith.

The dynamic non-linear structural model is described in section 3 (DHI/LIC, 1990).

In section 4 follows results of the analysis of bow collision to the piers both with respect to overall stability and damage with consequences for the use of the bridge, with respect to plastic deformations in the piers and with respect to risk of brittle failure of bearings and associated rupture of the bridge integrity.

Section 5 describes the analysis of sideways collision to the piers.

Section 6 describes the consequences of impact to the girders.

Finally in section 7 the accelerations in the rail girder are estimated for the various possible collisions and the results of an analysis of the consequences to a passing train is described.

The paper describes the analysis and results of the investigations of bow collision in rather detail due to the importance of the principal load case for bridge piers. The rest of the sections summarizes the main results of the other investigations in brief.

2. ACCIDENTAL LOAD AND DAMAGE CRITERIA

2.1 Accidental Load

After construction of the West Bridge the navigation in the Western Channel of Storebælt will be limited to minor vessels. The limit to maximum allowable size is at present a vessel size of 2,000 DWT, but this limit may be revised based upon the results of the final detailed investigations.

These minor vessels may collide with the bridge piers with very short warning time, because no procedure may detect, if they are on damage course, until they are very close to the bridge. The bridge is therefore designed for a full speed impact against the piers for such vessels.

These vessels are too low to be a danger to the girders.

For "illegal" vessels there may exist two types of collisions.

Some may by an error choose the Western Channel instead of the Eastern Channel in Storebælt. For those a warning system will be activated. The vessels are hopefully stopped, but anyhow there should be sufficient time to stop the traffic on the bridge. This is of importance, because such vessels may be so large, that they may give rise to damage to girders.

Finally there is a certain risk for ships being taken by the current or ice in connection with loss of control. Some of these may come from the local traffic to Nyborg harbour. For those there should also be a large probability of significant warning time, so traffic may be stopped on the bridge.

2.2 Damage Criteria

During the detailed dynamic ship impact investigations it became important to clarify the actual damage criteria.

The critical point is the bearings on top of the bridge piers. They in general allow the pier shafts to move parallel to the girders but not perpendicular to the girders.

For the perpendicular direction damage is equal to bearing breakage. For the parallel direction the bearing allow quite a large relative deformation between girder and top of pier shafts. But after a certain deformation the bearings will be loaded so oblique, that the bearing is damaged, and the girder may settle significantly. Thus a difficult repair is required including lifting of the girder and installation of new bearings. But further to this comes, that due to the geometry of the lower part of the piers the "weakest" point of the pier stability is overturning in the direction of the girders. By significant deformation an important destabilizing overturning moment is induced by the large dead weight load.

Above considerations led to that damage, which may result in disruption of normal traffic for a period of 0.5 - 1 month, was estimated to correspond to a residual top of pier shaft deformation of 0.5 m.

Through this definition a clear consistency was made between soil stability failure and actual bridge failures.

By excessive deformation there is also a risk, that the damaged pier needs to be pulled back in upright position, before it may work effectively as a future bridge girder support.

With respect to internal forces in the piers certain plastic yielding may be allowed, as remedial action such as local repair of concrete and extended corrosion protection may be introduced without interrupting the use of the bridge.

For the girders damage criteria can be divided in three categories:

- Minor damage with or without quick remedial action will allow certain use of the girder

- Complete damage to one of the girders

- Damage to both rail and roadway girder requiring repair before use of the bridge at all may be allowed.

Only the last is considered in the risk budget, as the consequences for our society is much less drastic, if either the road connection or the railway connection may still be used although with certain restrictions.

Finally it is required that the bearings are strong enough or have sufficient ductility to maintain connection in the direction perpendicular to the bridge between girders and pier shafts.

3. STRUCTURAL MODEL

3.1 Finite Element Model

To investigate the dynamic response for a ship impact on the Western Bridge a finite element model has been set up including a span with 10 piers of the bridge. For the calculations the LICengineering programme DYNON has been used. DYNON is a dynamic non-linear frame element programme.

All properties for the 10 piers are taken as for pier no. 18 in the major part of the analyses.

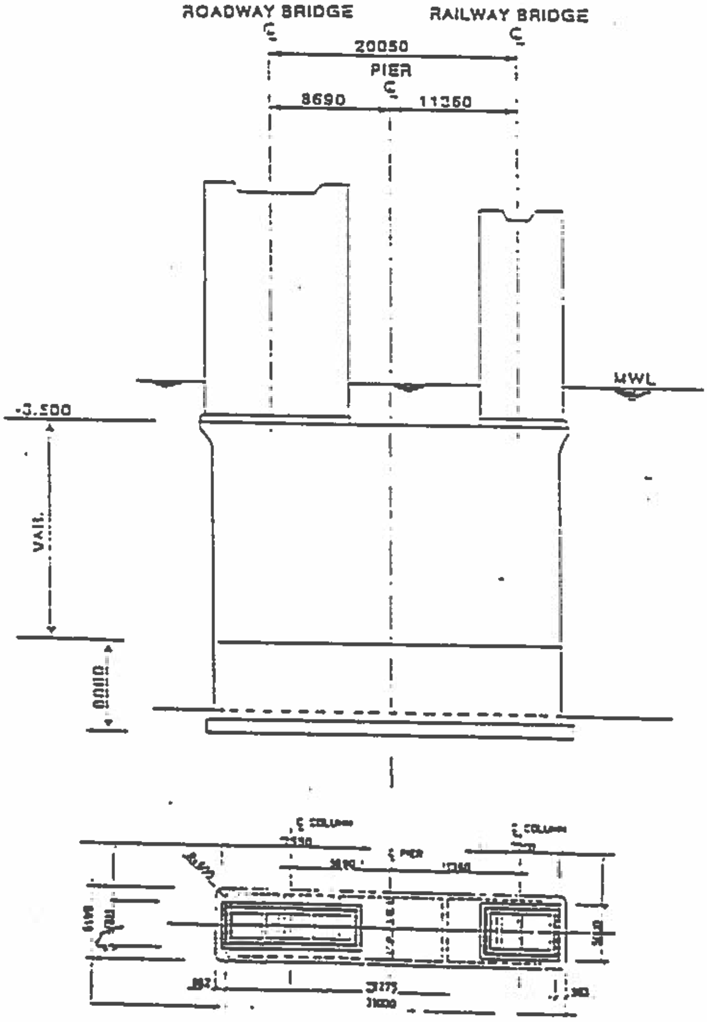

Fig. 3.1 General features of the piers.

Geometry

The bridge section consisting of 10 spans has been modelled by Timoshenko beams, see Figs. 3.2-3.3.

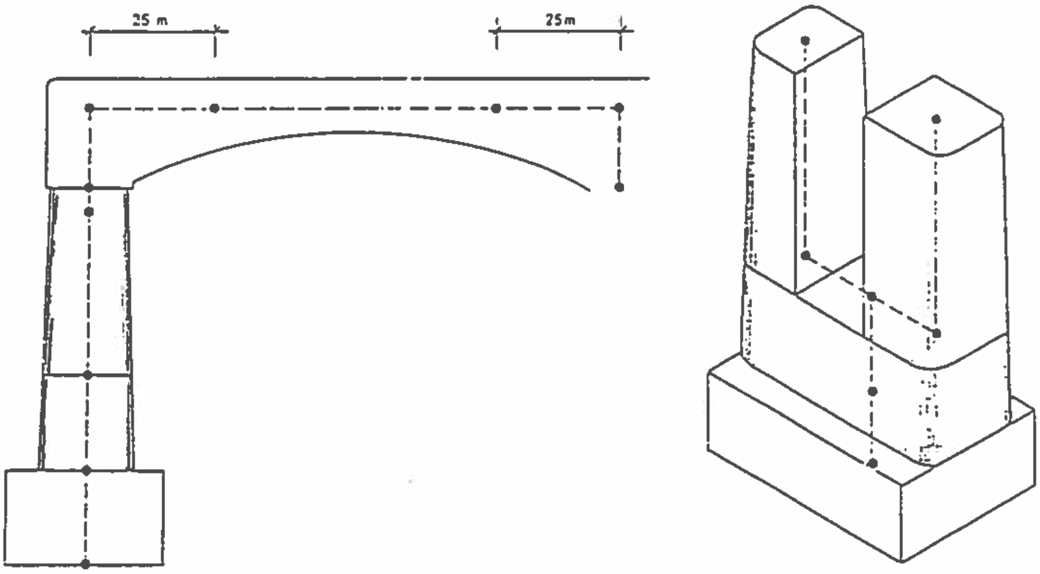

Fig. 3.2 Pier.

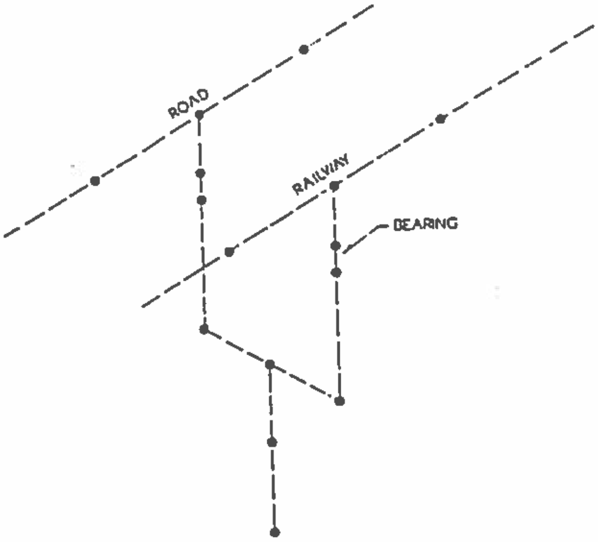

Fig. 3.3 Finite element model of pier and girders.

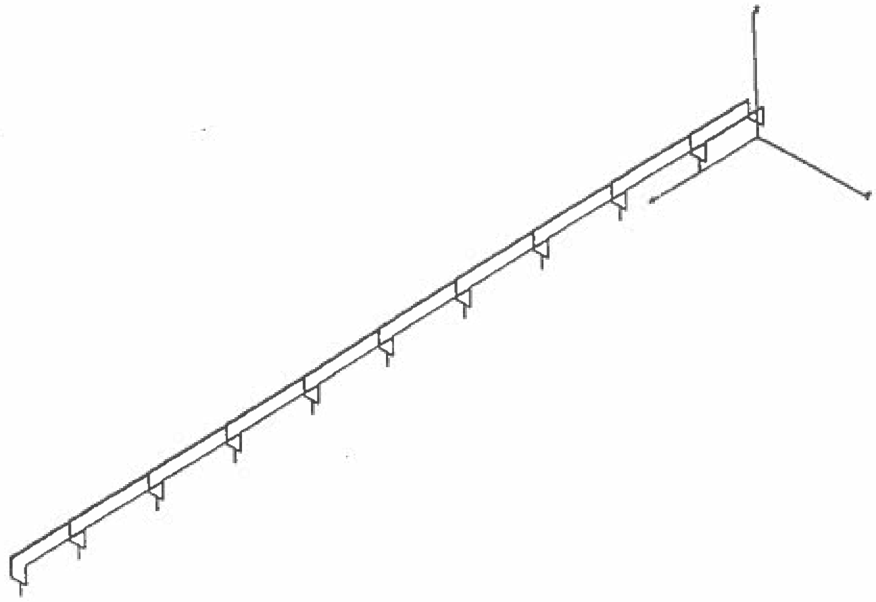

Fig. 3.4 Finite element model of bridge section.

The girders are modelled as beams and placed in the bending neutral axis. They are connected with the bearings at the piers with stiff beams.

Movements of the pier shaft perpendicular to the bridge will cause a bending and a torsional moment in the bridge deck and a transverse load.

Stiffness and Masses for the West Bridge

In this section the calculations of stiffness and masses per metre for the different parts of the structure will be described.

Fig. 3.5 presents the different types of beams used for the finite element model.

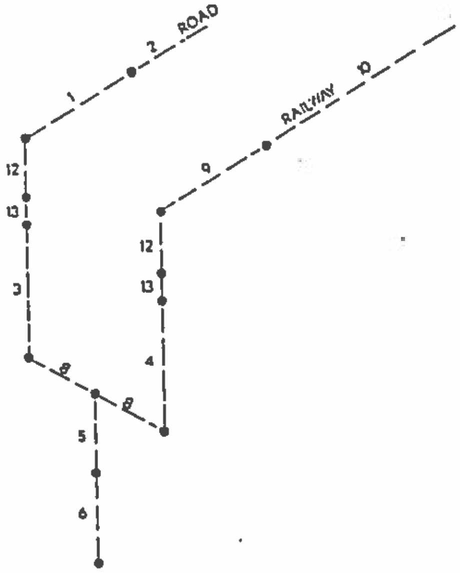

Fig. 3.5 The different beam types of the finite element model.

The beam type Nos. 1, 2, 5, 6, 9, 10 have closed cells and they are assumed to be "thin-walled". Their stiffnesses are calculated by use of "ISH-STYRKE-BASIC PROGRAMMEL" from the Department of Ocean Engineering, the Technical University of Denmark.

Beam Nos. 3 and 4 are rectangular and filled with concrete. Beam Nos. 8 and 23 are very stiff compared to the rest of the structure. Beam No. 13 is the link element used for the bearings. This element is non-linear, and therefore it include two stiffnesses.

General Assumptions

- Young modulus for concrete $E = 4 \times 10^{10}$ N/m^2
- Density for concrete $\rho_{cr} = 2{,}400$ kg/m^3
- Density for sand $\rho_s = 1{,}942$ kg/m^3
- Poisson ratio for concrete $\nu = 0.2$

- The reinforcing steel does not contribute to the stiffness.

- Added mass is taken into account for the piers with different masses for different degrees of freedom.

- Gravity is not included.

The sectional properties of the elements are presented in Table 3.1

```
-----------------------------------------------------------------------
                       -- ELEMENT TYPE DATA --
-----------------------------------------------------------------------
B.TYPE     EA          kGAz        kGAy         GK          EIz         EIy
          (Nm)        (Nm)        (Nm)       (Nm^3)      (Nm^3)      (Nm^3)
  1   0.8420E+12  0.1311E+12  0.3411E+12  0.7300E+12  0.3058E+14  0.6170E+12
  2   0.7024E+12  0.7457E+11  0.2971E+12  0.2949E+13  0.2070E+14  0.2070E+13
  3   0.2008E+13  0.1217E+13  0.1217E+13  0.2074E+14  0.2636E+14  0.2677E+13
  4   0.1440E+13  0.8743E+12  0.8743E+12  0.6586E+13  0.6221E+13  0.3000E+13
  5   0.1382E+13  0.3537E+12  0.3754E+12  0.1852E+14  0.1191E+15  0.9352E+13
  6   0.3474E+13  0.1204E+13  0.4057E+12  0.1293E+15  0.2959E+15  0.1047E+15
  8   0.2000E+13  0.2500E+12  0.2500E+13  0.1100E+14  0.1400E+16  0.1400E+16
  9   0.6412E+12  0.1895E+12  0.1571E+12  0.2492E+13  0.4996E+13  0.2372E+13
 10   0.4948E+12  0.1289E+12  0.1571E+12  0.2492E+13  0.4996E+13  0.2372E+13
 12   0.2000E+13  0.2500E+13  0.2500E+13  0.1100E+14  0.1400E+16  0.1400E+16
-----------------------------------------------------------------------
B.TYPE       A           Ay          Az           m          Ry          Rz
          (m^2)       (m^2)       (m^2)       (kg/m)       (m)         (m)
-----------------------------------------------------------------------
  1        20.20       15.10       6.200      54798.       2.52        8.17
  2        16.80       13.60       4.300      46638.       1.7         8.18
  3        50.20       42.60       42.60      150600.      1.44        3.24
  4        36.00       30.60       30.60      86400.       1.44        2.08
  5        35.81   -   20.56       17.12      0.39149E+06  2.5         9.1
  6        80.26       41.00       42.20      0.10015E+07  6.35        9.13
  8        400.0       160.0       1.600      0.           0.          0.
  9        15.20       8.700       7.600      52740.       2.96        3.1
 10        12.20       7.500       5.700      45540.       2.2         3.17
 12        20.20       15.10       6.200      0.           0.          0.
-----------------------------------------------------------------------

  Youngs Module  E =  4.E10
  Poissons Ratio ny = 0.2
  G = E/(2*(1+ny))
```

Table 3.1   The sectional properties of the beam types.

3.2 Damping

Damping is included in two ways:

1. The internal structural damping is included as Rayleigh damping $C = \alpha_1 M + \alpha_2 K$ where C is the damping matrix, M the mass matrix and K the stiffness matrix. When the damping ratio for two frequencies is known the coefficients α_1 and α_2 can be calculated from:

$$\alpha_1 = \frac{2\omega_1\omega_2}{\omega_2^2 - \omega_1^2}(\lambda_1\omega_2 - \lambda_2\omega_1)$$

$$\alpha_2 = \frac{2(\omega_2\lambda_2 - \omega_1\lambda_1)}{\omega_2^2 - \omega_1^2}$$

In all the computer runs for the ship impact analysis the damping ratio is assumed to be 2% for the frequencies $f_1 = 0.50$ Hz and $f_2 = 0.78$ Hz. These assumptions give a damping ratio as function of the frequency as shown in fig. 3.6.

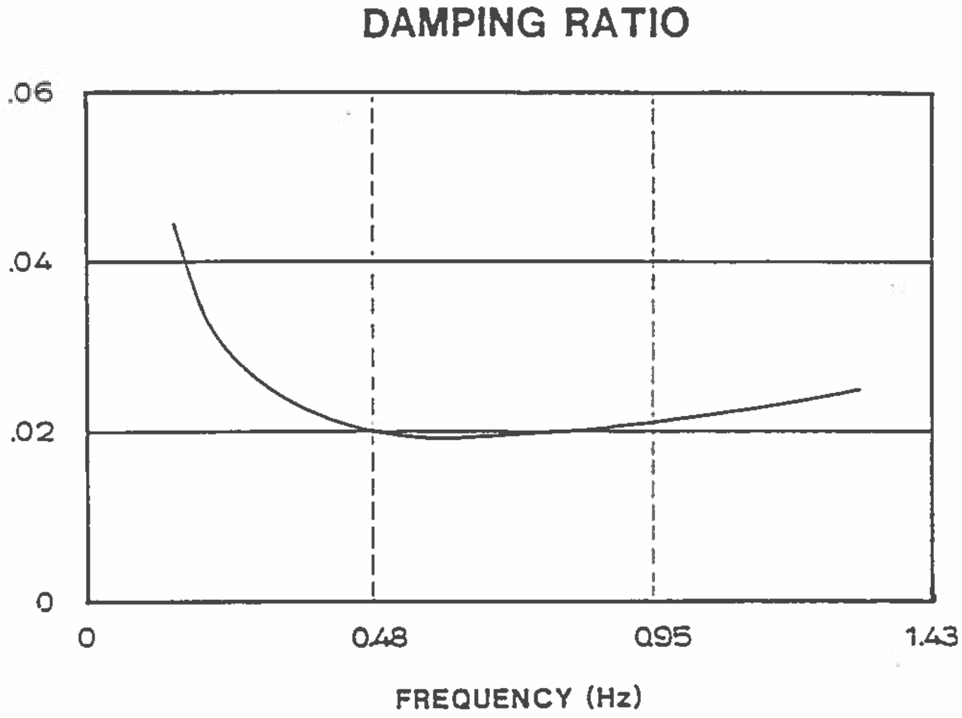

Fig. 3.6 Damping ratio as function of the frequency.

2. In some of the computer runs the soil stiffness was non-linear, which contributes to the damping.

3.3 The Soil/Structure Interaction

The response has been studied for linear as well as non-linear soil stiffness. The initial stiffness values equal for the linear and the non-linear case are calculated by the CCL consultant Friman Clausen.

The non-linear soil stiffness is defined as shown in Fig. 3.7 (see further section 4.3). When the motion reverse the initial soil stiffness is used, so that hysteresis occurs. See Fig. 3.8.

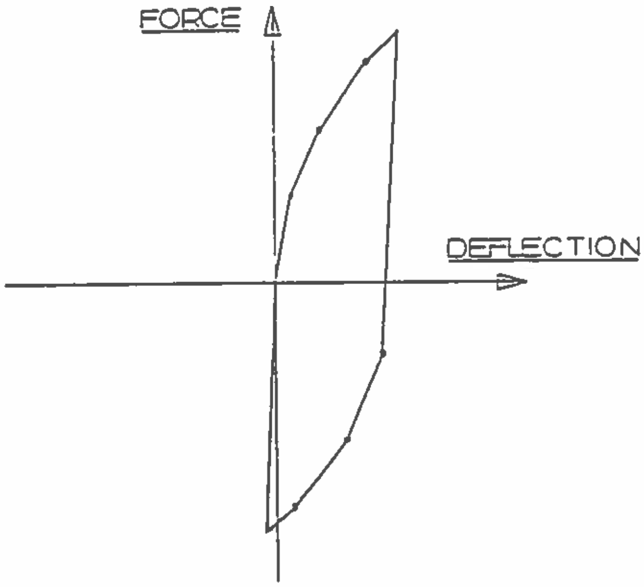

Fig. 3.7 Load deflection curve for non-linear soil.

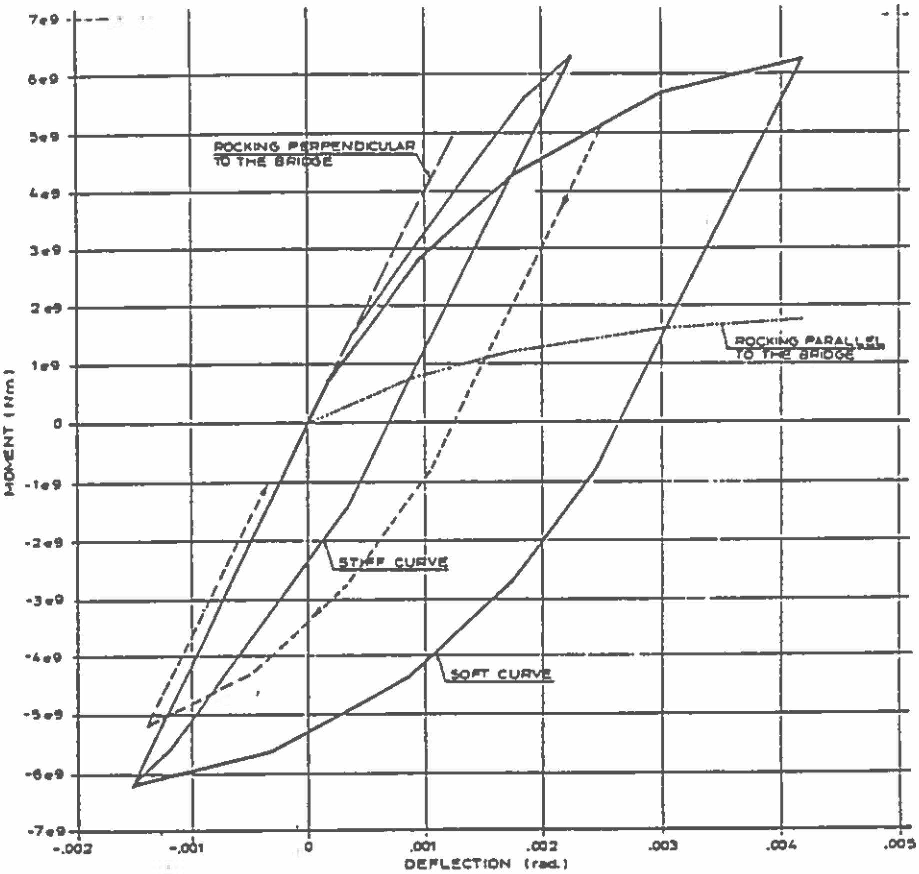

Fig. 3.8 Example of load deflection for bridge foundations with hysteresis.

3.4 Bearings

The bearings between the top of the pier and the bridge girder are modeled by a special link element. In this element the degrees of freedom are not coupled with each other.

These elements have an initial stiffness, but when the frictional forces in the bearings are exceeded the bridge girders can slide with a constant friction force. By use of these elements a realistic non-linear stiffness representation is achieved, but also the damping is represented correctly due to the possibility of hysteresis.

The stiffness of the bearings are presented in Table 3.2.

N/m	k_x N/m	k_y N/m	k_z N/m	k_{xx} Nm/Rad	k_{yy} Nm/Rad	k_{zz} Nm/Rad
Before sliding	$5 \cdot 10^9$	$2 \cdot 10^9$	$5 \cdot 10^9$	$1.4 \cdot 10^{13}$	1	1
After sliding	0	$2 \cdot 10^9$	$5 \cdot 10^9$	$1.4 \cdot 10^{13}$	1	1

Table 3.2 Stiffness for frictional bearing. These stiffnesses are applicable until a force level determined by the frictional coefficient, μ, in the bearings is reached.

The coordinate axes are defined in Fig. 3.9.

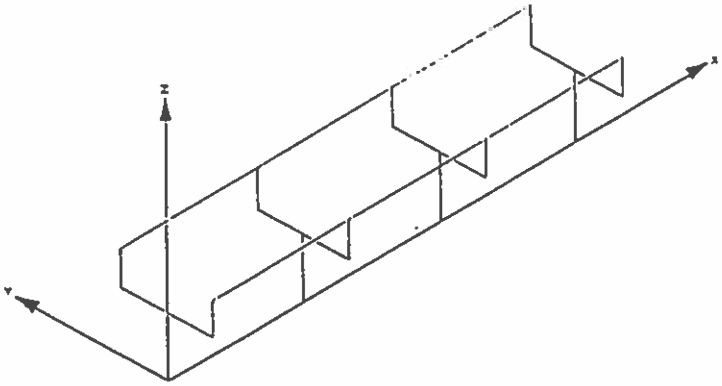

Fig. 3.9 Definition sketch for coordinate axis.

By this choice of stiffnesses the link element can only transfer moment to the bridge girder for bending around the x-axis. The pier is therefore locked to the girder perpendicular to the bridge, and sliding is permitted along the bridge, when the frictional force is exceeded.

3.5 Buffers

The rail girders in each bridge section are connected with the adjacent section by two hydraulic buffers in order to absorb shock forces. In the linear simulations these buffers are modelled as linear springs between a stiff wall and the rail girder. The stiffness of the two springs together is 750 MN/m. In the non-linear structural model the stiffness from the linear model is used as initial stiffness. When the force level exceeds the level of 9 MN, the buffer yields, and the stiffness is set to zero.

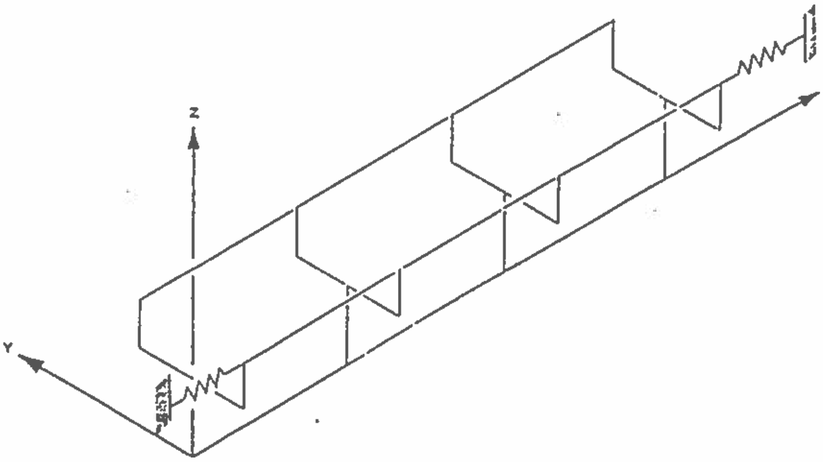

Fig. 3.10 Buffers

4. DYNAMIC EFFECTS OF BOW COLLISION ON PIERS

4.1 Load Assumptions

Based upon an analysis performed by DnV, see Kampmann (1991) the impact load for a direct bow collision has been estimated as shown in table 4.1. For a 2,000 DWT case the force curve is shown in fig. 4.1. For the other cases a suitable curve has been established by modifying the curve for a 2,000 DWT ship. Hence the indicated velocities and masses are approximate values.

BOW COLLISION LOAD ASSUMPTION

DWT	Duration (s)	Max force MN	Distribution	Impact Velocity m/s	Total mass t
1000	0.62	24	see fig 4.1	5.5	1700
1500	0.78	28		7.4	2300
2000	0.78	35		7.0	3167
3000	0.78	70		7.4	5700

Table 4.1 Bow collision load assumptions.

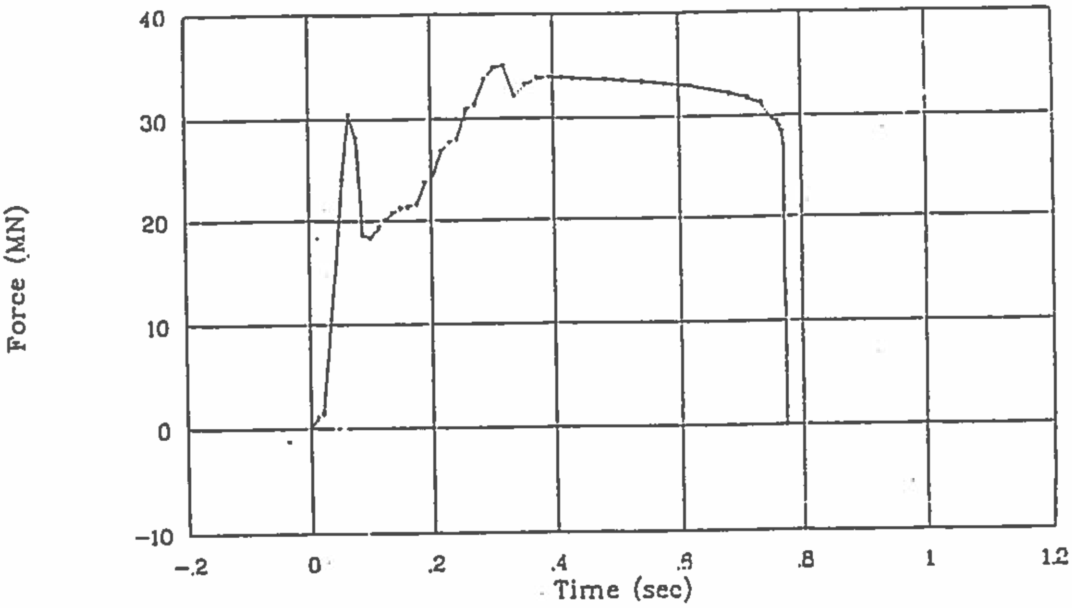

Fig. 4.1 Force time series

In all the following analysis, it is assumed, that the pier deformations are much smaller than the ship deformation. Then the force assumption for the pier may be used without any interaction from the pier deformation. (This is slightly conservative).

For all the dynamic analyses only the case, found most critical in the static analysis, is analyzed. This is 60° incidence angle with eccentricity, as it is assumed, that the bow hits the rear railway pier (fig. 4.2).

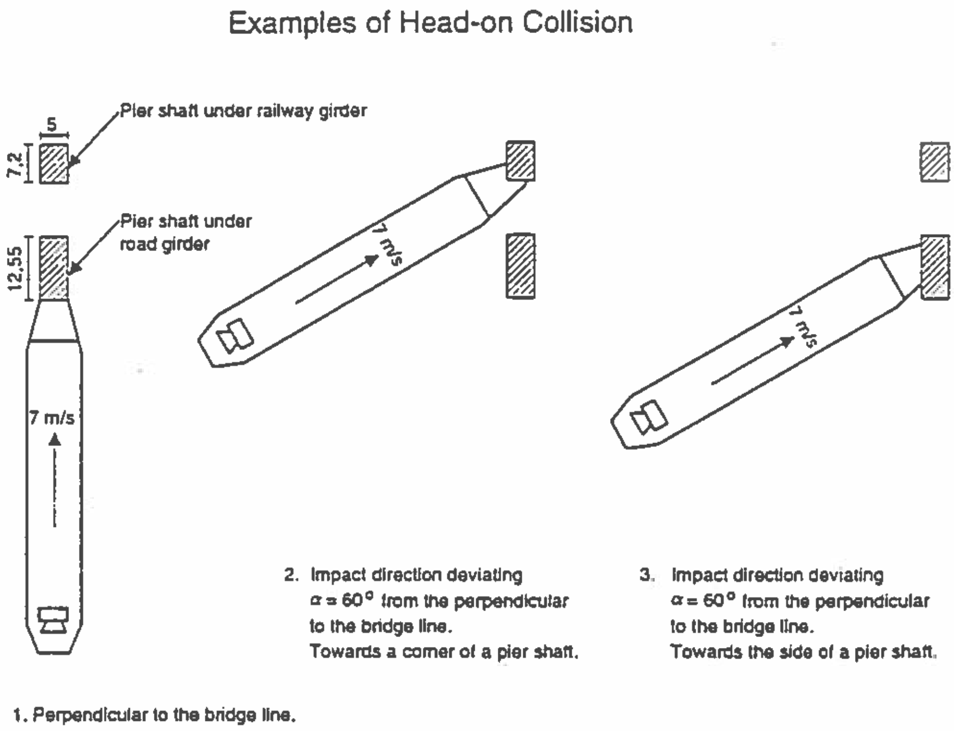

2. Impact direction deviating $\alpha = 60°$ from the perpendicular to the bridge line. Towards a corner of a pier shaft.

3. Impact direction deviating $\alpha = 60°$ from the perpendicular to the bridge line. Towards the side of a pier shaft.

1. Perpendicular to the bridge line.

Fig. 4.2 Schematic view of impact location

4.2 Dynamic effects on a one dimensional elastic system

The dynamic effect of an impact of a force shown in fig. 4.1 on a one dimensional elastic system is illustrated in fig. 4.3.

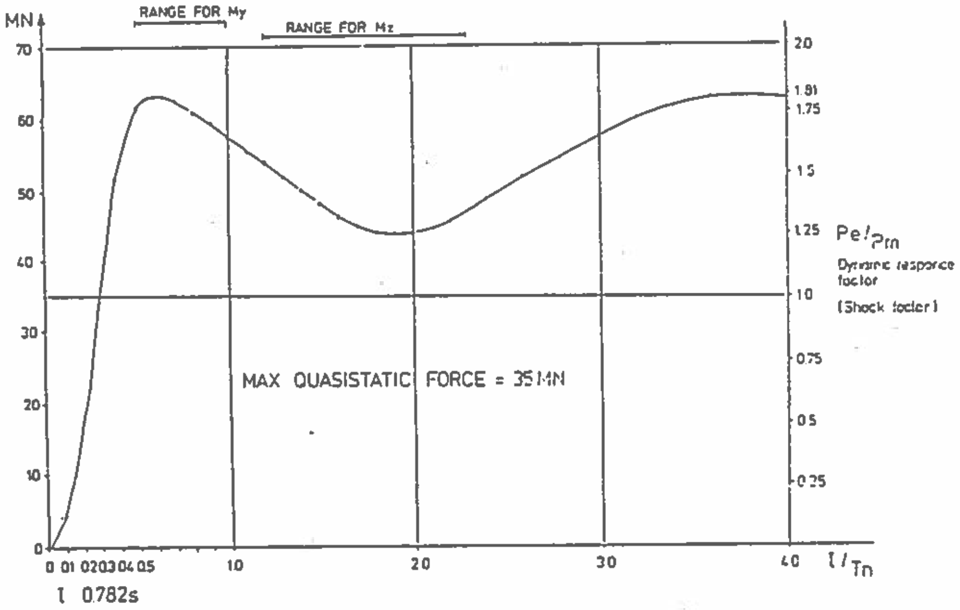

Fig. 4.3 Maximum dynamic response curve for various resonance periods

As shown above, it is clear, that it is critical, what the ratio τ /T_n between the load time τ and the resonance period T_n is.

On figure 4.3 actual ranges for τ /T_n are also shown. The most important force components for the bearing capacity are overturning moments parallel with bridge (M_y) and torsion moment (M_z).

The determined resonance periods T_n are estimated in fig. 4.4 for various foundation depths and soil conditions.

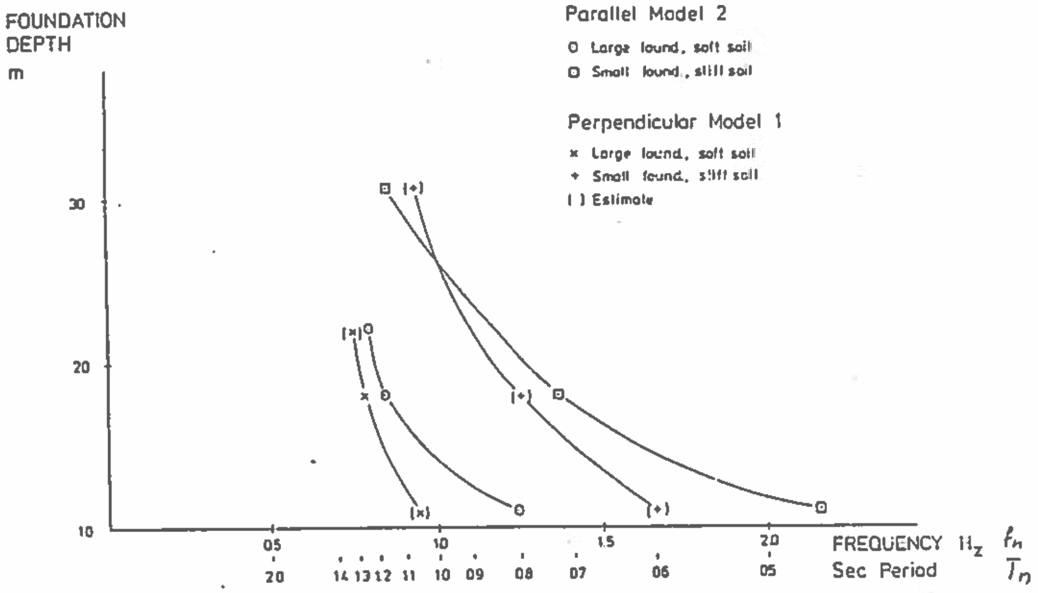

Fig. 4.4 Resonance frequencies for various foundation depths, size of foundation and soil conditions

Figure 4.3 demonstrates, that there is a risk of dynamic amplication factor for M_y of 1.4 to 1.8 and for M_z of 1.2 to 1.8.

This factor may in practice be different, because, interaction and phase difference between more vibration modes may give rise to other values than corresponding to a one dimensional elastic system.

4.3 Results of Dynamic Linear and Non-linear Analysis

A rather complex dynamic model has been implemented (see section 2).

The main assumptions for the analyses are

Linear Model Analysis Assumptions:

- 2 test models with one bridge section consisting of 10 bridge spans:
  Foundation depth 18 m "big" foundation, "weak" soil.

Foundation depth 29 m "small" foundation, "strong" soil.

- Foundation stiffness as determined by Frimann Clausen.
- Impact in elevation +1.5 m, $\alpha = 60°$ (incl. eccentricity).
- Bearings: Friction $\mu = 0.005$ to 0.01 parallel with bridge; stiffness perpendicular to bridge 2 MN/mm for fixed bearings.
- Buffers in end of railway girders at bridge section ends.

As mentioned above, it is clearly, that even the "linear" model is not completely linear, because it includes non-linear bearing elements.

"Non-linear" Model Analysis Assumptions:

- As for "linear" model except for a non-linear soil characteristic for respectively M_y and M_z (fig. 4.5).

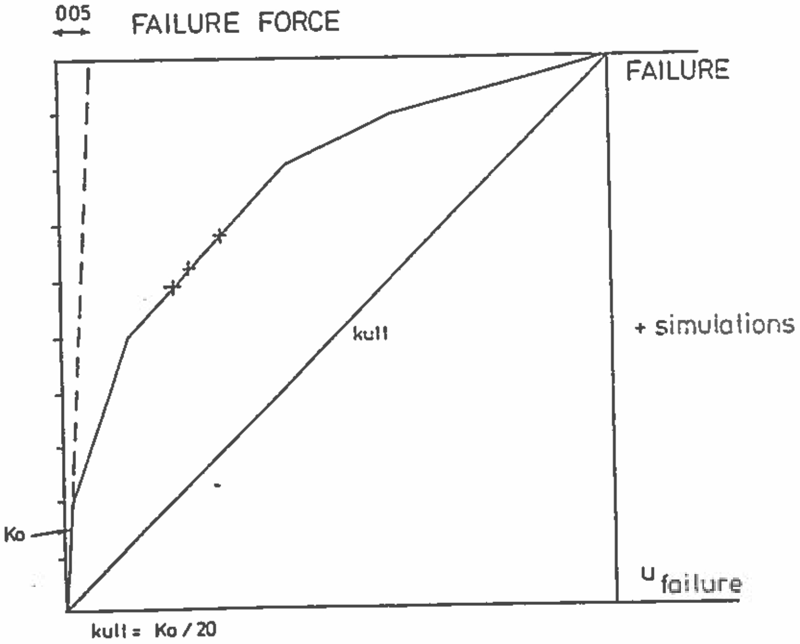

Fig. 4.5 Assumed non-linear soil characteristics.

The initial soil stiffness (K_0) corresponds to the values from the non-linear model. The ultimate rotation is assumed to be approximately 3°.

The matrix of simulating is shown in table 4.2.

	18 m water weak soil big footing	29 m water strong soil small footing	Non-linear bearings	Linear soil	Non-linear soil	Soil stiffness divided by 2	Soil stiffness multiplied by 2
sa1n	x		x	x			
sa2n	x		x	x		x	
sa3n	x		x	x			x
sb1n		x	x	x			
sb2n		x	x	x		x	
sb3n		x	x	x			x
JA1N-MY7	x		x		1 x		
JA1N-MY8	x		x		x		
JA1N-MY9	x		x		x		
JA1N-MYZ	x		x		2 x		
JA1N-MZ3	x		x		3 x		

Notes: 1 Non-linear soil, sliding at M_y = 700 MNm, 800 MNm 900 MNm respectively.
2 Non-linear soil, sliding in yy and zz at M_y = 900 MNm and M_z = 350 MNm.
3 Non-linear soil, sliding at M_z = 350 MN

Table 4.2 Simulations, ship impact collision, various foundation assumptions

Linear Model Results

The main linear model results are listed in table 4.3. The dynamic amplification is calculated relative to a static force of 35 MN, which is the peak value during the ship impact.

The dynamic application for overturning moment (M_y) is typical 1.55 (range 1.42 to 1.59), See fig. 4.6, Fig. 4.7 and Table 4.3.

Maximum elastic deformation of the rail pier top is 280 mm parallel to the bridge and 50 mm perpendicular to the bridge corresponding to a rotation of the foundation of respectively 0.5° and 0.1°. Such deformations are allowable for the substructure.

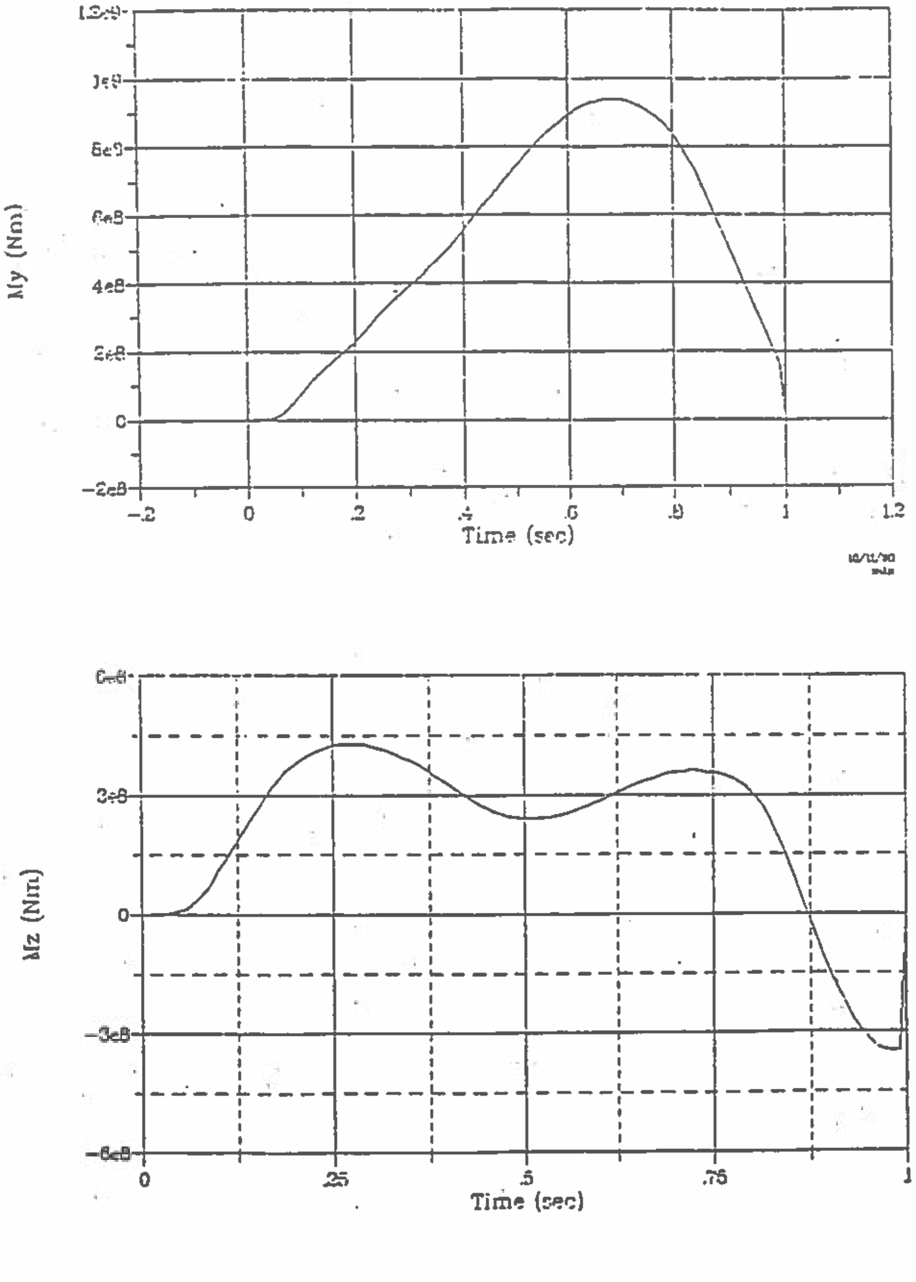

Fig. 4.6 Linear soil, foundation forces during ship impact

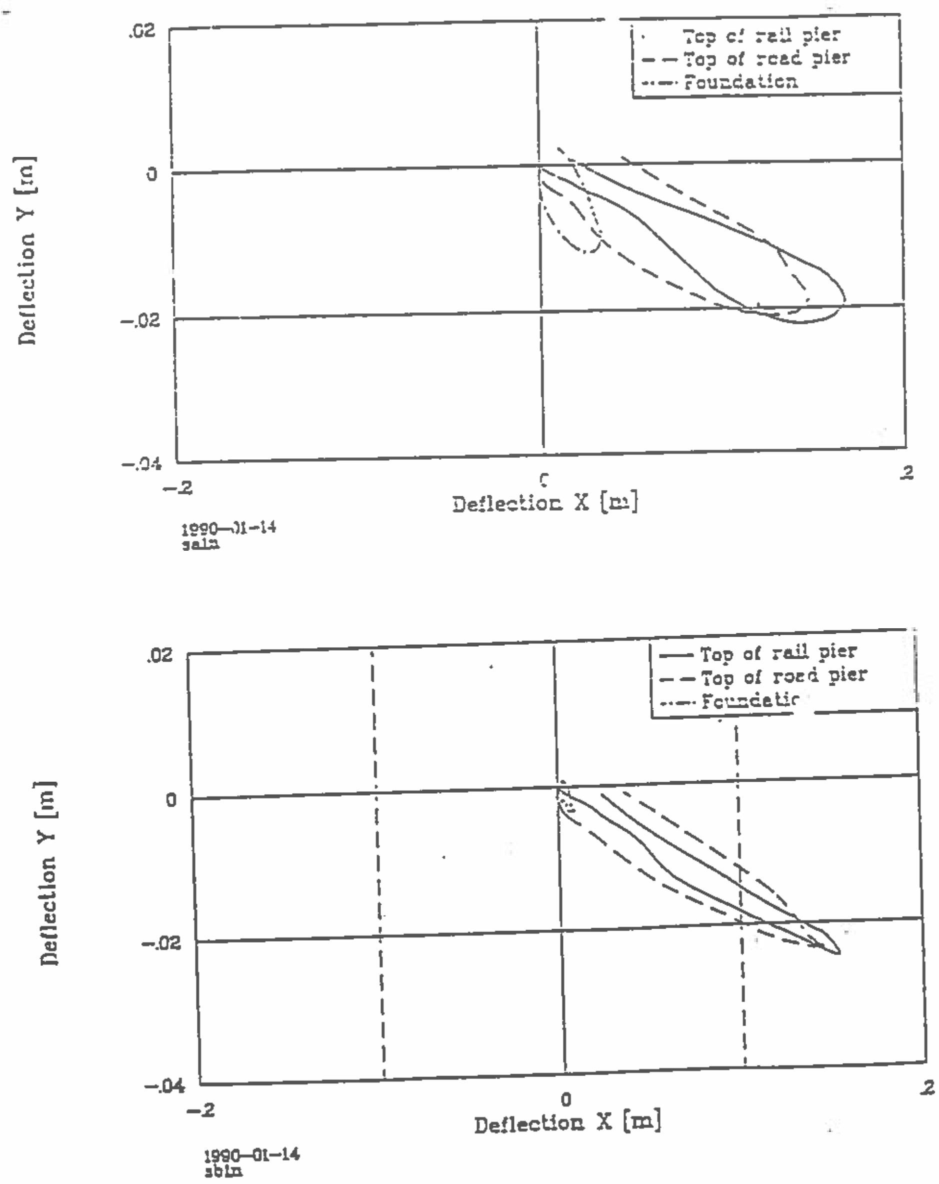

Fig. 4.7 Top of pier shaft deflections, linear soil (2 examples)

	F_x	F_y	M_y	M_y	M_z
Sa1n	1.68	0.97	0.82	1.59	1.25
Sa2n	1.77	1.00	1.03	1.44	1.51
Sa3n	1.58	1.14	1.29	1.52	1.28
Sb1n	1.85	1.11	1.07	1.56	1.34
Sb2n	2.05	1.02	0.96	1.56	1.25
Sb3n	1.85	1.25	1.12	1.52	1.74

Table 4.3 Amplification factor in foundation for an elastic soil (various foundation depths, various soil stiffnesses), see table 4.2.

In this analysis it is interesting to compare the results from an one dimensional impact response with the response of a 3-dimensional (nearly) elastic system.

The one dimensional results obtained for the same resonance frequencies as those of M_y and M_z on fig. 4.6 are shown in fig. 4.8.

The dynamic response has the same order of magnitude, but the response versus time is slightly different. This may be due to interference with higher frequency modes also existing in the 3-dimensional model and possibly also with effect of smaller non-linear elements still included in the "elastic" model.

But it illustrates, that the main physical understanding may be obtained through a simple one dimensional impact analysis.

Concerning the effects on the bearings, reference in made to the discussion in section 4.6.

Remark that the amplification of the forces in the foundation for F_x exceeds the theoretically value determined in section 2, where the upper limit was found to be 1.81.

In the worst case the exceedance is 13% and this may either be caused by the non-linear bearing friction or by interaction between more vibration modes in phase. Considering the shape of the curve for the F_x force the last possibility seems most likely. But it is of major importance, that the amplification factors for the most critical force component M_y in all cases are lower than for the theoretical one.

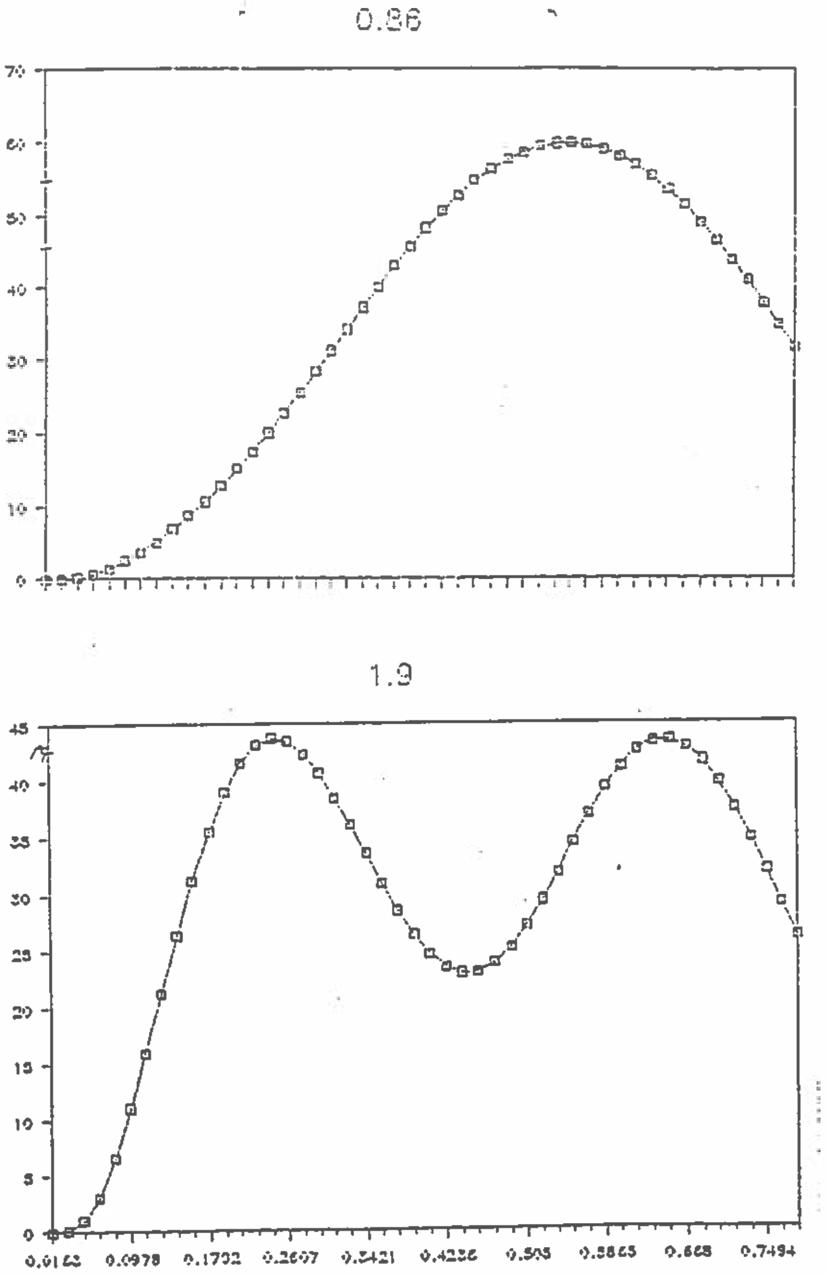

Fig. 4.8 Ship impact - one dimensional analyses.

Non-linear Model Results

The results of simulation with the non-linear model are illustrated on fig. 4.9 and 4.10.

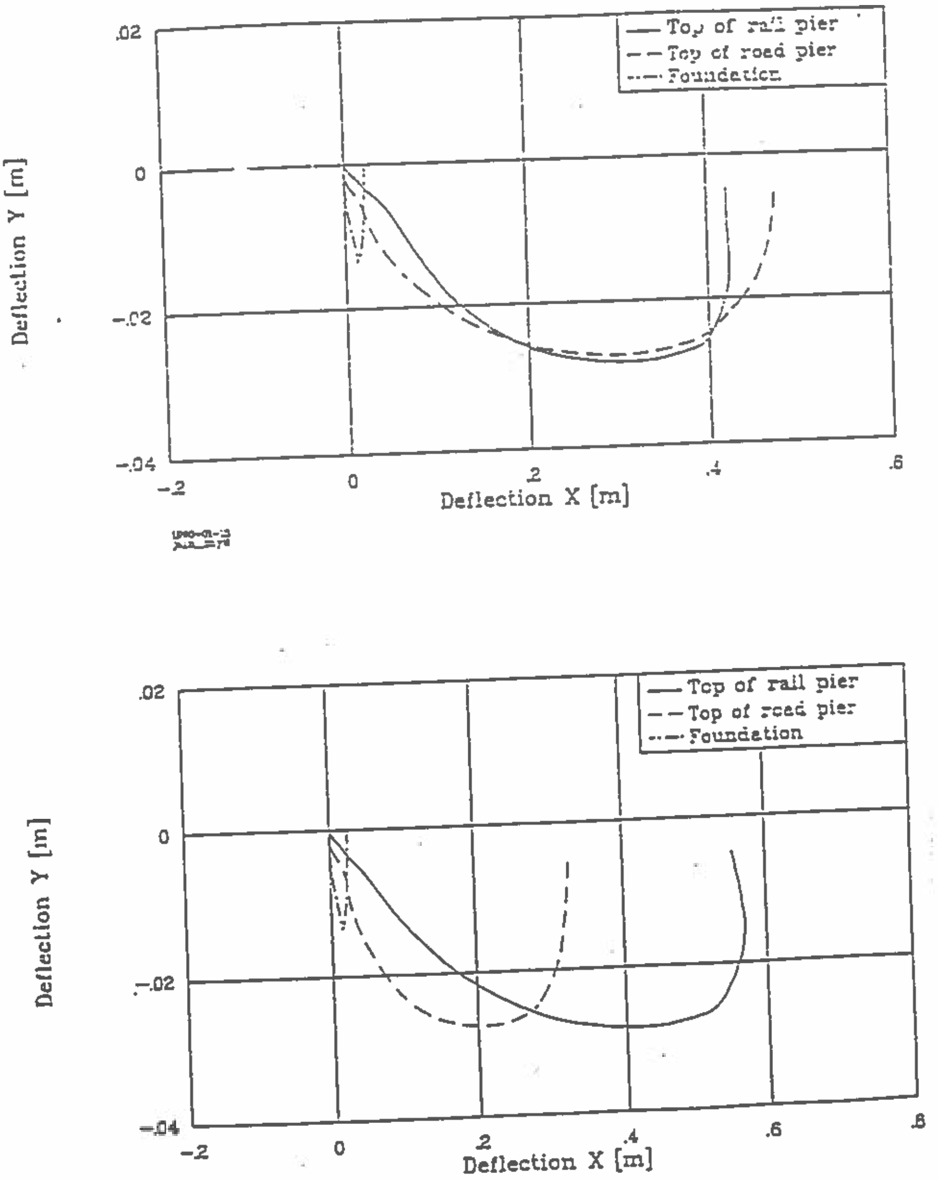

Fig. 4.9 Top of pier shaft deflections, nonlinear soil (2 examples)

Maximum (mainly residual) deformation of the rail pier top is 570 mm parallel to the bridge and 29 mm perpendicular to the bridge.

The top pier shaft deformation are mainly depending on:

- BBD design forces (≥ 40 MN) (governing the general registance of the piers).
- Size of torsional moment (M_z) coinciding with maximum overturning moment (M_y)

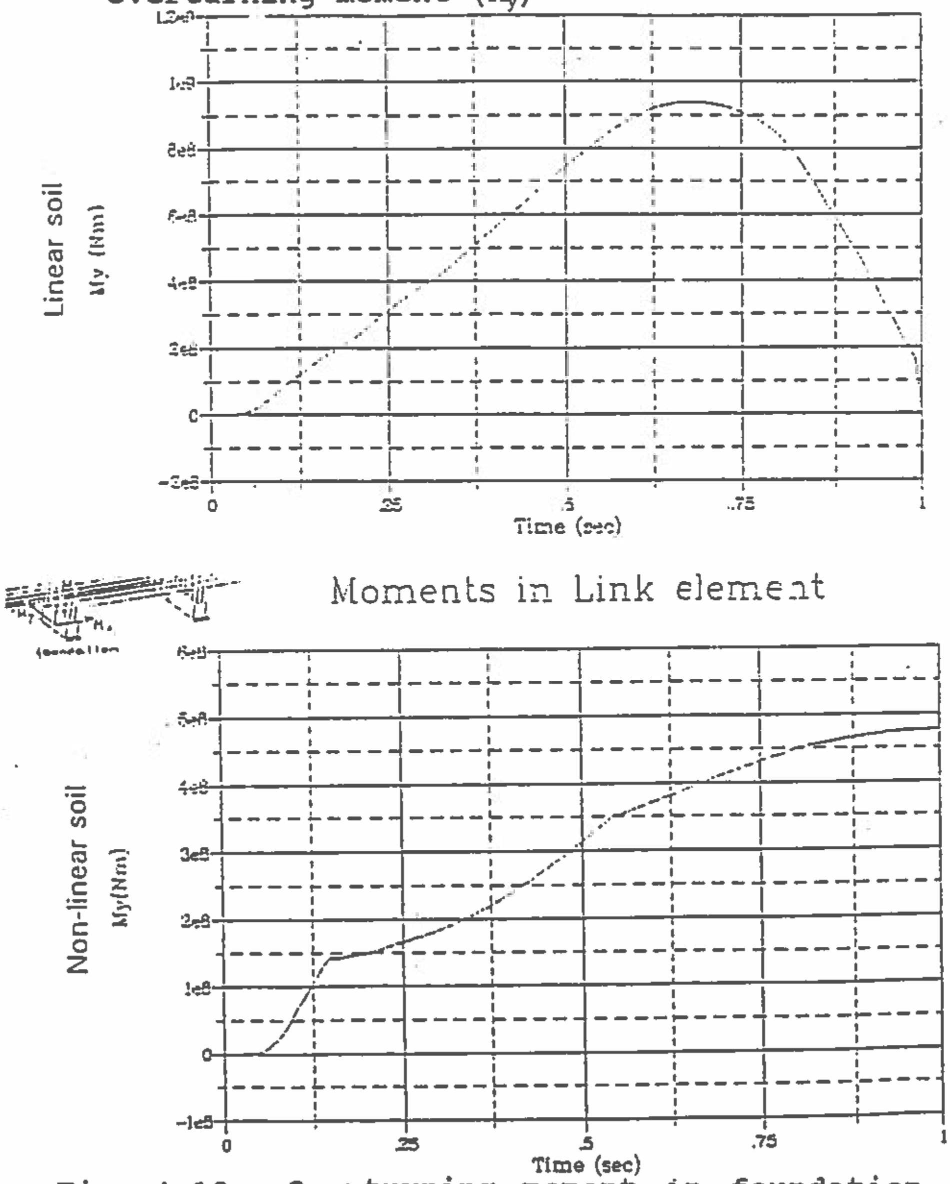

Fig. 4.10 Overturning moment in foundation around an axis perpendicular to the bridge (upper linear analysis, lower non-linear analysis)

Fig. 4.10 shows a comparison between the response in the main parameter, the overturning moment (M_y) parallel with the bridge, for linear and non-linear soil support.

It illustrates that non-linearities in the foundation characteristics stretches the response versus time, and it drastically change the character of the response.

4.4 Discussion of Main Results on Pier Stability During Bow collision

The main result in terms of residual plastic deformations are shown on fig. 4.11.

For other ship sizes than 2,000 DWT the results have been found by rough extrapolations of the results for 2,000 DWT.

It may be concluded, that through this type of analysis a big advantage is obtained due to the description of the order of magnitude of the absolute damage during an accidental load from ship impact.

Such type of analysis may lead to redesign including simple cost-effective means to limit the consequences of an accident, because the results show consequences and not only forces exceeding certain limits.

It may in certain cases be much more important to design the structure to include a high ductility limiting accidental consequences than to determine, when formal design forces are exceeded. In other words ductility is more important than maximum forces, when designing for accidental loads.

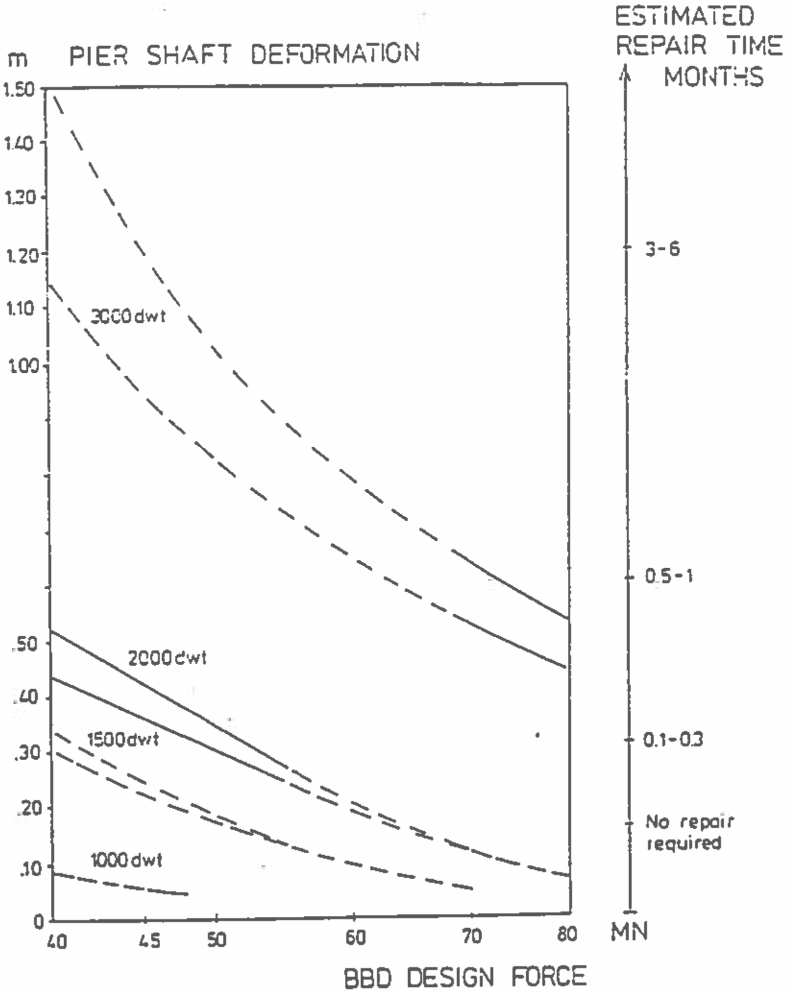

Fig. 4.11 Estimate of residual plastic deformations on top of pier shafts after bow collision

The ship impact analysis include several aspects, where conditions which may only be roughly estimated.

Theoretically an oblique incidence, for example, should result in lower impact forces, than completely normal incidence ($\alpha = 0°$). But there is a high risk, that the ship will be caught by the structure, so no rotation occurs. In that case, the impact force will be rather close to the normal incidence case, maybe with a slightly longer initial force increase. But it is more critical for the structure, because it coincides with a large destabilizing torque.

The deformations for respectively 1000 DWT, 1500 DWT and 3000 DWT vessels have been estimated by extrapolations of the calculated deformation, caused by the 2000 DWT vessel. Thereby they include an increased uncertainty.

The non-linear soil conditions used for the simulations was selected based on quite a rough estimate.

It is for example difficult to estimate, if the stabilizing effect of water suction has a sufficient long duration to be effective, because the piers are installed on gravel.

For gravel it may be possible to drain the stabilizing under pressure away, even within a load duration of 0.8 sec. A certain amount of sand, being placed below or inside the lowest part of the scour protection could result in larger stability for overturning, but it could cause more unfavourable stability conditions for sliding.

But the final cyclic soil investigation carried out on Norwegian Geotechnical Institute (NGI) mainly in connection with dynamic ice loads included the load case actual for ship impact, see NGI (1990). Fig. 4.12 shows a main result from these investigations.

By comparison with the preliminary estimate (fig. 4.5) used during the simulation it is seen, that the preliminary estimate was quite close to actual conditions and only slightly conservative (see fig. 4.12).

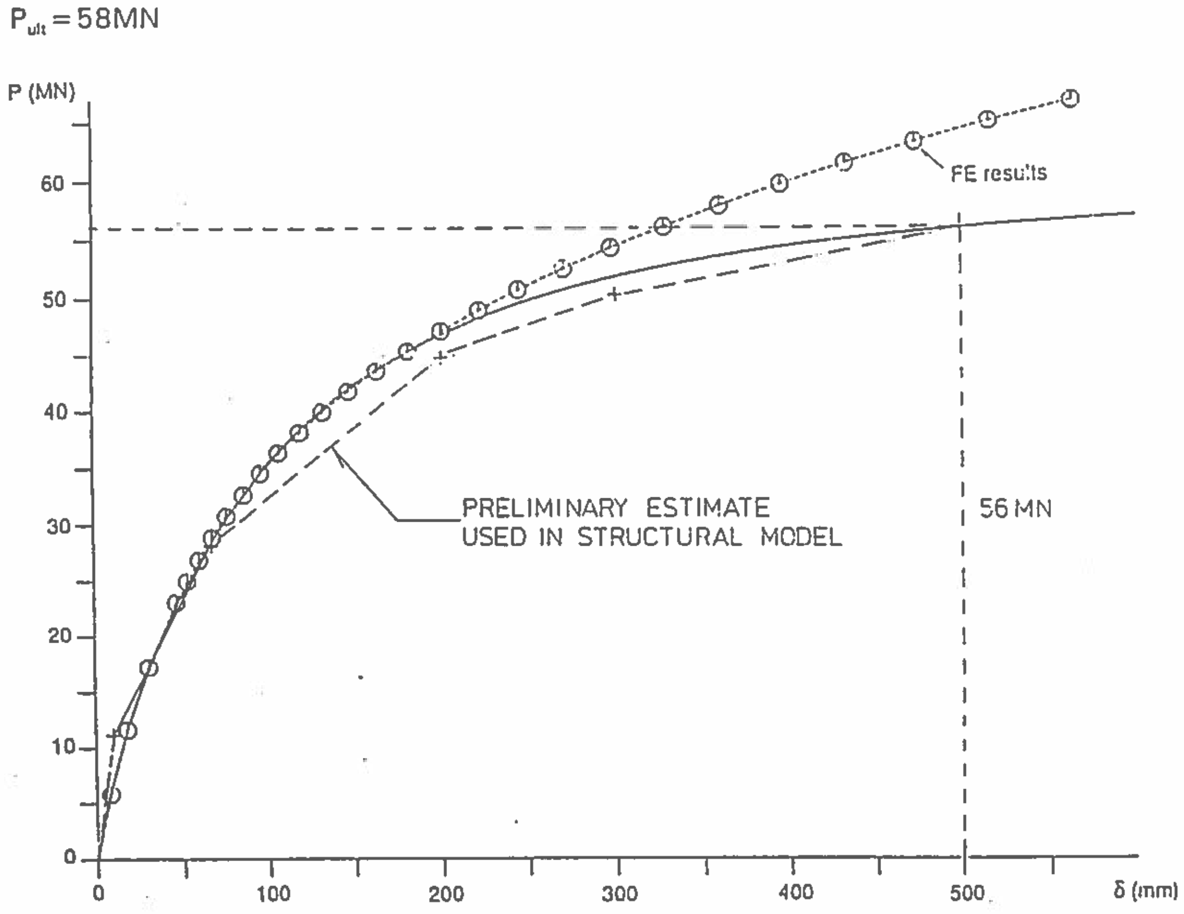

Fig. 4.12 Displacements at bridge deck vs. load

4.5 Sectional Forces in Substructure

The sectional forces have been analyzed by means of dynamic linear and non-linear analyses.

The geometry of the substructure is illustrated in Fig.4.12:

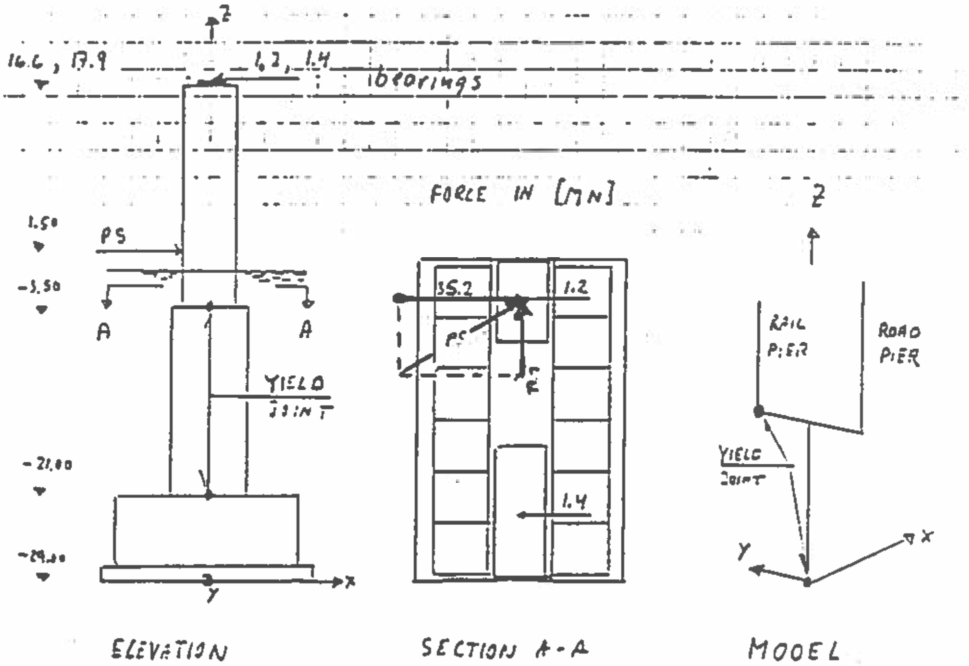

Fig 4.12. Geometry of substructure

From the linear analysis a description of the dynamic amplification to the sectional forces is obtained. Main results are illustrated in Fig. 4.13. Please note how different the dynamic amplification of the various sectional forces are and how they vary with the elevation.

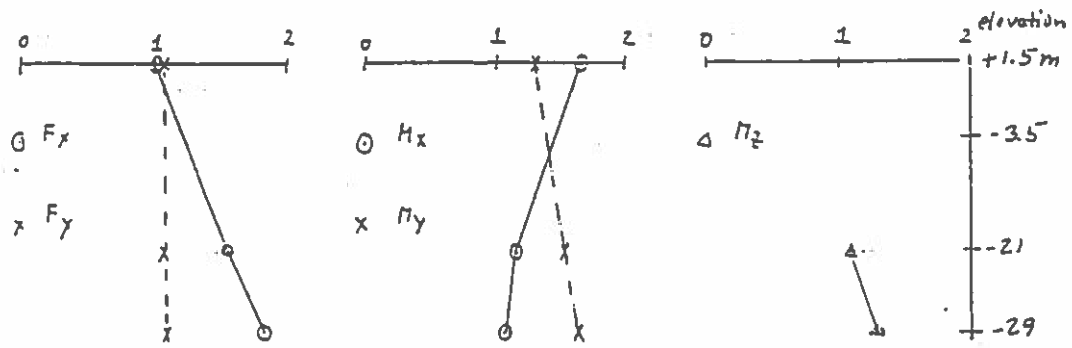

Fig 4.13 Variation of amplification factor on sectional forces with elevation

The non-linear model is used to quantify the amount of plastic deformation internally in the structure due to the bow collision. A conservative yielding assumption is used, which allows yielding only, if one of the sectional forces in the critical sections exceeds the unidirectional yield force/moment.

The maximum determined deformations are 4 x 10^{-7} m and 2 x 10^{-5} rad, respectively e.g. with limit practical importance.

For bow collision no critical forces were experienced in the bearings.

5. SIDEWAYS COLLISION TO PIERS

The piers are also exposed to a risk for sideways collision (see Fig. 5.1)

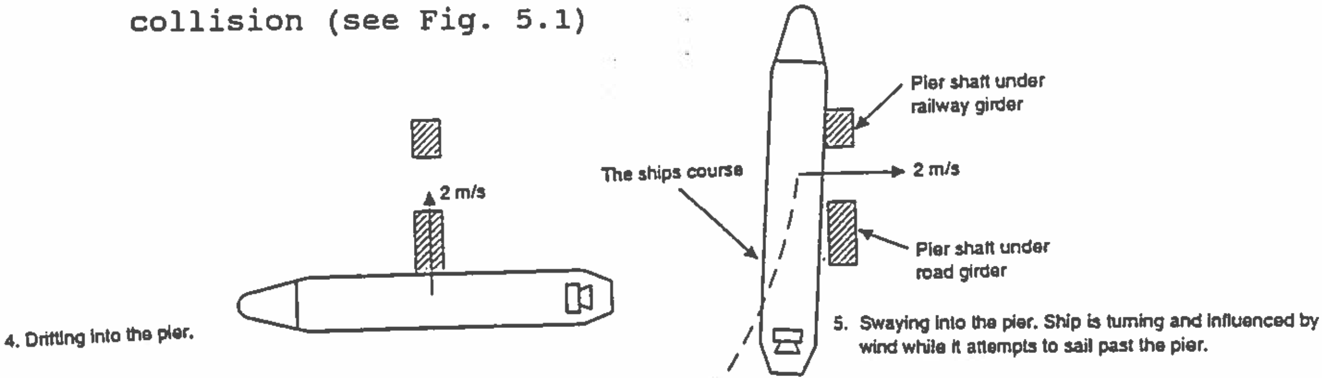

Fig. 5.1 Examples of sideways collision to bridge piers.

This load case include the maximum legal vessel, but as shown in Fig. 5.1 the assumed maximum incident velocity is here 2 m/s.

The maximum force is larger than for bow collision (47 MN for one pier shaft and 80 MN for two being hit), but due to the lower incident velocity the displacements of the pier top showed to be less than for bow collision.

The sectional forces in the complete pier caisson were also determined. Certain plastic deformation may be a result of the collision, because the allowed elastic sectional forces are exceeded. The dynamic amplification of the sectional forces are illustrated in Fig. 5.2, which uses the same geometry as already been defined in Fig. 4.1:

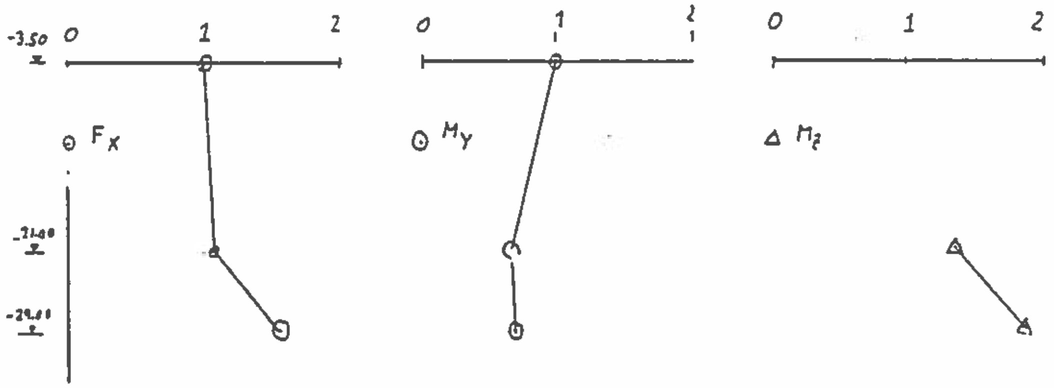

Fig. 5.2 Example of dynamic amplification of sectional forces for sideways collision.

The plastic deformations turned up to be less than for bow collision.

6. IMPACT TO GIRDERS

The load cases considered are illustrated in Fig. 6.1

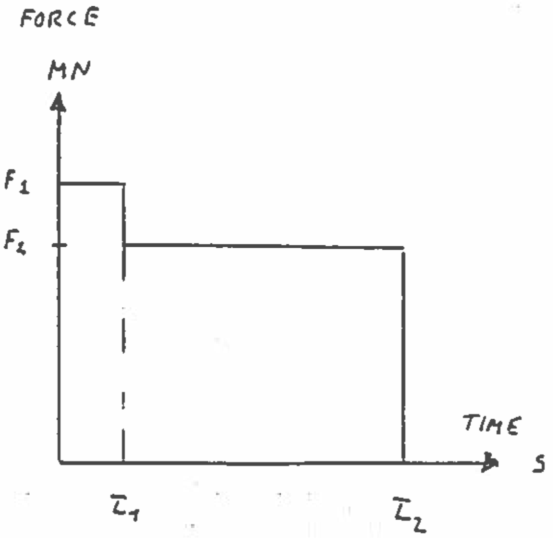

τ_1 s	τ_2 s	F_1 MN	F_2 MN
0.10	2.6	10	8.5
0.083	2.2	12.048	10.045
0.077	1.8	12.967	12.278
0.059	1.5	16.949	14.733

Fig 6.1 Load cases, ship impact to girders

The variation in the load cases represents the various heights of deck houses, which may hit the girders mainly depending upon the elevation of the girders.

The analysis of consequences of impact to the girders showed, that the bearings may be subject to brittle failure.

Impact with a load of 10 MN or more near a pier will cause deformations in the bearings, which are likely to be above the yielding capacity, if the bearings were designed for the 10 MN impact as specified in the original design basis.

The required yielding capacity should for the worst load case considered be up to 80 mm to be sufficient (see Fig. 6.2).

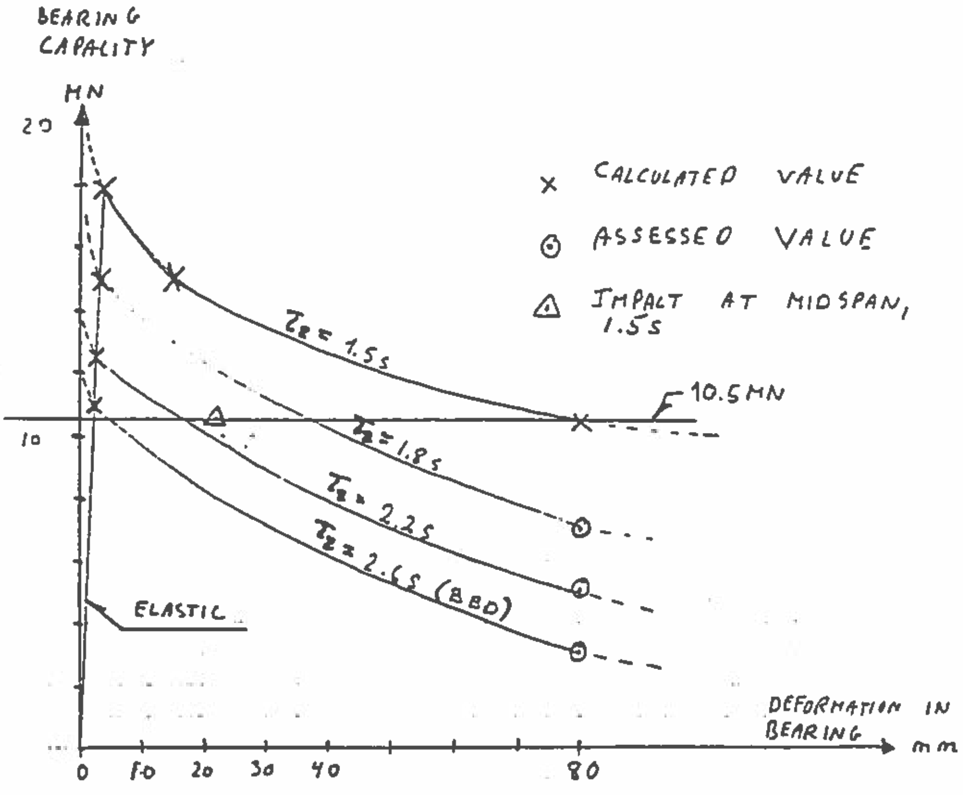

Fig 6.2 Deformations in bearings for ship impact to rail girder

Consequently the design of the bearings was improved. Each of the two bearings of the girder support are now designed for a 10 MN ship collision load. At each support 20 MN static load can be transferred. The bearings are still subject to brittle failure, but failure will not occur for a deck house impact load of 15 MN from a 2000 DWT ship. This load corresponds to a contact height of at least 6 m.

The results of the investigations illustrate the importance of carrying out dynamic simulations. The bearings showed to be a critical weak link, which could result in damage to the integrity of the bridge due to risk of brittle failure. But it is also important to realize, that a valid alternative to strength increase is to include sufficient ductility in the structure. Such considerations need to be included early in the project to allow modifications improving the ductility to be included in the design.

7. ACCELERATION IN RAIL GIRDER INDUCED BY SHIP COLLISIONS

7.1 Load Cases

Impact to Pier

The principal load case (force versus time) is the same as discussed in section 4 (see Table 4.1 and Fig. 4.1), but for this load case it acts perpendicular to the bridge.

Impact to Girders

Impact to girders of the deckhouse of a 2000 DWT has been analyzed by means of the load case giving 18 MN as maximum impact load, see fig. 6.2.

This load case corresponds to impact from 4 decks of the deckhouse, which is very unlikely. The impact load case of the BBD, corresponding to 2 decks, is approximately half the magnitude, but of longer duration. Accordingly the load case considered is conservative.

Two impact cases have been considered

- impact close to pier

- impact in the middle of a span

7.2 Induced Accelerations

Bow Collision to Pier

Instead of carrying out a new analysis the results of the previous analysis, ref. section 4 have been used, because the impact force perpendicular to the bridge in these analysis is equal to exactly half the impact force for a 0° bow collision. (Disregarding other force components from the simulations.

Test Run	Water depth m	Footing (m^2)	Soil stiffness	60°impact acc$_y$(max) m/s^2	0°impact acc$_y$(max) m/s^2
SA1N	18	20 x 40	"soft"	0.82	1.65
SA2N	-	-	"soft" : 2	1.20	2.40
SA3N	-	-	"soft" x 2	0.71	1.42
SB1N	29	20 x 30	"stiff"	0.94	1.80
SB2N	-	-	"stiff" : 2	1.08	2.16
SB3N	-	-	"stiff" x 2	0.85	1.71
				Determined in rail-girder above middle of pier shaft	

Table 7.1 Main results of bow collision to pier.

The maximum accelerations occur for the softest soils, and maximum occurs, when the effect of the impulse is released, and the structure accelerates backwards.

The load assumption is for this load case slightly conservative, because a less abrupt finish of the impact load will occur in practice. The impacting vessel will further take part in the oscillation, but such an additional mass of approximately 3000 t will only have limited reducing effect on the induced accelerations. The release of an impact force super imposed on a "prestressed" elastic system gives rise to larger acceleration than the original impact force see fig. 7.1.

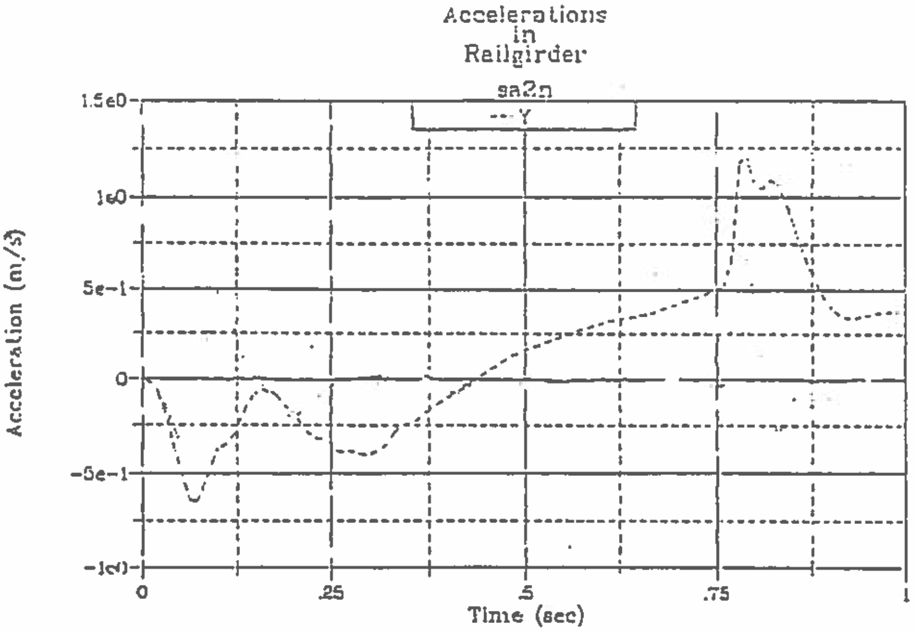

Fig. 7.1 Example on calculated accelerations

Girder Impact Close to Pier

The effect of a girder impact close to the pier, where no breakage occurs in the bearings, is shown in figure 7.2.

The impact results in a high acceleration peak, when the impact occurs, and when it disappears. But it is of larger importance, that these peak load initiate transverse vibration in the rail girder.

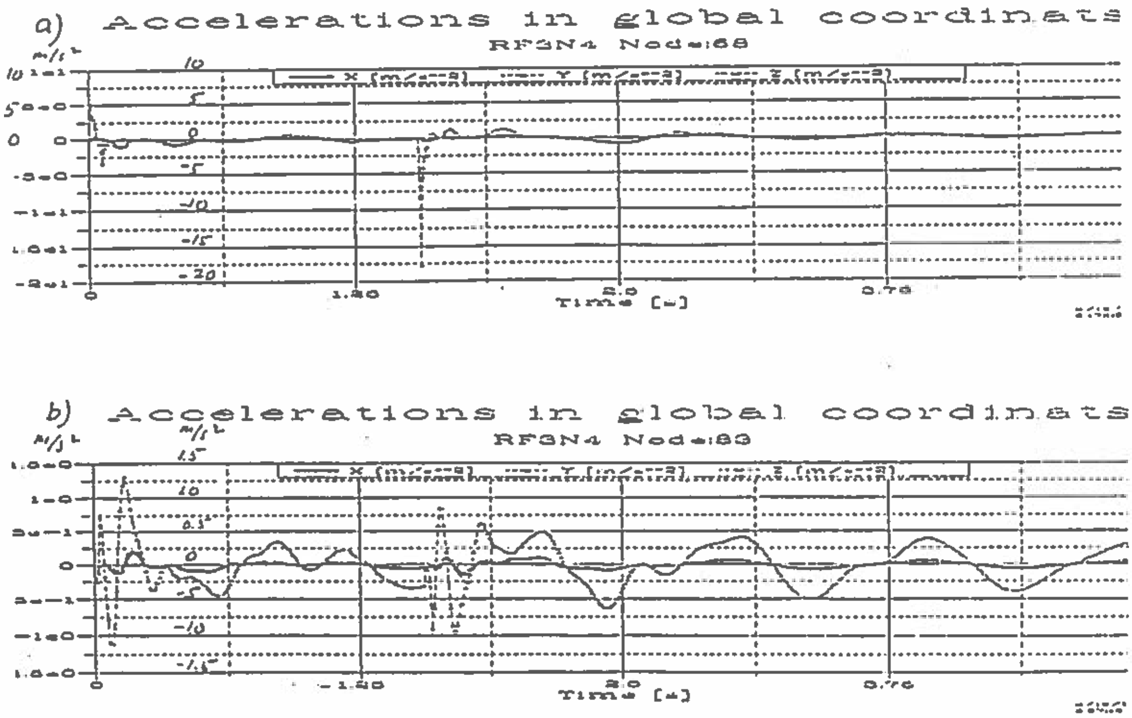

Fig. 7.2 Calculated accelerations, girder impact close to pier
a) Pier with impact
b) Neighbour pier

Girder Impact at Mid Span

The effect of a girder impact close to the middle of a girder, where no breakage occur to the bearings, is shown in fig. 7.3. Remark that in addition to the effect of the impulses significant oscillations occur also in this case. These oscillations have much larger effects on passing trains than the high peak values, because the frequency contents is much closer to the natural frequencies of the passing train.

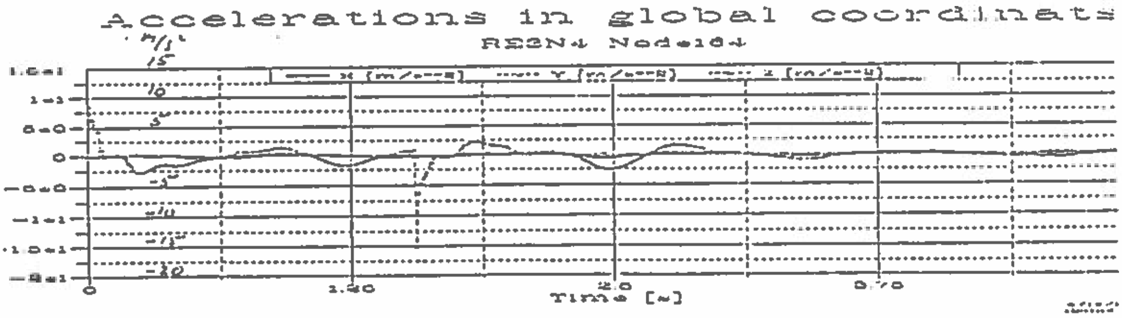

Fig. 7.3 Calculated accelerations, girder impact on mid of girder

7.3 Estimate of Effect on a Passing Train

Actual Period of Oscillations for Trains

The period of oscillation in the simple system is approximized by:

$$T_n = 2\pi \sqrt{\frac{I}{ka^2 n}}$$

in which:

I: Moment of inertia about longitudinal axis (kgm$_2$)
k: Spring coefficient (N/m)
a: Lever arm of torque (m)
n: Number of springs

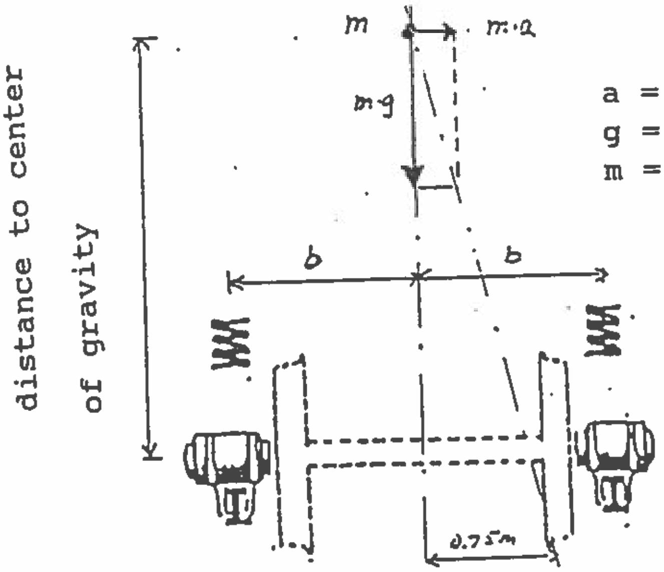

a = acceleration due to impact
g = gravitational acceleration
m = mass of train

Fig. 7.7 Simple train system

I, k and a for all Danish trains are not known accurately. Therefore there was used data from Canadian trains, see Table 7.2, in which the characteristics of two types of trains are shown.

	Mass (kg)	Moment of Inertia (kgm^2)	Spring Koeffi-cient (N/m)	Lever arm* (m)	n**
RDC	55,000	185,000	592,000	1	4
Locomotive	118,000	123,000	2,345,000	1	4

* Assumed value
** Simplified suspension system, one spring in each corner

Table 7.2 Characteristics of Canadian trains.

RDC is a three-unit rail diesel car train. The mass of 55,00 kg is more than the mass of a Danish IC/3 car, which is about 30,000 kg. The mass of the locomotive, 118,000 kg, corresponds closely to a Danish MZ locomotive.

Insertion of the values in table 7.2 in the equation for T_n yields:

RDC : T_n = 1.8 sec.
Locomotive : T_n = 0.7 sec.

From this follows that the actual period of oscillation (resonance periods) may be in the range of say

$0.6 \text{ sec} < T_n < 2.0 \text{ sec}.$

Simplified Method

An analysis of the movements demands a detailed description and simulation of the complete dynamic system involved. Such an analysis was carried out later in the project. Initially a more simple approach was used to evaluate the order of magnitude of the potential consequences for a passing train.

In this approach the movement of the train is equalized with a simple undamped oscillatory system (simple harmonic motion). Knowing the period of oscillation in this system, it is possible to estimate the amplification. The amplification has been for found by a response analysis following the method formulated by d'Alembert.

Effect on Passing Train by Bow Collision

The simplified analysis showed, that the critical condition to the passing train was not the maximum induced acceleration but more, that the impact resulted in transverse oscillations of the girders with frequencies rather close to the overturning resonance frequencies of a passing train.

Because the effect of damping in the train response was not included in the simple analysis no final conclusions could be reached. But the initial results indicated, that the impact could risk to be critical to a passing train. Therefore much more detailed investigations were initiated.

The results of the detailed investigations are described in the report from Talbot and summarized in a technical note from CCL.

It is concluded, that the trains react very violently due to the resonance. The analysis indicates, that neither derailment nor overturning will result. However, the safety margin against derailment and overturning is small, and the maximum accelerations experienced for the passengers may result in passengers being injured. Track shearing and wheel load criteria are seriously exceeded.

Although the analysis includes certain conservatism. The simulated case, which generates the bridge accelerations, corresponds to very conservatively estimated soil stiffnesses. Even though it is recommended to consider to limit the allowable sizes of legal ships to less than 2000 DWT.

A limit of the allowed size of legal ships to less than 1,000 DWT is anyhow planned based on the ship simulations carried out for the navigaton spans. This limit is equal to the present limit for navigation during construction.

It may also to be mentioned, that the simplified method had indicated the girder impact to be the most critical for the passing trains, where the more detailed analysis showed the pier impact to be more critical.

This show, that much awareness is required, when estimating ship impact creating oscillations interacting with resonance frequencies of passing trains.

8. REFERENCES

CCL (1990-92) "Dynamic Effect of Bow Collision"
"Dynamic Effects of Sideways Collision to Piers"
"Dynamic Effects of Impact to Girders"
"Acceleration in Rail Girder Induced by Ship Collision"
"Consequences to Trains of Accelerations of Bridge Girders caused by Ship Impact"
Technical Notes to A/S Storebæltsforbindelsen

Cherchas, D.B. et al., 1892, "Prediction of the Probability of Rail Vehicle Derailment During Grade Crossing Collision", J. of Dynamic Systems, Measurement and Control, June 1982, Vol. 104.

DHI/LIC (1990) Ship Impact, West Bridge, June 1990. Report to A/S Storebæltsforbindelsen.

DSB (1987), "Sporregler", 1987.01.01.

Kampmann, J. (1991): Risk of Ship Impact and Selected design events for ship impact to West Bridge, Present Seminar.

NGI (1990) "Bearing Capacity, Displacement at Backbow Carves under First Load Cycle" Technical Report, A/S Storebæltsforbindelsen.

Talbot (1992) Verhalten des Diesel-Triebzuges IC3 der DSB auf der Storebelt-Westbrucke bei Schiffskollisionen mit einem Bruckenpfeiler und einem Bruckentrager, report to CCL.

Geotechnical Design og Denmark's Great Belt West Bridge for dynamic loading

F. Thunbo Christensen (DHI), H. Gravesen (Dansk Geoteknik a/s, Carl Bro Group), P.S. Kristensen (COWIconsult) and J.R. Thomsen (LicEngineering)

Geotechnical design of Denmark's Great Belt West Bridge for dynamic loading

F. T. Christensen Danish Hydraulic Institute, DK-2970 Hørsholm, Denmark

H. Gravesen Dansk Geoteknik A/S (Carl Bro Group), DK-2600 Glostrup, Denmark

P. S. Kristensen COWIconsult A/S, DK-2830 Virum, Denmark

J. R. Thomsen LICengineering A/S, DK-2900 Hellerup, Denmark

Abstract

The design of the West Bridge across the Western Channel of the Great Belt in Denmark was governed by sea ice loads, wave loads and ship collision loads, all of which are dynamically fluctuating loads. The bridge layout was based on direct caisson foundation without pilings in water depths mostly around 23-27 metres. The resulting bridge design was sensitive to dynamic load fluctuations exciting a rocking mode vibration with the axis of rotation being horizontal and located beneath the base plate of the caisson. Eccentricity of loads furthermore caused unusually large torsional loads to be designed for. Cyclic soil tests were carried out to investigate soil behaviour at typical ice load frequencies, which are roughly an order of magnitude higher than those incurred from storm waves.

Key words: Foundation, geotechnical design, dynamic load, bridge pier, cyclic soil test, ice load, Great Belt.

1. Introduction

The inner Danish waters connect the North Sea and the Baltic Sea through three passages, The Little Belt, The Great Belt and The Sound. A bridge was erected across the Little Belt in 1933 and a second one added in 1968. The Great Belt is 18 km wide, and a bridge and tunnel system is currently under construction, after decades of debates. The Great Belt divides Denmark's population largely in halves. A similar crossing has been decided on for the Sound between Copenhagen in Denmark and Malmö in Sweden.

The Great Belt link consists of four main elements, viz.: a combined railway and road bridge across the western channel between Fyn and the tiny island of "Sprogø" at the centre of the Great Belt, an extensive dredging and land reclamation project increasing Sprogø to three times its original size, a railway tunnel beneath the eastern channel between Sprogø and Sjælland, and finally a suspension bridge for road traffic across the eastern channel, which is also the main shipping channel. The overall layout of the crossing is shown in Figure 1.

Invited keynote address
4th Canadian Marine Geotechnical Conference
St.John's, Newfoundland
Canada, 27-30 June 1993

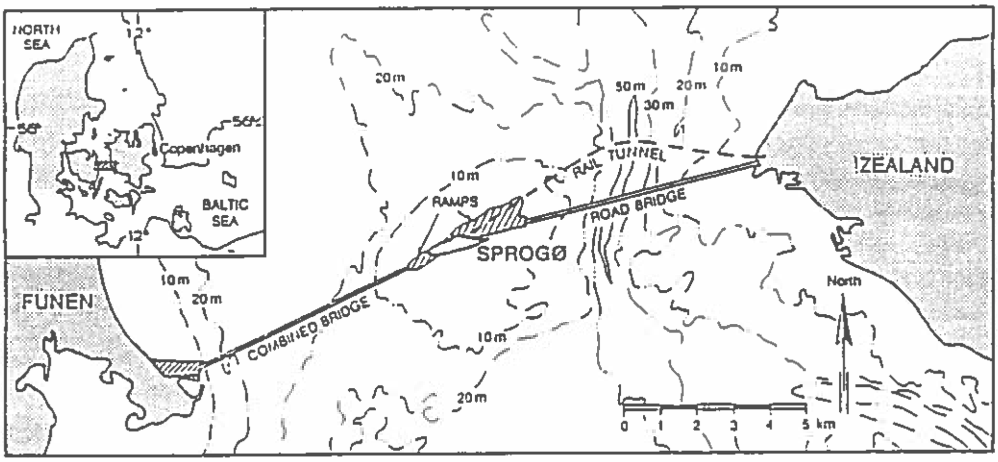

Figure 1. Overall layout of the crossing of Denmark's Great Belt.

This presentation concerns the West Bridge, which is a 6.6 km long low clearance (18 metres) concrete structure with a 110 meter span length. Two parallel box girders are supported on separate pier shafts, which share a common substructure in the form of a directly founded gravity caisson. There are 62 piers in total, placed in water depths ranging from 11 to 29 metres, with most of the piers in 23-27 metres of water. The caissons consist of a base plate in the size range of 17.5 by 29.5 metres (minimum) to 22.5 by 34.0 metres (maximum) depending on location. The bottom part is 6-9 meter high. On top of this is a plinth reaching up to 3.5 metres below sea level. The plinth supports two shafts reaching up to 18 metres above sea level. The largest caisson weighs around 7300 metric tonnes and the larger girders around 5700 tonnes. Soft sea bed material is removed, and a levelled stone bed of 1.5-4 metres thickness is placed at each pier site. After setting the caissons with a purpose-built catamaran crane vessel, they are filled with sand, and the support shafts are placed on top. Finally, girders are brought in by the crane. After the midspan joints are cast and continuity is established, the girders are adjusted and permanent bearings connected.

The piers must be designed to withstand environmental loads caused by wind, current, waves, ice pressure, settlement action, scouring and temperature changes as well as loads from human activities such as braking of traffic, ship collisions, fires and explosions. Most of the environmental loads are designed for in the ultimate limit state with design probabilities of exceedance of 10^{-2} per year, corresponding to an average recurrence time of 100 years, and associated partial coefficients ("safety factors") on loads and strength parameters. The ice pressure, however, was designed for in the accidental limit state (ALS) with a design probability of exceedance of less than 10^{-4} per year, but without partial coefficients. The reasoning behind using ALS was discussed by Christensen et al. (1991). Loads from level ice and from ship collisions are dynamically fluctuating loads. This presentation deals only with the dynamic loads from level ice.

2. Design Philosophy

High levels of safety are integral to the design and operation of the Great Belt Link, see e.g. Vincentsen and Spangenberg (1990). Risk acceptance criteria address two kinds of risk:

- Service disruptions
- User accidents

Separate sets of criteria have been established for each kind of risk. The main criteria are those pertaining to service disruption, and they have been stipulated by the Danish Parliament. User accident criteria relating to standard highway and railway risk levels have been defined by the Great Belt Link Organization. Only disruption criteria are described here.

The approved risk acceptance criteria for disruption address disruptions of traffic lasting more than a month. Three criteria shall be met:

- A criterion for simultaneous disruptions of both road and rail traffic referred to as "common mode" disruption.
- A criterion for road traffic disruption which includes the events affecting road failures only and the common mode failures.
- A criterion for rail traffic disruption which includes the events affecting rail failures only and the common mode failures.

The three criteria are independent of each other, and the risk levels associated with each are shown in Table 1 for the West Bridge. User risks are shown in Table 2. The individual modes in Table 1 include the common mode failure in each case. If the probability of disruption of both road and rail traffic, for more than a month, i.e. common mode, is equal to the approved risk acceptance criterion, 0.02 per 100 years, then the maximum allowed probability of disruption for more than a month of the road only is 0.08 per 100 years (0.1 - 0.02). The same applies for disruption of the rail only.

The risks pertaining to the entire link have to be distributed between the various elements. Only common mode failure is considered, since the road and railway are part of the same bridge in the Western Channel. Of the $2.0\mathrm{x}10^{-4}$ per year risk for common mode failure for the entire link, $1.8\mathrm{x}10^{-4}$ per year is allocated to the West Bridge, cf. Table 1. Common mode failure is considered very unlikely in the Eastern Channel, where road and rail are separated.

Ice loads that threat the piers are relevant to the common mode failure with an exceedance probability of $1.8\mathrm{x}10^{-4}$ per year. This risk has to be shared between ship collisions, dynamic ice loading and other accidental actions. This resulted in the following preliminary risk budget for the West Bridge (tender design):

Risk budget for West Bridge:

• Ship collisions:	1.0×10^{-4} per year
• Dynamic ice loads	0.2×10^{-4} per year
• Scour beneath piers:	0.1×10^{-4} per year
• Other acc. actions and contingency:	$0,5 \times 10^{-4}$ per year
• *Total disruption risk:*	*1.8×10^{-4} per year*

During the process of detailed design, changes in the risk budget have been made in order to optimize the design. The stated budget is therefore not the final risk budget for the West Bridge.

Consequence	Length of Disruption	Criterion Probability/ - 100 Years
APPROVED CRITERIA Service Disruption	> 1 Month	
Common Mode		0.018
- due to ship impact		0.01
Road		0.04*
Rail		0.04*
GUIDANCE Temporary Outage	2 - 30 days	
Common Mode		0.18
Road		0.4*
Rail		0.4*

Table 1. Approved criteria for service disruption and guidance for temporary outage of the West Bridge. The individual failure modes include the common mode failure in each case.

Consequence Class	Criterion
1 - 19 fatalities	$8 \cdot 10^{-3}$ per year
20 - 200 fatalities	$1 \cdot 10^{-5}$ per year
> 200 fatalities	$1 \cdot 10^{-6}$ per year
Individual risk: Road:	$9 \cdot 10^{-3}$ fatality/year
Rail:	$4 \cdot 10^{-3}$ fatality/year

Table 2. User risk acceptance criteria for the West Bridge. Additional risk.

3. Geology and geotechnical properties

Various site investigations have been carried out since the early 1960'ies with various crossing layouts. Numerous boreholes and vibrocores have been completed and supplemented with extensive seismic surveys. When the decision to construct the link was taken, the final layout became known, and detailed site investigations could thus proceed.

The occurrence of principal subsoil formations is shown in Figure 2. Danien limestone constitutes the base to any depth important to foundation design. Selandien, or upper palaeocene, deposits include calcarenite, calsiciltite and in several places also marl on top of the Danien deposits. Biostratigraphic investigations indicate that tectonic block-faulted movements have taken place after formation of the marl. Most of the upthrow blocks have been eroded, but areas of the profile in Figure 2 where Selandien sediments are missing represent such blocks. An example is the limestone ridge in the left part of the profile.

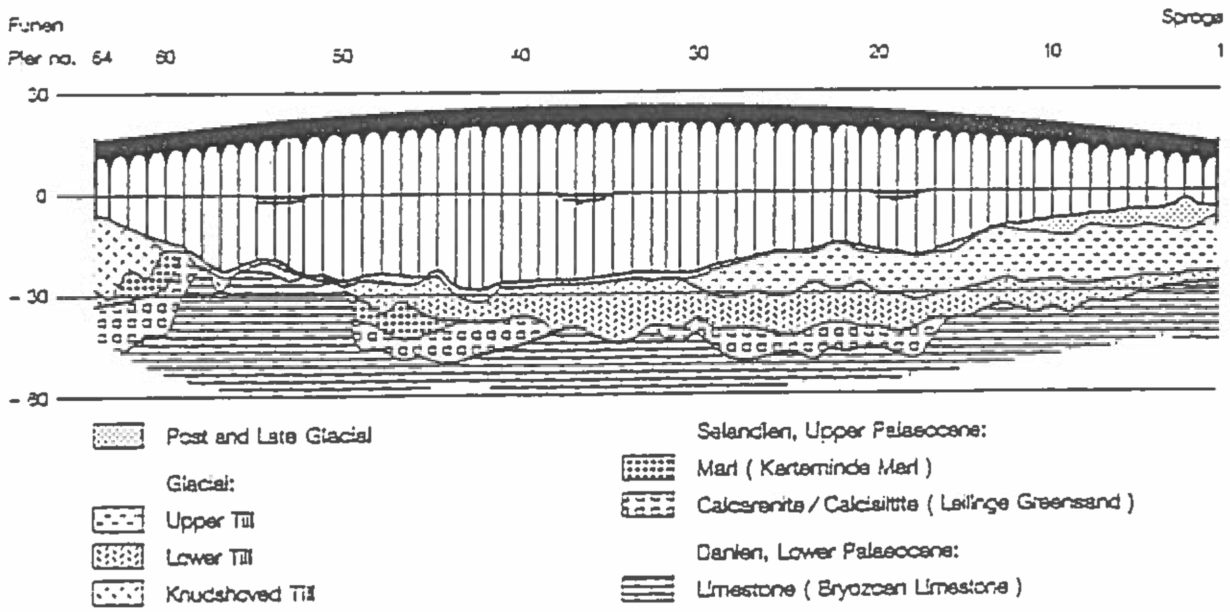

Figure 2. Soil profile at the bridge site.

The glacial deposits may be divided into three units:

- Knudshoved till,
- Lower till, and
- Upper till.

The former, which is an extremely hard clay and sand till, is found exclusively at the western part of the bridge. It has a high plasticity index of 10-20%, a natural water content of 12-30%, also high, and a $CaCO_3$ content above 30%. The lower till unit is comprised of alternating layers of clay till, sand till and melt water sand, while the upper till unit is predominantly a clay till. Both have plasticity indexes in the range 4-8%, liquid limits around 16% and natural water contents varying between 9% and 15%. The lower till has $CaCO_3$ contents above 30% and the upper till has less than 25% $CaCO_3$.

The upper till has a significantly decreasing undrained shear strength with depth, typically starting in the range 200-250 kN/m^2 and decreasing to 100-150 kN/m^2 near the bottom of the unit. The lower till generally has an undrained shear strength in the range 200-300 kN/m^2.

Late and post glacial sediments, mostly of less than 2 metres thickness, overlay the glacial deposits. They consist mostly of sandy marine sediments. In some areas thick deposits of freshwater gyttja are found, notably near the eastern end of the bridge. Owing to the limited water depth in this area, these sediments were removed to provide access for the marine construction equipment, and thus did not influence the design. Porsvig et al. (1989) has described the 3D information system containing all the relevant geotechnical data.

3.1 Detailed site investigations of soils

In the detailed site investigations program, two boreholes to 20-40 metres below sea bed and 8

Cone Penetration Tests (CPT) were carried out at each of the 62 pier locations, and a few additional of both in areas of highly varying conditions. Vane tests were conducted in cohesive materials and Standard Penetration Tests (SPT) in sand and gravel. Both disturbed and intact samples were taken, the latter as thin walled tubes, where advancing was performed by bailing. Some cores were taken as well, and Menard Pressuremeter Tests (MPT) were performed to assess properties of dubious limestone of the mentioned ridge in the western part of the profile. Most CPT's reached refusal at only a few metres beneath the sea bed, but at the eastern end of the profile refusal depths up to 20 metres were encountered. This corresponded to full penetration of the upper till unit. Mortensen et al. (1991) established a relation between the vane shear strength, c_v, and the cone resistance, q_c, for clay till of the upper till unit:

$$c_v = 0.10\ q_c \tag{1}$$

This relation was based on uncorrected in-situ data.

3.2 Laboratory investigations of soils

Laboratory tests were conducted to assess strength and deformation properties of the weaker parts of the limestone and of the clay till of the upper till unit. The preconsolidation stress, σ'_{pc}, proved almost impossible to estimate from traditional oedometer tests owing to the low plasticity and the heterogeneous nature of the soils. Triaxial tests were consequently used to verify the assessments.

The specimen was loaded in a triaxial cell to the σ'_{pc} determined in the oedometer tests, unloaded to the in-situ stress, and subjected to a triaxial compression test. The preconsolidation stress was then reassessed using the critical state method.

It was confirmed that the vane shear strength, c_v, and the undrained shear strength, c_u, were identical for the clay till:

$$c_v = c_u \tag{2}$$

Multistage tests further confirmed Mayne's (1988) SHANSEP relation between undrained shear strength, c_u, in-situ vertical stress, σ'_0 and preconsolidation stress, σ'_{pc}:

$$c_u = 0.4\ \sigma'_0\ (\sigma'_{pc}/\sigma'_0)^{0.85} \tag{3}$$

The undrained shear strength and the preconsolidation stress in the field were then assessed from equations (1), (2) and (3), cf. Foged and Steenfelt (1992) and Steenfelt and Foged (1992).

The oedometer tests showed that the initial tangential modulus of compressibility, K_t, for the preconsolidated soils could be expressed as:

$$K_t = K_{t,0} + \Delta K_t\ \sigma'_{red} \tag{4}$$

where $K_{t,0}$ and ΔK_t are constants, and σ'_{red} is the minimum vertical stress corresponding to unloading.

Because of the ice loads being dynamically fluctuating loads, a few triaxial tests were conducted to failure at very high relative strain rates. The results confirmed a substantial increase of the undrained shear strength with strain rate. Large scale sliding tests were also conducted, but because the governing mode of pier response to the ice loads is a rocking mode these sliding tests are not detailed in this presentation.

3.3 Dynamic soil tests

A comprehensive test program was initiated to determine the soil parameters to be used in combination with the dynamic ice loading. Owing to the dynamic interaction of the ice-structure-soil system, it was necessary to assume values of the soil properties, such that forces on the structure could be defined and its response calculated, see Christensen et al. (1991) and Kristensen et al. (1993). Based on the structural response, parameters for the dynamic soil test programme were defined. Results of the program have previously been presented by Andersen et al. (1992) and by Kleven and Andersen (1992). Before proceeding with the dynamic laboratory tests, the dynamic behaviour of the bridge is briefly outlined.

4. Dynamic behaviour of bridge

The bridge is divided into 6 sections each consisting of 10 or 11 spans, cf. Figure 3. Between each section there is an expansion joint. The central pier in each section is fixed to the bridge girders. The rest of the piers can move *parallel* to the bridge when the relatively small friction in the bearings is exceeded. In the *transverse* direction the bearings are fixed between parallel steel rods. Both the bearings for the rail girder and the road girder, respectively, are fixed (in the transverse direction) except for a small temperature tolerance. This strengthens the integrity of the structure by taking advantage of the strength of both of the bearings instead of only one.

It is of major importance for the behaviour of the dynamic system that the quite large mass of the superstructures thereby follows the pier shaft when piers oscillate in the transverse direction, while they follow the bridge piers in the parallel motion and during rotation only until the bearing friction is exceeded.

The piers are relatively stiff components from which follows that the "elastic" element in the system for all important frequencies is the supporting soil. Based on preliminary estimates of the foundation response matrix, the typical full-scale values of frequencies and stiffnesses for a unit load acting in still water level were determined using a finite element numerical model. The results are shown in Table 3.

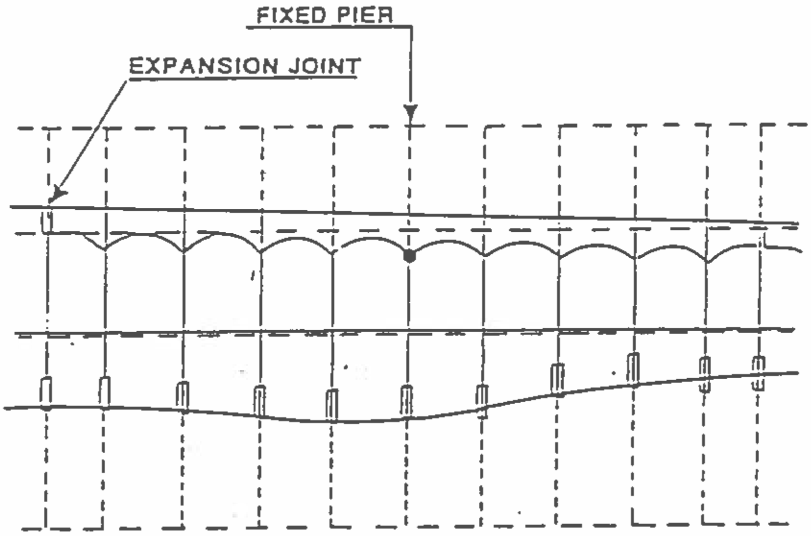

Figure 3. Conceptual profile of the Great Belt West Bridge.

Direction	Transverse x	Parallel y	Rotation r
Eigenfrequency (Hz)	0.78	0.84	2.07
Generalized stiffness			
- In GN/m	0.403*(1.17)	0.467	-
- In GNm/rad	-	-	299
Bearing friction	-	0.02	-

Table 3. Typical full scale values of eigenfrequencies and stiffnesses specified for the ice model tests (the number in the bracket is the originally determined value). The transverse stiffness was adjusted, cf. text.

The three main non-linearities are the frictional bearings of the bridge girders, the non-linear buffers between the rail sections (for each 10 or 11 spans), and the non-linear soil with large hysteresis and a frequency shift due to the change of stiffness. The friction coefficient for the bearings of the bridge girders has been estimated and a typical value of 0.02 resulted. Minimum and maximum values were 0.005 and 0.05. It is important to be able at an early stage to estimate the relative damping of the structural oscillations in order to allow prediction of the severity of the expected resonance. Simple energy methods were used. The oscillating pier is shown schematically in Figure 4.

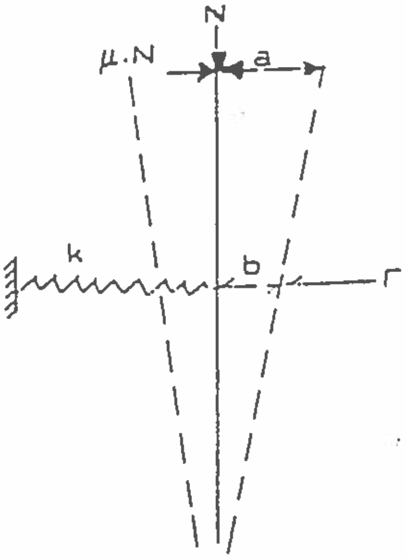

Figure 4. Driving and damping forces in bearings.

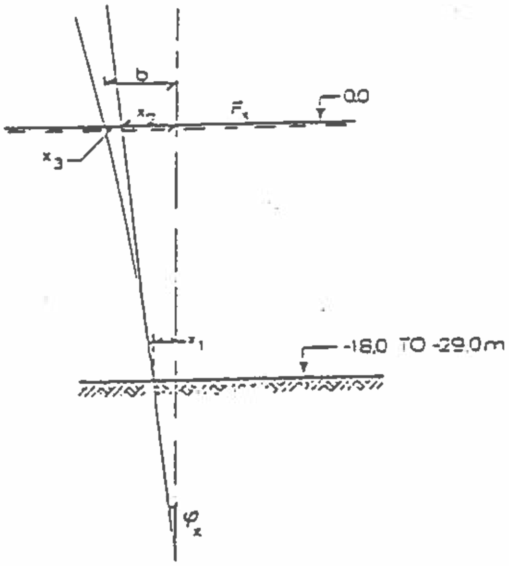

Figure 5. Parallel deformations of pier.

The external ice load acting at the water level is:

$$F = F_0 \cos(\omega t) \tag{5}$$

The stiffness related to the same level is denoted k, the gravity load from the superstructure is N and the friction force in the bearings amount to μN, where μ is assumed to be constant. The deflection of the pier top is denoted a and the deflection at water level is denoted b. The total elastic energy, E_t, and the absorption, ΔE, by the friction force becomes:

$$E_t = 0.5 \cdot b \cdot F_0 \tag{6}$$

$$b = F_0/k \tag{7}$$

$$\Delta E = 4\, a\mu N \tag{8}$$

With δ_f denoting the logarithmic decrement from frictional forces, the damping can be determined from:

$$2\delta_f = \frac{\Delta E}{E_t} = \frac{4a\mu N}{\frac{1}{2}bF_0} = 8\mu \frac{N}{F_0} \frac{a}{b} \tag{9}$$

$$\zeta_f = \frac{\delta_f}{2\pi} = \frac{2}{\pi} \mu \frac{N}{F_0} \frac{a}{b} \qquad \text{(critical damping } \zeta_f = 1.0\text{)} \tag{10}$$

For heavy superstructures even a small friction factor can give rise to significant damping. This is especially true for small amplitudes, e.g. in the ultimate and servicibility limit states, while for large force amplitudes the soil damping becomes relatively more important.

From computational modelling with elastic soil, the motion at the point of loading ($b = x_2 + x_3$) as well as the motions of the foundation plate (x_1, ϕ_x) for unit loads, can be determined. By use of the energy principle sketched in Figure 5 the relative weighting of the internal damping ratio in soil and structure, respectively, can be determined. The internal structural elastic energy, E_i, and the soil elastic energy, E_s, are given by:

$$E_i = 0.5\, F_0\, x_3 \tag{11}$$

$$E_s = 0.5\, F_0\, x_2 \tag{12}$$

with the definitions in Figure 5. For parallel motion the preliminary estimate resulted in:

$$\zeta_{x1}(\text{total}) = \zeta_{xf} + 0.14\, \zeta_{xi} + 0.86\, \zeta_{xs} \tag{13}$$

where ζ_{xf} is the frictional damping, ζ_{xi} the internal structural damping, and ζ_{xs} the internal hysteretic soil damping. This result together with the damping values in Table 4 demonstrate that the internal damping is dominated by internal hysteretic soil damping for large amplitudes (such as ALS), while at small amplitudes frictional damping will dominate. The preliminary estimates of total damping are shown in Table 4. The final values turned out somewhat differently because the dynamic response was significantly smaller than first assumed, due to soil backbone curvature and hysteresis, cf. section 5.

Mode	Frequency (Hz)	Friction ζ_f	Buffer ζ_b	Structure ζ_i	Soil ζ_s	Weighted Average ζ
Trans-versal	0.78	-	-	0.02	0.13-0.28	0.09-0.20
Parallel a) 1 pier	0.84	0.03-0.06	-	0.02	0.09-0.24	0.11-0.27
b) whole bridge section	(0.50)	-	0.04	0.02	0.09-0.24	0.12-0.25
Torsion	2.07	0.04-0.07	-	0.02	0.07-0.22	0.10-0.26

Table 4. Preliminary damping estimates. Friction and buffer damping are given relative to the total energy, while soil and structural damping are given relative to the sub-system energy. Frictional damping values are conservative estimates, i.e. small.

5. Foundation modelling

5.1 Preliminary Estimate of Ice Load

As mentioned above, this type of investigation basically requires all the results to be known a priori, in order to allow correct ice model tests, correct cyclic soil tests and foundation modelling. Best possible estimates of soil parameters were used to define test parameters for the ice model tests. The results of these may in turn be considered preliminary estimates for the soil loading. Soil response will then again affect ice-structure interaction and the circle continues. By re-analysis and adjustments the design may finally be completed through a series of iterations. The expected base plate area required and the expected ice induced foundation forces were estimated a priori. The latter is shown in Figure 6.

The expected ice load has a cyclic load component with an amplitude equal to the average load component. Note that Figure 6 is not an estimate of the direct ice load but an estimate of the equivalent force at the foundation base plate level.

5.2 Cyclic Soil Tests

In order to benefit from experience obtained in connection with their previous cyclic soil analyses for offshore platforms, the advanced soil tests were carried out at Norwegian Geotechnical Institute by Andersen and Hansteen (1990). The static tests consist of:

- Triaxial compression tests
- Triaxial extension test (one only)
- Direct simple shear tests

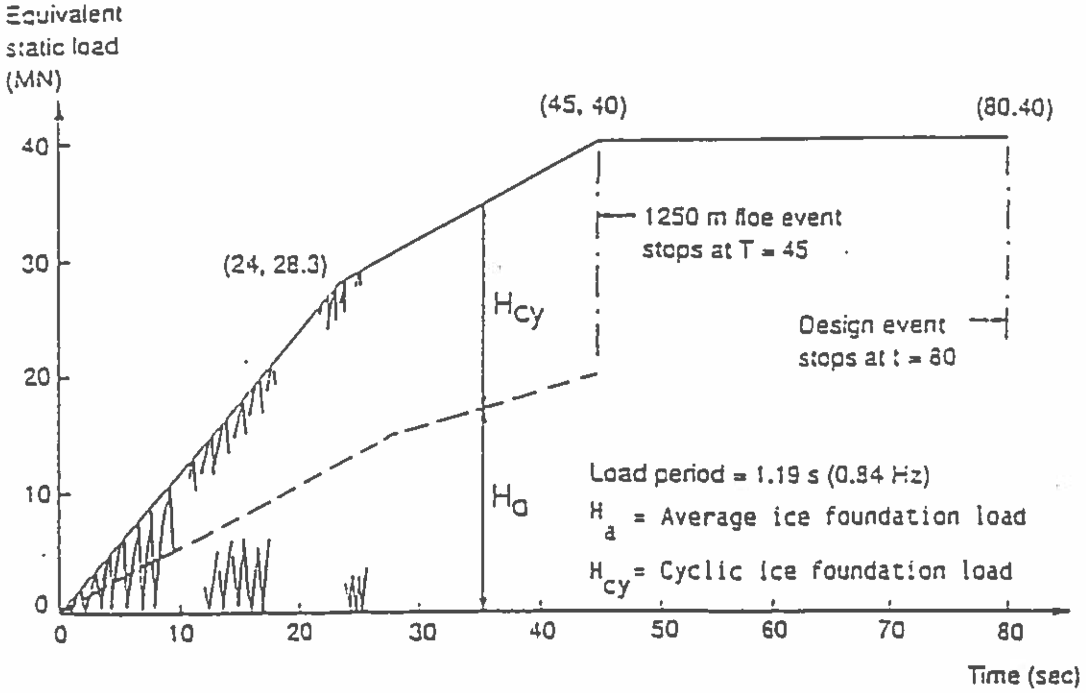

Figure 6. Initial estimate of design ice foundation load from a 1250 metres diameter ice floe and from a 2500 metres diameter ice floe.

A complete programme of cyclic direct simple shear tests and cyclic triaxial tests was performed on intact samples of both the soft and the stiff clay types. The tests were performed with varying average shear stress and with a constant, but different cyclic amplitude in order to establish a global relationship between the following parameters:

- Average shear stress
- Cyclic amplitude of the cyclic stress
- Number of cycles
- Pore pressure build-up
- Average strain
- Cyclic strain
- Cyclic stress-strain relationship

A complete programme of cyclic simple shear tests was also performed on disturbed glacial clay till in order to evaluate the consequences at the transition zone between intact soil and stonebed. The main results of the tests were as follows:

Static Tests

- The direct simple shear tests showed an undrained shear strength of approx. 70% of the shear strength determined by triaxial compression tests.

- One triaxial extension test showed an undrained shear strength of approx. 50% of the value obtained by triaxial compression test.

Cyclic Tests

- Large strains (failure) are observed for shear stresses lower than the static undrained shear strength. The higher the number of cycles, the lower are the stresses that may result in large strains.
- This effect is more pronounced for tests with a cycle time of 10 seconds than for tests with a cycle time of 1 second.
- The static undrained shear strength is smaller just after cyclic loading has taken place, before drainage takes place.
- Hysteretic, internal damping, has been found to agree reasonably with recommendations by Seed and Idriss (1970).

The direct results of the tests interpolated to give overall design values may be illustrated as shown in Figure 7. Alternatively, the results may be interpreted as relative shear strain in the points considered below the foundation plate. For a certain load condition both the cyclic and average shear strain may be found as shown in Figure 8. The results from more load cases may afterwards be combined as illustrated in Figure 9. By means of a finite element model the average cyclic and total foundation displacements may be determined, see Figure 10. Another result of the analysis is the stiffness and the damping, from which a resulting backbone curve may be determined, cf. Figure 11.

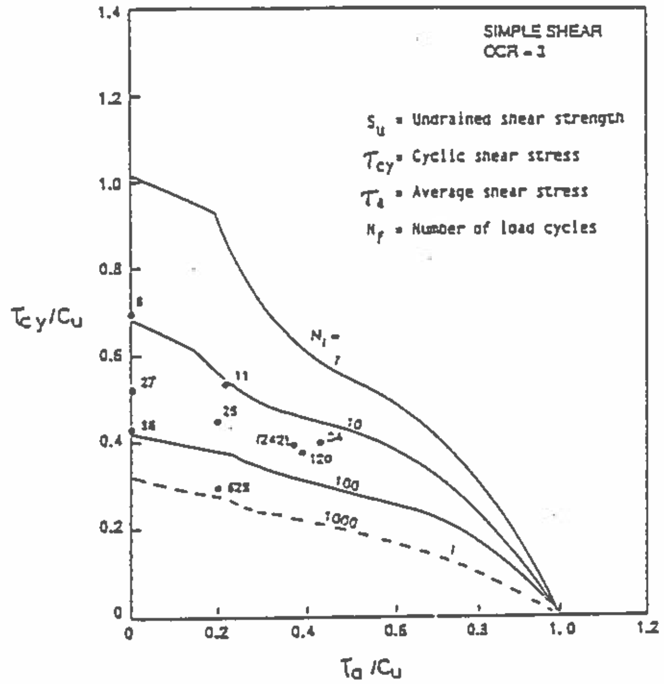

Figure 7. Number of load cycles to failure in direct simple shear tests as a function of normalized cyclic and average shear stresses.

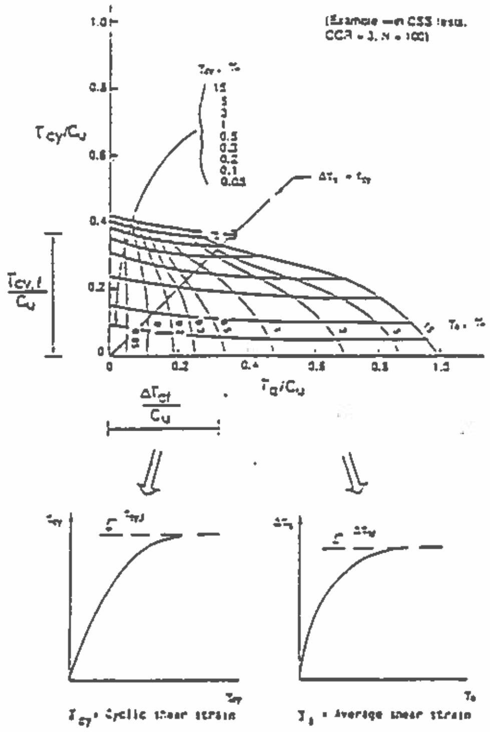

Figure 8. Illustration of how parameters to be used in computational analyses are determined from laboratory tests.

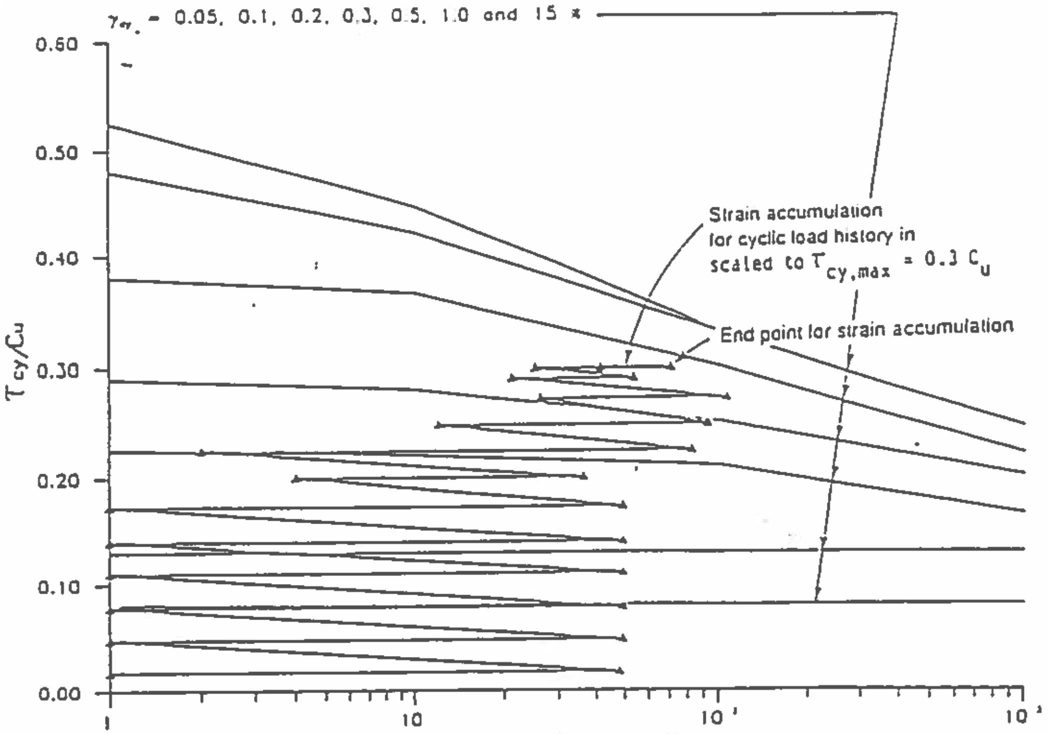

Strain contours for DSS tests on Storebælt clay till with OCR = 3 and $\tau_{cy} = \Delta\tau_s$.

Figure 9. Result of strain accumulation for the preliminary ice load history.

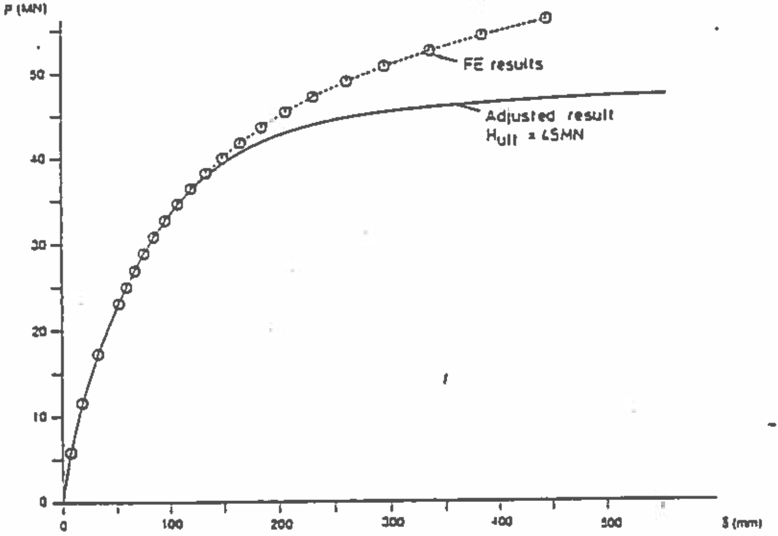

Figure 10. Total displacements at bridge deck versus ice load for a pier on stiff clay till.

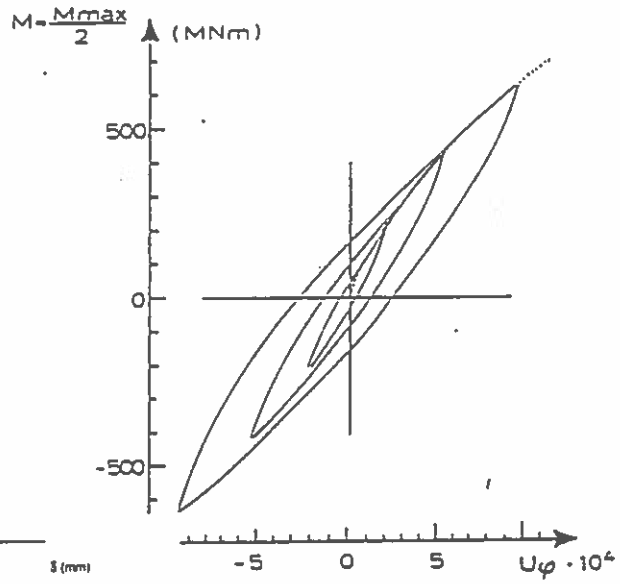

Figure 11. Backbone curve and examples of hysteresis loops for a pier on stiff clay till.

6. Implemented Design

6.1 Damage Criteria

The damage criteria is defined to be a "maximum total motion of the top of the pier shafts relative to the superstructure less than 0.5 m in the parallel direction". Such a deformation:

- just exceeds the maximum deformation which the selected bearings allow for without damage, while
- the additional destabilizing moment induced by the large dead weight force from the superstructure is still acceptable.

6.2 Selected Design Ice Load

The ice loads are dynamic in nature and consist of different components: 1) a low frequent buckling component due to breaking of ice floes, 2) a high frequent spalling component due to local cracking at the ice edges, and 3) a high frequent component due to ice crushing. The model tests showed that the crushing was of minor importance. High structural response will develop when the frequnency of the ice loads lock-in on the eigenfrequency of the bridge.

A non-linear numerical structural model was used to calculate the effect of the scaled ice loads on the full-scale bridge with its different damping and with its different structural behaviour from that of the experimental set-up in the ice model tests. The non-linear behaviour of soils was fully incorporated.

From the calculations it could be determined whether the bridge would be in resonance or not. With a linear bridge model, a heavy resonance could develop. It turned out that the curvature of the soil load-deflection curve combined with its hysteresis and the hysteresis of the bearings made the structural system sufficiently non-linear in the Accidental Limit State (ALS) that no resonance was created.

Since the buckling ice loads in Accidental Limit State (ALS) did not lock-in, there would be only limited amplification of the buckling loads. Therefore, in ALS the buckling loads could be fixed to the range 31-64 MN. By stretching the time series maximum resonance could be obtained. With the (limited) dynamic amplification in the ALS it was found that an equivalent static load of 8 MN should be used as the force amplitude for the spalling loads.

With a load level of 31-64 MN it was checked whether or not such forces can in fact be generatedin the Great Belt with its particular dimensions and environmental conditions even in the ALS. It was found that the forces were so high, that they would arrest the movement of the large ice floes. In case of large drifting ice floes, a few buckling events can be expected before the bridge pier arrests the ice. This means that a sustained situation as tested in the laboratory cannot exist in practice in the Great Belt. Therefore, the expected buckling load will be smaller than the maximum load determined in the ice model tests. Applying the short term statistics for peak buckling forces for ice sheet impacts gave a peak buckling load of 43 MN. The sequence leading from model test results to selected forces for an exceedance probability of 0.2×10^{-4} per year is illustrated in Table 5.

Source	Buckling	Force (MN)	Froude scaling (λ^3)
ICE MODEL TESTS			
1. Stiff model	1 mode	31-64	Average = 43 MN
2. Elastic Model $\zeta = 0.03$ and 0.05			
2.1 Large surface roughness on bridge pier	2 mode	70-110	
2.2 Normal surface roughness			
2.2.1 No lock-in between spalling and buckling	1 mode	31-64	Average = 43 MN
2.2.2 Lock-in between Spalling and buckling	2 mode	70-150	
NUMERICAL MODEL			
3. Linear model Resonance spalling Eventually lock-in	1 or 2 mode		
4. Non-linear model Only weak resonance Spalling Dyn.Load Factor = 1.5 Spalling 1.5x5 MN =8MN	1 mode	(31 to 64) ± 8 MN	
5. Limited load scenario	1 mode	43 ± 8 MN	

Table 5. Selected design ice forces with a 2×10^{-5} per year exceedance probability.

6.3 Final Results of Non-linear Response Modelling

The final analysis with the structural model included non-linear foundation modules, friction in bearings and a non-linear buffer. Some of the results are illustrated below. Figure 12 shows the moment/angular deflection plot for overturning parallel to the bridge illustrating how the backbone curve defined in Figure 11 acts in practice. The major non-linear element is a stiffness shift and much less hysteretic effect than assumed preliminarily in section 4. The moments at the base plate level is shown in Figure 13. The time series show only limited tendency towards resonance although the loading time series have been tuned to show maximum resonance between the spalling force and the pier eigenfrequencies.

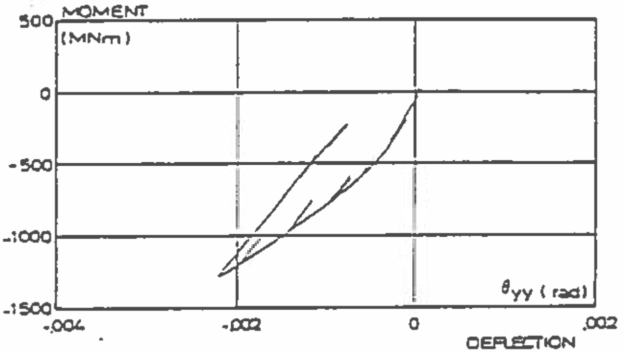

Figure 12. Overturning moment and angular deflection at foundation level.

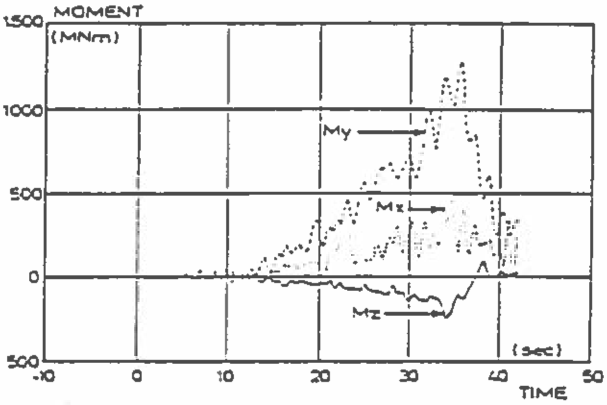

Figure 13. Sectional forces at foundation level.

The results of the ice model tests necessitated a re-analysis of the number of equivalent load cycles because the vibration component was significantly reduced relative to the preliminary estimate. The simplified ice load history is shown in Figure 14.

The equivalent number of load cycles could be estimated as shown in Figure 15, cf. Andersen and Hansteen (1990). The actual load case may be estimated to be equal to an equivalent number of load cycles N = 20. Finally, the bearing capacity of a centrally loaded pier versus number of load cycles could be determined as shown in Figure 16. The results in Figure 16 have included:

- Anisotropy of glacial till
- Strength increase due to dead load
- Existence of gravel pad
- Soil degradation due to cyclic loading

The original design basis was much more simple as it was based on the following assumptions:

- Isotropic soil
- No strength increase due to dead load
- No gravel pad

The effect of the quantified changes including torsion relative to the original design basis have been determined through an equivalent factor α acting on only one parameter - the shear strength - and describing the difference between the original design basis and final ice load design. This required among other things determination of actual undrained shear strength relative to the original undrained shear strength at foundation level determined during the site investigations by vane shear tests, CPT-point resistance and/or the assumption that vane shear tests reflect the results of the triaxial compression tests. This quite complicated analysis has led to the main results shown in Table 6, cf. Kristensen and Gravesen (1990).

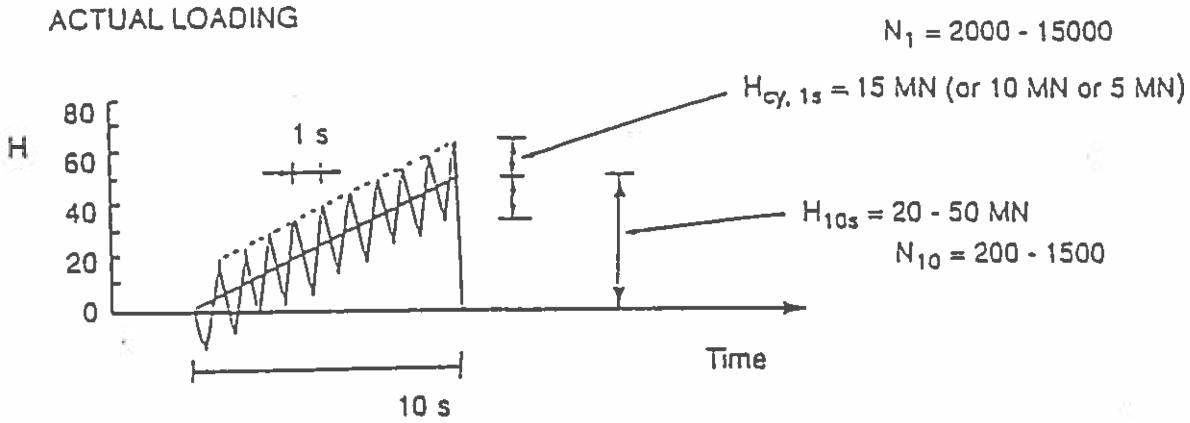

Figure 14. Load history used to approximate the revised actual ice load history.

No. of equivalent cycles, N_{eqv}, with H = 50 MN + $H_{cy,\,1s}$

N_{10s} \ $H_{cy,\,1s}$	0	5	15
200	30	35$^{2)}$- 50$^{1)}$	40 - 100
500	80	90 - 200	105 - 290
1500	300	315-590	375 - 750

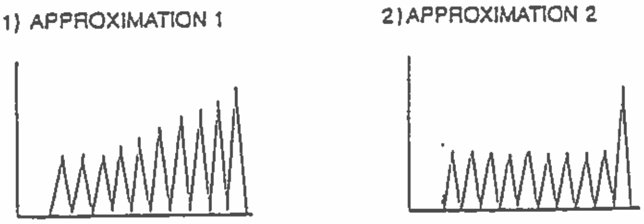

N_{eqv} at failure
N_{eqv} smaller below failure

Figure 15. Equivalent number of load cycles for the revised ice load history.

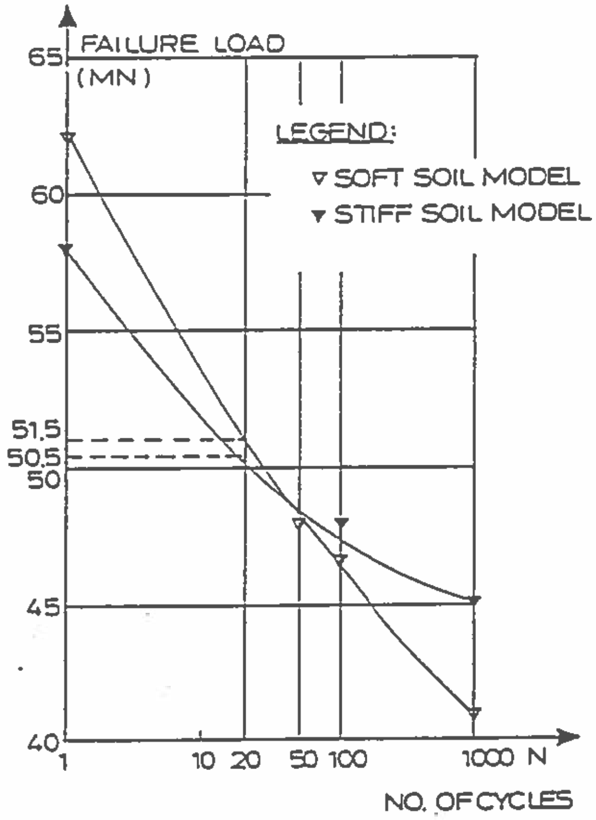

Figure 16. Horizontal failure load at still water level.

	Stiff soil model	Soft soil model
Foundation slab (m^2)	20.5 x 30.5	22 x 34
c_u, Static (kN/m^2)	225	150
c_u, Dynamic (kN/m^2)	209	140
Reduction Factor α (-)	0.93	0.93
Vertical load (MN)	243	215

Table 6. Deep seated failure. Results of comparison of a static design based on original undrained shear strength with a dynamic design accounting among others for actual undrained shear strength.

Another result shows that for the case of sliding failure, the dynamically reduced sliding resistance, k, should be determined from:

$$k = \tau_u / \sigma'_v = 0.38 \tag{14}$$

where τ_u is the sliding shear stress and σ'_v the effective vertical stress.

7. Experience Obtained

The following conclusions and recommendations for future projects are given:

- Ice loads have a high dynamic component very likely to lock-in to the resonance frequencies of the bridge structure.
- The bearing capacity of the soil is dependent on the number and type of load cycles, so advanced soil tests are a must with large ice forces.
- Damping in soil and change of stiffness cause very important reductions of the dynamic response.
- If acceptable, bridge piers should be rounded, so that unnecessary large ice forces are avoided.
- If acceptable, the piers should be given an inclined surface at the water level.
- Alternative connection should be included in the structural system for large relative deformations between piers and superstructure so local damage on a single pier can be avoided during accidental loading.
- The key word for structures designed in accidental limit state is ductility. All appropriate means to increase ductility should be used.
- Comprehensive formulations of design ice conditions should be made as early as possible in the project. For dynamically sensitive structures, the ice velocity should be included in the probabilistic model.

Physical model tests in ice showed that some dynamic amplification and frequency lock-in are likely to occur, cf. Christensen et al. (1991), Christensen and Klinting (1992), Timco et al. (1993) and Christensen et al. (1993). Ice loading typically contains energy at higher frequencies than for example storm wave loading, and the available experience with dynamic soil properties is quite limited for marine structures in the high frequency range. The bearing capacity is furthermore very dependent on the number of load cycles, so detailed dynamic soil tests are necessary for accurate design. Hysteresis and backbone curvature for the soil contribute significantly to system damping in accidental limit state design. Consequently, structural ductility should also be encouraged in the design.

8. Conclusion

Dynamic ice loads and soil properties for the Great Belt West Bridge have been investigated. The objective was to verify that the specified design complies with risk acceptance criteria. For some of the piers dynamic ice loading is governing for the design.

The investigation combined advanced analyses of extreme ice properties, of ice-structure interaction in both physical and numerical models, of marine dynamic soil mechanics, of structural response and of risk strategies to check the final design of the Great Belt West Bridge for extreme ice loads. The advanced level of the analyses was necessary because of some relatively unique features of the bridge. The length of the bridge and the geography of the area, leave the relatively light-weight piers exposed to ice forces from unusually large attack angles.

The design was carried out in the accidental limit state, while certain critical points were checked in ultimate and servicibility limit states as well. For the West Bridge the real advantage of designing in the accidental limit state is that the engineer is forced to think in terms of consequences as well as design forces, and thus favour ductility as well as large load resistance capacity.

The Great Belt West Bridge is scheduled for completion in the fall of 1993. Figure 17 on the next page shows a westward view of the halfway completed bridge, photographed on 12 September 1992.

9. Acknowledgements

The analyses described were carried out on behalf of the Great Belt Link Ltd. Their permission to publish the results is gratefully acknowledged. The authors furthermore wish to acknowledge the high standard of services provided for the project by Norwegian Geotechnical Institute.

The first and last authors represent the joint venture of Danish Hydraulic Institute and LICengineering Ltd. acting as special consultants to the Great Belt Link Ltd. in all matters related to water and ice. The second and third authors represent the joint venture CCL consisting of COWIconsult Ltd., Carl Bro Group Ltd. and Leonhardt Andrä und Partner, acting as general consultants to the Great Belt Link Ltd.

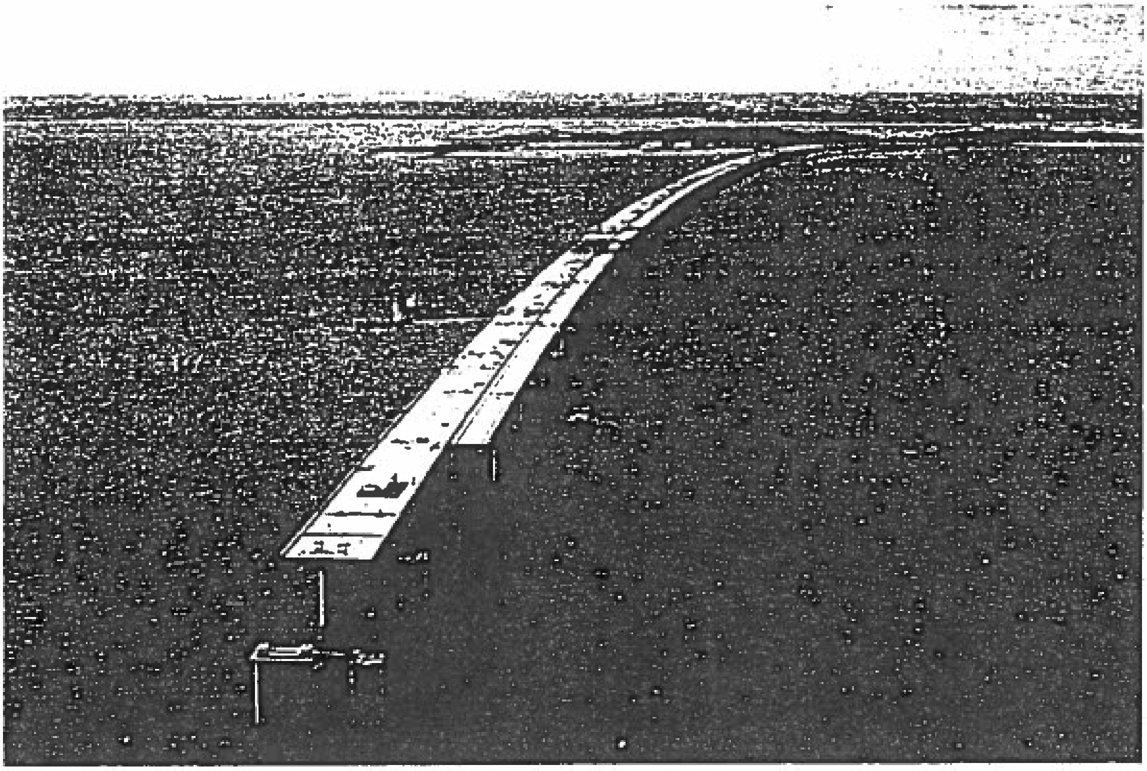

Figure 17. Aerial westward view of the Great Belt West Bridge more than halfway completed on 12 September 1992. Photo by Jan Kofod Winther.

References

Andersen, K.H. and Hansteen, O.E. 1990. Storebælt Western Bridge, bearing capacity, displacements and backbone curves under ice loading. Report by Norwegian Geotechnical Institute for the Great Belt Link Ltd.

Andersen, K.H., Hansteen O.E. and Gutierrez, M. 1992. Bearing capacity, displacements, stiffness and hysteretic damping of Storebælt bridge piers under ice loading. Bulletin no.10, Danish Geotechnical Society, Lyngby, Denmark. (In preparation). A draft has been published in Proc. Seminar on Design of Exposed Bridge Piers, Part 1 Dynamic Ice Load, Danish Society of Hydraulic Engineering.

Christensen, F.T. and Klinting, P., 1992. Ice loads on a vertical bridge pier at two different model scales. ASCE Journal of Cold Regions Engineering, 6(3): pp. 93-110.

Christensen, F.T., Gravesen, H., Thomsen, J.R., Ennemark, F. and Spangenberg, S. 1991. Accidental limit state ice loads on bridge piers. Permanent International Association of Navigation Congresses, PIANC Bulletin, 72: pp. 15-30.

Christensen, F.T., Timco, G.W. and Nwogu, O:G. 1993. Compliant model tests with the Great Belt West Bridge piers in ice, Part 2: Analyses of results, Cold Regions Science and Technology, Elsevier, In preparation.

Foged, N. and Steenfelt, J.S. 1992. An engineering geological approach to preloaded clay till strength, Nordic Geotechnical Engineers' Meeting, NGM-92, Aalborg, Denmark.

Kleven, A. and Andersen, K.H. 1992. Cyclic laboratory tests on Storebælt clay till. Bulletin no.10, Danish Geotechnical Society, Lyngby, Denmark. (In preparation). A draft has been published in Proc. Seminar on Design of Exposed Bridge Piers, Part 1 Dynamic Ice Load, Danish Society of Hydraulic Engineering.

Kristensen, P.S. 1991. Bearing capacity of ice exposed pier. Effect of torsion. Comparison between conventional and advanced design. Dynamic properties of soil for ice load. A case history of bridge pier design for Western Bridge, Storebælt. Bulletin no.8, Danish Geotechnical Society, Lyngby, Denmark.

Kristensen, P.S. and Gravesen, H. 1990. Dynamic properties of soil for ice load. Report by COWIconsult, Carl Bro and Leonhardt Andrä und Partner (CCL) joint venture for the Great Belt Link Ltd., Revision 0, dated 16 July 1990.

Kristensen, P.S., Erichsen L. and Sørensen, C.S. 1992. Great Belt - Foundation of the West Bridge. 11th Nordic Geotechnical Engineers' Meeting, NGM-92, Aalborg, Denmark.

Kristensen, P.S., Gravesen, H., Andersen, K.H., Hansen, Aa. and Spangenberg, S. 1993. Dynamic properties of soil for ice load: A case story of bridge pier design for the Great Belt West Bridge. Bulletin no.10, Danish Geotechnical Society, Lyngby, Denmark. (In preparation).

Mayne, P.W. 1988. Determining OCR in clays from laboratory strength. ASCE J. of Geotechnical Engineering, 114(1): pp 76-92.

Mortensen, J.K., Hansen, G. and Sørensen, B. 1991. Correlation of CPT and field vane tests for clay tills. Bulletin no.7, Danish Geotechnical Society, Lyngby, Denmark.

Porsvig, M., Christensen, M.F. and Hansen, Aa. 1989. Great Belt Information System with a 3D-model. Proceedings, 12th International Conference on Soil Mechanics and Foundation Engineering, Rio de Janeiro, Brazil.

Seed, H.B. and Idriss, I.M. 1970. Soil moduli and damping factors for dynamic response analysis. Report EERC 70-10, Earthquake Engineering Research Center, University of California, Berkeley, California, U.S.A.

Steenfelt, J.S. and Foged, N. 1992. Clay till strength - SHANSEP and CSSM. Nordic Geotechnical Engineers' Meeting, NGM-92, Aalborg, Denmark.

Timco, G.W., Nwogu, O.G. and Christensen, F.T. 1993. Compliant model tests with the Great Belt West Bridge piers in ice, Part 1: Test methods and key results. Cold Regions Science and Technology, Elsevier, in press.

Vincentsen, L.J. and Spangenberg, S. 1990. Safety management system for the Great Belt Link. Proceedings, 2nd symposium on Strait Crossings, pp.527-531, Trondheim, Norway. Published by A.A. Balkema, Rotterdam, The Netherlands.

Die 6,6 km lange West-Brücke über den Grossen Belt als Beispiel einer Spannbetonbrücke für den Strassen- und Eisenbahnverkehr für gezielt hohe Lebensdauer

Dietrich Hommel (Leonhardt, Andrä und Partner)
(at present employed in Carl Bro Group)

Dietrich Hommel, Stuttgart

Die 6,6 km lange West-Brücke über den Großen Belt als Beispiel einer Spannbetonbrücke für den Straßen- und Eisenbahnverkehr für gezielt hohe Lebensdauer

1. Einführung

1.1 Die Große Belt Verbindung

Nach mehreren vergeblichen Anläufen in der Vergangenheit eine feste Verbindung über den großen Belt zu schaffen, ist mit einem im Mai 1987 im Dänischen Parlament verabschiedeten Gesetz die Grundlage für die Realisierung geschaffen worden. Der Große Belt trennt Dänemarks Bevölkerung von etwa 5 Millionen Menschen in etwa zwei gleiche Teile. Die bestehenden Fährverbindungen für Straße und Eisenbahn haben die beschleunigte, wirtschaftliche Entwicklung in Jütland und auf Fünen bedingt durch deren unmittelbaren Anschluß an Mitteleuropa nicht verhindern können. Neben der Verbindung über den Großen Belt werden geplant die Überquerungen des Öresunds, Schweden-Dänemark, und des Fehmarn Belt, Dänemark-Deutschland, die in den kommenden 10–15 Jahren Realität werden sollen.

Eine staatliche Aktiengesellschaft A/S Storebaeltsforbindelsen oder STOREBAELT wurde vom Verkehrsministerium gegründet, der die Planung und Bauausführung sowie das Betreiben der festen Verbindung übertragen wurde. Die mit 18 Milliarden DKr (1988) veranschlagten Gesamtkosten sollen über Benutzergebühren finanziert werden. Die Eisenbahnverbindung soll 1994 fertig sein und in Betrieb gehen, drei Jahre früher als die Straßenverbindung, die 1997 folgen soll.

Die Verbindung über den Großen Belt benutzt die kleine Insel Sprogö zwischen den Inseln Fünen und Seeland *(Bild 1)*, als Mittler zwischen der kombinierten Straßen- und Eisenbahnbrücke über den westlichen Teil und den getrennten Bauwerken Eisenbahntunnel und Straßenbrücke im östlichen Teil. Die Hauptdaten der 3 Teile sind:

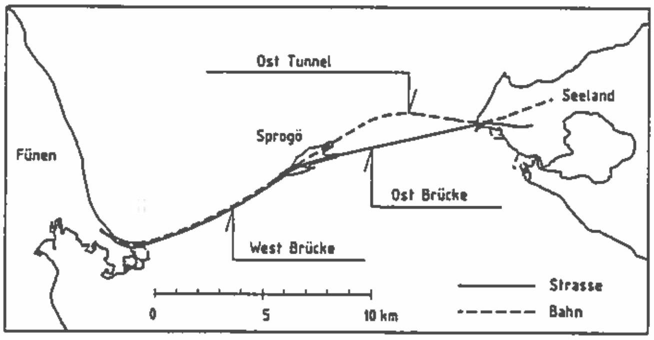

Bild 1. Großer Belt, Übersicht mit den drei Bauwerken

- West Brücke von 6,6 km Länge, 2 Gleise + Autobahnquerschnitt auf getrennten Überbauten 18 m lichte Höhe für die Schiffahrt, Vergabe im Juni 1989.
- Ost Tunnel mit 8,0 km Länge, 2 eingleisige Tunnelröhren bis zu 80 m unter dem Wasserspiegel, Vergabe im November 1988.
- Ost Brücke mit 6,8 km Länge, Autobahnquerschnitt, Hängebrücke mit 1624 m Hauptöffnung und 65 m lichter Höhe mit anschließenden Vorlandbrücken von 1500 m bzw. 2500 m, Vergabe im Oktober 1991.

1.2 Die Entwicklung zum Ausführungsentwurf

Im November 1987 hat STOREBAELT die Ausschreibungsplanung dem Joint Venture CCL übertragen, das von den Ingenieuren COWIconsult A/S, Carl Bro A/S beide aus Dänemark und Leonhardt, Andrä und Partner GmbH gebildet wurde und in dem COWIconsult die Federführung übernommen hatte. Die Ausschreibungsunterlagen für 3 Ent-

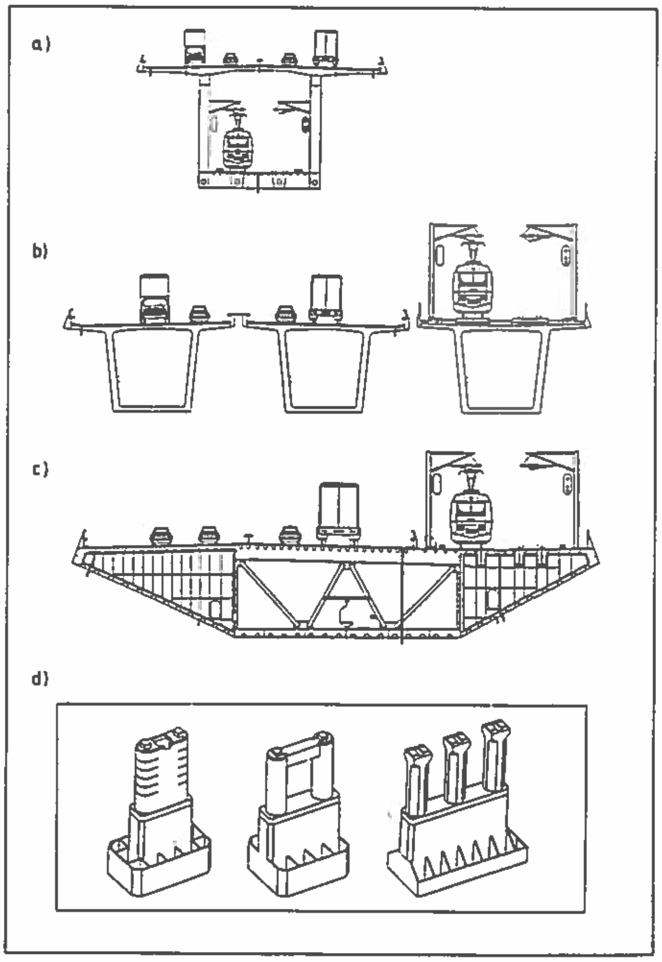

Bild 2. Überbau-Querschitte der 3 Ausschreibungsentwürfe

würfe wurden parallel bearbeitet und im April 1988 den prequalifizierten Bietergruppen übergeben. Diese Entwürfe *(Bild 2)* waren:

- Doppelstöckiges Stahlverbundfachwerk mit Straße oben und Eisenbahn unten; Spannweite 144 m, Länge 42x144 = 6048 m.
- Spannbetonhohlkastenbrücke mit 3 getrennten Überbauten; Spannweite 105 m, Länge 58x105 = 6090 m.
- Stahlhohlkastenbrücke als einstöckige Lösung; Spannweite 120 m, Länge 51x120 = 6120 m.

Die Entwürfe sahen eine konstante Bauhöhe vor und waren in jeweils 5 Durchlaufträger unterteilt.

Die Submission fand im November 1988 statt und neben Angeboten auf die ausgeschriebenen Entwürfe wurden auch Varianten und Sondervorschläge abgegeben mit Angebotssummen zwischen 2400 und 4700 Millionen DKr. Die Auswertung und weitere technische Klärung der Angebote führte zur Aufnahme der Vertragsverhandlungen über einen Sondervorschlag als Spannbetonbrücke mit veränderlicher Bauhöhe und nur zwei getrennten Überbauten. Die Perspektive *(Bild 3)* zeigt den Entwurf von Fünen aus gesehen. Ein wesentlicher Bestandteil des Sondervorschlages war die Montage von Großfertigteilen mit einem speziellen Schwimmkran, der universell für Unter- und Überbauten eingesetzt werden kann.

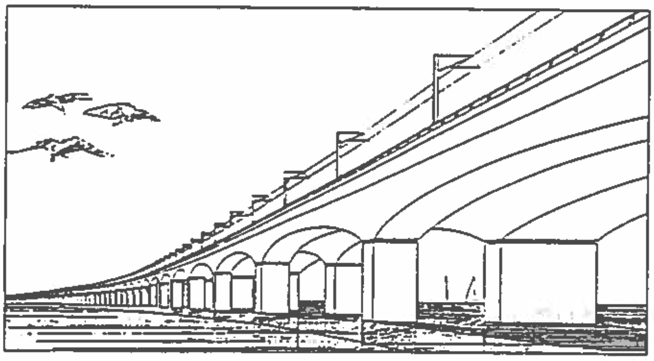

Bild 3. Perspektive der West Brücke nach dem Sonderentwurf

Nach der Überarbeitung des Sondervorschlages und dem Abschluß der Verhandlungen wurde der ARGE EUROPEAN STOREBAELT GROUP (ESG) der Auftrag zur Detailplanung und Bauausführung der West Brücke im Juni 1989 zu einem Festpreis von 3160 Mill. DKr übertragen.

STOREBAELT hat an CCL die Auswertung der Bodenuntersuchung und die Festlegung der bodenmechanischen Entwurfsparameter, eine unabhängige Überprüfung von ESG's Detailbearbeitung, die Planung der mechanischen und elektrischen Ausrüstung, die Koordinierung zwischen allen Beteiligten der Detailplanung sowie die technische Assistenz während der Bauüberwachung übertragen.

2. Beschreibung des Ausführungsentwurfs

2.1 Allgemeines

Die Gesamtlänge der West Brücke von 6612 m ist in 6 Durchlaufträger mit je 1047 bzw. 1157 m Länge aufgeteilt, die aus 8 oder 9 Feldern mit Normalspannweiten von 110,40 m und 2 Endfeldern von 81,75 m aufgebaut sind. Zwei Schifffahrtsöffnungen von 18 m lichter Höhe und 70 m Breite sind etwa 2900 m östlich von Fünen angeordnet und erlauben die Passage von 2000 BRT-Schiffen; höhere oder größere Schiffe, das sind 4% der Segelboote und 20% der Handelsschiffe, müssen den östlichen Teil benutzen. Die Fischereifahrzeuge können weiterhin den bis zu 28 m tiefen westlichen Teil befahren.

In den 5 Fugen zwischen den Durchlaufträgern bzw. an den 2 Widerlagerfugen treten Gesamtverschiebungen von bis zu 1400 mm bzw. 600 mm auf.

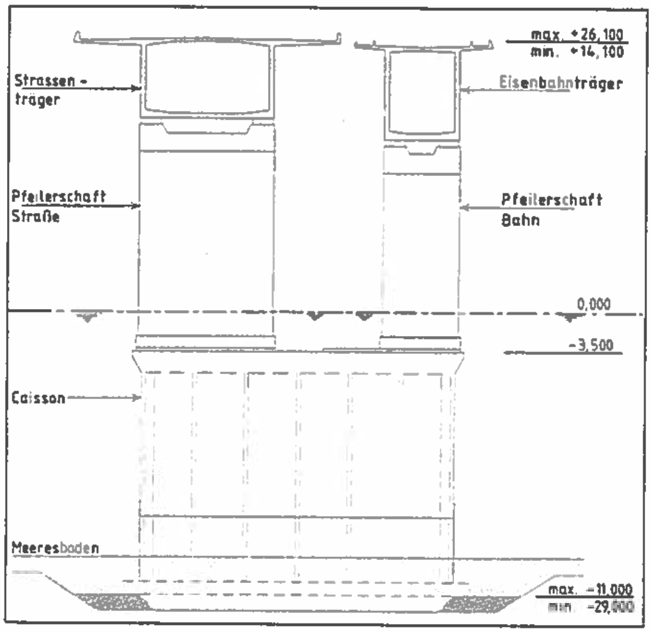

Bild 4. Hauptbestandteile der West Brücke

Den prinzipiellen Aufbau der West Brücke bestehend aus 2 getrennten Überbauten je einen für Straße und Eisenbahn, 2 Pfeilerschäften unterschiedlicher Abmessungen und einem gemeinsamen Caisson zeigt *Bild 4*. Die folgenden Großelemente werden an Land vorgefertigt

Caissons		62 Stück
Pfeilerschäfte	2 x 62	124 Stück
Straßenträger	57 Standard-, 12 Sonderelemente	69 Stück
Eisenbahnträger	ebenfalls	69 Stück

das sind insgesamt 324 Elemente von bis zu 7100 t Gewicht, die mit dem Schwimmkran transportiert und montiert werden.

Durch Ortbetonfugen zwischen Caisson und Pfeilerschäften einerseits und zwischen den Überbauträgern andererseits werden die Teilsysteme Unter- bzw. Überbauten realisiert.

2.2 Die Unterbauten und deren Gründung

62 Pfeiler bestehend aus 2 Pfeilerschäften und einem Caisson und 2 Widerlager bilden die Unterbauten, die von Sprogö beginnend von 1 bis 64 bezeichnet sind *(Bild 5)*. Die tertiären Ablagerungen (Danien-Kalkstein und Mergel) sind von Grundmoränen aus der älteren Saale- oder jüngeren Weichseleiszeit überlagert. Die oberen, postglacialen Schichten von bis zu 2 m Dicke sind ohne Bedeutung für die Gründungen. Während Kalkstein und Mergel hohe Scherfestigkeiten von Cu> 225 kN/m² aufweisen, sind die verschiedenen Moräneschichten oder Geschiebemergel sehr unterschiedlich. Die Schicht bei Knudshoved ist ein sehr steifer Ton und gut geeignet. Die obere Geschiebemergelschicht ist im wesentlichen ein toniger Lehm,

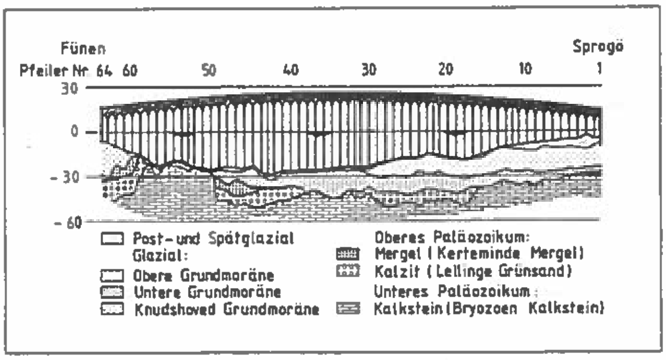

Bild 5. Geologischer Längsschnitt mit Achsenbezeichnung

dessen Steifigkeit mit zunehmender Tiefe abnimmt bei einer Scherfestigkeit von 200–250 kN/m² im oberen und 100–150 kN/m² im unteren Bereich mit gleichzeitig beträchtlichen Schwankungen in horizontalen Ebenen. Die untere Schicht zeigt eine zwischen Ton, sandigem Lehm und Schmelzwassersand wechselnde Zusammensetzung, ist aber eine ausreichend steife Schicht mit Cu = 200–300 kN/m².

Alle Pfeiler 2 bis 63 werden auf einem nach dem Aushub eingebauten und verdichteten Steinbett von 1,5 bis 4,0 m Dicke direkt gegründet, dessen Oberkante zwischen –11 m und –29 m variiert. Die Aushubtiefen schwanken zwischen 2 m und 4 m über weite Bereiche und erreichen bis zu 15 m im östlichen Teil, wo teilweise sehr tief gegründet werden mußte. Die Caissons werden zusätzlich mit Sand ballastiert.

Die beiden Widerlager 1 und 64 werden in Spundwandbaugruben unter Wasserhaltung als konventionelle, den Zugang zu den Überbauten ermöglichende Konstruktionen hergestellt und hier nicht näher beschrieben.

Den Aufbau eines Caissons beschreibt am Beispiel von Caisson 38 das *Bild 6*. Dieser 24 m hohe Caisson (maximale Höhe 26 m) besteht aus einer Fundamentplatte von 1,15 m Dicke und 22,5 m x 34,0 m Abmessungen auf der 7 Wände in Quer- und 4 in Längsrichtung des Caissons zur Lasteinleitung angeordnet sind. Der untere Caissonteil mit 4 Längswänden ist 9 m hoch, und nur der Caissonschaft von 6,4 m x 30 m zwischen den inneren Längswänden setzt sich bis zur oberen, 2 m dicken Abschlußplatte mit der Oberkante auf –3,5 m fort. Die äußeren Caissonzellen sind mit oberen Deckplatten versehen, die neben einer tragenden Wirkung auch ein Auskolken des Sandballastes verhindern.

Die Fundamentplatte ist mit etwa 2 MN/m in Querrichtung vorgespannt, ebenso sind in 4 Querwänden vertikale Spannglieder mit oberen Spezialankermuttern eingebaut, um später die Gesamtlast des Caissons an das Hubgeschirr des Schwimmkranes zu übertragen. Die Lastübertragung vom Caissonschaft zur Fundamentplatte wird in der Regel durch Aussteifungswände in allen Querachsen verbessert.

Bild 7 gibt eine Übersicht über Pfeilerschäfte der Straßenbrücke im Bereich der Schiffahrtsöffnungen. Der Höhenunterschied des Schaftes an einer Fuge, z.B. Nr. 32, gegenüber den anderen Schäften wird deutlich, und zudem ist der unterschiedliche Grad einer Magerbetonfüllung im Schaftinneren zu sehen: Regelpfeiler bis +2,5 m, Pfeiler 41–32 nahe der Schiffahrtsöffnung bis +5 m und alle Fugenpfeiler bis 2 m unterhalb des Pfeilerkopfes. Die Schafteigengewichte betragen bis zu 1800 t und die größten Längen 20 m bis 23 m. Die Ansicht eines Straßenpfeilerschaftes in *Bild 8* zeigt die Hauptabmessungen von 5 m x 12,55 m und läßt erkennen, daß jeder Schaft drei verschiedene Abschnitte aufweist. Der untere Bereich ist zur Aufnahme hoher, lokaler Lasten aus Eisdruck oder Schiffsanprall mit Wanddicken von 850 mm und zwei zusätzlichen, aussteifenden Wänden sehr robust ausgebildet; der zweite Abschnitt ist mit 500 mm Wanddicke als rechteckiger Querschnitt und der Pfeilerkopf auf 3 m Höhe massiv vorgesehen.

Die Schäfte für den Eisenbahnüberbau sind mit den Hauptabmessungen 5 m x 7,2 m ähnlich ausgebildet mit nur einer Zwischenwand im unteren Bereich. Alle Schäfte weisen zur Verminderung des lokalen Eisdruckes und aus ästhetischen Gründen abgerundete Kanten auf. Auf dem

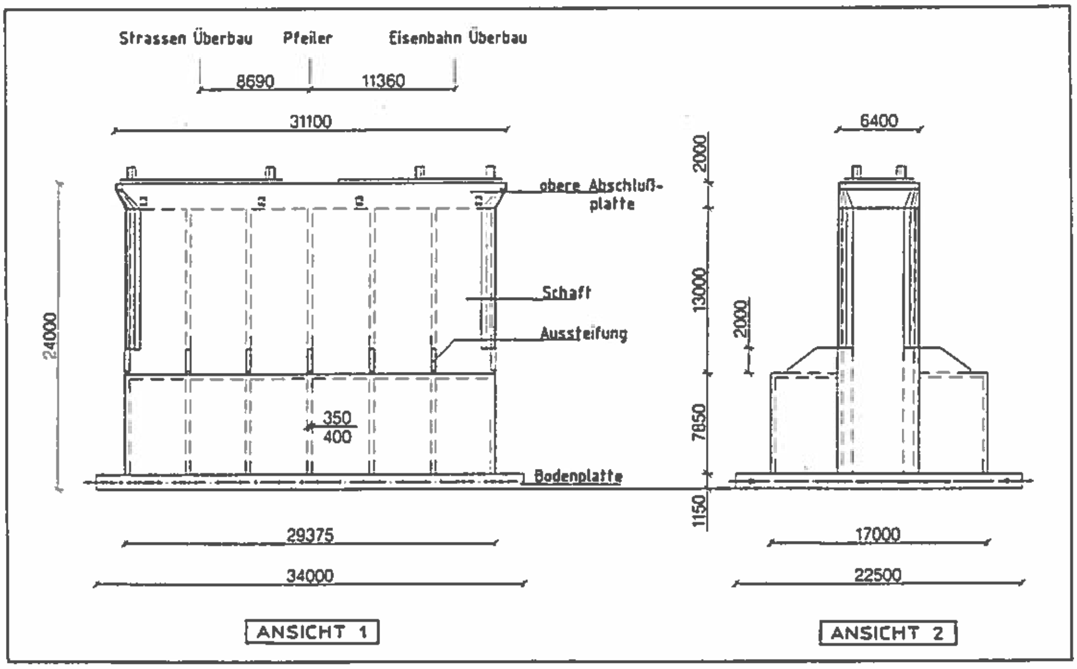

Bild 6. Ansichten von Caisson 38

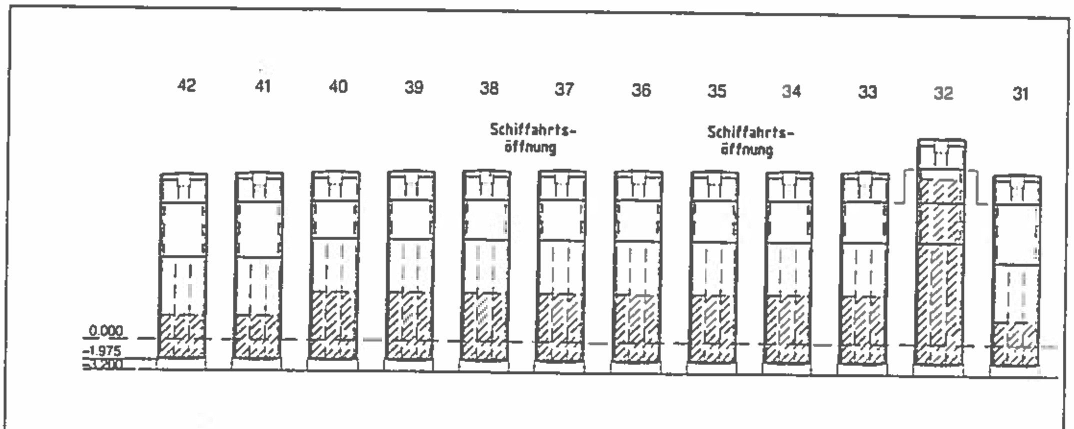

Bild 7. Übersicht der Pfeilerschäfte in Brückenmitte

					Festpunkt						Dehnfuge	
Pfeiler Nummer	42	41	40	39	38	37	36	35	34	33	32	31
Oberkante Pfeilerschaft	+17,137	+17,316	+17,470	+17,601	+17706	+17,788	+17,845	+17878	+17,886	+17,870	+21,403	+17,801
Schafthöhe	19112	19291	19445	19576	19681	19763	19820	19853	19861	19845	23378	19776
Oberkante Füllbeton	+2,500	+2,500	+5,000	+5,000	+5,000	+5,000	+5,000	+5,000	+5,000	+5,000	+17,353	+2,500
Gesamtgewicht des vorgefertigten Schaftes	15290	15360	16320	16380	16420	16460	16480	16490	16500	16490	17940	15560

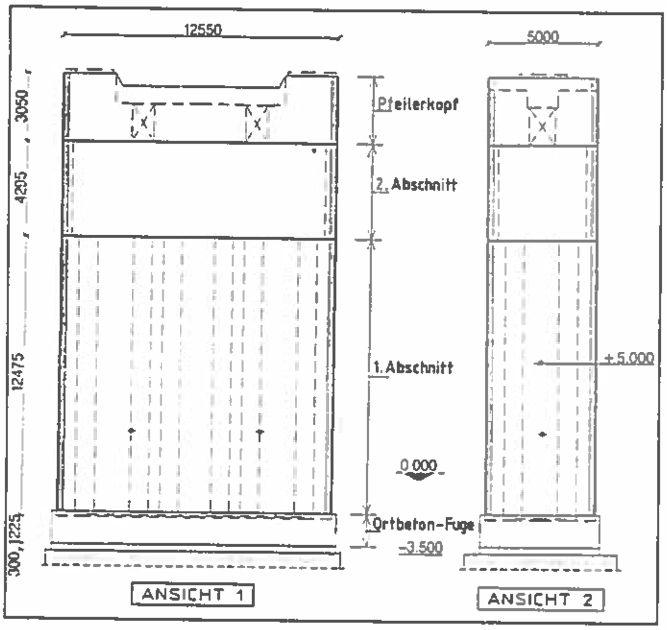

Bild 8. Pfeilerschaft für den Straßenüberbau in Achse 36

Pfeilerkopf sind in der Regel 2 Lagersockel für die Topflager und ausreichende Stellflächen für hydraulische Pressen vorgesehen; auf den Fugenpfeilern sind bei gleichen Abmessungen 4 Lager unterzubringen.

2.3 Die Überbauten

Der Eisenbahnträger folgt mit seiner Achse der Trasse der West Brücke, die mit einem Radius von 20000 m durchgehend gekrümmt ist, die Straßenträgerachse liegt 20 m südlich davon *(Bild 9)*. Die Gradiente wird von der Oberkante der nördlichen Schiene bestimmt und folgt ebenfalls einer durchgehenden Ausrundung mit 500000 m; die maximale Neigung beträgt an den Widerlagern 0,7%.

Die Bauhöhe der Überbauten beträgt für Eisenbahn- bzw. Straßenträger am Pfeiler 8,69 m bzw. 7,34 m und im Feld 5,13 m bzw. 3,78 m. Die Veränderung der Bauhöhe um 3,56 m zwischen Pfeiler und Feldmitte folgt bei beiden Trägern der gleichen Geometrie, die Unterkante des Eisenbahnträgers liegt 1,94 m tiefer. Zwischen den Überbauten verbleibt ein freier Spalt von 1,35 m Breite; die äußeren Randbalken sind in ihrer Außenfläche geneigt um eine optische Betonung zu erzielen.

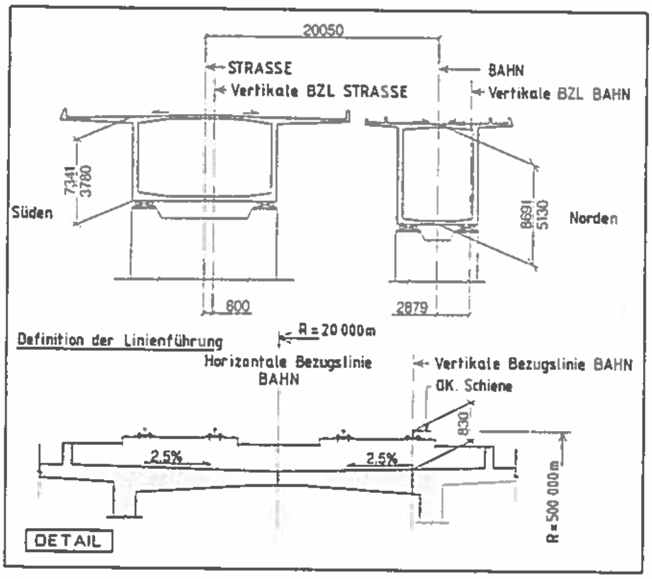

Bild 9. Genereller Querschnitt durch beide Überbauten

Den 25 m breiten Straßenträger mit einer 12,45 m breiten Bodenplatte und lotrechten Stegen mit konstant 500 mm Dicke zeigt *Bild 10* im Querschnitt an der Stütze und im Feld. Die Fahrbahnplatte ist in Querrichtung vorgespannt mit Spanngliedern alle 600 mm und die Längsvorspannung ist sowohl in der Fahrbahnplatte wie der Bodenplatte in der Stegnähe angeordnet. Alle innerhalb der Stege liegenden Spannglieder werden in Lisenen in den Kastenecken verankert; die anderen am Stegende der Betonierabschnitte wobei nur ein Spannglied in einer Lage zu liegen kommt.

Bild 11 beschreibt den Eisenbahnträger, der 13 m breit ist und eine Bodenplatte von 7,1 m Breite und wiederum lotrechte Stege mit 500 mm Dicke hat. Die Vorspannung folgt dem System des Straßenträgers mit halber Anzahl der Querspannglieder und gleichartiger Anordnung der Längsspannglieder. Neben den Randbalken sind

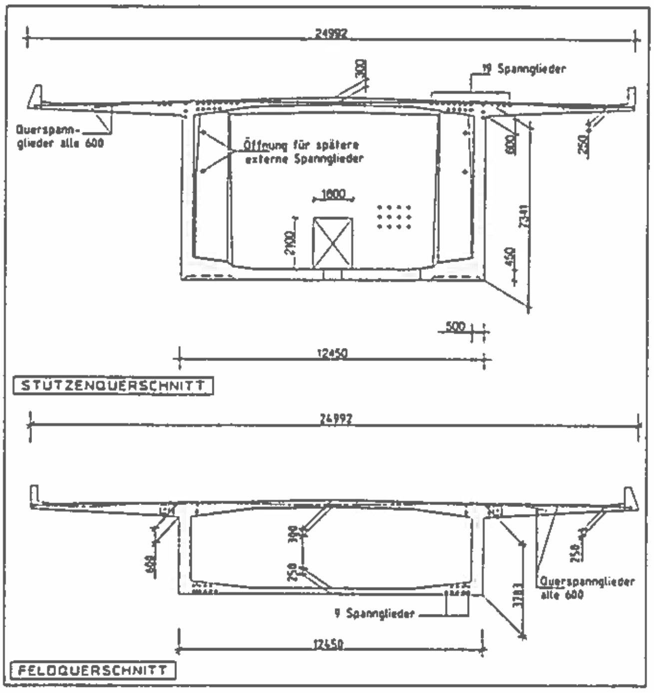

Bild 10. Stützen- und Feldquerschnitt des Straßenträgers

2 Schotterbegrenzungsbalken auf der Fahrbahnplatte angeordnet.

Die Vorspannung erfolgt durch Spannglieder mit 0,6"- Litzen

quer VSL	SO-H 6-4	mit 1060 kN Bruchlast
längs VSL	EC 6-22	mit 5830 kN Bruchlast

die auf maximal 82,5% beim Spannvorgang gespannt und permanent mit bis zu 75% ausgenutzt werden. In Längsrichtung sind die Spannglieder wie folgt verteilt:

	Stütze	Feld
Straßenträger	38	18
Eisenbahnträger	36	16

Alle Stützenspannglieder werden im Zuge der Vorfertigung eingebaut, gespannt und injiziert, während die gesamte Feldvorspannung erst nach dem Fugenschluß folgen kann.

Einen typischen Längsschnitt durch einen Träger zeigt *Bild 12* aus dem die Anordnung der Lisenen ersichtlich ist. Die Träger werden mit 108,4 m Länge in den 5 Abschnitten A bis E mit Teillängen von 18 m und 27,2 m vorgefertigt. Die verbleibende Ortbetonfuge ist damit 2 m breit und dient gleichzeitig zum Ausgleich von Toleranzen beim Versetzen der Caissons. Die Gewichte der Trägerelemente betragen zirka 5700 t bzw. 4300 t.

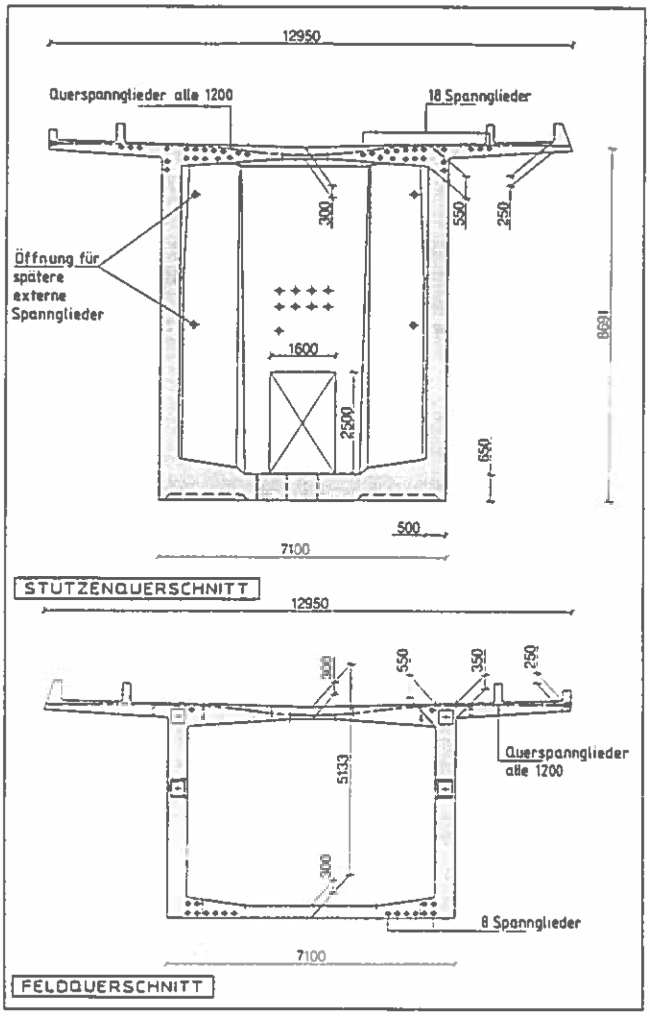

Bild 11. Stützen- und Feldquerschnitt des Eisenbahnträgers

Die Überbauabschnitte mit konstanter Bauhöhe in den Endfeldern werden als getrennte, etwa 26 m lange Elemente mit gleichartiger Detailierung und Vorspannung geplant und hergestellt.

2.4 Besonderheiten der Ausrüstung der West Brücke

Die eisenbahnspezifische Ausrüstung wurde von der Dänischen Staatsbahn (DSB) geplant und von ESG in die Ausführungsplanung übernommen. Sie umfaßt Maßnahmen zur Signalisierung, zum elektrischen Zugbetrieb, eine umfassende Erdungsanlage, Fluchtwege vom Eisenbahn- zum

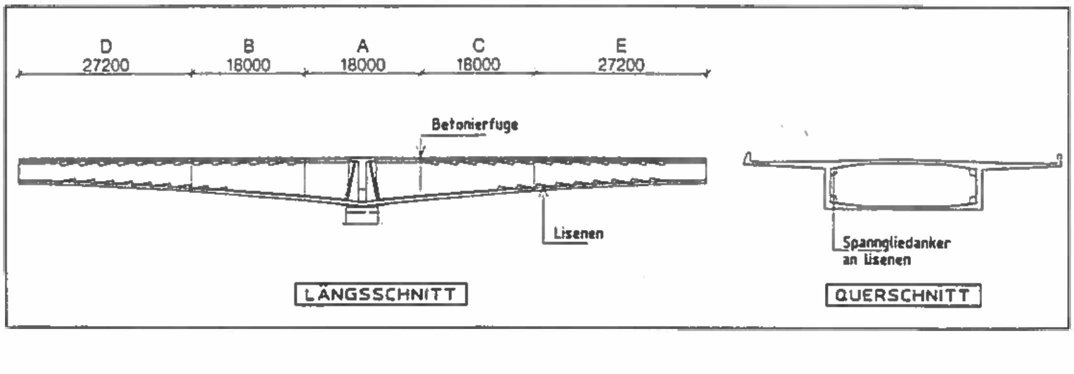

Bild 12. Typischer Längsschnitt eines Trägers mit Betonierfugen

Straßenträger und vielfältige Installationen im Hohlkasten mit Verbindung durch einbetonierte Leerrohre zu allen Ausrüstungselementen auf dem Überbau. Das Schottergleis wird auf der abgedichteten und mit einem Schutzbeton versehenen Fahrbahnplatte aufgebracht und erhält eine Entwässerung.

Die Ausrüstung des Straßenträgers umfaßt eine Erdung des nördlichen Randbalkens, elektrische Versorgungseinrichtungen, Vorkehrungen für Straßenverkehrsleitsysteme und eine Brückenbeleuchtung, Schutzleitplanken in der Fahrbahnmitte und an den Randbalken sowie eine Entwässerung und den Fahrbahnbelag.

Beide Überbauten erhalten die notwendige Ausstattung zum Markieren und Sichern der Schiffahrtsöffnungen und sind über die beiden Widerlager und über Stahltreppen zwischen den Überbauten an den 5 Zwischenfugen zugänglich. In den Hohlkästen können mit elektrisch angetriebenen Spezialfahrzeugen kleinere Ausrüstungsteile zur Unterhaltung transportiert werden.

Die Fugen der Straßenbrücke werden mit wasserdichten Fahrbahnübergängen überbrückt bei denen maximal 16 Dehnprofile mit 80 mm Weg entsprechend 1280 mm Gesamtweg zur Anwendung kommen. Die 7 Fugen der Eisenbahnbrücke enthalten jeweils zwei hydraulische, auf Druck wirkende Puffer, die Bewegungen in der Fuge unter Bremslasten auf maximal 30 mm begrenzen, während langsame Bewegungen unbehindert erfolgen können. Die beiden Widerlagerfugen werden von Standardschienenauszügen SA 60-830 überbrückt, die von der Deutschen Bundesbahn entwickelt wurden und bereits bei vielen Brücken der Neubaustrecken im Einsatz sind. Die 5 mittleren Fugen mit maximalen Wegen von 1400 mm erfordern die Anordnung von zwei der Auszüge SA 60-830 Rücken-an-Rücken zusammen mit einer speziellen, stählernen Unterstützungskonstruktion, die so gesteuert wird, daß der Gesamtweg immer in zwei gleich große Wege an jedem der Auszüge aufgeteilt wird.

Alle Lager sind als Topflager mit zwei seitlichen Führungsleisten ausgebildet, die maximal 50 MN Vertikallast und 10 MN Horizontallast aufnehmen.

3. Besondere Entwurfsgrundlagen

3.1 Allgemeines

Für die Planung der Großen Belt Verbindung wurde eine Lebensdauer der Konstruktionen von 100 Jahren zugrunde gelegt. Das Festlegen und Überprüfen der charakteristischen Belastungen beruht auf dieser Lebensdauer und umfangreichen Risikoanalysen, die für die einzelnen Teile wie die gesamte Verbindung durchgeführt wurden. Die maßgebenden Kriterien waren Betriebsunterbrechungen von unterschiedlicher Dauer und Unfälle mit ihren Konsequenzen für die Bauwerke und deren Benutzer sowie die volkswirtschaftlichen Gesamtfolgen. Die wesentlichen Ergebnisse der Risikoanalyse für die West Brücke sind in *Tabelle 1* zusammengestellt. Darin umfaßt die Schiffskollision Fahrzeuge mit mehr als 2000 BRT, da bis zu dieser Größe die Auswirkungen bereits deterministisch im Entwurf berücksichtigt werden und keinen Beitrag zu einem Risiko mehr leisten können. Für die Eislasten ist aufgrund ausführlicher Studien die in 10000 Jahren einmal auftretende Situation als Basis festgelegt worden.

Die Bandbreite des Risikos aus Schiffskollisionen ergibt sich aus der noch nicht hinreichend genau bekannten Wirkung eines „Vessel-Traffic-Service-System“ (Überwachungssystem), das im Großen Belt installiert werden wird und etwa 14 sm nördlich und südlich der Verbindung erfassen soll. Vergleichbare Systeme sind im Englischen Kanal und in Japan, Bucht von Tokio und Bisan-Seto Straße, in Betrieb. Der Grenzwert von 1,8% für die West Brücke wird eingehalten und dies ist gleichzeitig der Anteil aus dem gesamten Risikobudget der für diesen Teil zur Verfügung steht. Die größte Gefahr für die Sicherheit der West Brücke geht damit von großen Schiffen aus, die fälschlicherweise im westlichen Teil navigieren.

Tabelle 1. Ergebnisse der Risikoanalyse für die West Brücke

Ereignis	Risiko [% pro 100 Jahre]	
	ermittelt	Grenzwert
– Schiffskollision	0,62 ... 0,90	1,00
– Eislasten	0,60	0,80
– Kolkeinfluß	0,10	
– Schäden an Rampen infolge Hochwasser oder Wellen	0,10 ... 0,20	
– Brand und Explosionen	0,05	
Summe:	1,47 ... 1,85	1,80

3.2 Besondere Berechnungsannahmen

Neben den Dänischen Vorschriften sind besondere Berechnungsannahmen für die West Brücke in einem „BBD“ genannten Dokument zusammengefaßt worden. Das Nachweiskonzept beruht auf partiellen Sicherheitsbeiwerten für Lasten und Materialien auf der Basis von charakteristischen Werten und festgelegten Lastfallkombinationen. Nachgewiesen werden der Gebrauchszustand und die Bruchzustände für Normal- und Sonderlasten (Wellen und Strömung, Eislasten, Schiffsanprall). Betriebsfestigkeitsnachweise sind wo erforderlich ebenfalls zu führen.

Die Begrenzung von Spannungen und Rißbreiten unter Gebrauchslasten sind wie in *Tabelle 2* beschrieben festgelegt. Zusätzlich sind Grenzwerte für Verformungen, insbesondere für den Eisenbahnträger, definiert. Ebenso ist für den Eisenbahnbetrieb ein Komfortniveau einzuhalten, das heißt die vertikale Beschleunigung beim Überfahren eines Zuges darf nicht mehr als 0,2 x g für die Passagiere von Personenzügen betragen. Die größte Beschleunigung tritt an einer Fuge zwischen Durchlaufträgern auf, da dort die Trägerdurchbiegung einen zusätzlichen Drehwinkelknick erzeugt, der wesentlich zur Laufunruhe beiträgt.

Tabelle 2. Begrenzung von Spannungen und Rißbreiten im Gebrauchszustand

	Lastkombination	Druckspannung	Rißbreite in [mm]
a.	Alle ständigen Lasten einschl. Vorspannung	1/3 fck	*)
b.	a + 50% Verkehrslast	1/2 fck	0,2 (0,3)
c.	a + Temperaturwirkungen	1/2 fck	0,3 (0,4)

*) keine Zugspannungen in vorgespannten Bauteilen und Pfeilerschäften oberhalb von –2,0 m

(...) Werte in Klammern für Pfeilerbereiche unterhalb von –2,0 m

fck = 45 MPa

3.3 Anforderungen an Betonkonstruktionen

Der Entwurf von Betonkonstruktionen für eine gezielte Lebensdauer geht von der folgenden Zielvorgabe aus:

> Eine Betonkonstruktion soll so entworfen, ausgeführt und unterhalten werden, daß sie unter den zu erwartenden klimatischen Einwirkungen ihre Sicherheit, ihre Gebrauchsfähigkeit und ein zufriedenstellendes Aussehen über einen bestimmten Zeitabschnitt aufrecht erhalten kann, ohne daß unvorhergesehen hohe Ausgaben zur Unterhaltung oder Reparatur notwendig werden.

Diese Vorgabe erfordert Entscheidungen zu den Berechnungsvoraussetzungen, zum Qualitätssicherungsniveau für Planung und Ausführung sowie zu Unterhaltungsstrategie und -technik. Für die West Brücke wurden definiert:

- Anwenden der Elastizitätstheorie
- nur zwei Betonsorten mit besonderen Anforderungen
- umfangreiche Kontrollen während der Ausführung
- Qualitätssicherung nach ISO 9001 von Anbeginn an
- Erstellen eines „Operation/Maintenance Manual".

Durch die Zusammenarbeit zwischen Bauherrn, Planer, Unternehmer und Betreiber unter Beachtung von Vorgaben soll das Ziel einer Lebensdauer von 100 Jahren erreicht werden.

In diesem Zusammenhang sind an die Zusammensetzung, Herstellung, Verarbeitung und Nachbehandlung des Betons besondere Anforderungen zu stellen. Die wesentlichen Daten sind in *Tabelle 3* zusammengestellt. Während die Betone A und B in stationärer Schalung verwendet werden, hat ESG für das Gleiten der Caissonwände einen von Beton B abgeleiteten Typ mit einer größeren Wasserzugabe geprüft und gewählt.

Tabelle 3. Beton; Anforderungen und Prüfungen

Betonrezepturen
Typ A : Pfeilerschäfte, Randbalken der Straßenträger
Typ B : alle anderen Teile
Typ 200 : Caissonwände in Gleitschalung (von ESG gewählt).

Bestandteil [kg/m3]	Typ A	Typ B	Typ 200 (B)
Portlandzement	331	333	338
Flugasche	40	40	74
Microsilika	20	20	20
Wasser	133	133	154
Sand 0/8	438	430	537
Granit 8/16	450	446	368
Granit 16/32	639	628	554
W/Z effektiv	0,34	0,34	0,38
W/Z maximal	0,35	0,45	

Zusatzmittel : BV, LP, FM

Besondere Anforderungen und Prüfungen

Anforderungen

- Nachbehandlung bis zu 240 bzw. 96 Reifestunden
- Temperaturdifferenz innerhalb eines Bauteiles < 20 °C
  zwischen altem / neuem Beton < 12 °C
- Chlorideindringen D ~ $6 \cdot 10^{-13}$ m²/s bei 20 °C
  für Typ A; für B eine Größenordnung größer

Prüfungen

- Betonierversuche für unterschiedliche Bauteile
- LOK- oder CAPO-Tests zusätzlich zu Zylinderprüfungen

Um eine reduzierte Dauerhaftigkeit auszuschließen, wurde für die Caissons ein kathodischer Korrosionsschutz eingeführt, der auf der Basis von Zink-Kupferanoden arbeitet, die nach 5–7 Jahren zu erneuern sind.

3.4 Mehrstufen-Strategie zur Dauerhaftigkeit

STOREBAELT hat in Zusammenarbeit mit den beteiligten planenden Ingenieuren und externen Beratern eine Mehrstufen-Strategie zum Sicherstellen der Dauerhaftigkeit der Betonkonstruktionen entwickelt, die einen wirtschaftlichen Einsatz von insgesamt 1,1 Millionen Kubikmeter Beton gewährleisten soll.

Neben dem Beschreiben der Transportmechanismen von aggressiven Substanzen sind mögliche Schutzmaßnahmen zu identifizieren. Diese sind z.B.:

- hochwertiger Beton
- größere Betondeckung, eventuell mit einer Hautbewehrung
- epoxidharz-beschichtete Bewehrung
- kathodischer Korrosionsschutz oder Vorbereitungen dafür
- Oberflächenbeschichtung oder Schutzmantel
- gute Detaillierung wie Mindestneigung, gerundete Kanten, geringe Fugenanzahl u.s.w.

Sie werden richtig geplant nacheinander zur Wirkung gebracht.

Während für den Eisenbahntunnel die möglichen Schutzmaßnahmen vollständig angewendet wurden, war für die West Brücke eine Entscheidung unter Einbeziehen der langfristig zu erwartenden Gesamtkosten zu treffen, da hier später einzuführende Schutzmaßnahmen aufgrund der Zugänglichkeit ebenso berücksichtigt werden können. Das Abwägen der technischen und wirtschaftlichen Gesichtspunkte hat zu der Wahl folgender Maßnahmen geführt:

- nur 2 Betonsorten A und B
- Beton A ist um eine Größenordnung dichter hinsichtlich Chlorideindringens
- Pfeilerschäfte und Randbalken aus Beton A; sonst Beton B
- Betondeckung von
  70 + 5 mm Pfeilerschäfte außen
  50 + 5 mm Caissons, Widerlager, Pfeilerschäfte innen
  45 + 5 mm Überbauten außen
  30 + 5 mm Oberseite Fahrbahnplatten, Überbauten innen
- Kontrolle des Fortschreitens des Chlorideindringens.

Die zuletzt genannte Kontrolle geschieht mit eingebauten Sensoren *(Bild 13)*, an drei verschiedenen Positionen in Brückenlängsrichtung sowohl in den Pfeilerschäften als auch in den Überbauten. Über Anschlüsse für Registriergeräte kann entweder eine permanente oder zu beliebigen Zeitpunkten durchzuführende Kontrolle gewählt werden. Gemessen werden Stromstärke zwischen einem Anodenstab bzw. Bewehrungsstab und dem Kathodenstab, das Potential zwischen Referenzzelle und Anoden-, Bewehrungs- und Kathodenstab, sowie der Widerstand zwischen verschiede-

Straßenträger und vielfältige Installationen im Hohlkasten mit Verbindung durch einbetonierte Leerrohre zu allen Ausrüstungselementen auf dem Überbau. Das Schottergleis wird auf der abgedichteten und mit einem Schutzbeton versehenen Fahrbahnplatte aufgebracht und erhält eine Entwässerung.

Die Ausrüstung des Straßenträgers umfaßt eine Erdung des nördlichen Randbalkens, elektrische Versorgungseinrichtungen, Vorkehrungen für Straßenverkehrsleitsysteme und eine Brückenbeleuchtung, Schutzleitplanken in der Fahrbahnmitte und an den Randbalken sowie eine Entwässerung und den Fahrbahnbelag.

Beide Überbauten erhalten die notwendige Ausstattung zum Markieren und Sichern der Schiffahrtsöffnungen und sind über die beiden Widerlager und über Stahltreppen zwischen den Überbauten an den 5 Zwischenfugen zugänglich. In den Hohlkästen können mit elektrisch angetriebenen Spezialfahrzeugen kleinere Ausrüstungsteile zur Unterhaltung transportiert werden.

Die Fugen der Straßenbrücke werden mit wasserdichten Fahrbahnübergängen überbrückt bei denen maximal 16 Dehnprofile mit 80 mm Weg entsprechend 1280 mm Gesamtweg zur Anwendung kommen. Die 7 Fugen der Eisenbahnbrücke enthalten jeweils zwei hydraulische, auf Druck wirkende Puffer, die Bewegungen in der Fuge unter Bremslasten auf maximal 30 mm begrenzen, während langsame Bewegungen unbehindert erfolgen können. Die beiden Widerlagerfugen werden von Standardschienenauszügen SA 60-830 überbrückt, die von der Deutschen Bundesbahn entwickelt wurden und bereits bei vielen Brücken der Neubaustrecken im Einsatz sind. Die 5 mittleren Fugen mit maximalen Wegen von 1400 mm erfordern die Anordnung von zwei der Auszüge SA 60-830 Rücken-an-Rücken zusammen mit einer speziellen, stählernen Unterstützungskonstruktion, die so gesteuert wird, daß der Gesamtweg immer in zwei gleich große Wege an jedem der Auszüge aufgeteilt wird.

Alle Lager sind als Topflager mit zwei seitlichen Führungsleisten ausgebildet, die maximal 50 MN Vertikallast und 10 MN Horizontallast aufnehmen.

3. Besondere Entwurfsgrundlagen

3.1 Allgemeines

Für die Planung der Großen Belt Verbindung wurde eine Lebensdauer der Konstruktionen von 100 Jahren zugrunde gelegt. Das Festlegen und Überprüfen der charakteristischen Belastungen beruht auf dieser Lebensdauer und umfangreichen Risikoanalysen, die für die einzelnen Teile wie die gesamte Verbindung durchgeführt wurden. Die maßgebenden Kriterien waren Betriebsunterbrechungen von unterschiedlicher Dauer und Unfälle mit ihren Konsequenzen für die Bauwerke und deren Benutzer sowie die volkswirtschaftlichen Gesamtfolgen. Die wesentlichen Ergebnisse der Risikoanalyse für die West Brücke sind in *Tabelle 1* zusammengestellt. Darin umfaßt die Schiffskollision Fahrzeuge mit mehr als 2000 BRT, da bis zu dieser Größe die Auswirkungen bereits deterministisch im Entwurf berücksichtigt werden und keinen Beitrag zu einem Risiko mehr leisten können. Für die Eislasten ist aufgrund ausführlicher Studien die in 10000 Jahren einmal auftretende Situation als Basis festgelegt worden.

Tabelle 1. Ergebnisse der Risikoanalyse für die West Brücke

Ereignis	Risiko [% pro 100 Jahre]	
	ermittelt	Grenzwert
– Schiffskollision	0,62 ... 0,90	1,00
– Eislasten	0,60	0,80
– Kolkeinfluß	0,10	
– Schäden an Rampen infolge Hochwasser oder Wellen	0,10 ... 0,20	
– Brand und Explosionen	0,05	
Summe:	1,47 ... 1,85	1,80

Die Bandbreite des Risikos aus Schiffskollisionen ergibt sich aus der noch nicht hinreichend genau bekannten Wirkung eines „Vessel-Traffic-Service-System" (Überwachungssystem), das im Großen Belt installiert werden wird und etwa 14 sm nördlich und südlich der Verbindung erfassen soll. Vergleichbare Systeme sind im Englischen Kanal und in Japan, Bucht von Tokio und Bisan-Seto Straße, in Betrieb. Der Grenzwert von 1,8% für die West Brücke wird eingehalten und dies ist gleichzeitig der Anteil aus dem gesamten Risikobudget der für diesen Teil zur Verfügung steht. Die größte Gefahr für die Sicherheit der West Brücke geht damit von großen Schiffen aus, die fälschlicherweise im westlichen Teil navigieren.

3.2 Besondere Berechnungsannahmen

Neben den Dänischen Vorschriften sind besondere Berechnungsannahmen für die West Brücke in einem „BBD" genannten Dokument zusammengefaßt worden. Das Nachweiskonzept beruht auf partiellen Sicherheitsbeiwerten für Lasten und Materialien auf der Basis von charakteristischen Werten und festgelegten Lastfallkombinationen. Nachgewiesen werden der Gebrauchszustand und die Bruchzustände für Normal- und Sonderlasten (Wellen und Strömung, Eislasten, Schiffsanprall). Betriebsfestigkeitsnachweise sind wo erforderlich ebenfalls zu führen.

Die Begrenzung von Spannungen und Rißbreiten unter Gebrauchslasten sind wie in *Tabelle 2* beschrieben festgelegt. Zusätzlich sind Grenzwerte für Verformungen, insbesondere für den Eisenbahnträger, definiert. Ebenso ist für den Eisenbahnbetrieb ein Komfortniveau einzuhalten, das heißt die vertikale Beschleunigung beim Überfahren eines Zuges darf nicht mehr als 0,2 x g für die Passagiere von Personenzügen betragen. Die größte Beschleunigung tritt an einer Fuge zwischen Durchlaufträgern auf, da dort die Trägerdurchbiegung einen zusätzlichen Drehwinkelknick erzeugt, der wesentlich zur Laufunruhe beiträgt.

Tabelle 2. Begrenzung von Spannungen und Rißbreiten im Gebrauchszustand

	Lastkombination	Druckspannung	Rißbreite in [mm]
a.	Alle ständigen Lasten einschl. Vorspannung	1/3 fck	*)
b.	a + 50% Verkehrslast	1/2 fck	0,2 (0,3)
c.	a + Temperaturwirkungen	1/2 fck	0,3 (0,4)

*) keine Zugspannungen in vorgespannten Bauteilen und Pfeilerschäften oberhalb von –2,0 m

(...) Werte in Klammern für Pfeilerbereiche unterhalb von –2,0 m

fck = 45 MPa

3.3 Anforderungen an Betonkonstruktionen

Der Entwurf von Betonkonstruktionen für eine gezielte Lebensdauer geht von der folgenden Zielvorgabe aus:

> Eine Betonkonstruktion soll so entworfen, ausgeführt und unterhalten werden, daß sie unter den zu erwartenden klimatischen Einwirkungen ihre Sicherheit, ihre Gebrauchsfähigkeit und ein zufriedenstellendes Aussehen über einen bestimmten Zeitabschnitt aufrecht erhalten kann, ohne daß unvorhergesehen hohe Ausgaben zur Unterhaltung oder Reparatur notwendig werden.

Diese Vorgabe erfordert Entscheidungen zu den Berechnungsvoraussetzungen, zum Qualitätssicherungsniveau für Planung und Ausführung sowie zu Unterhaltungsstrategie und -technik. Für die West Brücke wurden definiert:

- Anwenden der Elastizitätstheorie
- nur zwei Betonsorten mit besonderen Anforderungen
- umfangreiche Kontrollen während der Ausführung
- Qualitätssicherung nach ISO 9001 von Anbeginn an
- Erstellen eines „Operation/Maintenance Manual".

Durch die Zusammenarbeit zwischen Bauherrn, Planer, Unternehmer und Betreiber unter Beachtung von Vorgaben soll das Ziel einer Lebensdauer von 100 Jahren erreicht werden.

In diesem Zusammenhang sind an die Zusammensetzung, Herstellung, Verarbeitung und Nachbehandlung des Betons besondere Anforderungen zu stellen. Die wesentlichen Daten sind in *Tabelle 3* zusammengestellt. Während die Betone A und B in stationärer Schalung verwendet werden, hat ESG für das Gleiten der Caissonwände einen von Beton B abgeleiteten Typ mit einer größeren Wasserzugabe geprüft und gewählt.

Tabelle 3. Beton; Anforderungen und Prüfungen

Betonrezepturen
Typ A : Pfeilerschäfte, Randbalken der Straßenträger
Typ B : alle anderen Teile
Typ 200 : Caissonwände in Gleitschalung (von ESG gewählt).

Bestandteil [kg/m3]	Typ A	Typ B	Typ 200 (B)
Portlandzement	331	333	338
Flugasche	40	40	74
Microsilika	20	20	20
Wasser	133	133	154
Sand 0/8	438	430	537
Granit 8/16	450	446	368
Granit 16/32	639	628	554
W/Z effektiv	0,34	0,34	0,38
W/Z maximal	0,35	0,45	

Zusatzmittel : BV, LP, FM

Besondere Anforderungen und Prüfungen

Anforderungen

- Nachbehandlung bis zu 240 bzw. 96 Reifestunden
- Temperaturdifferenz innerhalb eines Bauteiles < 20 °C
  zwischen altem / neuem Beton < 12 °C
- Chlorideindringen $D \sim 6 \cdot 10^{-13}\ m^2/s$ bei 20 °C
  für Typ A; für B eine Größenordnung größer

Prüfungen

- Betonierversuche für unterschiedliche Bauteile
- LOK- oder CAPO-Tests zusätzlich zu Zylinderprüfungen

Um eine reduzierte Dauerhaftigkeit auszuschließen, wurde für die Caissons ein kathodischer Korrosionsschutz eingeführt, der auf der Basis von Zink-Kupferanoden arbeitet, die nach 5–7 Jahren zu erneuern sind.

3.4 Mehrstufen-Strategie zur Dauerhaftigkeit

STOREBAELT hat in Zusammenarbeit mit den beteiligten planenden Ingenieuren und externen Beratern eine Mehrstufen-Strategie zum Sicherstellen der Dauerhaftigkeit der Betonkonstruktionen entwickelt, die einen wirtschaftlichen Einsatz von insgesamt 1,1 Millionen Kubikmeter Beton gewährleisten soll.

Neben dem Beschreiben der Transportmechanismen von aggressiven Substanzen sind mögliche Schutzmaßnahmen zu identifizieren. Diese sind z.B.:

- hochwertiger Beton
- größere Betondeckung, eventuell mit einer Hautbewehrung
- epoxidharz-beschichtete Bewehrung
- kathodischer Korrosionsschutz oder Vorbereitungen dafür
- Oberflächenbeschichtung oder Schutzmantel
- gute Detaillierung wie Mindestneigung, gerundete Kanten, geringe Fugenanzahl u.s.w.

Sie werden richtig geplant nacheinander zur Wirkung gebracht.

Während für den Eisenbahntunnel die möglichen Schutzmaßnahmen vollständig angewendet wurden, war für die West Brücke eine Entscheidung unter Einbeziehen der langfristig zu erwartenden Gesamtkosten zu treffen, da hier später einzuführende Schutzmaßnahmen aufgrund der Zugänglichkeit ebenso berücksichtigt werden können. Das Abwägen der technischen und wirtschaftlichen Gesichtspunkte hat zu der Wahl folgender Maßnahmen geführt:

- nur 2 Betonsorten A und B
- Beton A ist um eine Größenordnung dichter hinsichtlich Chlorideindringens
- Pfeilerschäfte und Randbalken aus Beton A; sonst Beton B
- Betondeckung von
  70 + 5 mm Pfeilerschäfte außen
  50 + 5 mm Caissons, Widerlager, Pfeilerschäfte innen
  45 + 5 mm Überbauten außen
  30 + 5 mm Oberseite Fahrbahnplatten, Überbauten innen
- Kontrolle des Fortschreitens des Chlorideindringens.

Die zuletzt genannte Kontrolle geschieht mit eingebauten Sensoren *(Bild 13)*, an drei verschiedenen Positionen in Brückenlängsrichtung sowohl in den Pfeilerschäften als auch in den Überbauten. Über Anschlüsse für Registriergeräte kann entweder eine permanente oder zu beliebigen Zeitpunkten durchzuführende Kontrolle gewählt werden. Gemessen werden Stromstärke zwischen einem Anodenstab bzw. Bewehrungsstab und dem Kathodenstab, das Potential zwischen Referenzzelle und Anoden-, Bewehrungs- und Kathodenstab, sowie der Widerstand zwischen verschiede-

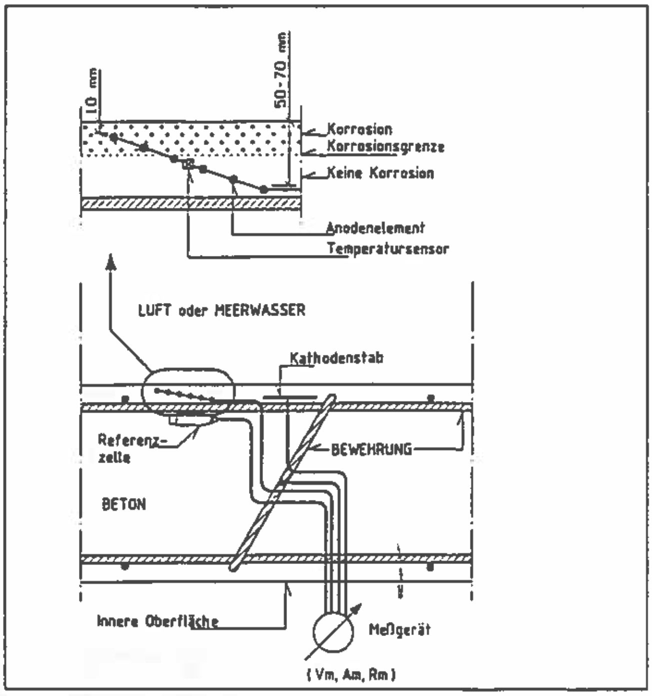

Bild 13. Sensorenanordnung zur Kontrolle der Korrosion

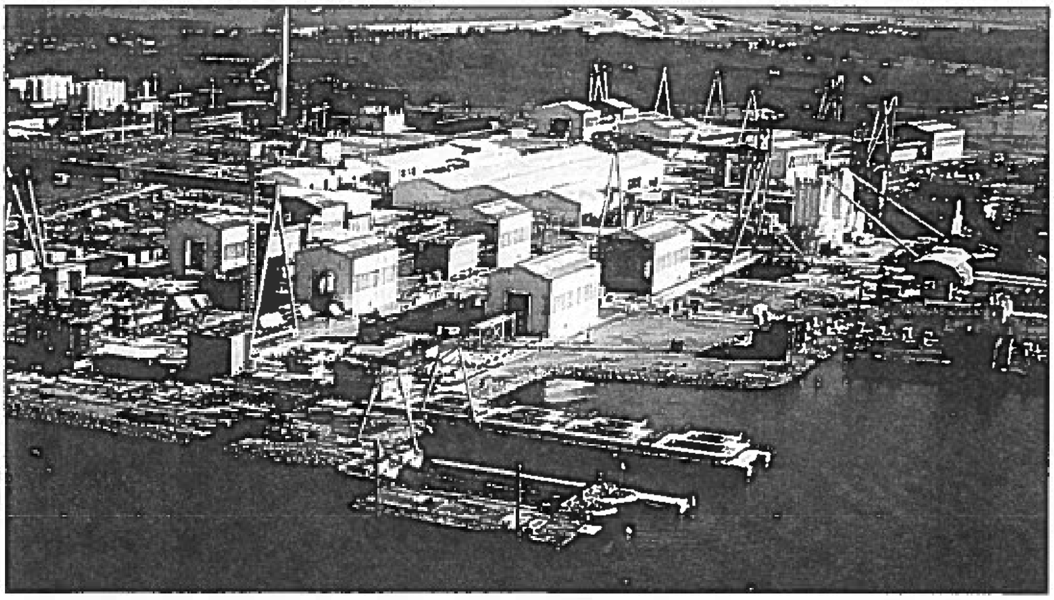

Bild 14. Herstellungsplatz Lindholm von Westen gesehen

nen Anodenstäben. Zusätzlich wird die Temperatur über Widerstandsmessungen bestimmt. Die Auswertung verwendet Ergebnisse von Kalibrierungsversuchen im Labor, ist aber darüberhinaus auf am Bauwerk gewonnene Erfahrungen angewiesen.

4. Herstellen der Elemente

4.1 Herstellungsplatz in Lindholm

Im südwestlich von der Brücke liefenden Nyborg Fjord ist der Herstellungplatz auf einem aufgefüllten Gelände, genannt LINDHOLM errichtet worden. Das Ausführungskonzept von ESG erfordert die Herstellung von großen Elementen in 5 Produktionslinien, je eine für Eisenbahnträger, Straßenträger und Pfeilerschäfte sowie zwei für Caissons. Die größten Transportgewichte betragen 7100 t für die Caissons, 5700 t bzw. 4300 t für die Straßen- bzw. Eisenbahnträger und 1800 t für die Schäfte.

Innerhalb der Fertigung werden alle Elemente auf Gleitbahnen verschoben; dazu ist jede Ferigungslinie mit einer „skidding machine" ausgestattet, die etwa 5% der Vertikallast als Verschubkraft aufbringen muß. Die Vertikallast wird über die Gleitbahnen – rostfreier Stahl und Teflon – direkt in die Fundamentbalken übertragen. Die für die Träger eingesetzten Verschubschlitten können die Überbauelemente zusätzlich hydraulisch heben, um sie von ihren Lagerpunkten zuerst abzuheben und später wieder abzusetzen.

Eine Übersicht über den Herstellungsplatz vermittelt *Bild 14*, das die Pfeilerschaft-Fertigungslinie im Vordergrund zeigt und dahinter die Fertigungslinie für Eisenbahnträger erkennen läßt.

4.2 Herstellung der Caissons

Einen Überblick über die beiden Fertigungslinien für Caissons vermittelt *Bild 15* auf dem im Vordergrund der Schwimmkran „Svanen" zu sehen ist. Die Pontons wurden in La Coruña, Spanien hergestellt und nach Rotterdam geschleppt wo der Kranaufbau montiert wurde. Danach hat der Schwimmkran die Reise nach Nyborg rund Skagen auf eigenem Kiel absolviert.

In den beiden Fertigungslinien werden Caissons parallel hergestellt, zuerst wird die Bodenplatte in einer ersten Position bewehrt und dann zum Betonieren in die zweite Position verschoben. Dort werden die Wände in einer Gleitschalung hergestellt, die von einen Portal aus über Litzen von Hebern ohne Gebrauch von Kletterstangen gehoben wird. Damit ist die Schalung universell für unterschiedliche Caissonhöhen einsetzbar und zugleich mit dem Portal zwischen den beiden Fertigungslinien verfahrbar. Abschließend werden die untere und obere Abschlußplatte auf verlorener Schalung betoniert. Einige fertige Caissons zeigt *Bild 16*.

4.3 Herstellung der Pfeilerschäfte

Die Pfeilerschäfte werden jeweils als ein zu einem Caisson gehörendes Paar auf einer Plattform gemeinsam her-

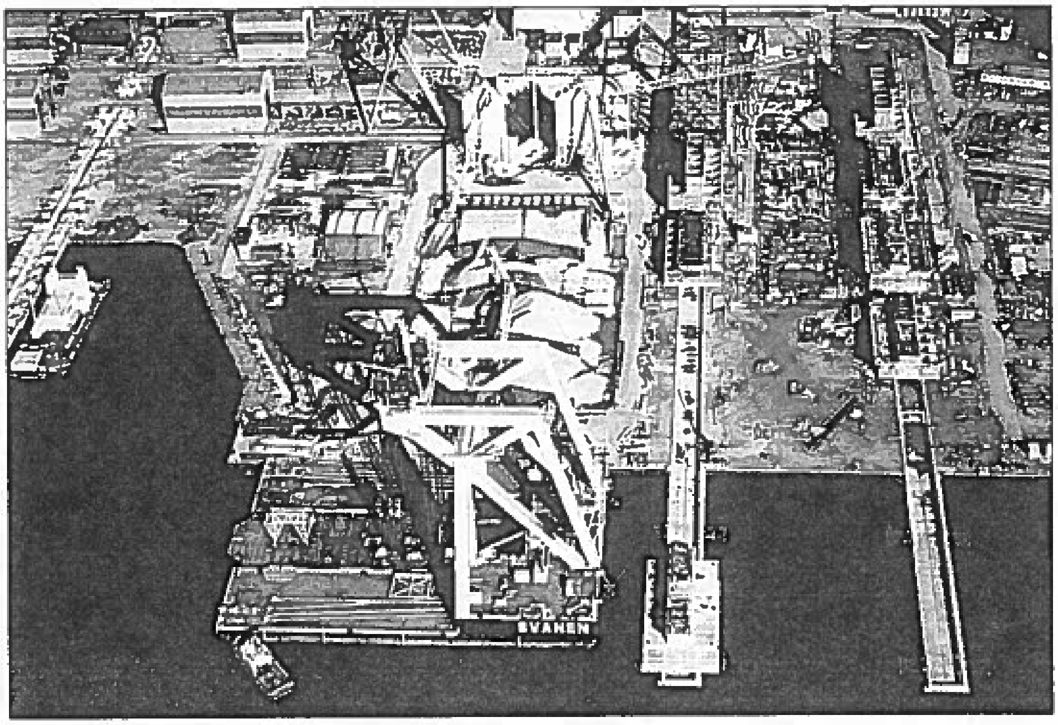

Bild 15. Fertigungslinien der Caissons mit Schwimmkran im Vordergrund

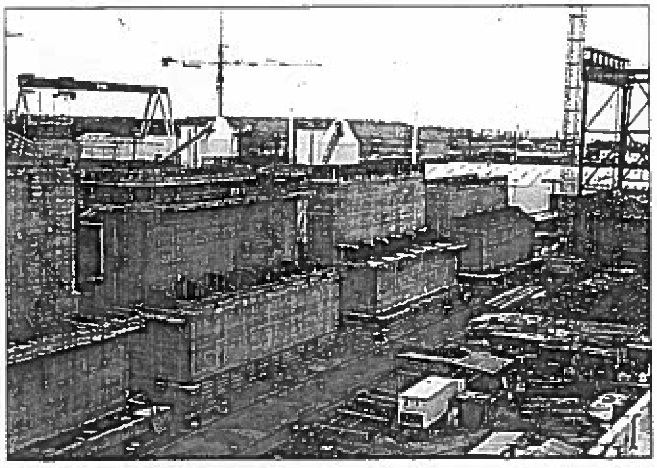

Bild 16. Fertiggestellte Caissons mit Gleitgerüst am Bildrand rechts

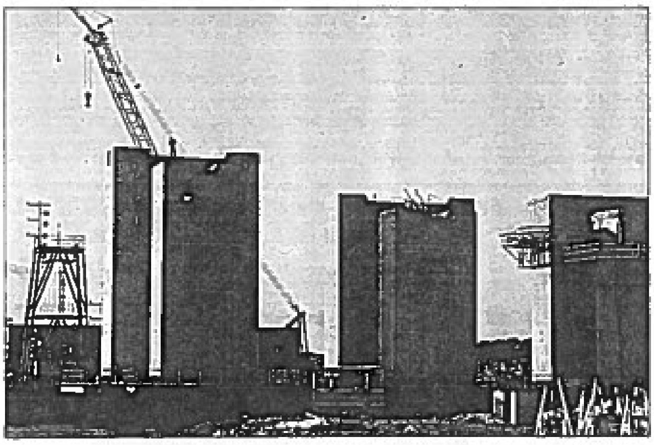

Bild 17. Pfeilerschäfte in der Fertigungslinie, hoher Schaft eines Trennpfeilers links im Bild

gestellt. Die Bewehrungskörbe werden weitgehend vorgefertigt. Der Schaft wird entsprechend seinen unterschiedlichen Querschnitten in 3 Abschnitten betoniert, unterer ausgesteifter und normaler Querschnitt sowie Pfeilerkopf. Fertige Schäfte zeigt *Bild 17*, auf dem das höhere linke Schaftpaar zu einem Trennpfeiler gehört.

4.4 Herstellung der Brückenträger

Die verschiedenen Stufen der Trägerherstellung sind in beiden Fertigungslinien gleich und am Beispiel von *Bild 18*, das die Fertigungslinie der Straßenträger im Vordergrund zeigt, soll die Herstellung näher beschrieben werden. In den 6 Arbeitsstationen jeder Fertigungslinie wird in den Posi-

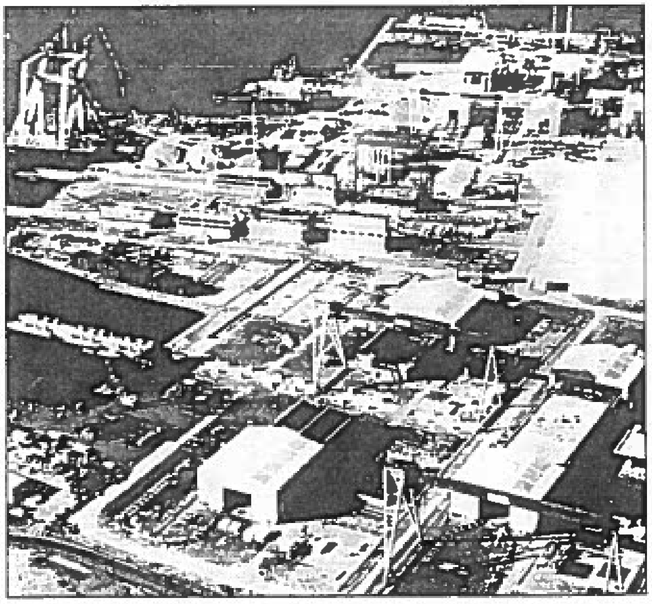

Bild 18. Blick auf den Herstellungsplatz von Osten mit Straßenträgerlinie im Vordergrund, Position 1 am rechten Bildrand

tionen 1, 3 und 5 in Stahlschalungen zuerst der Abschnitt A, danach die Abschnitte B, C und anschließend die Abschnitte D, E betoniert. Dies erfolgt im Schutz von mobilen Produktionshallen in denen die Erhärtung der Trägerabschnitte durch Dampf von 40–50°C gesteuert wird und ein Ausschalen erst nach 96 Reifestunden erfolgt. Bei ausreichender Betonfestigkeit werden die Träger vorgespannt und jeweils über die Zwischenstationen 2 und 4 zur nächsten Position als symmetrische Träger verschoben. In der Position 6 werden alle Spannglieder injiziert und erforderliche Nachbesserungsarbeiten durchgeführt. Die folgenden Positionen der Fertigungslinien sind Lagerplätze für fertige Träger und von der letzten Position werden die Träger später vom Schwimmkran aufgenommen.

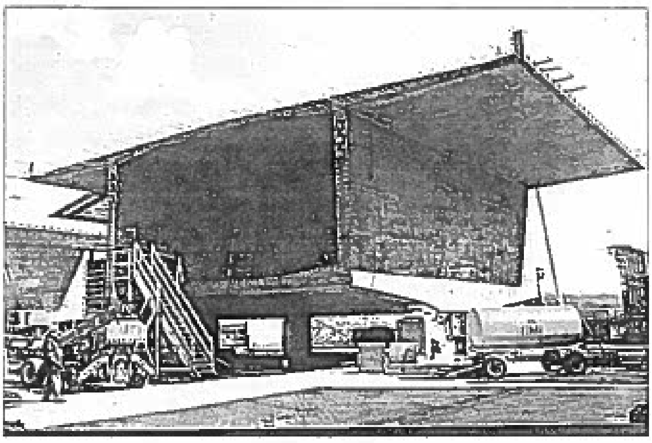

Bild 19. Abschnitt A eines Straßenträgers in Position 2

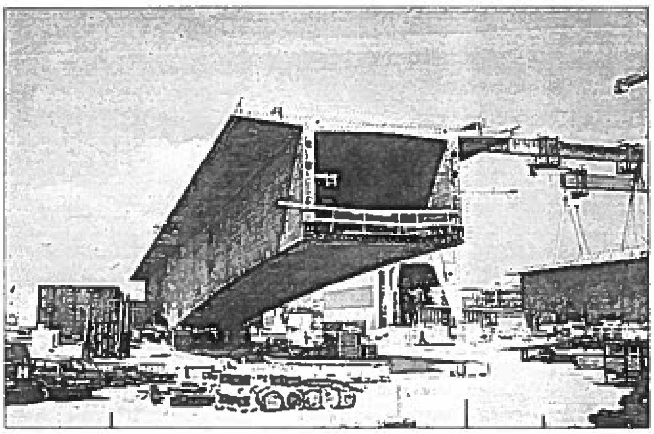

Bild 20. Eisenbahnträger von 108 m Länge, Abschnitte D,B,A,C,E

Den Abschnitt A eines Straßenträgers zeigt *Bild 19* und einen fertigen, 108 m langen Eisenbahnträger das *Bild 20.*

5. Gründungsarbeiten, Transport und Montage

5.1 Gründungsarbeiten

Die Caissons werden direkt in Tiefen von 12–33 m unter der Meeresoberfläche und 2–15 m unter dem Meeresboden gegründet. Der Aushub der Fundamentsohlen erfolgte mit einem Eimerkettenbagger. Nach der Überprüfung der Gründungssohle durch Bohrungen und CPT's wird eine speziell ausgerüstete Hubinsel positioniert, von der aus die Sohle gesäubert und überprüft wird *(Bild 21).* Danach wird von der Hubinsel eine 1,5 m dicke Steinschüttung eingebaut und von einem Flächenvibrator auf etwa 1,2 m verdichtet. An einigen Gründungen sind bis zu 4 m dicke Steinschichten vorgesehen, die lagenweise eingebaut und verdichtet werden. Eine 0,3–0,6 m obere Lage loser Steine wird anschließend eingebaut und sehr genau abgezogen. Darauf wird später der Caisson direkt aufgesetzt, ein Injizieren unter der Betonplatte erfolgt nicht.

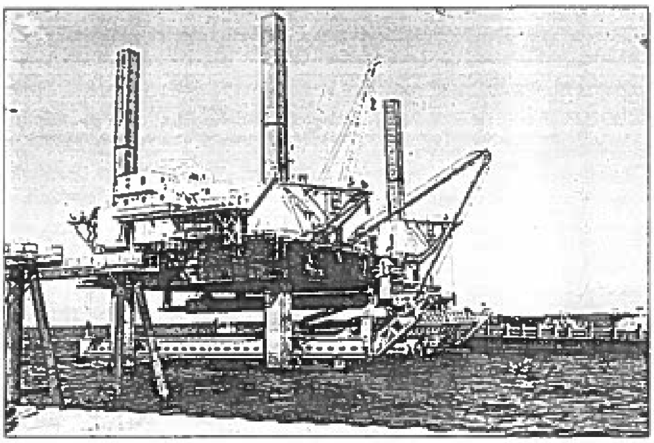

Bild 21. Hubinsel Buzzard verlegt Steinschüttung am Pfeiler 63

5.2 Transport und Montage

5.2.1 Unterbauten

Bevor die Caissons zum Transport bereit sind, werden auf der Oberseite zwei stählerne Fangdämme installiert, die von –3,5 m bis über die Wasseroberfläche reichen, um den An-

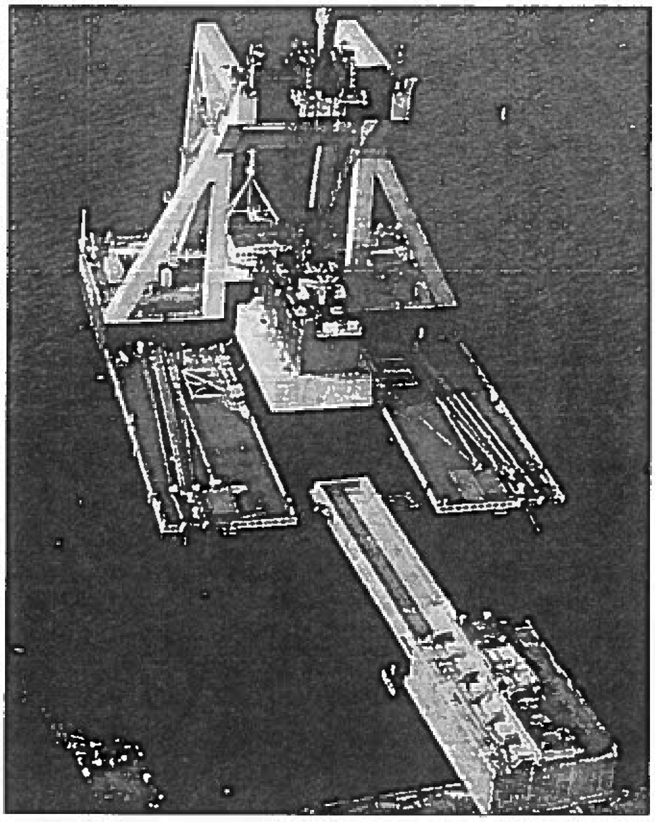

Bild 22. Der erste Caisson wird vom Schwimmkran abtransportiert

schluß der Pfeilerschäfte im Trockenen zu ermöglichen. *Bild 22* zeigt wie ein fertig ausgerüsteter Caisson vom Schwimmkran aufgenommen wird.

Nach dem Absetzen des Caissons auf der Steinschüttung wird der verbleibende Aushubraum verfüllt und um den Caisson herum in zwei Lagen ein Erosionsschutz gegen Auskolkungen eingebaut. Der Caisson wird mit Sand gefüllt, um die Standsicherheit gegen große Horizontallasten aus Eisdruck, Schiffsanprall oder Wellengang zu erzielen.

Die Pfeilerschäfte werden als ein Paar transportiert und dann nacheinander auf den Caisson abgesetzt. Die Fuge wird anschließend bewehrt und betoniert und nach einer Reifezeit von 96 Stunden kann die Schalung und der Fangedamm entfernt werden. Auf den Pfeilerköpfen werden die endgültigen Topflager und hydraulische Pressen als temporäre Auflagerpunkte für die Trägermontage angeordnet.

5.2.2 Überbauten

Die Überbauten werden in der Reihenfolge zuerst Straßenträger, *(Bild 23)* und dann Eisenbahnträger vom Schwimmkran transportiert und auf die Pressen auf dem Pfeilerkopf abgesetzt. Die 2 m breite Fuge zwischen zwei aufeinander folgenden Trägern wird unter geschützten Bedingungen und teilweise mit Dampferhärtung geschlossen *(Bild 24)*. Danach werden die Feldspannglieder vorgespannt und injiziert. Anschließend erfolgt der Verguß der Lagerfugen zum Pfeiler und zum Überbau. Das Trägerpaar – ein Einfeldträger mit 2 Kragarmen – wird auf die Topflager abgesetzt. Der Aufbau des Durchlaufträgers erfolgt durch Schließen der Fugen zwischen den Trägerpaaren vom Festpunkt aus. Zum Einstellen der Lager, die ohne Voreinstellung bei der Montage verwendet werden müssen, werden die Träger vorher durch hydraulische Pressen in den offenen Fugen verschoben.

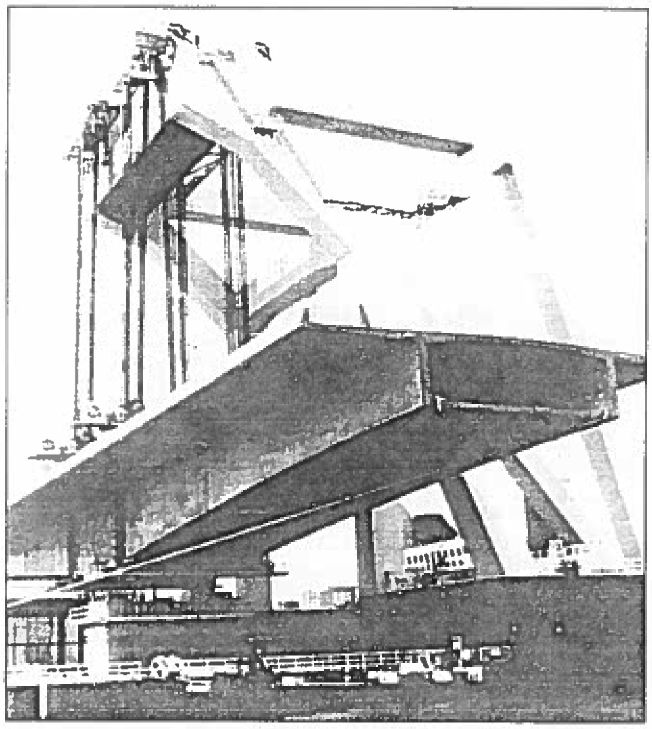
Bild 23. Straßenträger 63 beim Ablassen auf den Pfeiler 63

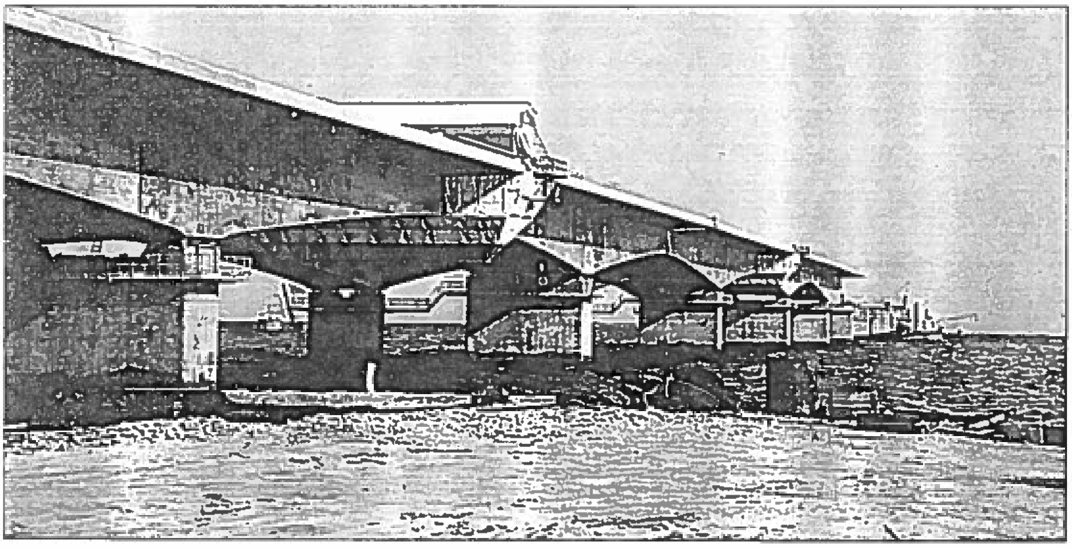
Bild 24. Blick entlang von montierten Straßenträgern mit Schutzzelt für das Betonieren der Fugen in Feldmitte

6. Stand der Arbeiten

Ende März 1992 waren etwa 2000 m, das sind knapp ein Drittel der Gesamtlänge, montiert und teilweise endgültig miteinander verbunden. Der Fortschritt der West Brücke wird zur Zeit durch die Herstellung der Elemente bestimmt. Alle 10 Tage werden die Teile für ein Brückenfeld bestehend aus einem Caisson, zwei Pfeilerschäften und zwei Trägern gefertigt und montiert. Nach dem gültigen Terminplan wird der Eisenbahnbetrieb Ende 1994 aufgenommen werden, der Straßenverkehr soll 1997 folgen.

7. Schlußbemerkung

A/S Storebaeltsforbindelsen wird an dieser Stelle für die Zustimmung zur Veröffentlichung dieses Vortrages gedankt.